Physique de la biogenèse des corps lipidiques

Aymeric Chorlay

PSL
UNIVERSITÉ PARIS

THÈSE DE DOCTORAT
DE L'UNIVERSITÉ PSL

Préparée à l'École Normale Supérieure

Physique de la Biogenèse des Corps Lipidiques

Soutenue par
Aymeric CHORLAY
Le 29 novembre 2019

Ecole doctorale n° 564
Physique en Île de France

Spécialité
Physique de la matière biologique

Composition du jury :

Alenka, ČOPIČ Dr, Institut Jacques Monod	*Rapportrice*
Annie, VIALLAT Dr, Université Aix Marseille	*Rapportrice*
Bruno, ANTONNY Dr, IPMC	*Examinateur*
Cécile, SYKES Dr, Institut Curie	*Examinatrice*
Damien, BAIGL Pr, Ecole Normale Supérieure	*Président*
Jacques, PROST Dr, Institut Curie	*Invité*
Abdou Rachid, THIAM Dr, Ecole Normale Supérieure	*Directeur de thèse*

ENS | PSL

Remerciements

Tout d'abord, je souhaite remercier Rachid THIAM, sous la direction duquel ce travail a été réalisé. J'ai particulièrement apprécié la confiance qu'il m'a toujours témoigné, et la façon dont il m'a aidé à trouver le bon cheminement en choisissant judicieusement nos outils et en me faisant prendre du recul, aux moments où je m'égarais. Merci Rachid, je pense avoir beaucoup appris avec toi, toujours avec bonne humeur, passion et efficacité. Je garderais un souvenir impérissable de ces trois années !

Je remercie Alenka Copic, Annie Viallat, Bruno Antonny, Cecile Sykes, Damien Baigl et Jacques Prost d'avoir accepté de faire partie de mon jury de thèse et d'avoir nourri de leurs sciences les réflexions lors de ma soutenance. J'adresse en particulier mes sincères remerciements à Alenka Copic et à Annie Viallat qui ont bien voulu être les rapportrices de mon travail, et ainsi apporter deux regards complémentaires à celui-ci.

Je remercie aussi Lionel Fôret, avec qui j'ai eu, à de nombreuses reprises, de longs échanges qui ont nourri mes recherches et mes réflexions. Je l'en remercie sincèrement.

J'exprime ma gratitude à Jorge Kurchan et Jean Francois Allemand, de m'avoir accueilli au Laboratoire de Physique Statistique de l'École Normale Supérieure puis au tout nouveau Laboratoire de physique de l'École Normale Supérieure, et remercie Nora Sadaoui, Annie Ribaudeau, Benoît Paulet et Fabienne Reina, et Dounia Benzouak pour leur humour et leur aide face aux démarches administratives, pas toujours très simples, ainsi que Zaire Dissi pour sa précieuse aide informatique.

Je remercie enfin tous les membres de notre équipe au laboratoire, et plus particulierement : Kalthoum pour la bonne humeur et le soutien psychologique musclé en cas de coup de mou, Dalila, pour la bienveillance et les éclats de rire, Alexandre, pour les "viens voir deux minutes" suivis par une demi heure de discussion passionné, Mohyeddine, pour sa gentillesse et son aide précieuse sur les questions de biologie cellulaire, Lucie, pour la relecture professionnelle et la détection infaillible de fautes d'orthographe, Dominique et Sophie, chers cothèses, compagnons de rédaction, de galère et de remonte moral à la montagne, ca y est on l'a fait qui l'eut cru !! et pour finir Vincent et Chloé, pour la bonne humeur générale au labo !

Je souhaite finalement remercier tous ceux qui m'ont soutenue pendant cette période de ma vie, et avec qui j'ai passé de précieux moments le reste du temps, Alex, Pauline, Vincent, Judith, Gaetan, Lise, Grégoire, Blandine, Benoit, Jean Phillippe, Eunok, Thomas, Charlène, Kevin, Elodie, Adrien, Alizée, Guillaume, Sophie et Marie bien sûr. C'est vrai que l'amitié double les joies et réduit la moitié des peines ! Et c'est aussi à eux que je dois ce travail !

Je veux aussi remercier ma famille sans qui je ne serait pas arrivé jusque là ! Merci mes chers parents Anne et Eric, mes grands parent Pierre et Monique, ma soeur Ennata et mon frère Olwen, je nous vous dis pas assez combien vous comptez pour moi. J'ai aussi une pensée toute particulierement émue pour mon Papy Gérard et ma mamie Michelline qui m'ont inoculé le virus de la curiosité et de l'esthétique qui ne m'a jamais quitté tout au long de cette thèse.

Et bien sûr Océane qui m'a aidé à garder ma motivation, à rediger l'introduction, à organiser ce manuscrit et ma pensée. Merci pour tes encouragements, tes attentions bienveillantes et ton soutien indéfectible.

Cette thèse est également la tienne. Merci du fond du cœur Océane !

Sommaire

Introduction

Pour survivre, le vivant doit être capable de s'adapter aux diverses causes de changement. Dans un environnement où les ressources en énergie sont fluctuantes, il lui est indispensable de pouvoir gérer les apports et les consommations d'énergie. Pour assurer le maintien de son fonctionnement qui nécessite un apport régulier en énergie, il doit avant tout être en mesure d'en stocker une partie afin de survivre en cas de pénuries.
Dans nos sociétés modernes où la surconsommation de sucre et de graisse est de plus en plus présente, nous constatons une augmentation des maladies liées à une gestion déficiente des flux d'énergie : par exemple, la surabondance de nutriments peut provoquer l'obésité et un mauvais stockage est souvent associé à différentes pathologies telles que certains types de neuro-dégénérescence, le diabète, la stéatose du foie et des maladies cardiovasculaires. Dans ce contexte, il devient alors nécessaire de mieux comprendre les mécanismes du métabolisme énergétique et les études dans ce domaine se multiplient.
Au niveau cellulaire, l'apport d'énergie se fait par l'intermédiaire de nutriments tels que les sucres, les graisses, les acides aminés, etc., provenant d'une alimentation externe ou fabriquée in situ comme c'est le cas chez les plantes grâce à la photosynthèse. Pour maintenir son métabolisme en cas de carence nutritive, la cellule doit être capable de stocker l'énergie. Dans la plupart des cellules eucaryotes, le processus de stockage commence par la production de molécules à haut potentiel énergétique, à savoir des lipides neutres (typiquement les triglycérides ou les stérol ester). Ces lipides neutres sont par la suite accumulés pour former des gouttelettes d'huile appelées corps lipidiques.

Les corps lipidiques sont généralement considérés comme des réservoirs d'énergie. C'est effectivement leur fonction principale car les lipides neutres qu'ils stockent peuvent être utilisés pour produire de l'ATP, grâce à la béta-oxydation. Néanmoins, de récentes découvertes mettent en lumière la richesse de ces organelles qui semblent avoir des fonctions plus variées. Par exemple, lors de l'expansion cellulaire, les lipides neutres stockés peuvent être utilisés comme matériaux de construction pour les membranes. La formation des corps lipidiques permet aussi de protéger la cellule de la lipotoxicité en isolant des acides gras, glycérolipides toxiques et stérols intra-membranaires à l'intérieur de leurs noyaux huileux [1–3].
La surface des corps lipidiques est aussi un lieu où se concentrent certaines protéines. Si la plupart sont des protéines liées au métabolisme des corps lipidiques (synthèse de lipides neutres et lipolyse), d'autres, comme les histones, les utilisent comme plateforme de stockage[4].
Suite à une décennie de recherche intense sur la biologie des corps lipidiques, il est de plus en plus clair que les corps lipidiques sont des organelles cruciales pour le métabolisme cellulaire qui collaborent avec un grand nombre d'autres organelles, comme par exemple, le réticulum endoplasmique, les mitochondries, les vacuoles, les lysosomes, les peroxysomes, etc. Les grandes avancées dans ce domaine suscitent un dynamisme toujours plus grand, et soulèvent de nouvelles questions telles que celles se rapportant au mode de recrutement des protéines à

leur surface, aux mécanismes d'interaction avec les autres organelles et aux processus relatifs à leur valorisation ou leur dégradation.

Parmi ces questions encore non élucidées, le mécanisme de la biogenèse des corps lipidiques occupe une place de premier rang : c'est en effet une étape cruciale, car c'est au cours de leur formation que les corps lipidiques acquièrent la plupart des caractéristiques qui détermineront leur utilisation future par la cellule.
Même si la formation des corps lipidiques est aujourd'hui largement méconnue, on peut proposer un mécanisme de formation suivant une succession d'étapes conceptuelles : dans un premier temps, en cas de surabondance de nutriments, des lipides neutres sont produits par un processus complexe qui se termine par une étape catalysée par des enzymes situées au niveau de la membrane du réticulum endoplasmique. Du fait de leur forte hydrophobicité, il est probable que les lipides neutres ainsi produits trouvent refuge dans la zone hydrophobe située entre les deux feuillets de la bicouche du réticulum endoplasmique. Ces lipides neutres sont ensuite accumulés à l'intérieur de la membrane du réticulum, et finissent probablement par démixer en formant une petite lentille huileuse. Cette lentille continue à grandir en absorbant un nombre croissant de lipides neutres, et bourgeonne dans le cytoplasme de la cellule pour devenir un corps lipidique. C'est probablement lors de cette formation que les corps lipidiques recrutent à leur surface les protéines clés qui détermineront leurs fonctions futures dans la cellule. Enfin, il est possible que certains corps lipidiques finissent par se détacher du réticulum endoplasmique.
A la fin de cette formation, le corps lipidique mature est composé d'un noyau de lipides neutres (principalement des triglycérides et stérol esters), entouré d'une monocouche de phospholipides provenant du réticulum endoplasmique, dans laquelle sont insérés différents types de protéines.

Puisque les corps lipidiques forment par définition une émulsion intracellulaire d'huile dans l'eau, leur formation peut donc être vue comme un mécanisme d'émulsification de gouttelettes d'huile dans le cytoplasme. C'est pour cela que nous avons décidé d'utiliser les outils de la physique de la matière molle, adaptés à la description d'un tel phénomène. Ils devraient ainsi apporter une compréhension originale au mécanisme de la biogenèse des corps lipidiques et répondre à **la problématique de ce manuscrit, à savoir : comment se forment les corps lipidiques ?**
Plus précisément, nous essaierons de déterminer à l'aide d'un modèle *in vitro* les paramètres physico-chimiques contrôlant le bourgeonnement des CLs. Ensuite, nous chercherons à comprendre quels outils la cellule peut utiliser pour maîtriser ce bourgeonnement et quelles sont les conditions nécessaires à son bon déroulement. Enfin, nous étudierons les paramètres modulant le recrutement de certains motifs protéiques à la surface des CLs.

Partie I :

État de l'art

Chapitre 1

Généralités sur les corps lipidiques

1. Préambule : Histoire des corps lipidiques.

Les matières grasses, que l'on appelle aujourd'hui les lipides, ont commencé relativement tôt à être utilisées par l'homme. On s'en sert en effet depuis l'antiquité comme source d'énergie, particulièrement pour l'éclairage, comme par exemple dans les lampes à huile. Mais elles servaient aussi de matière première pour la confection du savon (savon d'Alep, de Marseille), premier détergent contenant des tensioactifs de synthèse. Un des composants principal de ces matières grasses, les triglycérides (TGs), ont été découverts et caractérisés dans les années 1800. En 1894, Richard Altman relate sa première observation de stockage de TGs dans la cellule [5], il relève plus particulièrement la présence d'accumulation de globules huileux qu'il considère comme étant des dépôts inertes de matières grasses dans les cellules. Ce point de vue perdurera pendant de nombreuses années, jusqu'à ce que l'on se ré-intéresse à leurs fonctions dans les années 2000. On comprit alors qu'il s'agissait d'organelles très dynamiques qui ont un rôle crucial dans le métabolisme énergétique cellulaire. On découvrit que c'était des gouttelettes huileuses principalement constituées de TGs et de sterol ester (SEs), qui, contrairement aux autres organelles cellulaires, ont la particularité d'être délimitées par une monocouche de phopholipides dérivées du réticulum endoplasmique [6]. Ces organelles furent rebaptisées corps lipidiques (CLs) ou gouttelettes lipidiques.
Ce chapitre met en perspective une partie des connaissances établies sur ces organelles particulières et présente les concepts de physique que nous avons utilisés pour comprendre le mécanisme de leur biogenèse.

2. Qu'est ce qu'un corps lipidique ?

Les corps lipidiques (CLs), ou lipid droplets (LDs) en anglais, sont des organelles dynamiques, principalement retrouvées dans les cellules eucaryotes, dont le rôle principal est de stocker des lipides. La taille des CLs varie de quelques centaines de nanomètres à quelques centaines de micromètres selon le type cellulaire et le degré de maturation et l'état métabolique de la cellule. Par exemple, les CLs des levures ont souvent un diamètre inférieur au micron alors que chez les adipocytes, on observe des gouttes lipidiques uniques pouvant dépasser la dizaine voir la centaine de microns (Figure 1). Les lipides stockés dans ces CLs, peuvent être valorisés soit comme source d'énergie, ou en fournissant des matériaux de construction pour la fabrication des nouvelles membranes, par exemple lors de l'expansion cellulaire. Les CLs sont donc des organelles qui jouent un rôle central dans le métabolisme de la cellule.

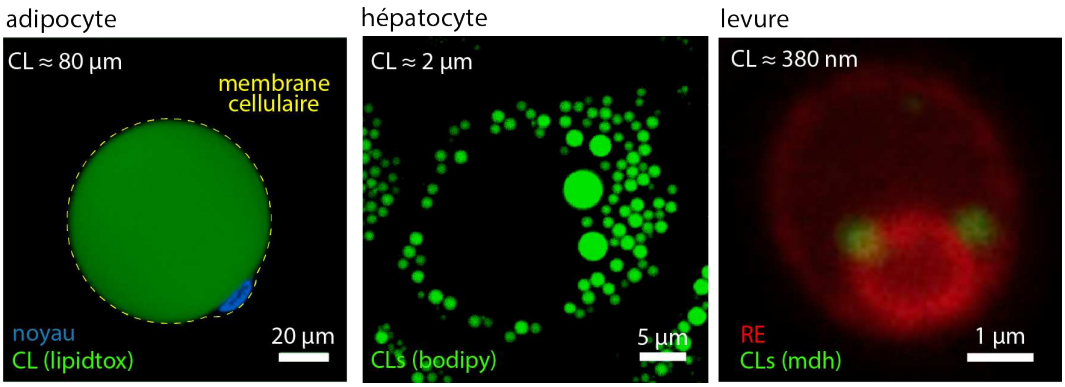

Figure 1 – **Exemple de corps lipidiques de taille très variées selon le type cellulaire** : respectivement, adipocyte blanc de souris (Hagberg et al., 2018) CLs, hépatocyte humain (huh7) et levure Saccharomyces Cerevisiae (Chorlay et al. 2019).

Ils sont ainsi présents dans une grande variété de types cellulaires : des hépatocytes aux neurones, des cellules cancéreuses aux levures en passant par les cellules végétales[7,8]. Ce sont des organelles qui sont principalement situées dans le cytoplasme de la cellule même si, dans certains types cellulaires, des CLs ont parfois été observés dans le compartiment nucléaire[9]. Ce contact avec le cytoplasme est en effet crucial pour le métabolisme car une grande partie des protéines et enzymes qui utilisent les lipides sont situés dans le cytoplasme. De plus, les CLs interagissent quasiment avec toutes les organelles cytoplasmiques en échangeant avec elles lipides et protéines[10].

3. D'où proviennent les CLs ?

Les CLs sont principalement formés *de novo* à partir du réticulum endoplasmique[11,12] (RE). Le RE est une organelle présente dans le cytoplasme des cellules eucaryotes qui est constitué d'une membrane (bicouche de phospholipides) en continuité avec la membrane nucléaire. La membrane du RE délimite son intérieur appelé « Lumen du réticulum », du cytoplasme de la cellule. Les principales activités du RE sont la synthèse et le transport de protéines par la voie ribosomale, et la production de lipides (phospholipides membranaires, cholestérol, stéroïdes...). Le RE est donc une organelle centrale qui fournit une grande partie des matériaux lipidiques et protéiques qui composent la cellule, et plus particulièrement le lieu de synthèse des lipides neutres qui sont les principaux constituants des CLs[13].

Pendant des périodes riches en apports énergétiques, ces lipides neutres formés en grande quantité sont rassemblés pour constituer une phase huileuse à l'intérieur de la membrane. Cette dernière délamine cette bicouche pour donner naissance à une nouvelle organelle : le corps lipidique (Figure 2). La plupart des CLs sont formés dans le cytoplasme et restent connectés au RE par des « ponts membranaires » encore peu caractérisés (Figure 2). Contrairement aux autres organelles, la surface du CL est composée d'une monocouche de phopholipides provenant probablement des feuillets du réticulum[14]. On peut supposer que cette particularité influence directement les interactions des CLs avec les protéines et les autres organelles, et détermine ainsi ses fonctions au sein de la cellule.

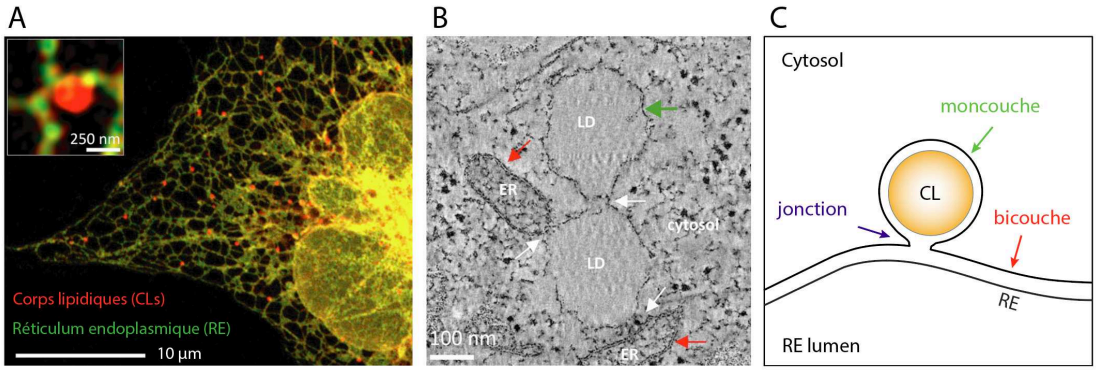

Figure 2 – **Les corps lipidiques sont formés à partir du réticulum endoplasmique.** **A** Cellule de COS-1 (fibroblastes de rein de singe vert d'Afrique) observées au microscope présentant des CLs (rouge) en formation à partir du réticulum endoplasmique (vert). Image de Kassan et al. 2013. **B** Image de cellule de COS-1 (Tomographie électronique) montrant des CLs en contact avec la membrane de RE (flèches violettes). Les flèches rouges indiquent la bicouche du RE et la flèche verte la monocouche de phospholipides qui délimite le CL. Image de Kassan et al. 2013. **C** Vue schématique d'un CL en contact avec son organelle mère, le RE. Les flèches suivent le même code de couleur qu'en B.

4. Quels sont les rôles des CLs dans la cellule ?

Même si les CLs ont été considérés pendant des décennies comme des inclusions passives de matières grasses, il est maintenant reconnu que ce sont des organelles complexes et dynamiques qui ont un rôle central dans la régulation de l'homéostasie des lipides.

Au-delà de leur rôle très étudié de régulateur du métabolisme énergétique, les CLs sont en effet de plus en plus regardés comme étant aussi des intermédiaires et des plateformes pour des processus biologiques plus variés. En effet, de plus en plus d'études suggèrent que les CLs participent aussi à la neutralisation de lipides toxiques, au contrôle de la qualité des protéines et qu'ils sont au centre des mécanismes d'infection de certain pathogènes.

4.1. Stock d'énergie et de matériaux :

Le principal rôle physiologique des CLs est de stocker des lipides, de manière à pouvoir les réutiliser ultérieurement en cas de besoin. Ils ont ainsi un rôle de tampon énergétique dans le métabolisme de la cellule.

Pendant les périodes où la cellule a accès à d'importantes quantités d'énergie, elle peut stocker une partie du surplus en transformant les nutriments surabondants en lipides neutres qui sont accumulés dans les CLs (Figure 3 A). Les lipides neutres stockés pourront ensuite être réutilisés comme source d'énergie grâce à la bêta-oxydation des acides gras qui les composent (Figure 3 B). L'accumulation de CLs permet ainsi une amélioration de la survie dans un environnement pauvre en nutriments, comme ce qui a été montré chez la levure[15,16].

Les CLs peuvent aussi être valorisés comme matériaux précurseurs des phospholipides nécessaires à la formation de membranes pendant les phases de remodelage et de prolifération cellulaire. A l'inverse, en cas de disette, la cellule peut aussi consommer une

partie de ses organelles pour les transformer en lipides neutres qui seront stockés dans les CLs et servirons par la suite de source d'énergie palliative. Le CL est donc l'organelle centrale qui tamponne ce va-et-vient entre source d'énergie, nutriments et matériaux de construction cellulaire.

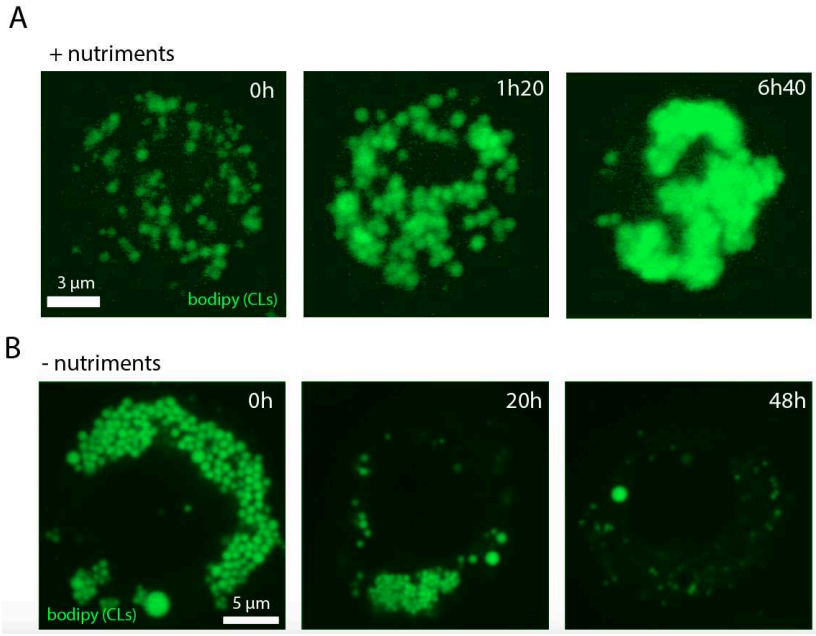

Figure 3 – **Les CLs stockent et fournissent des nutriments sous forme de lipides neutres. A**, Image au microscope de cellule de drosophile (Drosophilia S2) au cours du temps après incubation avec des nutriments (acide gras 1mM). La quantité de CLs (marqué avec du Bodipy vert) augmente significativement. Barre d'échelle 3 µm. Adapté de Guo et al. 2018. **B**, Image au microscope de cellule de drosophile (Drosophilia S2) au cours du temps observée dans un milieu pauvre en lipides. Après 48h, les CLs sont consommés par la cellule et leur quantité est drastiquement diminuée. Barre d'échelle 5 µm. Adapté de Kory et al. 2015.

Pour pouvoir valoriser les lipides neutres stockés dans leurs noyaux, les CLs doivent être capables de restituer les acides gras (AGs) qui les composent aux organelles destinées à les utiliser. La première manière de récupérer des acides gras est appelée la lipolyse. Ce processus est principalement mené par l'action de lipases cytoplasmiques qui se lient à la surface des CLs et hydrolysent les triglycérides (TG) pour produire des acides gras (Figure 4). Dans les tissus adipeux et chez de nombreux autres types cellulaires, l'hydrolyse des TG se fait par une cascade de lipase dont la première est appelée ATGL (adipose triglycéride lipase[17]). Ces acides gras seront ensuite dirigés vers les organelles compétentes telles que les mitochondries. Une autre manière de remobiliser les lipides neutres contenus dans les CLs est de les dégrader directement via l'autophagosome qui englobe les CLs et digère ces derniers (Figure 4). Les acides gras qui sont produits peuvent ensuite être redirigés vers la mitochondrie en vue de produire de l'énergie[18] ou dans le RE pour produire de la membrane. Les acides gras ainsi libérés doivent ensuite être dirigés vers les organelles compétentes pour les valoriser. Pour favoriser cette opération, il semblerait que les CLs établissent des points de contact avec les organelles concernées (Figure 4).

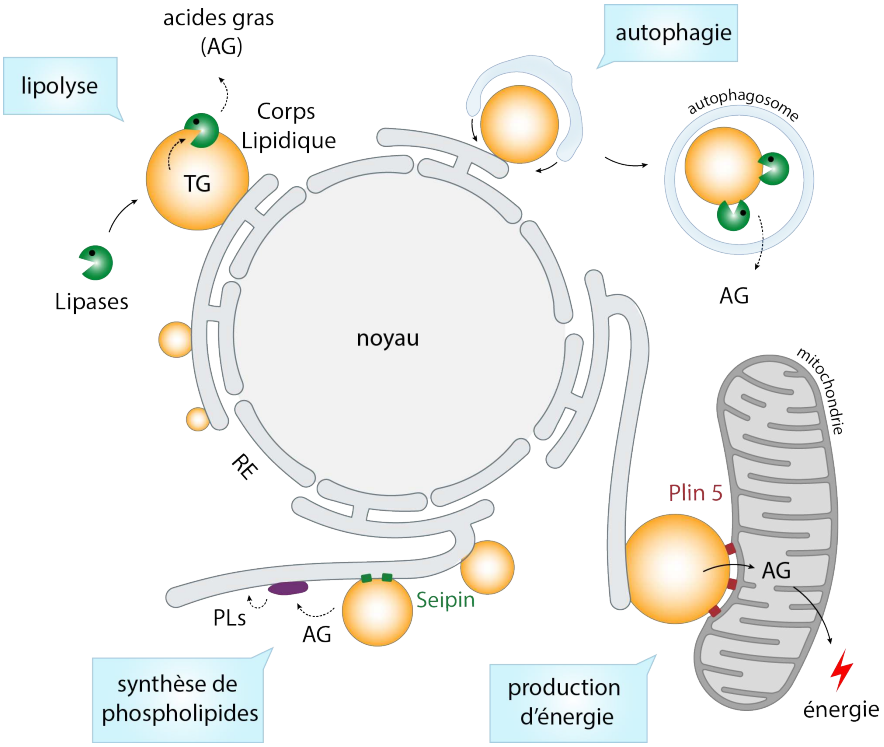

Figure 4 – **Les lipides neutres contenus dans les CLs peuvent être remobilisés en les transformant en acides gras valorisables par le métabolisme de la cellule.** Les deux voies principales de production d'acides gras sont : 1) la lipolyse où des enzymes recrutées autour des CLs « découpent » les lipides neutres, par exemple des triglycérides (TG), pour produire des acides gras et 2) l'autophagie des CLs, où ces derniers, englobés par la membrane d'un autophagosome, vont être digérés par des enzymes présentes à l'intérieur et ainsi libérer leurs acides gras. Les acides gras ainsi produits pourront être valorisés par la cellule par exemple pour produire de l'énergie au niveau des mitochondries ou être transformés en phospholipides par des enzymes présentes au niveau du RE. Il est supposé que l'interaction CLs-mitochondries soit stabilisée par la protéine perilipine 5 (Plin 5) et que la Seipin soit indispensable à la régulation des points de contact CLs-RE. (Figure inspiré de Henne et al 2018)

Chez les mammifères, certains CLs paraissent interagir étroitement avec les mitochondries. Cette interaction est particulièrement proéminente dans les muscles du cœur[19,20], ce qui semble suggérer que les CLs interagissent avec les mitochondries pour faciliter un transfert d'acides gras vers la mitochondrie. Cette dernière les utilise pour produire de l'énergie grâce à la bêta-oxydation et au cycle de Krebs (Figure 5). Pour appuyer cette possibilité, il a été démontré, en utilisant des acides gras marqués incorporés dans des lipides neutres, qu'il existait bien un transfert d'acides gras entre les CLs et les mitochondries lors de régimes pauvres en énergie[21]. Des études supposent que l'interaction nécessaire entre les mitochondries et les CLs serait même stabilisée par des protéines spécifiques comme la perilipine 5 [22] (Figure 4).

Les acides gras (AG) peuvent aussi être valorisés pour produire les phopholipides nécessaires à la construction de membranes. Le principal lieu de synthèse de phospholipides se situe au niveau du feuillet cytoplasmique du RE [23]. On peut donc proposer que les CLs

puissent rester en relation avec le RE de manière à pouvoir adresser plus efficacement les acides gras nécessaires à la synthèse de phopholipides (Figure 4).

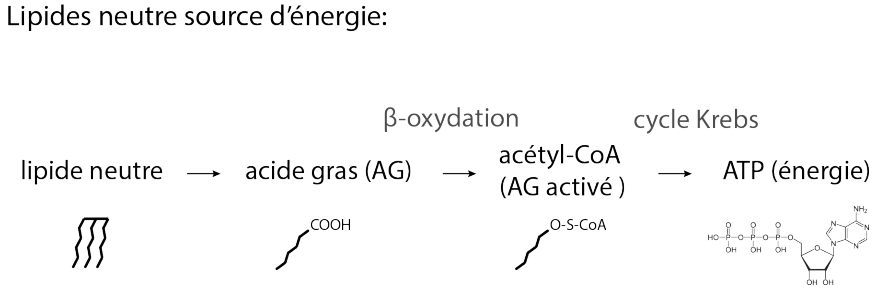

Figure 5 – **Vue schématique de la cascade de réactions permettant la production d'énergie à partir des lipides neutres contenus dans les CLs**. Les lipides neutres sont d'abord découpés pour produire des acides gras qui une fois activés lors de la beta-oxydation sont consommés dans le cycle de Krebs pour produire de l'adénosine triphosphate (ATP) molécule dont l'hydrolyse fournit l'énergie chimique nécessaire à la survie de la cellule.

Pour être capables de valoriser efficacement leurs lipides neutres, les CLs doivent donc être cpables d'interagir avec plusieurs organelles et enzymes qui se trouvent dans le cytoplasme. On comprend donc l'importance de contrôler précisément le lieu de la formation des CLs pour leur permettre de mener à bien leur fonction essentielle.

4.2. Protéger la cellule de la lipotoxicité :

En plus de servir de réservoirs d'énergie pendant les périodes de faible apport en nutriments, les corps lipidiques ont aussi des fonctions de neutralisation d'espèces toxiques qui peuvent mettre en danger la cellule en cas d'accumulation trop importante.

C'est le cas des lipides simples (e.g. des acides gras ou des stérols) qui, s'ils sont présents en trop grande quantité, s'accumulent dans le RE et altèrent ses propriétés, ce qui empêche le RE d'assurer correctement ses fonctions essentielles à la survie de la cellule (synthèse de lipides, génération de membranes, sécrétion de protéines). Des mécanismes sont donc mis en place pour neutraliser ces lipides toxiques en les transformant en lipides neutres non toxiques. Ces derniers sont alors dirigés vers les CLs dont ils alimentent la formation. La formation des CLs peut ainsi être considérée comme une manière de drainer les lipides toxiques hors de la membrane du RE pour les séquestrer à l'intérieur du noyau des CLs (Figure 6).

Effectivement, les cellules cultivées dans un milieu riche en acides gras produisent de nombreux CLs [25] et il a été observé que les cellules ayant une biogenèse des corps lipidiques déficiente présentaient un plus fort taux de mort cellulaire [3]. Ceci indique que la conversion des acides gras en triglycérides est généralement un facteur de protection contre la lipotoxicité induite par les acides gras [26]. L'accumulation anormale de lipides simples peut effectivement déclencher un stress du réticulum endoplasmique, ce qui provoque l'activation de l'UPR (Unfolded Protein Response, un des principaux mécanismes de réponse au stress) et endommage la cellule.

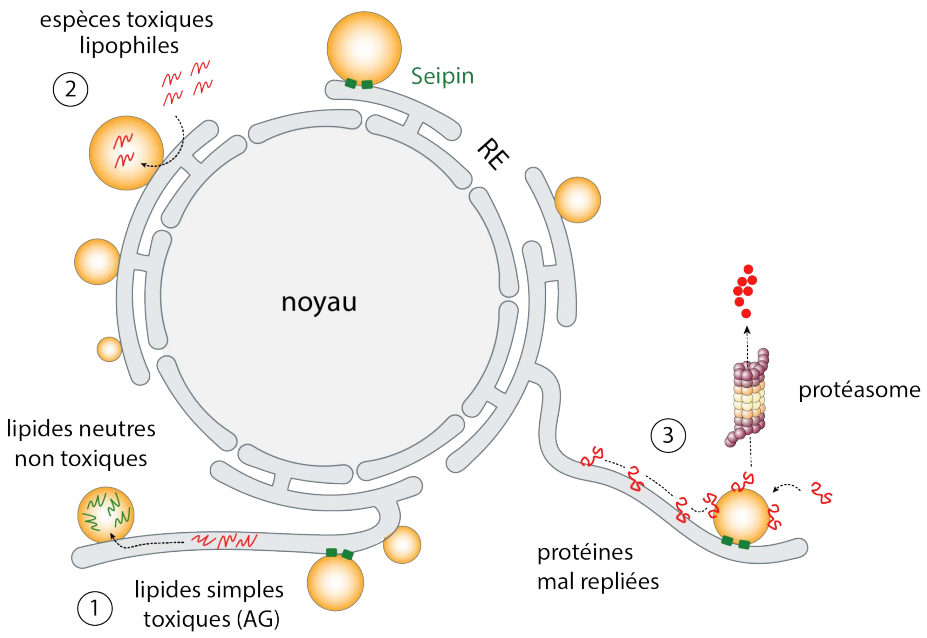

Figure 6 – **Les CLs, organelles protectrices contre la lipotoxicité et les protéines mal repliées.** 1. Les lipides simples (e.g Acide Gras), qui sont toxiques pour le RE, sont drainés hors de sa membrane pour être séquestrés sous forme de lipides neutres dans les CLs. 2. Les CLs séquestrent aussi d'autres espèces toxiques lipophiles à l'intérieur de leurs noyaux de lipides neutres. 3. Des protéines non fonctionnelles mal repliées sont concentrées à la surface des CLs avant d'être probablement dégradées par des protéasomes. (Figure inspiré de Henne et al 2018)

Pour pouvoir neutraliser les lipides simples toxiques en les séquestrant dans leur noyau, les CLs doivent entretenir une interaction efficace avec le RE. Au cours de leur formation, certains CLs semblent en effet rester connectés physiquement au RE par l'intermédiaire de ponts de phospholipides (Figure 2), comme ce qui a été observé chez la levure [27] ou encore chez les mammifères sur des zones de membrane étendues en forme de coquetiers [28,29]. Une des fonctions de ces points de contact serait ainsi de permettre aux lipides neutres synthétisés dans le réticulum endoplasmique de rentrer dans les corps lipidiques en formation et de participer à leur grossissement. Les caractéristiques de tels ponts sont pour l'instant peu décrites mais on peut imaginer que certains phopholipides et certaines protéines pourraient être recrutés dans ces zones de contact, contrôlant ainsi leur topologie et régulant la communication entre le RE et le CL en formation. Il a été récemment proposé que la Seipin (Figure 6), une protéine transmembranaire co-localisant avec ces points de contact RE-CL, soit impliquée dans le maintien et l'établissement de tels ponts de communication [24,106].

Les CLs peuvent aussi protéger la cellule des effets de certaines espèces de lipophiles toxiques qui s'accumulent directement dans les noyaux de lipides neutres hydrophobes (Figure 6). Par exemple, il a été montré que certains lipides toxiques produits par les mitochondries (acylcarnitines) sont dirigés vers les CLs, ce qui les isole du reste de la cellule et prévient leur lipotoxicité [31].

4.3. Contrôle de la qualité des protéines :

A l'instar de leur rôle dans le traitement des lipides toxiques, il semblerait que les corps lipidiques soient capables de réguler la présence de protéines non fonctionnelles en les orientant vers des processus de dégradation.

En effet, il a été récemment proposé que les corps lipidiques puissent être capables d'avoir un rôle complémentaire aux chaperonnes cytoplasmiques, en prévenant la toxicité associée aux protéines mal repliées [30]. Il a été ainsi observé que, dans le cas de cellules de levures exposées à un stress protéotoxique induit par la chaleur (connu pour provoquer un dépliage majeur des protéines), les protéines mal repliées sont accumulées à la surface des CLs [32].
On peut comprendre qu'une protéine mal repliée expose ses résidus hydrophobes qui, pour éviter un contact défavorable avec la phase aqueuse, seront probablement plus enclins à se réfugier au contact de la monocouche et du noyau huileux des CLs. Les particularités physico-chimiques à l'origine de ce recrutement spécifique à la surface des CLs et non des autres membranes cellulaires restent cependant pour l'instant peu connues. Il est probable que ces protéines déficientes soient alors acheminées vers des structures assurant leur dégradation, telles que les protéasomes (Figure 6).

Les corps lipidiques sont donc suspectés de servir de réservoir pour les protéines mal repliées destinées à être détruites. Si elles n'étaient pas isolées sur les CLs, ces protéines pourraient en effet former des agrégats toxiques dans le RE [33].

4.4. CLs et agents infectieux :

Pour leur réplication et leur croissance, les pathogènes intracellulaires sont dépendants d'une partie des nutriments et des ressources présents dans la cellule hôte qu'ils infectent. Il n'est donc pas surprenant que les CLs, sources concentrées de lipides et de cholestérol, soient détournés par les pathogènes intracellulaires. de nombreux agents infectieux intracellulaires, que ce soit des virus, des bactéries ou des protozoaires, profitent des corps lipidiques de la cellule hôte à un moment de leur cycle de vie. Par exemple, la bactérie *Chlamydia* et le protozoaire *Toxoplasma* semblent tous les deux récupérer des lipides en entraînant des corps lipidiques près la zone vacuolaire où ils se répliquent [34–36]. Certains virus tel que l'hépatite C utilisent même les gouttes lipidiques comme des plateformes de réplication [37]. Pour de nombreux agents infectieux intracellulaires, l'interaction avec les CLs semble donc être essentielle à leur prolifération. Mieux comprendre ces interactions pourrait ouvrir la porte à de nouvelles approches thérapeutiques.

Conclusion

Les CLs prennent part à de nombreux processus cellulaires tels que la régulation du métabolisme énergétique, la neutralisation ou la séquestration d'espèces toxiques, mais aussi à de nombreux autres processus non abordés dans ce manuscrit. Ils assurent ces fonctions complexes en contact étroit avec d'autres organelles cytoplasmiques avec qui ils doivent être capables d'interagir de manière efficace.

Pour leur permettre de mener à bien ces missions, il est nécessaire que leur formation soit contrôlée de manière à ce qu'une une majorité de CLs soit en contact avec le cytoplasme de la cellule. Il est également important que leurs caractéristiques physicochimiques (monocouche, type de lipides neutres), grâce auxquelles ils semblent recruter des protéines spécifiques, soient finement modulées.

5. De quoi sont composés les CLs ?

5.1. Un noyau de lipides neutres

Les corps lipidiques possèdent un noyau de lipides neutres (Figure 7), formant une phase huileuse principalement composée de triglycérides (TG) et de stérol esters (SE) mais pouvant aussi contenir des rétinyl esters, des cires et des éther-lipides. La diversité des lipides neutres stockés permet à la cellule de répondre à des besoins spécifiques qui varient selon les types cellulaires. Les TGs forment une source d'énergie et sont également nécessaires à la formation de nouveaux phospholipides. Les stérol esters permettent de produire du cholestérol, molécule élémentaire régulant la fluidité de certaines membranes cellulaires. Les huiles et cires plus spécifiques sont utilisées par des cellules spécialisées : par exemple, le squalene retrouvé chez certains poissons [38,39], ou certaines cires retrouvées à la surface de nombreuses plantes pour contrôler l'évaporation [40]. La cellule utilise donc toute la variété physicochimique des lipides pour adapter ses ressources aux besoins spécifiques qu'elle rencontre.

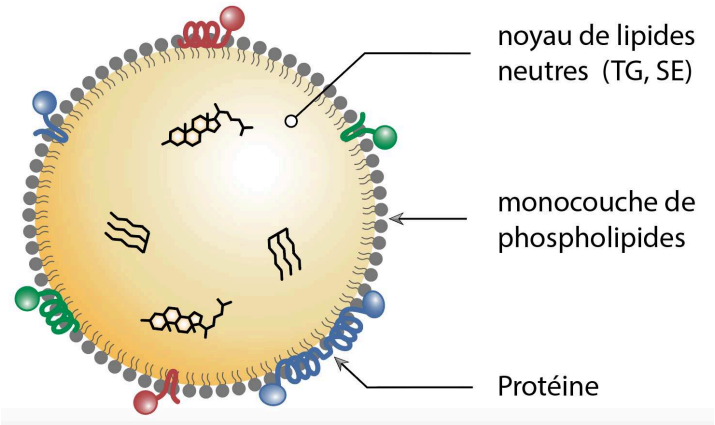

Figure 7 – **Structure et composition d'un corps lipidique** : les CLs sont formés d'un noyau de lipides neutres principalement des triglycérides et des stérol-esters (TG, SE), recouvert par une monocouche de phopholipides où sont implanté de nombreuses protéines.

5.2. Une monocouche de phospholipides :

Contrairement aux autres organelles qui sont toutes délimitées par une bicouche de phospholipides, le noyau des CLs est recouvert par une monocouche de phospholipides

provenant du réticulum endoplasmique [14,41]. Elle est principalement composée de phosphatidylcholine (PC) et de phosphatidylethanolamine (PE) [42]. Les caractéristiques particulières qui différentient la monocouche des CLs de la bicouche des autres organelles sont loin d'être connues [41]. Il a cependant été avancé qu'elles puissent directement influencer le recrutement des protéines spécifiques aux CLs et qu'elles soient ainsi l'un des principaux facteurs régulant ses interactions avec les autres organelles [24,43] (revues correspondantes [44–46]).

5.3. Un protéome de surface :

La monocouche de phospholipides des CLs contient aussi de nombreuses protéines [30,47]. Depuis l'identification des perilipines, protéines recrutées à la surface des CLs qui jouent un rôle crucial dans la régulation du métabolisme des lipides [48–50], des études utilisant des analyses par microscopie [51,52] ou par spectroscopie de masse[47] ont montré que les CLs possédaient entre 50 et 200 différents types de protéines à leur surface [53] .

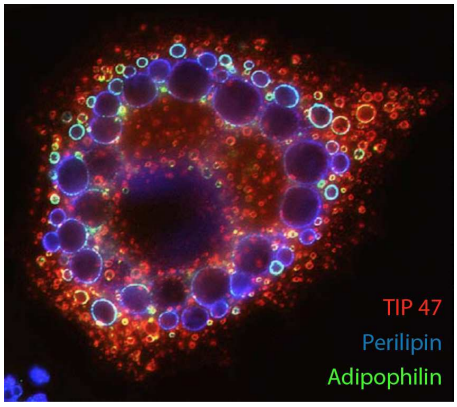

Figure 8 – **Illustration de la diversité des protéines recrutées à la surface des CLs.** Image au microscope d'un adipocyte (3T3-L1) dont certaines protéines associées aux CLs ont été révélées à l'aide d'anticorps marqués : TIP47 en rouge, Perilipin en bleu et Adipophilin en vert. On notera le recrutement spécifique des différentes protéines selon la taille des CLs. Adapté de Wollins et al. 2006.

Même si le rôle de beaucoup d'entre elles reste inconnu, certaines ont été identifiées comme ayant un rôle dans le métabolisme des lipides, comme par exemple dans la synthèse de triglycérides et de stérols. D'autres contrôleraient les propriétés de surface des CLs comme les perilipines qui empêcheraient une lipolyse intempestive en protégeant les triglycérides de l'action des lipases [48–50]. Certaines perilipines sont aussi suspectées d'être nécessaires à l'établissement de points de contact entre les CLs et différentes organelles comme par exemple la perilipine 5 pour les mitochondries [22]. La présence de protéines à la surface des CLs permet aussi à la cellule de différencier les CLs des autres organelles et de distinguer des sous-populations de CLs. On a effectivement observé dans certaines cellules que les CLs ne présentaient pas les même protéines de surface selon leur taille et leur composition en lipides neutres [54–57] (Figure 8).

Le protéome qui recouvre la surface semble donc permettre aux CLs de réguler leurs fonctions au sein de la cellule.

5.4. Mode de recrutement des protéines :

Pour accomplir leur tâche, les protéines qui fonctionnalisent les CLs doivent être sélectivement recrutées à leur surface. Même si les mécanismes contrôlant ce recrutement spécifique ne sont pas encore connus, il est probable qu'ils reposent sur une compatibilité entre les propriétés physicochimiques uniques de la monocouche et les structures d'ancrage des protéines.
On peut tout d'abord écarter les structures en hélices transmembranaires, car le noyau hydrophobe des CLs est trop épais pour permettre une insertion traversante de ces domaines protéiques. Un recrutement par l'intermédiaire de ces domaines transmembranaires exposerait en effet au moins une des deux parties hydrophiles des domaines à des interactions défavorables avec le noyau de lipides neutres.

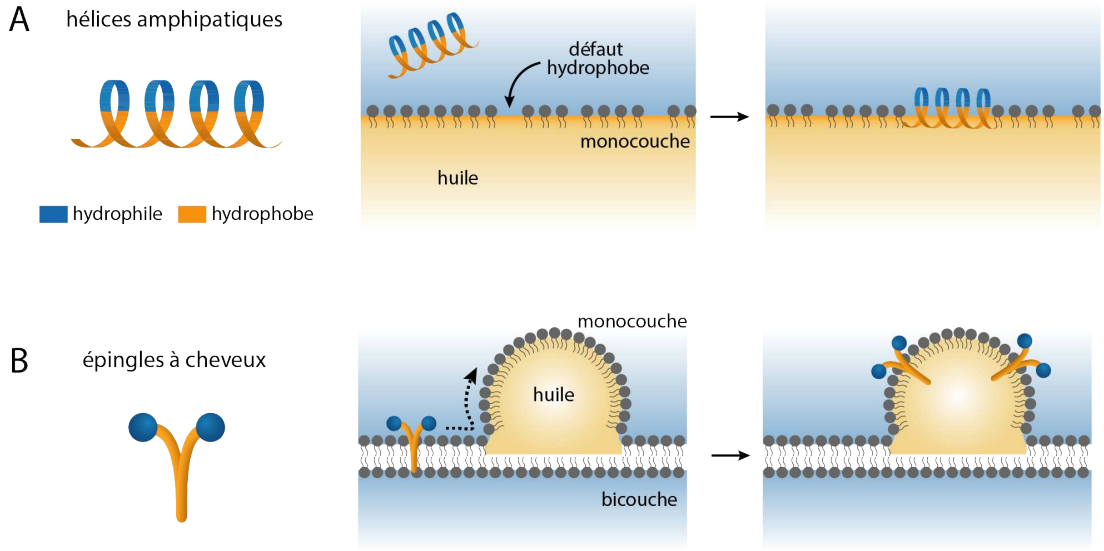

Figure 9 – **Structure permettant aux protéines de cibler la surface des CLs recouverte par une monocouche de phopholipides. A**, Les hélices amphipathiques (HAs) sont des structures protéiques en forme d'hélice qui possèdent deux parties, une hydrophile l'autre hydrophobe, leur conférant une activité de surfactant. La partie hydrophobe des HAs réduit les interactions défavorables avec la phase aqueuse en entrant en contact avec la phase hydrophobe du CL, se recrutant ainsi à sa surface. **B**, Les structures en épingles à cheveux possèdent un domaine fortement hydrophobe habituellement inséré dans le centre hydrophobe des bicouches, leur permettant d'être relocalisés à la surface des CLs.

Les protéines associées aux CLs doivent donc interagir directement avec la monocouche ou être capable de s'ancrer dans le noyau huileux. Deux principaux domaines protéiques ont été proposés pour jouer ce rôle: les hélices amphipathiques et les structures dites en « épingles à cheveux » [58].

Les hélices amphipathiques sont organisées en hélice alpha, qui une fois repliée, présente une partie hydrophobe et une partie hydrophile (Figure 9 A). Elles se comportent donc comme des molécules amphiphiles qui pourront interagir avec la monocouche des CLs. La CCTα (enzyme de synthèse des phospholipides) et la Vipérine (une protéine antivirale) sont des protéines solubles (CCTα dans le noyau, Vipérine dans le cytoplasme) qui possèdent ce

type de structures en hélices amphipathiques et qui peuvent s'associer aux CLs [59,60] . D'autres comme la perilipine 4 possèdent des hélices amphipathiques géantes dont la répétition de motifs amphipathiques permettrait un recrutement collaboratif plus efficace à la surface des CLs [61].
On ne sait cependant pas ce qui permet à ces protéines d'être recrutées préférentiellement sur la monocouche des CLs et non sur les bicouches des autres organelles, mais il a été proposé que des différences de tension surface soient à l'origine d'une telle sélectivité [62]. En effet, les membranes formées par des bicouches sont souvent décrites comme des surfaces fluides et déformables à très basse tension (env. 0.01 mN/m[63]), alors que les CLs peuvent présenter des tension de surface bien plus grandes (env. 2 mN/m[64]). Ces hautes tensions peuvent potentiellement résulter de l'exposition dynamique et partielle des lipides neutres à travers la monocouche de phospholipides qui fournirait des zones de contact hydrophobes favorisant le recrutement des hélices amphipathiques.

L'autre structure présente chez certaines protéines retrouvées à la surface des CLs est dite en « épingle à cheveux ». Elles présentent un domaine fortement hydrophobe qui vient habituellement s'insérer dans le centre hydrophobe des bicouches, comme par exemple dans le réticulum endoplasmique [62] (Figure 9 B). Les protéines utilisant ce type de domaine sont relocalisées à la surface des CLs lors de la formation des ces derniers quand ils partagent un contact avec le RE. La cause de cette migration de protéines possédant des domaines en « épingle à cheveux » n'est pas encore élucidée. Il a cependant été avancé qu'elle pourrait être favorisée par un effet tensioactif des protéines qui, une fois à la surface des CLs, stabiliseraient leur monocouche en diminuant leur énergie de surface [62].

Certaines protéines utilisent probablement un de ces deux types de domaines protéiques pour être recrutées à la surface des CLs, mais les paramètres qui contrôlent cette interaction spécifique restent encore largement méconnus. Comprendre et caractériser ces mécanismes de recrutement est crucial car la couverture protéique des CLs définit leur futur au sein de la cellule, c'est-à-dire comment ils seront stockés, valorisés ou dégradés.

Chapitre 2 :

Mécanisme de formation des CLs.

Les CLs sont des organelles importantes qui ont des rôles cruciaux dans le métabolisme cellulaire, allant de la gestion des surplus d'énergie, à la détoxification du RE en passant par le contrôle de la qualité des protéines. Pour mener à bien ces tâches, ils doivent être formés dans le cytoplasme de la cellule, garder une continuité avec le RE et posséder des caractéristiques physicochimiques de surface bien précises, de manière à recruter les protéines qui détermineront leur future utilisation. C'est principalement au cours de leur formation qu'ils vont acquérir ces caractéristiques spécifiques, faisant de la biogenèse des CLs une étape déterminante de leur existence. Nous proposons ici une revue synthétique des connaissances actuelles portant sur le processus de formation des CLs, qui reste encore peu caractérisé à ce jour.
De manière à faciliter la description du processus de biogenèse des CLs, il nous a semblé utile de le représenter par une succession d'étapes conceptuelles indicatives, car en réalité, il suit peut-être chronologie différente (Figure 10).

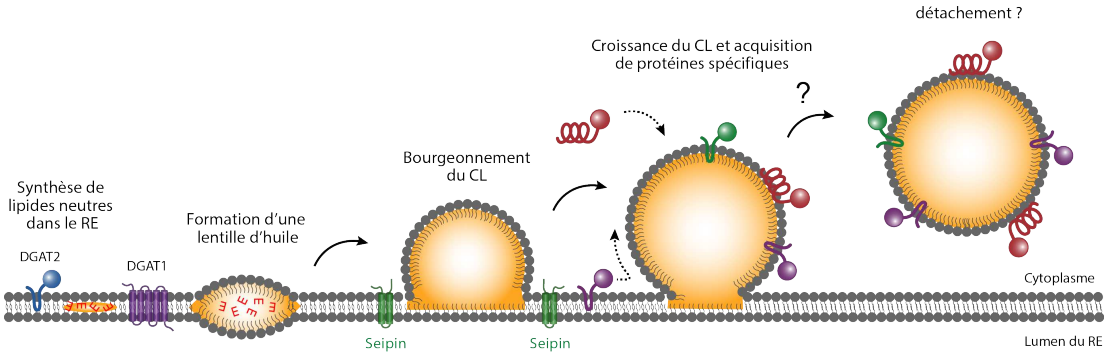

Figure 10 – **Etapes conceptuelles de la formation des CLs à partir du RE.** Synthèse de lipides neutres, formation d'une lentille huileuse, accumulation de lipides neutres et bourgeonnement (i.e émergence) du CL. Acquisition de la couverture protéique et possible détachement du RE. La protéine Seipin est une protéine indispensable à la formation des CLs, qui est recruté au point de jonction entre le RE et les CLS en formation. DGAT, diacylglycerol acyltransferase, catalysant la dernière étape de synthèse des lipides neutres. (Figure inspiré de Walther et al 2017)

1. Synthèse de lipides neutres à l'intérieur du RE

En cas de surabondance de nutriments, la cellule enclenche le processus de formation des CLs. Cela commence par une stimulation de la production de lipides neutres (principalement des triglycérides (TGs) et des stérol-esters (SEs)) au niveau du réticulum endoplasmique [13].

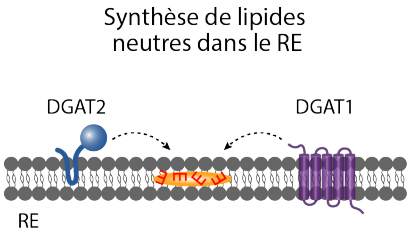

Figure 11 – **Synthèse de lipides neutres dans la bicouche du RE.**

Dans la plupart des cellules, les glycérolipides tels que les TGs sont produits par une voie de synthèse qui utilise du glycerolphosphate et de la fatty acétyl-CoA, un acide gras activé [65]. L'étape finale permettant d'obtenir du TG est catalysée par les enzymes diacylglycerol acyltransferase, DGAT1 et DGAT2 [66–68] (Figure 11). Il a été montré que ces deux enzymes sont nécessaires à la formation initiale des corps lipidiques [56,69].

DGAT1, qui est exclusivement localisée dans le réticulum endoplasmique, est une enzyme transmembranaire qui catalyse la réaction d'estérification nécessaire à la synthèse des lipides neutres. Même si son rôle prédominant est la synthèse de TG, c'est une enzyme qui peut estérifier une grande variété de substrats, tels que le diacylglycerol, le retinol, le monoacylglycerol, et des alcools à chaines longues [70]. Elle joue aussi un rôle dans la neutralisation des excès de lipides provenant de l'extérieur de la cellule [71] et pourrait ainsi prévenir les effets délétères des lipides toxiques à l'origine du stress du réticulum endoplasmique.

DGAT2, au contraire, est localisée à la fois au niveau du réticulum endoplasmique et des corps lipidiques [56,72,73]. Elle ne possède pas de domaine transmembranaire, mais une structure hydrophobe en « épingle à cheveux », lui permettant possiblement de s'accrocher à la surface du réticulum ou des corps lipidiques. Il semblerait que ce soit une enzyme majeure de la synthèse de TG à partir d'acides gras [71,74–76].

Les SEs que l'on retrouve dans la plupart des CLs, sont aussi formés au niveau du réticulum endoplasmique, par exemple par les enzymes Are1 et Are2 chez les levures [77] ou par les enzymes acyl CoA:cholesterol acyltransferase chez les mammifères [66,78,79].

Les lipides neutres synthétisés trouvent ensuite probablement refuge dans l'espace entre les feuillets de phospholipides composant la membrane du réticulum. Il est supposé qu'ils y évoluent sous forme dissoute sans former de phase distincte, jusqu'à une certaine concentration du moins. Même si certains travaux de simulation moléculaire dynamique portent sur le comportement des ces lipides neutre à l'intérieur d'une bicouche [80], il n'existe pas encore de caractérisation expérimentale et théorique complète de ces lipides dissous. On peut cependant avancer que ces derniers doivent sûrement influencer les caractéristiques physico-chimiques de la bicouche et qu'ils ne peuvent pas être accumulés en trop grande quantité sans perturber profondément la membrane du RE.

2. Formation d'une lentille d'huileuse dans le RE

Quand la concentration des molécules de lipides neutres dispersées dans le réticulum endoplasmique atteint un certain niveau, elles finissent par démixer pour former une lentille huileuse de quelques nanomètres (Figure 12). Longtemps restée hypothétique, la présence de ces lentilles naissantes a à été attestée par microscopie électronique dans le RE de la levure [81] (Figure 13).

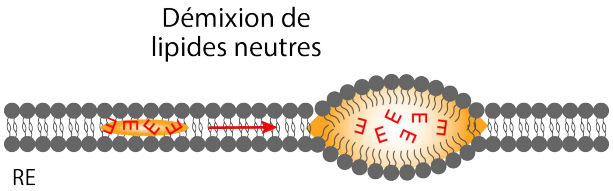

Figure 12 – **Formation d'une lentille d'huile.** A partir d'une certaine concentration de lipides neutres, une lentille d'huile se forme probablement à la suite d'un processus de nucléation.

Même si le mécanisme de formation de ces lentilles reste largement méconnu, il a été proposé qu'elles résultent d'un phénomène de nucléation. C'est-à-dire que les lipides neutres dissous dans la bicouche du RE démixent et se condensent pour former une lentille d'huile de manière à réduire leurs interactions avec les phopholipides de la membrane. Cette formation de lentilles serait ainsi favorisée par le plus faible coût énergétique de l'interaction lipide neutre–lipide neutre par rapport à l'interaction lipide neutre–chaine carbonée des phospholipides [82]. La transition vers une lentille huileuse dans le réticulum endoplasmique diminuera ainsi la quantité de lipides neutres dissous dans le reste de la bicouche, permettant ainsi de réduire son énergie globale. Il a en effet été montré que seulement 3 % de TG peut être supporté sous forme dispersée dans une bicouche avant que des gouttelettes d'huile apparaissent [64,83].

Il n'a pas encore été déterminé si les cellules possédaient des sites spécifiques dédiés à la nucléation de lentilles de lipides neutres. Cependant, le modèle de nucléation prédit par exemple que la composition en phospholipides de la membrane du RE et certaines protéines restreignant la diffusion des phospholipides pourraient hypothétiquement avoir un rôle dans la formation des lentilles.

La formation d'une lentille d'huile à l'intérieur de la bicouche déforme et courbe les feuillets de phospholipides qui composent cette dernière. Certains types de phospholipides possèdent une courbure intrinsèque positive (tels que le dioleoyl-phosphatidylinositol (DOPI) ou le Phosphotidine lysophosphatidylcholine (LPC)) qui est à même d'abaisser l'énergie nécessaire à la déformation des feuillets de phopholipides du RE. Il est donc possible que la cellule tire parti des propriétés de ces lipides en les concentrant dans certaines zones du réticulum pour favoriser la formation localisée de lentilles d'huile [82,84].

Il est aussi probable que des protéines soient impliquées dans la formation des lentilles. Par exemple, la protéine FIT2 a été proposée comme régulatrice du partitionnement des lipides neutres à l'intérieur du réticulum endoplasmique, pouvant ainsi moduler la formation des lentilles à l'origine des CLs (Gross et al. 2011). D'autres protéines comme la perilipin3

pourraient aussi jouer un rôle en stabilisant les lentilles de lipides neutres nouvellement formées [85–87]. Dernièrement certains travaux ont proposé que les protéines Seipin et Pex30 pourraient agir de concert de manière à organiser des domaines membranaires spécifiques favorisant la formation des CLs [88].

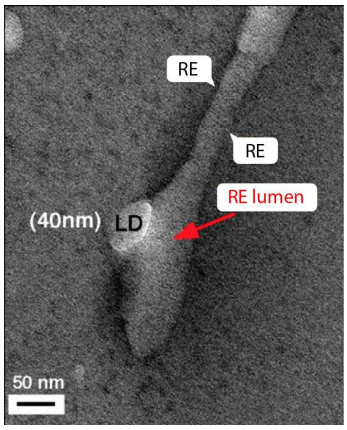

Figure 13 – **Accumulation de lipides neutres formant une lentille d'huile dans le RE.** Observation de cellules de Saccharomyces cerevisiae au microscope cryo électronique après avoir induit la production de TG. Un CL en forme de lentille (LD pour lipid droplet, corps lipidique en anglais) est visible au niveau de la membrane du RE. Adapté de Choudary et al. 2015.

Certaines protéines pourraient ainsi favoriser la nucléation de lentilles de TG dans certaines zones du réticulum endoplasmique ou l'empêcher dans d'autres régions spécifiques [89,90]. Cependant, les fonctions de ces protéines dans la formation des corps lipidiques sont loin d'être totalement élucidées.

3. Bourgeonnement des corps lipidiques

3.1. Un bourgeonnement finement contrôlé

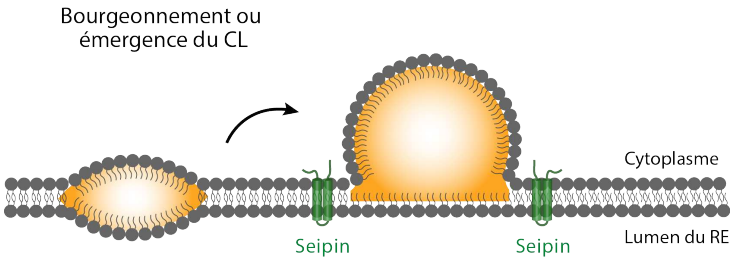

Figure 14 – **Bourgeonnement, aussi dénommé émergence, du CL dans le cytoplasme cellulaire.**

Quand suffisamment de TG est accumulé, la lentille de lipides neutres bourgeonne et ce principalement dans le cytoplasme de la cellule (Figure 14). On ne sait pourtant toujours pas si toutes les gouttes lipidiques bourgeonnent complètement, ou si une partie d'entre elles, voire toutes, restent en contact avec le réticulum endoplasmique. Il a cependant été montré, du moins chez la levure, qu'une fraction d'entre elles reste physiquement connectée avec le réticulum [27]. D'un autre côté, on a observé dans certaines cellules de mammifères, des corps lipidiques qui semblaient complètement détachés du réticulum [91]. Même si la plupart des CLs semblent bourgeonner dans le cytoplasme de la cellule, il a aussi été rapporté que certains

d'entre eux conservent un contact luminal [92,93] voire bourgeonnent à l'intérieur du lumen du RE. Ces CLs sont probablement impliqués dans la synthèse de lipoprotéines ou de lipoparticules virales qui sont produites dans le lumen du RE [94,95]. Une régulation si fine de la directionnalité du bourgeonnement nécessite donc un mécanisme de contrôle très efficace qui doit surement tirer profit de tous les leviers physico-chimiques associés aux corps lipidiques et à la membrane dont ils émergent (type de phospholipides, de lipides neutres, énergie de la membrane, courbure, etc.).

3.2. Les mécanismes de bourgeonnement dans la cellule.

Dans la cellule, les mécanismes de bourgeonnement sont omniprésents, plus particulièrement lors de la formation de vésicules destinées à la sécrétion extracellulaire ou à la communication inter-organelles. Ainsi, la biogenèse de vésicules à partir des membranes du Golgi, du réticulum endoplasmique ou de la paroi cellulaire est souvent facilitée et contrôlée par des protéines manteaux, les complex protein I et II (COPI et COPII) et les Clathrines respectivement. Ces protéines agissent en s'ancrant à la surface des membranes puis en polymérisant pour créer des structures sphériques qui entraînent avec elles la membrane formant ainsi une vésicule [96] (Figure 15 A). La taille des vésicules formées avoisine les 100 nanomètres.

Il a longtemps été avancé que de tels manteaux protéiques puissent aussi réguler le bourgeonnement des CLs. Il a en effet été montré *in vitro* que COPI était capable de former des nano-gouttes d'huile ayant une taille caractéristique ne dépassant pas les 60 nm [97] (Figure 15 B). Cependant, la plupart des CLs observés en cellule ont des tailles bien supérieures avec par exemple une taille moyenne aux alentours de 1 micromètre chez les hépatocytes (Figure 15 C). Il semble donc que ce type de protéines ne soit pas capable de fournir l'énergie nécessaire à la formation des CLs observé *in vivo* [64].
En effet, pour provoquer la déformation nécessaire au bourgeonnement du CL, l'interaction latérale entre les protéines du manteau doit être supérieure à la tension de surface du CL en formation, i.e. l'énergie par élément de surface de monocouche créée par le bourgeonnement du CL [98]. L'énergie d'interaction des protéines telles que COPI ou les Clathrines se situent autours de 0.1 mN/m [98–101], ce qui est largement suffisant pour induire la formation de vésicules à partir de la bicouche qui ont des tensions faibles aux alentours de 0.01 mN/m [63]. Cependant, cela est insuffisant pour déformer la surface des CLs qui ont des tensions parfois mesurées au-delà de 2 mN/m [64].

Si l'on veut calculer l'énergie totale nécessaire au bourgeonnement d'un petit CL de 100 nm, cela nécessite un apport de 10^4 KbT alors qu'un manteau de COPI peut seulement fournir 10^3 KbT [102]. Il est donc très peu probable que ces protéines manteaux soient responsables du bourgeonnement des CLs.

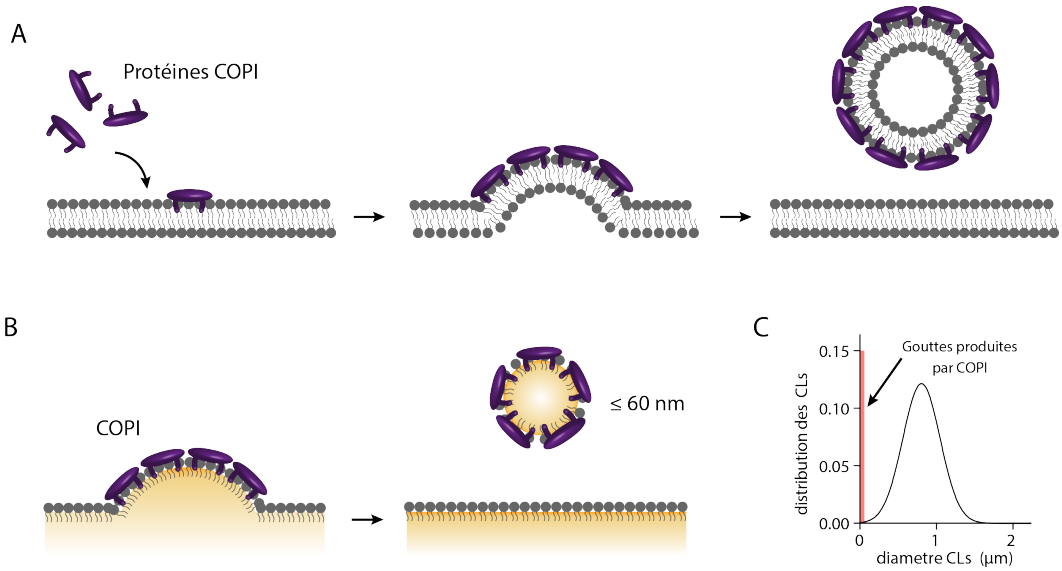

Figure 15 – **Bourgeonnement à l'aide de protéines manteau. A**, Formation de vésicules à partir d'une bicouche à l'aide de protéines manteaux de type COPI. **B**, COPI permet de former des nano-gouttelettes d'huile d'une taille maximale d'environ 60 nm. **C**, Cependant la taille de ces nano-gouttelettes est bien insuffisante pour rendre compte de la taille des CLs observés *in vivo* comme ici par exemple chez les cellules HeLa (adapté de Ben M'barek 2017).

Il a donc été avancé que le processus de bourgeonnement puisse tirer parti des propriétés particulières des lentilles d'huile et suivre un processus de démouillage, au cours duquel la lentille préalablement nucléée, bourgeonne et émerge dans le cytoplasme [103]. Il est probable que la diminution graduelle de l'angle de contact entre la goutte et la bicouche du réticulum endoplasmique permet l'émergence de la goutte lipidique, qui finirait potentiellement par se détacher totalement du réticulum après une étape de fission (Figure 16) [62]. Le bourgeonnement des corps lipidiques serait ainsi contrôlé par les paramètres physicochimiques des interfaces.

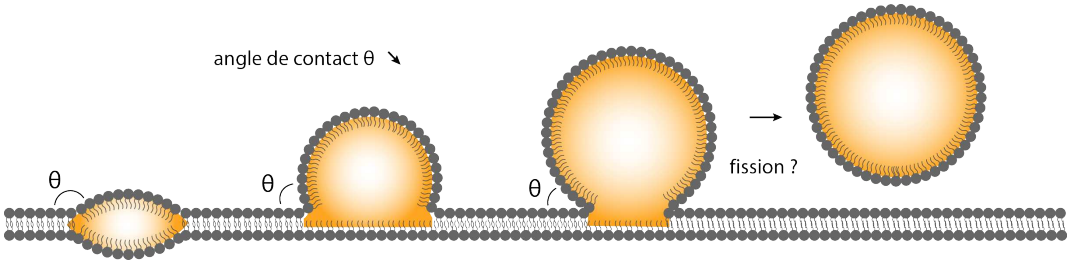

Figure 16 – **Bourgeonnement hypothétique d'un CL suivant un mécanisme de démouillage.** L'angle de contact θ entre la lentille et la bicouche diminue graduellement grâce à une modulation des paramètres physicochimiques des interfaces, pour aboutir à l'émergence du CL. Ce bourgeonnement pourrait aboutir sur un détachement complet du CL de la bicouche par une possible étape de fission.

Pour contrôler ce processus complexe de formation, il est probable que certaines protéines soient impliquées dans la régulation des paramètres contrôlant le bourgeonnement. Certains travaux supposent ainsi que des enzymes produisant des lipides spécifiques (diacylglycerol)

favorisent le bourgeonnement [104]. D'autres avancent que certaines protéines pourraient être directement recrutées à la surface des corps lipidiques de manière à moduler le bourgeonnement, comme par exemple certaines perilipines (plin3)[85]. Un troisième type de protéines peuvent être indirectement impliquées dans le bourgeonnement des CLs. Il s'agit de protéines transmembranaires du RE : Seipin et FIT2 qui sont les deux principales protéines identifiées à ce jour comme étant des régulatrices clés de la formation des CLs [81,105–107]. Ces deux protéines sont localisées à la jonction entre les CLs naissant et le RE [81,108], et pourraient jouer un rôle de «garde-barrière», en se plaçant autour de la goutte lipidique en formation et en régulant l'accès des protéines ou de certains phospholipides à la surface de la goutte. Le rôle de ces différents acteurs protéiques garde encore à ce jour de nombreuses zones d'ombre et les mécanismes physiques permettant la formation directionnelle des CLs restent à découvrir.

4. Croissance des CLs

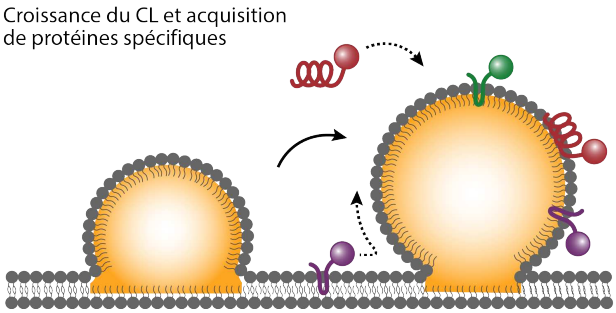

Figure 17 – **Croissance du CL et acquisition de protéines spécifiques à partir du RE ou du cytoplasme.**

Les CLs vont continuer à grandir en rassemblant de plus en plus de lipides neutres (Figure 17). Ces lipides neutres peuvent être engendrés par de la machinerie du réticulum endoplasmique évoquée précédemment et migrer dans le CL par le pont qui le relie à la membrane. Il est aussi possible qu'ils soient produits directement à la surface des gouttes lipidiques. En effet, il a été montré chez la levure que l'enzyme de la synthèse des lipides neutres DGAT2 du RE est recrutée à la surface des CLs en croissance [11,56]. Il faut cependant préciser que toutes les gouttes lipidiques ne sont pas sujettes à cette croissance. Dans les cellules de mammifères, une fraction d'entre elles conserve de petites tailles, de 400 à 800 nm [56]. La raison de la formation de cette sous-population de CLs reste à ce jour largement méconnue.

C'est au cours de cette croissance que les CLs vont recruter dynamiquement à leur surface la plupart des protéines qui détermineront leurs fonctions futures (Figure 17). Ces protéines proviennent soit du cytoplasme [109], de la membrane du RE [11,56] ou bien possiblement du lumen du RE [92]. Le contact avec le RE et les différents compartiments de la cellule déterminera donc probablement le protéome spécifique des futurs CLs ainsi que leur fonction biologique. Ceci souligne d'autant plus l'importance d'un contrôle efficace du bourgeonnement des CLs.

5. Rester ou non en contact avec le réticulum.

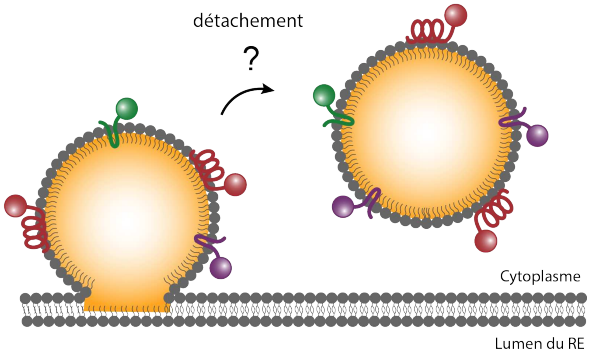

Figure 18 – **Etape de fission hypothétique permettant de séparer le CL du RE.**

La plupart des modèles proposent une éventuelle libération des CLs du RE (Figure 18). Les preuves les plus tangibles d'un détachement éventuel sont apportées par l'étude des tissus mammaires où les corps lipidiques cytoplasmiques sont libérés des cellules pour former des globules gras présents dans le lait [110]. On observe aussi chez la Drosophile, lors du développement des ovocytes, que des CLs passent de cellules nourrices vers l'ovocyte par un courant cytoplasmique [111]. Ces phénomènes semblent indiquer que certains CLs sont capables d'être détachés de leur organelle d'origine. Néanmoins, il manque encore de preuves formelles pour accréditer le détachement régulier de CLs du RE chez les métazoaires.

Il est donc probable qu'une grande partie des CLs restent connectée à la membrane du RE par l'intermédiaire de jonctions spécialisées. Une partie significative de la surface des CLs est en effet étroitement associée avec le réticulum endoplasmique [112]. Ces jonctions peuvent avoir des longueurs importantes (150 nm dans les cellules humaines A431 et 1 µm chez la drosophile) et les observations au microscope électronique suggèrent qu'il s'agit, comme il en était question précédemment, d'un canal communication efficace entre les deux organelles [56,106]. C'est à travers de telles jonctions stabilisées que le RE et les CLs pourraient échanger des protéines, des phospholipides et des lipides neutres.

Conclusion

La formation des CLs est donc un processus complexe qui, bien que crucial pour le métabolisme, n'est que partiellement compris. Il semble reposer sur des paramètres physico-chimiques surement modulés par des agents protéiques dont le rôle est encore vague. Néanmoins, on peut remarquer que les cellules utilisent une grande diversité de lipides pour constituer leurs corps lipidiques suivant leurs états métaboliques ou leurs rôles dans l'organisme [93,113–116]. Elles s'adaptent ainsi à leurs besoins en utilisant toutes les caractéristiques physicochimiques à leur disposition. Comme les cellules, il serait donc avantageux de tirer parti des outils de la physicochimie pour investiguer les mécanismes relatifs aux CLs.

Chapitre 3 :

CLs et Physique des émulsions.

Une cellule à l'intérieur de laquelle on trouve des corps lipidiques peut être considérée comme une émulsion dont la phase dispersée est formée par l'huile des corps lipidiques et la phase continue par le cytoplasme aqueux de la cellule. La biologie des corps lipidiques repose ainsi sur les principes de la physique des émulsions [44,103].
Il a en effet été proposé que certains phénomènes décrits par la science des émulsions régissaient le comportement et la formation des CLs. Par exemple, des évènements de coalescence de petits CLs, favorisés par la présence de certains phopholipides, seraient à l'origine de la formation des CLs géants retrouvés lors de la stéatose du foie [55]. D'autres avancent aussi que les CLs pourraient grossir sous l'action du murissement d'Ostwald, qui provoque la migration des lipides neutres des petites gouttes lipidiques vers les plus grandes [117,118]. Comme il en a été question précédemment, il a aussi été suggéré que les phénomènes de démouillage et de séparation de phase puissent être à l'origine de la formation des corps lipidiques [103].
Ces quelques exemples illustrent comment les CLs peuvent se comporter selon des principes décrivant le comportement des émulsions. La physique des émulsions offre un angle d'attaque prometteur pour étudier les CLs et répondre aux questions ayant trait à leur formation.

1. Les émulsions, généralités

1.1. Phases, interfaces, et processus d'émulsification

Les émulsions sont des mélanges de phases non miscibles où l'une des phases est dispersée dans la seconde (Figure 19). La première est dite phase dispersée et forme des gouttes de tailles variables dans la seconde qui est appelée phase continue. Dans le cas de CLs dans une cellule, la phase dispersée correspond aux gouttes huileuses (CLs) et la phase continue à l'intérieur aqueux de la cellule, c'est-à-dire son cytoplasme.

Les émulsions sont relativement instables du point de vue thermodynamique. En effet, les phases sont non miscibles, ce qui indique que leurs constituants préfèrent avoir des interactions entre eux plutôt qu'avec ceux de la phase opposée. Cette interaction défavorable est à l'origine d'une tension de surface, c'est-à-dire une énergie par surface de contact entre les deux phases (Figure 19). L'Etat d'énergie la plus faible est donc celui qui présente le moins de surface de contact entre les deux phases, ce qui n'est absolument pas le cas avec la multitude de petites gouttes de phase dispersée dans la phase continue.

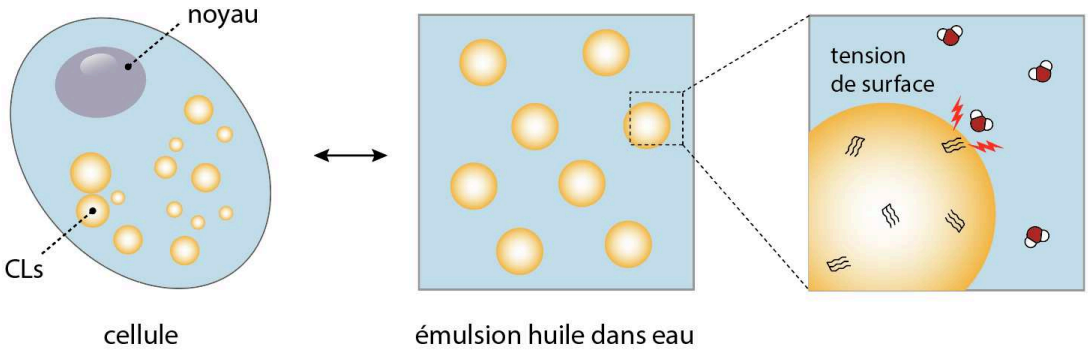

Figure 19 – **CLs : un problème de physique des émulsions.** Les CLs peuvent être vus comme une émulsion d'huile dans l'eau. La stabilité des émulsions est contrôlée par la tension de surface provenant de l'interaction défavorable entre les molécules d'huile et d'eau.

Une émulsion à haute tension de surface aura donc tendance à minimiser la surface de contact et les gouttelettes se rassembleront par des processus activés par la tension de surface (Figure 20) tel que la fusion des gouttes entre elles (coalescence) ou le murissement d'Oswald [119]. Le paramètre clé contrôlant la stabilisation des émulsions est donc la tension de surface qu'il est important de minimiser en vue de maintenir une émulsion. Ceci peut être réalisé à l'aide de molécules tensioactives qui, une fois localisées à l'interface, abaissent son énergie et donc sa tension (Figure 20). C'est ce que fait la cellule en couvrant ses CLs d'une monocouche des tensioactifs les plus répandus dans le vivant : des phospholipides.

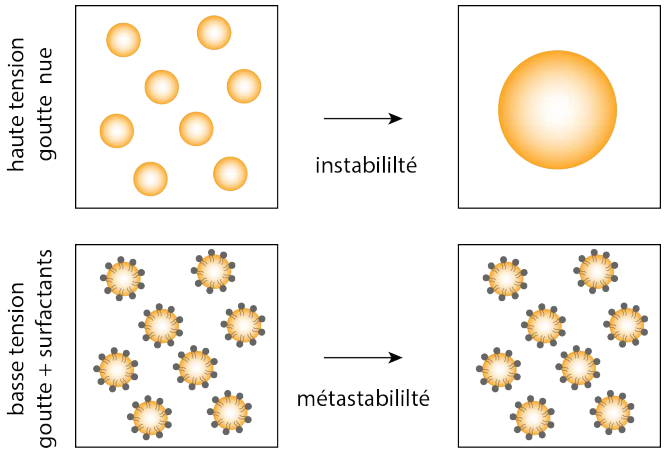

Figure 20 – **Stabilité des émulsions.** Une émulsion est naturellement instable et a tendance à reformer une phase continue. Plus les gouttes présentent une haute tension de surface (gouttes nues) plus l'émulsion sera instable. La présence de surfactants, abaisse la tension de surface et permet la formation d'émulsions métastables à grande durée de vie.

Il faut noter que la présence de cette couche de phospholipides à la surface des noyaux huileux des CLs est une protection pour la cellule, car une interface à haute tension a tendance à abaisser son énergie en recrutant à sa surface toutes sortes de molécules. Dans la cellule, des gouttes d'huile nues auraient un effet dévastateur car elles agglomèreraient à leur surface les protéines du cytoplasme, empêchant alors le bon fonctionnement de la cellule.

Cependant, si la tension de surface est régulée précisément, la cellule pourrait utiliser la propriété tensioactive de certaines protéines : si une énergie de surface trop grande pourrait agglomérer un grand éventail de protéines, une énergie de surface modérée pourrait favoriser le recrutement de certaines protéines spécifiques aux fonctions des CLs. La cellule a donc tout intérêt de réguler intelligemment la tension de surface de ses CLs, par exemple en jouant sur les types de phopholipides qui les recouvrent.

1.2. Les Phospholipides

Parmi les lipides qui entrent dans la composition de la structure de la cellule, les phopholipides sont les principaux constituants des membranes cellulaires [120].
Ce sont des molécules amphiphiles qui sont composées d'une tête polaire hydrophile et d'une queue apolaire hydrophobe, comportant une ou deux chaînes d'acides gras (Figure 21). Cette structure présentant deux parties aux propriétés physico-chimiques opposées permet aux phospholipides d'avoir un effet tensioactif important : dans le cas d'une interface eau-huile, la tête hydrophile va se positionner en direction de la phase aqueuse et la queue hydrophobe vers la phase huileuse. Les interactions tête-eau et queue-huile étant favorables, le phospholipide va ainsi écranter le contact eau-huile et donc diminuer l'énergie de surface de l'interface (Figure 21).

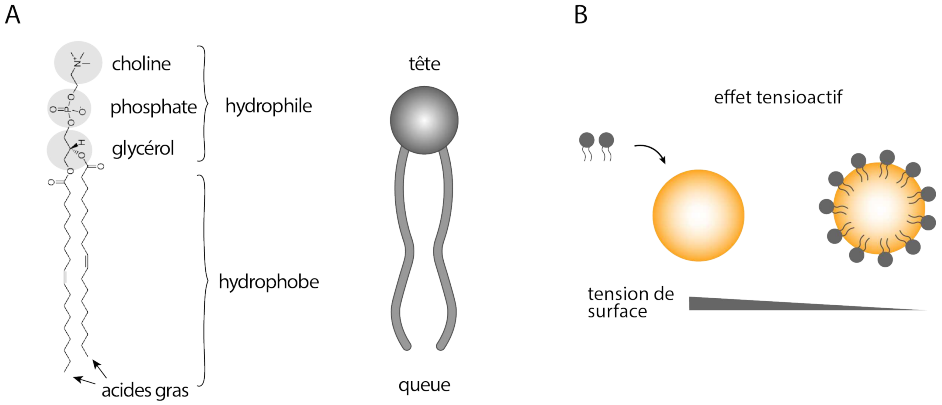

Figure 21 – **Phospholipides structure et effet tensioactif. A**, Les phospholipides sont des molécules amphiphiles présentant deux parties distinctes : la partie hydrophile, la tête, et la partie hydrophobe, la queue. La structure du DOPC (1,2-dioleoyl-sn-glycero-3-phosphocholine), ici donnée en exemple, possède une queue formée de deux acides gras. **B**, Le recrutement des phopholipides à l'interface de contact entre deux phases (hydrophile et hydrophobe) permet d'écranter les interactions défavorables et réduit l'énergie de surface, i.e. diminue la tension de surface. Les phopholipides sont donc des molécules tensioactives.

1.3. Organisation des phospholipides.

Les phospholipides sont donc des molécules tensioactives qui seront naturellement recrutées aux interfaces, et plus particulièrement à la surface d'une émulsion d'huile dans l'eau telle que les CLs (Figure 22).

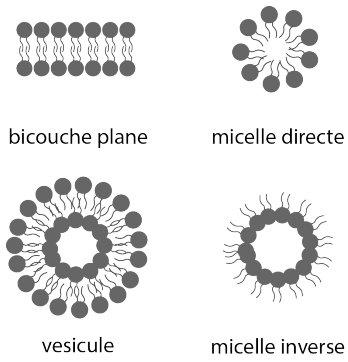

Figure 22 – **Représentation schématique des structures formées par les phopholipides** : bicouche plane, micelle, micelle inverse et vésicule. Ces structures se forment en milieu aqueux de manière à protéger au maximum leurs parties hydrophobes du milieu aqueux. Les micelles inverses ne permettent cette protection que lorsqu'elles s'agencent entre elles et forment un réseau de micelles inverses, les parties hydrophobes se mettant en contact et l'eau se trouvant au centre de la micelle inverse.

Quand les phospholipides sont mis en milieux aqueux, ils peuvent aussi former une grande variété de structures selon l'amplitude relative de leurs forces hydrophobe et hydrophile et leur géométrie (Figure 22). La structure la plus répandue dans les cellules est la bicouche phospholipidique qui compose l'essentiel des membranes cellulaires. On peut aussi trouver des micelles directes, des micelles inverses et des vésicules de tailles variables (Figure 22). La formation de telles structures peut aussi être modulée par la nature du solvant, la concentration d'un sel ou la température [121].

1.4. Déformation d'une interface

La déformation d'une interface, comme c'est le cas lors du bourgeonnement d'un corps lipidique, est régulièrement accompagnée d'une augmentation de surface de l'interface et de la création de zones courbées (Figure 23, A).

Augmenter la surface d'une interface expose de plus en plus les constituants des deux phases et multiplie ainsi les interactions défavorables. Pour augmenter la surface d'une quantité ΔA, il faudra fournir une énergie $\Delta E = \gamma * \Delta A$, où γ est la tension de surface de l'interface (Figure 23, B). On comprend alors qu'une interface présentant une basse tension de surface sera plus aisée à déformer.

Courber une interface provoque des contraintes latérales sur les molécules présentes à la surface. Le module de courbure est une grandeur qui reflète la propension d'une surface à se courber sous une action extérieure : plus le module est petit, plus il sera facile de courber l'interface ; plus il est grand, plus cela sera énergétiquement défavorable. Un autre paramètre décrit la courbure que la surface adopterait si aucune contrainte ne lui était appliquée : la courbure spontanée de l'interface. Plus l'état de courbure de l'interface sera proche de la courbure spontanée, plus son énergie sera basse (Figure 23, B). Le coût énergétique par unité de surface pour courber une interface de module de courbure K, $E = K/2 * (C - Co)^2 + K_g\, C_g$, avec $C = (C_1 + C_2)/2$, la courbure imposée, Co la courbure spontanée de l'interface, K_g le module de courbure gaussien et $C_g = C_1 C_2$ la courbure gaussienne où C_1et C_2 sont les courbures principales de l'interface. La structure des molécules présentes à l'interface

influencera directement l'énergie de courbure de l'interface en modifiant par exemple le terme de courbure spontanée *Co* ou la valeur des modules de courbure.

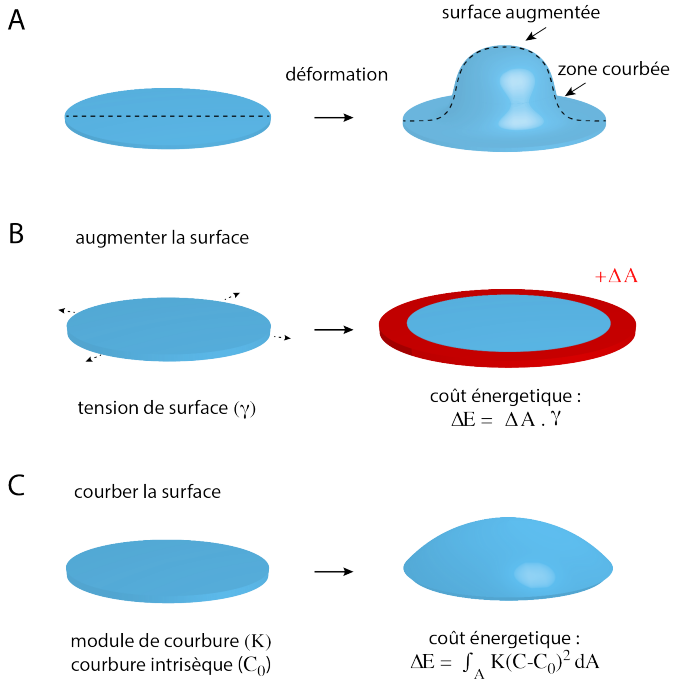

Figure 23 – **Déformation d'une interface et énergies mises en jeux. A**, La déformation d'une interface peut produire deux effets principaux : une augmentation de sa surface et la formation de zones courbées. **B**, Augmenter la surface d'une interface a un coût énergétique qui est directement proportionnel à la tension de surface de l'interface (γ). **C**, Courber la surface a aussi un coût énergétique dépendant du module de courbure (K) de l'interface et de sa courbure spontanée Co.

Pour faciliter la formation d'un corps lipidique, il est donc préférable que les modules de courbure et la tension de surface soient relativement faibles et que la courbure spontanée soit favorable à la déformation souhaitée.

1.5. Diffèrent types de phospholipides

De manière à former un CL, il faut être capable de déformer une interface et d'agir sur sa tension de surface et son énergie de courbure. Pour cela, il se trouve que les tensioactifs tels que les phopholipides sont des outils très efficaces.

La cellule possède un très grand éventail de phospholipides à sa disposition dont les têtes peuvent varier de composition, de taille (encombrement stérique) et de charges et dont les queues peuvent varier de longueur de ramification et de nombre d'insaturations [122].

Ces paramètres permettent d'influencer directement le pouvoir tensio-actif des phospholipides mais aussi leur géométrie propre [123]. On peut ainsi avoir des phospholipides ayant une géométrie cylindrique, si la section de la tête hydrophile est de taille comparable à celle de la partie hydrophobe, une géométrie conique, si la section de la tête plus grande que celle de la queue, ou bien une géométrie trapézoïdale, si la section de la queue plus grande

que celle de la tête (Figure 24). Suivant ces géométries, les phospholipides auront tendance à former des structures différentes : des bicouches planes pour la géométrie cylindrique, des micelles directes pour la géométrie conique, et des micelles inversées pour la géométrie trapézoïdale. A noter que pour les micelles inversées, il faut que la phase huileuse se trouve à l'extérieur de la micelle.

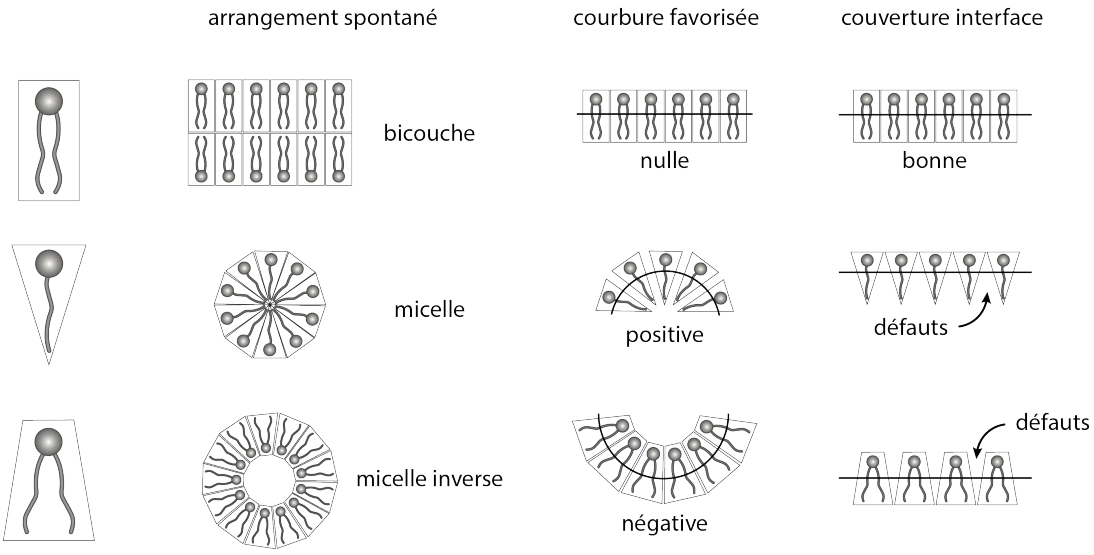

Figure 24 – **Influence de la géométrie des phospholipides.** Les phospholipides peuvent présenter des géométries différentes suivant leur structure moléculaire : cylindriques (haut), coniques (milieu) et trapézoïdaux (bas). Selon leur géométrie intrinsèque, ils auront tendance à former des structures différentes : des bicouches pour les cylindriques, des micelles pour les coniques et des micelles inverses pour les trapézoïdaux. Les topologies adoptées reflètent directement la courbure favorisée par ces molécules : les phospholipides cylindriques ont une courbure intrinsèque nulle, les phospholipides coniques une courbure intrinsèque positive et les phospholipides trapézoïdaux une courbure intrinsèque négative. La géométrie des phospholipides influence aussi directement leur capacité à couvrir une interface et donc leur pouvoir surfactant.

Si les différents types de phospholipides forment naturellement de telles structures, c'est que leurs géométries les prédisposent à favoriser un arrangement présentant des courbures différentes. Les phospholipides cylindriques favorisent les courbures nulles, les phospholipides coniques les courbure positives et les phospholipides trapézoïdaux les courbure négatives (Figure 24). C'est pour cela que l'on parle de la courbure intrinsèque des phospholipides pour décrire leur géométrie.

La présence de phospholipides de géométrie variable pourra donc directement influencer la courbure spontanée de l'interface (Co) et son module de courbure. Par exemple, des phospholipides coniques favoriseront la déformation de la surface dans le sens positif, c'est-à-dire dans le sens du bourgeonnement présenté en Figure 23.
Comme il en était question précédemment, la tension de surface de l'interface peut aussi être diminuée par la présence de phospholipides. Ces derniers écrantent les interactions défavorables entre les deux phases. Plus leur densité est grande, moins les défauts de couverture laissent interagir les deux phases et plus la tension est faible. (Figure 21).

Ainsi, les différents types de phospholipides peuvent aussi affecter la tension de surface car, suivant leur géométrie, ils sont plus ou moins capables de fournir une couverture homogène à l'interface. Par exemple, les phospholipides cylindriques sont de très bons surfactants qui permettent d'atteindre de basses tensions [44,55,103,124] alors que les phospholipides trapézoïdaux ou coniques laissent de plus nombreux défauts, ce qui en fait de moins bons tensioactifs (Figure 24). Il faut cependant nuancer en précisant que des mélanges de ces phospholipides de géométries différentes pourront sûrement fournir de très bonnes couvertures grâce à des effets de complémentarité de forme.

2. Emulsions et bourgeonnement

2.1. Topologie et caractéristiques du CL en formation

Lors de leur formation, les corps lipidiques naissent à l'intérieur de la bicouche phospholipidique qui compose le RE. La surface du CL est donc délimitée par une monocouche de phospholipides recouvrant une phase huileuse. Cette monocouche est en continuité avec la bicouche du RE (Figure 25).

Le corps lipidique se présente donc sous la forme d'une goutte d'huile dans l'eau couverte d'une couche de phospholipides rattachée à une bicouche. La formation et le bourgeonnement d'un tel objet sont directement influencés par sa capacité à se déformer, et donc probablement par sa tension de surface et son module de courbure.

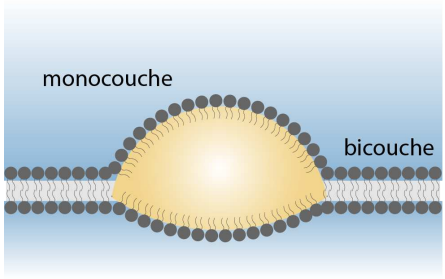

	monocouche	bicouche
tension	2 mN/m	0.01 mN/m
module de courbure	10 KbT	20 KbT

Figure 25 – **Topologie d'un CL en formation dans une bicouche.** Quand il est encapsulé à l'intérieur d'une bicouche de phospholipides, le CL dé-lamine la bicouche pour former deux monocouches de phospholipides qui délimitent son noyau huileux. Ce système est donc constitué de deux monocouches en continuité avec une bicouche. Un ordre de gradeur de la tension de surface des monocouches et de leur module de courbure est respectivement 2 mN/m et 10 K_bT. Pour la bicouche les valeurs caractéristiques avancées sont aux alentours de 0.01 mN/m et 20 K_bT.

2.2. Tension de surface

De la monocouche :

Les deux monocouches du CL ne sont rien d'autre que des interfaces entre une phase aqueuse et une phase huileuse. La phase huileuse très hydrophobe du CL est occultée par la tête des phospholipides qui forment une couche fluide à sa surface. Ainsi, comme il en était question précédemment, plus la monocouche sera dense, c'est-à-dire que l'huile sera

fortement occultée, plus la tension de surface du CL sera faible. Par contre, si la monocouche présente des défauts, des molécules d'huile seront exposées à la phase aqueuse et la tension de surface sera plus grande.

Il ne faut cependant pas oublier que le type d'huile qui compose le noyau de la goutte lipidique joue aussi un rôle important pour la détermination de la tension de surface des CLs. En effet, toutes les huiles ont des structures moléculaires différentes et ne partagent pas toutes les mêmes affinités avec l'eau. Certaines huiles ont des tensions hautes (Triolein env. 35 mN/m) d'autres ont des tensions plus basses (Squalene env. 25 mN/m). Un même niveau de défaut dans la monocouche de phospholipides ne conduira pas à une même tension de surface selon les types d'huile utilisés.

Les tensions de monocouche mesurées sur des CLs extraits de cellules avoisinaient les 2 mN/m[64]. Cette haute tension (par rapport aux bicouches souvent considérées comme ayant une tension négligeable) reflèterait la présence des défauts de couverture évoqués ci-dessus qui ont été suspectés d'être à l'origine du recrutement des protéines à la surface des CLs, et notamment des protéines possédant des hélices amphipathiques à forts résidus hydrophobes [125]. Cependant, on peut aussi penser que les protéines ciblant les CLs puissent aussi être sensibles à la composition huileuse des CLs, ce qui, comme nous l'avons remarqué, influence directement la tension de surface eau-huile.

De la bicouche :

La bicouche en continuité avec la monocouche des CLs en formation est souvent considérée comme un objet fluide et déformable. Elle est formée de deux feuillets de phospholipides tête-bêche qui adhèrent par l'intermédiaire des queues hydrophobes des deux feuillets.

Cette membrane entoure et supporte le CL en formation. Suivant ses contraintes internes elle peut donc exercer des forces sur ce dernier et ainsi agir sur sa forme et son comportement. La tension de surface associée à une telle membrane a été évaluée aux alentours de 0.01 mN/m [126], bien inférieure à la tension relevée pour les CLs (proche de 2 mN/m [64]). Cependant, il est tout à fait envisageable que certaines protéines modulent cette tension en remodelant la composition phospholipidique, ou en modifiant directement sa forme, par l'intermédiaire de moteurs moléculaires [64,127,128]. Il serait ainsi possible que la bicouche entourant le CL en formation puisse influencer sa formation.

La réciproque est aussi envisageable : la membrane du RE est aussi le lieu où les lipides neutres sont produits et ensuite dirigés vers les CLs. Si ces lipides neutres ne sont pas bien extraits de la membrane, il est possible que leur accumulation influence les propriétés de la membrane, et plus particulièrement sa tension.

De manière à tester ces hypothèses, il serait possible d'utiliser des membranes modèles dont on pourrait moduler la tension de bicouche. Par exemple, il est possible de moduler la tension de bicouche d'une Giant Unilamellar Vesicule (GUV) à l'aide de micropipettes [129] ou en jouant sur les pressions osmotiques du milieu [130].

2.3. La courbure

Le module de courbure (K) de la bicouche pourrait aussi être un paramètre régulant la forme et le comportement du CL, par exemple en privilégiant les courbures positives favorables au bourgeonnement.

Un calcul de loi d'échelle montre cependant que cette contribution peut être négligée. En effet, en comparant les énergies mises en jeu par la tension de surface à celles de la courbure, on obtient une taille caractéristique au-delà de laquelle la tension de surface domine le comportement : $L > \sqrt{K/\gamma}$ où K est le module de courbure caractéristique et γ la tension de surface caractéristique. La plupart des CLs ont des tailles bien supérieures à 50 nm [131] et l'on obtient $L_c \sim 20\,nm$ pour $K \sim 10\,K_bT$ et $\gamma \sim 1\,mN/m$, qui sont des valeurs typiques de module de courbure et de tension pour une monocouche [102,132]. La tension de surface domine donc le comportement des CLs qui ont une taille supérieure à 20 nm.

Cependant, il se peut que le module de courbure influence la forme des CLs au tout début de leur formation, comme l'observation des lentilles d'huile semble le confirmer [133] (Figure 13), et que la tension prenne le dessus pour des CLs plus grands [134].

2.4. Bourgeonnement et démouillage

Dans la vie de tous les jours, on peut observer des phénomènes d'émulsification qui se réalisent sans action de quelconques protéines. Ce type de phénomène est favorisé quand la création de goutte, c'est-à-dire la formation de nouvelle surface entre les deux phases ne coûte que très peu d'énergie au système. Cela revient à conserver une tension de surface très faible entre les deux phases. C'est en suivant ce raisonnement qu'il a en effet été proposé que le bourgeonnement des CLs soit thermodynamiquement favorisé par une diminution de la tension de surface de la monocouche et de la bicouche [135–138].

Le comportement d'un CL dans une bicouche de phospholipides étant contrôlé de manière prépondérante par des effets de tension de surface, on aurait tendance à le comparer à des systèmes similaires provenant de la science des émulsions.

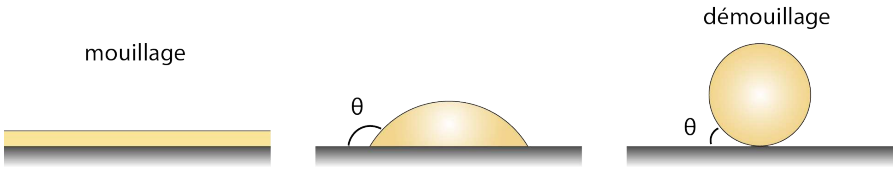

Figure 26 – **Illustration du phénomène de démouillage.** Un liquide déposé sur une surface solide peut mouiller la surface et former un film qui la recouvre complètement. Dans un cas de démouillage, le liquide forme une goutte qui fait un angle de contact θ avec le substrat. Dans le cas d'un démouillage total ; l'angle θ tend vers 0 et la goutte devient sphérique. Le degré de mouillage de la goutte sur le substrat est relié à la tension de surface entre le substrat et le liquide de la goutte.

En regardant de plus près le bourgeonnement des CLs où des lipides neutres étalés dans une bicouche se rassemblent pour former un CL sphérique, il est possible de faire le rapprochement rudimentaire avec la situation d'un mouillage de liquide sur une surface

plane solide. Le CL en train d'émerger de la bicouche du RE rappelle les différents degrés d'étalement d'une goutte de liquide déposée sur une surface [139]. Un liquide déposé sur une surface solide peut soit s'étaler complètement, soit mouiller la surface de manière partielle en définissant un angle avec la surface de contact appelé angle de contact θ (Figure 26). Le cas d'une goutte complètement démouillée, comme une goutte d'eau à la surface d'une plume de canard, correspondrait à la topologie d'un CL sphérique quasiment détaché du réticulum. Le passage de la lentille d'huile au CL complètement bourgeonné serait décrit par une diminution graduelle de l'angle de contact θ (Figure 26). Pour arriver à cette situation de démouillage quasi complet, il faudrait effectivement que la tension entre l'air et le liquide soit bien plus faible que la tension entre le liquide et le substrat. Ceci est en effet concordant avec l'idée qu'un bourgeonnement du CL serait favorisé par une diminution de sa tension de surface [135–138].

Cependant, ce système modèle n'autorise le bourgeonnement que dans une seule direction, du fait de la non déformabilité du substrat sur lequel est posé le liquide. Il est donc très probable que ce système modèle soit un peu trop grossier pour décrire précisément le comportement d'un CL en formation.

2.5. Système à trois phases

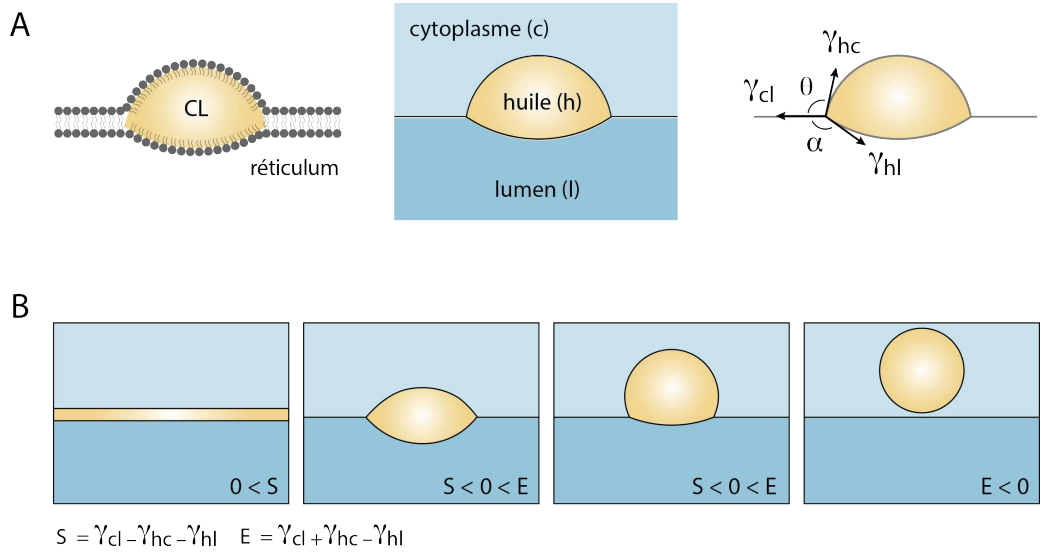

Figure 27 – **Système de mouillage à trois phases et CLs. A**, Un CL dans une bicouche peut être considéré comme une phase huileuse située entre deux phases aqueuses que sont le cytoplasme et le lumen du RE. Cette situation est analogue à celle d'un système de mouillage à trois phases dont la topologie (angles α,θ) est régie par un équilibre des tensions de surface entre les trois phases c, h et l. **B**, Selon les valeurs respectives des tensions, le système peut présenter trois situations : un mouillage total si S>0, un mouillage partiel si E>0>S et un démouillage total si E<0. Ce système à trois phases reproduit donc un bourgeonnement analogue à celui des CLs en formation. (Figure inspiré de forêt & Thiam et al 2016)

Le système formé par le CL en formation dans la bicouche du RE peut être plus précisément approximé par un système à trois phases qui a été bien caractérisé dans de précédents travaux [103,140,141]. Dans un tel système, une phase est située à l'interface entre deux autres phases non miscibles en formant une lentille. Le corps lipidique en formation correspondrait à la phase formant la lentille (phase huile, h), la bicouche quant à elle serait une matérialisation de l'interface entre la phase supérieure (cytoplasme, c) et la phase inférieure (lumen, l).

Dans le système à trois phases, la forme et la position de la lentille sont directement influencées par un équilibre de forces au point de contact des trois phases. Ces forces découlent directement des tensions de surfaces des trois interfaces (Figure 27 A).

La goutte d'huile (h) est sujette aux tensions γ_{hc} et γ_{hl} qui ont tendance à tirer sur les deux points de contact entre les phases et à rendre la goutte sphérique. A l'opposé, la tension γ_{cl} entre les deux phases continues a tendance à étaler la goutte. Dans le cas extrême, si $\gamma_{cl} > \gamma_{hc} + \gamma_{hl}$, la goutte d'huile est complètement étalée et forme un film en mouillage total. La position de la goutte est déterminée par l'équilibre des tensions huile-cytoplasme (γ_{hc}) et huile-lumen (γ_{hl}). Si par exemple la tension huile-cytoplasme (γ_{hc}) est inférieure à celle huile-lumen (γ_{hl}), la goutte formera une lentille décentrée vers le cytoplasme (Figure 27 B). Dans le cas extrême, c'est-à-dire si $\gamma_{hl} > \gamma_{hc} + \gamma_{cl}$, la goutte bourgeonnera totalement dans le cytoplasme en démouillant complètement (Figure 27 B).

Il est ainsi possible de définir deux paramètres qui reflètent l'équilibre des tensions et déterminent les cas limites d'étalement et de bourgeonnement de la goutte d'huile. Le premier, le paramètre de Spreading, $S = \gamma_{cl} - \gamma_{hc} - \gamma_{hl}$, définit la limite de mouillage complet du film d'huile (le mouillage est complet quand $S > 0$). Le deuxième, le paramètre d'Emergence, $E = \gamma_{cl} + \gamma_{hc} - \gamma_{hl}$, décrit la limite de bourgeonnement total (démouillage total) dans le cytoplasme (le démouillage est total si $E < 0$). Les différentes topologies possibles sont récapitulées dans la Figure 27 B.

Ce système à trois phases est un système modèle bien caractérisé [140,141] qui mime donc le comportement d'un CL en formation encapsulée dans la bicouche du RE, en ne prenant en compte que des effets de tension de surface. Il met ainsi en lumière une nouvelle approche basée sur la physique des interfaces permettant de mieux appréhender les mécanismes de formation des CLs.

Conclusion

Les CLs sont des gouttelettes d'huile intracellulaires qui sont impliquées dans de nombreux processus nécessaires à la survie de la cellule. Ils ont principalement un rôle dans la gestion de l'énergie et des matériaux de construction, mais aussi dans la détoxification et la protection contre le stress métabolique. Pour mener à bien ces tâches, ils doivent être capables de réguler leurs propriétés physicochimiques et les liens qu'ils entretiennent avec les autres organelles cellulaires. La plupart de ces spécificités sont acquises lors de leur formation. La biogenèse des CLs à partir du RE est donc une étape déterminante de leur existence. Comme les CLs forment une émulsion intracellulaire, il est tout naturel d'utiliser les outils de la science des émulsions pour décrire et comprendre leur comportement. Ce travail de thèse a donc pour objectif d'étudier la biogenèse des corps lipidiques à l'aide d'outils de la physique des émulsions, et plus précisément de répondre à la question suivante : **Comment se forment les corps lipidiques ?** Pour y répondre, nous avons procédé de la manière suivante :

Pour commencer, nous avons mis au point un système modèle recréant *in vitro* la topologie d'une goutte lipidique dans le réticulum endoplasmique, ce qui permet de moduler d'une manière très précise les paramètres liés à la formation d'un corps lipidique. Ce système sera décrit en détail dans le quatrième chapitre présentant le matériel et méthodes que nous avons mis en place.

Grâce à ce système modèle, nous avons étudié les paramètres physiques contrôlant le bourgeonnement de gouttes lipidiques artificielles. Les résultats expérimentaux présents dans le cinquième chapitre démontrent que le comportement d'une goutte lipidique dans une membrane est régi par un équilibre de tensions de surface. Elle émerge de la membrane du côté de sa monocouche présentant la plus faible tension de surface. Ce résultat met en lumière de nouvelles pistes pour comprendre la manière dont la cellule pourrait contrôler la direction de formation des corps lipidiques.

Il a été établi que les corps lipidiques doivent être formés principalement dans le cytoplasme, afin de pouvoir réguler le métabolisme énergétique de la cellule. Dans un sixième chapitre, nous avons donc voulu comprendre comment la cellule pouvait assurer cette émergence unidirectionnelle. Nous avons découvert qu'une asymétrie de densité de phospholipides, ou un déséquilibre d'insertion de protéines, détermine la direction du bourgeonnement des gouttes lipidiques artificielles. Plus précisément, le bourgeonnement se produit du côté de la monocouche présentant la plus importante densité de phospholipides et/ou de protéines. Dans un contexte cellulaire, nous avons montré que la synthèse de phospholipides facilite la bonne émergence des corps lipidiques dans le cytoplasme.

Lors de sa formation, le corps lipidique recrute des protéines spécifiques à sa surface qui détermineront ses futures fonctions biologiques. La plupart de ces protéines possèdent des domaines de liaison en hélices amphipathiques. Bien que l'on observe que les hélices amphipathiques sont capables de cibler d'une manière sélective certains corps lipidiques ou certains sous-groupes de corps lipidiques, les mécanismes derrière ce phénomène restent largement méconnus. Les résultats de notre recherche présentés dans septième chapitre suggèrent que l'affinité entre les hélices amphipathiques et le type de lipides neutres présents dans le noyau est le facteur principal régulant cette spécificité de recrutement. Les défauts de couverture ou les défauts de packing des phospholipides modulent simplement la surface accessible.

Partie II :

Matériel et Méthodes

Chapitre 4 :

Système modèle et outils de caractérisation

1. Fabrication et manipulation d'un système modèle

Pour étudier précisément les mécanismes de la biogenèse des CLs à l'aide de concepts de la physique des émulsions, nous avons mis en place différents outils et modèles. Le principal modèle est un système minimal qui permet de reproduire la topologie d'un CL en formation à l'intérieur d'une bicouche. Les outils de la physique des émulsions nous ont quant à eux permis de caractériser les propriétés physicochimiques de nos systèmes modèles telles que leur tension de surface, leur densité de phopholipides, l'effet du recrutement de protéines, etc.
Le chapitre suivant décrit les méthodes et le matériel nécessaire à la réalisation de notre système modèle et à la mesure de ses caractéristiques.

1.1. Formation de membranes modèles : la GUV

Les CLs se forment à partir du RE qui est une bicouche de phospholipides. La première étape de la réalisation du système modèle est donc de produire une bicouche de phospholipides stable et suffisamment grande pour pouvoir la manipuler. La solution idéale est la vésicule géante unilamellaire ou Giant Unilamellar Vesicle (GUV) en anglais. Les GUVs sont des vésicules sphériques de quelques dizaines de micromètres formées par une bicouche de phospholipides (Figure 28).

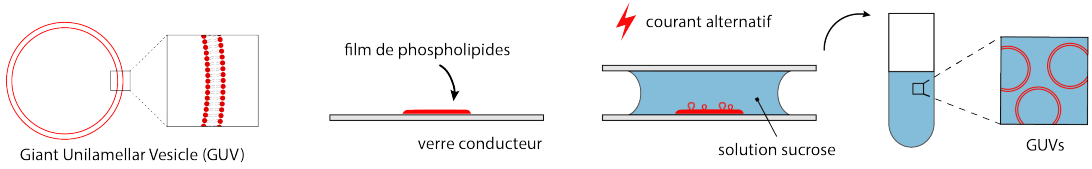

Figure 28 – **Production de vésicules géantes unilamellaires (GUVs) par électro-formation.** Une GUV est constituée d'une bicouche de phopholipides sphérique de quelques dizaines de micromètres à une centaine de micromètres. Production : un film de phopholipides est déposé par évaporation à la surface d'un verre conducteur. Il est recouvert d'une solution de sucrose qui est contenue dans l'espace clos formé par une autre plaque de verre conducteur. Un courant alternatif est appliqué aux deux plaques et la force électrique résultante provoque le bourgeonnement de GUVs dans la solution. La solution de GUVs est alors collectée pour utilisation ultérieure.

Pour produire des GUVs, la méthode la plus efficace est l'électro-formation. Cela consiste à déposer des phospholipides à la surface d'une électrode plane de verre conducteur (Indium Tin Oxyde). Ces phospholipides formeront un film lipidique après évaporation du solvant.

Ensuite, une chambre est constituée à l'aide d'une deuxième plaque de verre conducteur. Cette chambre est remplie d'une solution aqueuse de sucrose (Figure 28). Les deux plaques sont alors soumises à un courant alternatif de quelques Volts pendant une heure et demi, qui en exerçant une force électrostatique sur les phospholipides, provoque la formation de vésicules. Ces dernières sont ensuite transférées dans un tube à essai et sont prêtes à être utilisées (Figure 28). Le phospholipide le plus fréquemment utilisé pour former les membranes est du DOPC (1,2-dioleoyl-sn-glycero-3-phosphocholine) qui est un des phospholipides majoritaires du RE, mais la fabrication de GUV en utilisant cette méthode permet de choisir précisément la composition de la membrane : il suffit de déposer le mélange de phospholipides désiré sur le verre conducteur avant de lancer l'électro-formation.

1.2. Système modèle du bourgeonnement des CLs : la DEV

Les CLs en formation sont composés d'une phase huileuse insérée entre les deux feuillets de la bicouche du réticulum endoplasmique. De manière à reproduire cette topologie, il faut proposer un système modèle qui possède une bicouche à l'intérieur de laquelle se trouve une goutte huileuse. La technique retenue utilise des GUVs comme bicouche modèle et une émulsion d'huile physiologique (triolein ou squalene) comme phase huileuse. Les GUVs sont mises en contact avec l'émulsion de microgouttelettes d'huile dans l'eau obtenue par sonication (Figure 29). Les microgouttelettes qui ont une haute tension de surface, se réfugient à l'intérieur de la bicouche, minimisant ainsi leur énergie. Les gouttelettes ainsi insérées entre les deux feuillets de la membrane finissent par se rassembler en une seule gouttelette plus massive par des phénomènes de fusion latérale (Figure 29). On obtient alors un système modèle stable qui reproduit la topologie d'un CL en formation à l'intérieur du RE et que l'on a baptisé DEV pour Droplet-Embedded-Vesicle.

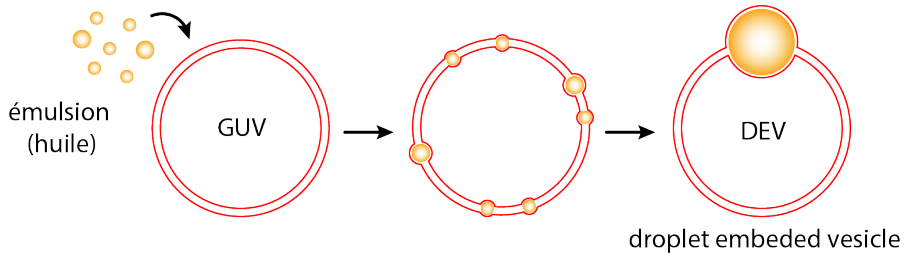

Figure 29 – **Système modèle de CLs dans une bicouche : DEV (Droplet Embeded Vesicle).** Des GUVs sont mises en contact avec une émulsion d'huile (lipides neutres). Les gouttes d'huile pénètrent à l'intérieur de la bicouche des GUVs. Elles se rassemblent par fusion latérale pour former une unique goutte encapsulée dans la bicouche reproduisant la topologie d'un CL en formation à l'intérieur de la bicouche du RE.

1.3. Manipulation des DEVs

Afin d'observer les DEVs de manière optimale, nous avons mis au point un système de manipulation précise de ces objets micrométriques. Les DEVs produites sont observées à l'aide d'un microscope confocal dans une goutte de milieu déposée sur un porte-échantillon en verre (Figure 30). Les mouvements de convection dans cette goutte, dus à l'évaporation

du milieu aqueux, rendent difficile l'observation des DEVs. Nous avons donc mis en place un système de micromanipulation mettant en jeu deux micropipettes connectées à des seringues, permettant d'attraper les DEVs en appliquant une petite succion (Figure 30). Les micropipettes sont aussi connectées à des capteurs de pression, ce qui permet de pouvoir quantifier et contrôler les aspirations imposées. Comme il en sera question dans le paragraphe suivant, les micropipettes reliées aux capteurs de pression permettent aussi de mesurer et d'imposer des tensions de surface.

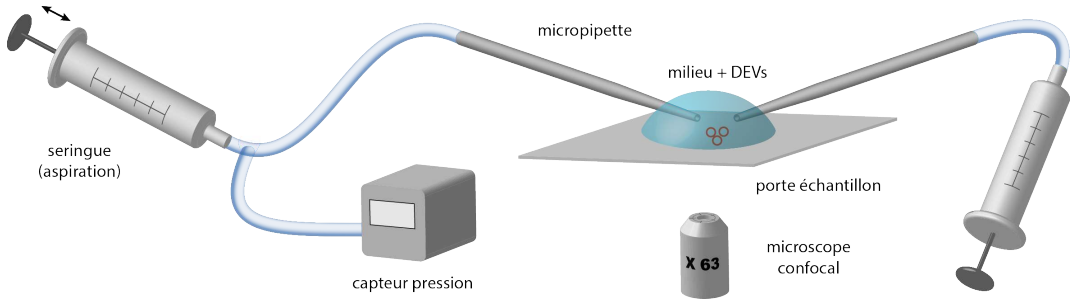

Figure 30 – **Représentation schématique du système de manipulation des DEVs permettant de mesurer leur tension de surface.** Les objets sont manipulés à l'aide de micropipettes (quelques micromètres de diamètre) aspirantes reliées à des seringues. La position des pipettes est contrôlée par deux manipulateurs micrométriques. Le capteur de pression permet une mesure de la tension de surface des objets. Le tout est adapté à un microscope confocal pour l'observation.

Grâce à ce système de micromanipulation, il devient alors possible de manipuler précisément les DEVs et de les observer selon l'angle que l'on désire. Une petite aspiration dans les micropipettes permet, par un effet ventouse, de saisir à la fois la goutte d'huile et la membrane de la vésicule (Figure 31) et ainsi de les positionner de la manière souhaitée. Il est alors possible de relever le niveau de bourgeonnement de la goutte, les angles de contact entre la membrane et la phase huileuse, tout comme le degré d'étalement de la goutte d'huile.

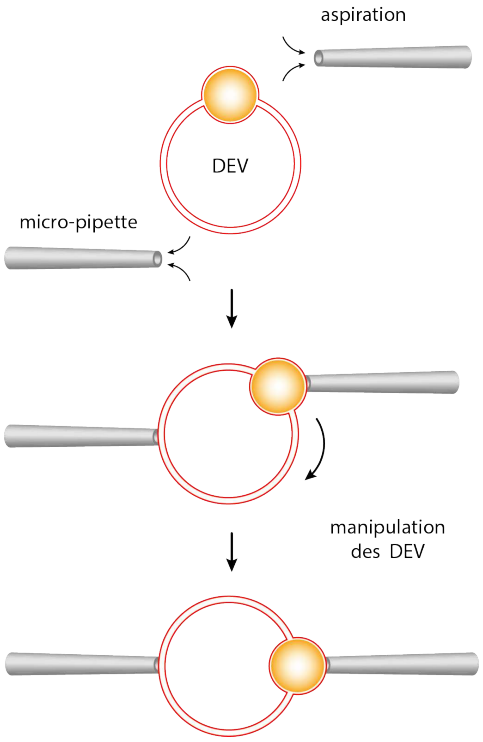

Figure 31 – **Illustration d'une méthode de manipulation des DEVs.** Une légère aspiration est appliquée aux micropipettes à l'aide des seringues qui leur sont reliées. La bicouche et la goutte d'huile sont ainsi attrapées par un léger effet ventouse. Il est alors possible de les manipuler l'une par rapport à l'autre, par exemple en les mettant sur la tranche.

1.4. Mesure de tension de surface

En plus de permettre une manipulation des DEVs, le système de micropipettes relié à un capteur de pression permet de mesurer directement la tension de surface de la vésicule et de la goutte d'huile qui composent la DEV [129]. Effectivement, si on applique une aspiration suffisante, une partie de la surface, par exemple de la vésicule, rentre à l'intérieur de la micropipette (Figure 32). On se retrouve alors dans une situation d'équilibre où la tension de surface de la vésicule peut être déterminée à l'aide de la loi de Laplace. Cette loi établit un lien entre la différence de pression d'un coté et de l'autre d'une interface (ΔP), les rayons de courbure principaux de l'interface (R_1 , R_2) et la tension de surface (γ), selon l'expression suivante :

$$\Delta P = \frac{\gamma}{\frac{1}{R_1} + \frac{1}{R_2}}$$

ou comme ici pour une sphère de rayon R :

$$\Delta P = \frac{2\gamma}{R}.$$

En appliquant cette formule deux fois à la surface de la vésicule, une fois sur la partie à l'extérieur de la pipette et une autre à l'intérieur (Figure 32), et en considérant que la tension de surface de la membrane de la vésicule γ est la même partout, on obtient la loi suivante :

$$\gamma = \frac{\Delta P}{2\left(\frac{1}{R_p} - \frac{1}{R_g}\right)}$$

Où γ, R_p et R_g sont respectivement la tension de la membrane, le rayon interne de la pipette et le rayon de la vésicule ; $\Delta P = P_0 - P$ est la pression de succion, c'est-à-dire la différence de pression entre la pression dans le milieu (P_0) et la pression imposée à l'intérieur de la pipette (P).

En mesurant la pression de succion, grâce à un capteur de pression, et les rayons de la pipette et de la vésicule, grâce au microscope, il est alors possible de remonter à la valeur de la tension de surface.

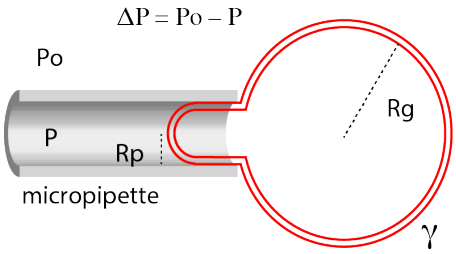

$$\gamma = \frac{\Delta P}{2\left(\frac{1}{R_p} - \frac{1}{R_g}\right)}$$

Figure 32 – Mesure de tension de surface à l'aide d'une micropipette. Une différence de pression (ΔP) aspire une petite langue de la membrane à l'intérieur de la pipette. Une mesure des rayons de la pipette et de la vésicule permet, en appliquant deux fois la loi de Laplace, de remonter à la tension de surface de la bicouche. La méthode permet également de mesurer la tension de surface d'une goutte d'huile.

Le même raisonnement est valable pour n'importe quel type d'interface, et il est donc possible de mesurer avec la même méthode la tension de surface de la goutte d'huile de la DEV. Il faut cependant noter qu'il n'est possible d'appliquer cette loi que s'il n'y a pas de phénomènes d'adhérence entre la pipette et la surface aspirée car cela aurait pour effet d'introduire des forces d'adhésion empêchant l'application de la loi de Laplace. C'est pour cela que la surface de la pipette est traitée avec de la protéine BSA (Bovine Sérum Albumine) qui prévient l'adhésion de la membrane.
Si une petite aspiration permet de sonder la tension de surface de la vésicule ou de la goutte, la loi énoncée reste valable pour des aspirations plus grandes. Il est donc possible, en imposant des succions croissantes, d'aspirer des langues de plus en plus grandes et ainsi de moduler à volonté la tension de surface des objets aspirés. Cependant, une succion trop grande finit soit par rompre la membrane de la vésicule, soit par aspirer totalement l'objet d'étude dans la pipette, ce qui met directement fin à l'expérience.

2. Caractérisation d'une monocouche de phospholipides.

2.1. Monocouche de phospholipides à l'interface eau-huile

Les caractéristiques de la surface des CLs sont modulées par les phospholipides qui forment une monocouche à sa surface. La densité de cette monocouche de phospholipides

définit le nombre de défauts hydrophobes et contrôle directement la tension de surface du CL (Figure 33 A). Ces paramètres ont probablement un impact sur le comportement du CL dans la bicouche (tension de surface de la monocouche dictant la topologie) et sur le recrutement de protéines spécifiques à sa surface (défauts hydrophobes). Il nous est alors paru important de mettre en place une méthode permettant de décrire précisément une monocouche de phospholipides à l'interface eau-huile, et plus particulièrement de mesurer sa densité de phospholipides.

Une monocouche de phospholipides à l'interface eau-huile peut être considérée comme un fluide à deux dimensions, où l'agitation des molécules (phospholipides) donne naissance à une pression à deux dimensions, appelée pression latérale (π), qui est reliée à la densité de phospholipides (Γ), (Figure 33 B). L'interface couverte de phospholipides possède aussi une élasticité (E) qui reflète les interactions attractives entre phospholipides et qui dépend elle aussi de la densité de phospholipides (Figure 33 C). Notre but est de mesurer la pression latérale et l'élasticité de l'interface et d'en déduire la densité de phospholipides.

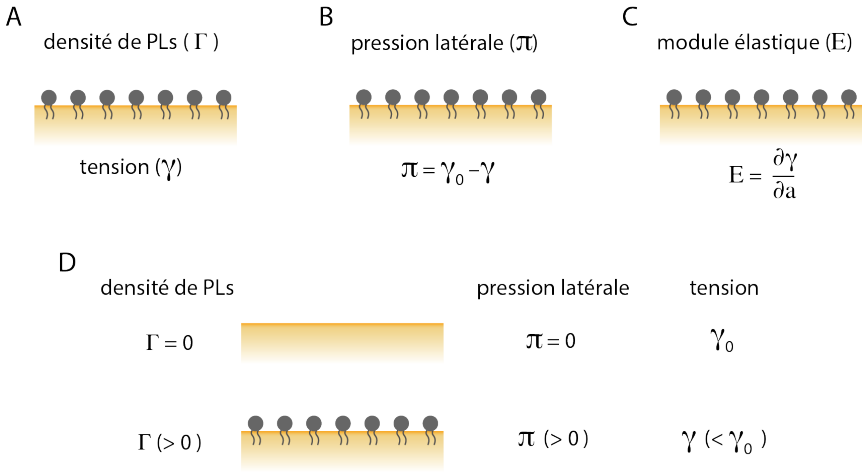

Figure 33 – **Paramètres physiques d'une monocouche de phospholipides à l'interface eau-huile. A**. La densité de phospholipides (Γ) influence directement la tension de surface de l'interface (γ) : plus la densité est grande plus la tension est faible. **B.** La présence de phospholipides à l'interface produit une pression latérale (π), qui reflète les interactions répulsives latérales dans le gaz à 2D que forme les phospholipides à la surface. Cette pression est définie par $\pi = \gamma_0 - \gamma$, où γ_0 est la tension de surface de l'interface eau-huile nue. **C**. la monocouche possède aussi un module élastique (E), défini comme la variation de tension associée à une variation d'aire (a) de l'interface : $E = \partial\gamma/\partial A$. **D**. Une interface nue (sans phospholipides) possède donc une densité $\Gamma = 0$, une tension γ_0 et une pression latérale $\pi = 0$. Si la densité de phopholipides (Γ) augmente, la tension de surface (γ) diminue et la pression latérale (π) augmente. Notons que le module élastique (E) augmente aussi.

La pression latérale (π) à l'intérieur de la monocouche est définie de la manière suivante : $\pi = \gamma_0 - \gamma$, où γ_0 est la tension de surface de l'interface eau-huile nue et γ la tension de surface en présence d'une certaine quantité de phospholipides (Figure 33 A,B). S'il n'y a aucun phospholipide à la surface, la pression dans le film est nulle ; si la densité augmente, la pression augmente (Figure 33 D). Mesurer la pression latérale d'une monocouche de

phospholipides à l'interface eau-huile revient donc seulement à mesurer la tension de surface de l'interface en connaissant au préalable la tension de l'interface nue.
L'élasticité est quant à elle décrite par son module élastique $E = \partial\gamma/\partial A$ (Figure 33 C), qui se mesure en faisant subir à l'interface une variation d'aire et en observant la réponse de la tension de surface.

2.2. Le modèle de Frumkin.

Pour déterminer la densité de phospholipides dans la monocouche, il reste cependant à établir un lien entre la pression latérale, le module élastique et la densité de phospholipides, ce qui revient à définir une équation d'état pour le système. Frumkin a appréhendé ce problème en construisant un isotherme d'absorption qui utilise un modèle de réseau à deux dimensions [142,143]. Le modèle de Frumkin permet d'obtenir une expression de la pression latérale dans la monocouche (π) et de son module élastique (E) en fonction de Γ, la densité surfacique molaire de phospholipides, Γ_∞, la densité surfacique molaire des phospholipides extrapolée pour une pression infinie, et h, l'enthalpie d'absorption des phospholipides à l'interface eau-huile [143] .

$$\pi = -RT\,\Gamma_\infty \left[\mathrm{Ln}\left(1 - \frac{\Gamma}{\Gamma_\infty}\right) - \frac{h\,\Gamma^2}{RT\,{\Gamma_\infty}^2} \right]$$

$$E = RT\,\Gamma_\infty \left[1 - \frac{\Gamma}{\Gamma_\infty\left(1 - \frac{\Gamma}{\Gamma_\infty}\right)} + 2\frac{h\,\Gamma^2}{RT\,{\Gamma_\infty}^2} \right]$$

Grâce à ces équations, si l'on est capable de déterminer expérimentalement un isotherme E-π et de le fiter en modulant les paramètres h et Γ_∞, il est alors possible de remonter directement à la densité de phospholipides à l'interface Γ.

2.3. Détermination de la densité de phospholipide à l'interface Γ

Tensiomètre à goutte pendante pour mesurer l'isotherme E-π

Pour produire expérimentalement un isotherme E-π d'une interface eau-huile recouverte d'une monocouche de phospholipides, nous avons utilisé un tensiomètre à goutte pendante qui permet de reproduire la topologie voulue et de mesurer en temps réel la pression latérale et les modules élastiques de la monocouche.

Principe de fonctionnement :

Cet appareil est constitué d'une seringue remplie d'huile reliée à une aiguille coudée plongée dans de l'eau (Figure 34). Le profil de la goutte d'huile est analysé par une caméra qui, grâce à un logiciel développé par Teclis Instruments (Longessaigne, France), calcule directement la tension de surface de la goutte d'huile. La valeur de la tension de surface sans phospholipides (γ_0) permet alors de calculer la pression latérale (π) (Figure 34). Le système permet aussi de mesurer la valeur du module élastique (E) en faisant varier l'aire de la

goutte d'huile de façon sinusoïdale et en relevant simultanément la valeur de la tension de surface (γ) (Figure 34).

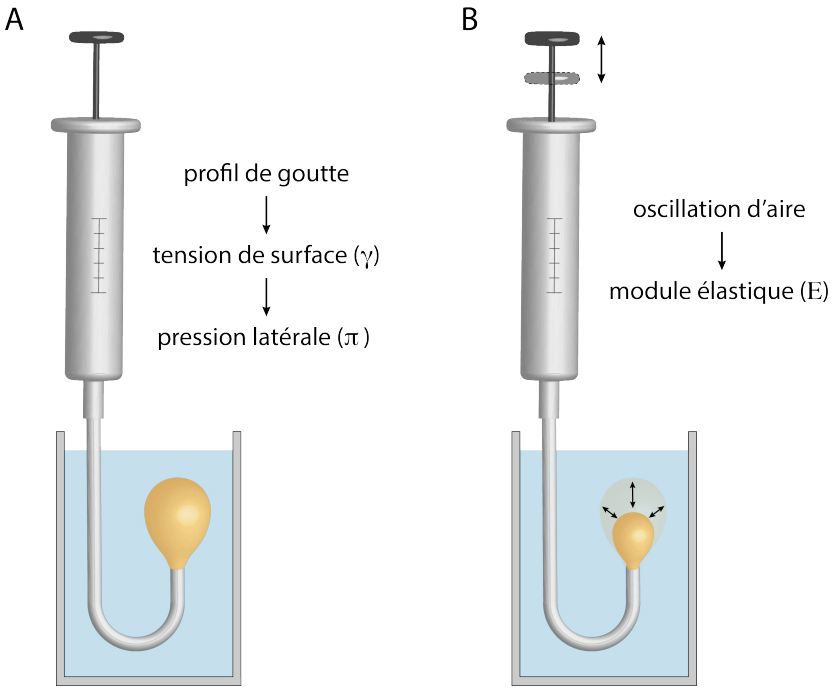

Figure 34 – **Fonctionnement du tensiomètre à goutte pendante. A**. Une goutte d'huile couverte de phospholipides est formée au bout d'une aiguille connectée à une seringue. Le profil de la goutte et les densités des phases mises en jeu permet de mesurer la tension de surface (γ) et donc d'obtenir la pression latérale de la monocouche (π). **B.** Une oscillation de l'aire de la goutte, en imposant un va et vient cyclique au piston de la seringue tout en mesurant la tension de surface, permet de calculer la valeur du module élastique de l'interface $E = \partial\gamma/\partial A$.

Méthode de détermination de la densité de phospholipides grâce à l'isotherme E-π

Une goutte d'huile est formée au bout de l'aiguille coudée, et des phospholipides sous forme de liposomes sont ajoutés à la phase aqueuse. Ils se relocalisent à l'interface eau-huile. La valeur de la pression est calculée en continu par le système. Après avoir attendu la stabilisation de la pression latérale (équilibre d'adsorption des phospholipides atteint), une variation sinusoïdale de l'aire de la goutte est imposée grâce à la seringue, et le module élastique (E) est relevé (Figure 35). Puis, la goutte d'huile est comprimée (réduction d'aire), les oscillations sont répétées, et le module élastique (E) est relevé de nouveau. En répétant ainsi l'opération, on obtient un isotherme E-π (Figure 35).

Cet isotherme peut alors être fité en utilisant les équations de Frumkin, ce qui permet d'estimer la valeur de la densité de phospholipides de la monocouche (Γ) en fonction de la pression (π) (Figure 34). Grâce à cette technique, il est donc possible de caractériser la densité de phospholipides à la surface d'une monocouche seulement en connaissant sa pression latérale ou sa tension de surface. Il faut cependant noter que la mesure de la densité de phospholipides est estimée à l'aide d'un fit qui est basé sur un modèle théorique faisant

des approximations dans la description d'une monocouche. Il existe aussi d'autres modèles théoriques tel que celui de Volmer [144] ou de van der Waals [143] pour décrire les monocouches de phospholipides. Ces modèles ne prennent pas en compte des mélanges de phospholipides de types différents.

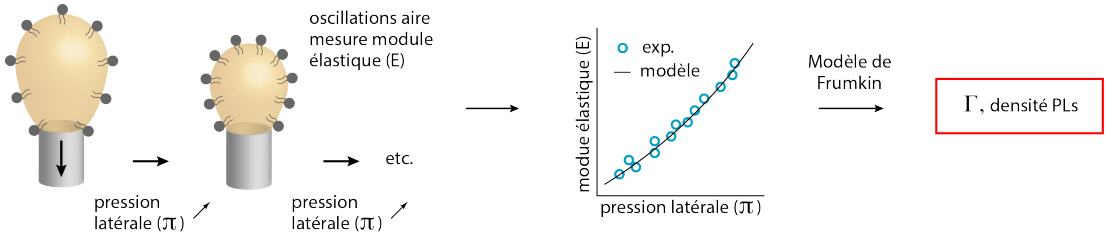

Figure 35 – **Détermination de la densité de phospholipides.** La tension d'une goutte d'huile recouverte d'une monocouche de phospholipides est mesurée en continu par le tensiomètre. La pression latérale est augmentée par une diminution de l'aire de la goutte, puis relevée. Une oscillation d'aire permet ensuite de mesurer le module élastique. L'opération, répétée plusieurs fois pour différentes valeurs de pression, permet de produire un isotherme E, π qui est ensuite fité par les équations du modèle de Frumkin donnant ainsi accès à la densité de phospholipides.

3. Caractérisation des interactions protéines-interface huileuse.

De manière à caractériser les interactions entre des protéines purifiées et la surface de gouttes d'huile recouverte ou non de phospholipides, il est possible d'utiliser le tensiomètre à goutte pendante.

Tout d'abord, on produit une goutte d'huile au bout de l'aiguille du tensiomètre. Une fois que la tension de l'interface est stable, on introduit les protéines dans la phase aqueuse environnante. Les protéines diminuent la tension de l'interface en s'y recrutant (Figure 36 A). Le saut de tension renseigne sur le pouvoir surfactant de la protéine testée.
Une fois l'équilibre atteint, il est possible de caractériser l'intensité de l'interaction entre les protéines et la surface de la goutte. Pour cela, on comprime la surface de la goutte en aspirant un volume d'huile avec la seringue du tensiomètre, puis l'on maintient l'aire constante (Figure 36 B). La concentration surfacique de protéines augmente du fait de la compression, et la tension de surface diminue. Si l'interaction entre la protéine et l'huile est forte, les protéines restent associées à la surface malgré la compression latérale, et la tension de surface reste constante (Figure 36 B). Dans le cas où l'interaction est faible, les protéines qui se retrouvent compactées latéralement ont tendance à se détacher de l'interface, provoquant une relaxation de la tension de surface qui se met alors à augmenter.
Grâce à cette méthode, il est possible de comparer la force des interactions de protéines avec différents types d'huile, et inversement. La même méthode est aussi applicable pour caractériser l'interaction de protéines avec une goutte préalablement recouverte par une monocouche de phospholipides.

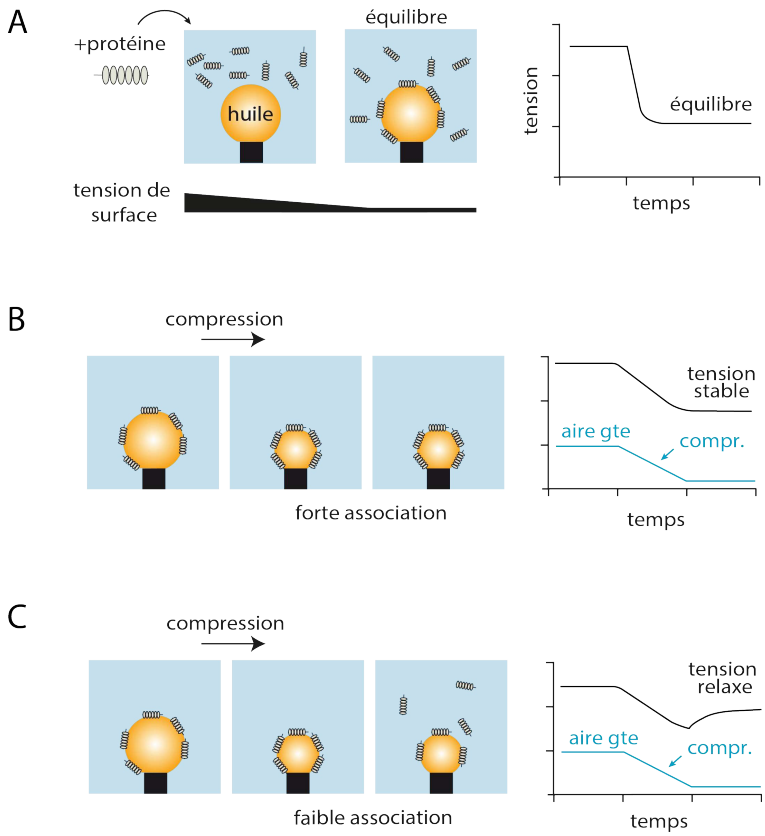

Figure 36 – **Caractérisation des interactions protéines-interface huileuse**. **A** Une goutte d'huile est produite au bout d'une aiguille de tensiomètre à goutte pendante. Les protéines ajoutées à la phase aqueuse sont recrutées à l'interface provoquant une baisse de tension de surface. A l'équilibre, la tension atteint un plateau. **B** Si les interactions entre protéines et goutte (gte) sont fortes, la compression de la goutte (diminution d'aire) ne provoque pas de détachement de protéines et la tension reste stable après compression. **C** Si les interactions entre protéines et goutte sont faibles, les protéines se détachent de l'interface et la tension relaxe.

Conclusion

Le système modèle que nous avons développé permet donc de reproduire *in vitro* la topologie d'un CL en formation à l'intérieur d'une bicouche. Grâce à lui, il est possible de moduler précisément la composition phospholipidique de la membrane, de choisir le type d'huile composant le noyau de la goutte et d'observer directement l'effet de ces paramètres physicochimiques sur le comportement du CL modèle.

Le système de micromanipulation, en plus de rendre possible la manipulation précise de nos objets d'étude, permet de moduler et de mesurer les tensions de surface de la bicouche et de la monocouche du CL modèle. Pour aller plus loin dans la caractérisation, la technique de la goutte pendante permet de remonter à une estimation de la densité de phospholipides sur une monocouche à une tension de surface donnée. Cette technique permet aussi d'estimer l'affinité protéine-monocouche.

Ces méthodes nous ont permis d'étudier efficacement les paramètres physiques contrôlant le bourgeonnement d'un CL artificiel comme il en sera question dans le chapitre suivant. Il est a notter que les details des materiels et protocoles experimentaux sont decrit de manière précise dans les sections « Materiel and Methods » des articles qui composent la suite de ce manuscrit.

Partie III :

Résultats et publications

Organisation des résultats

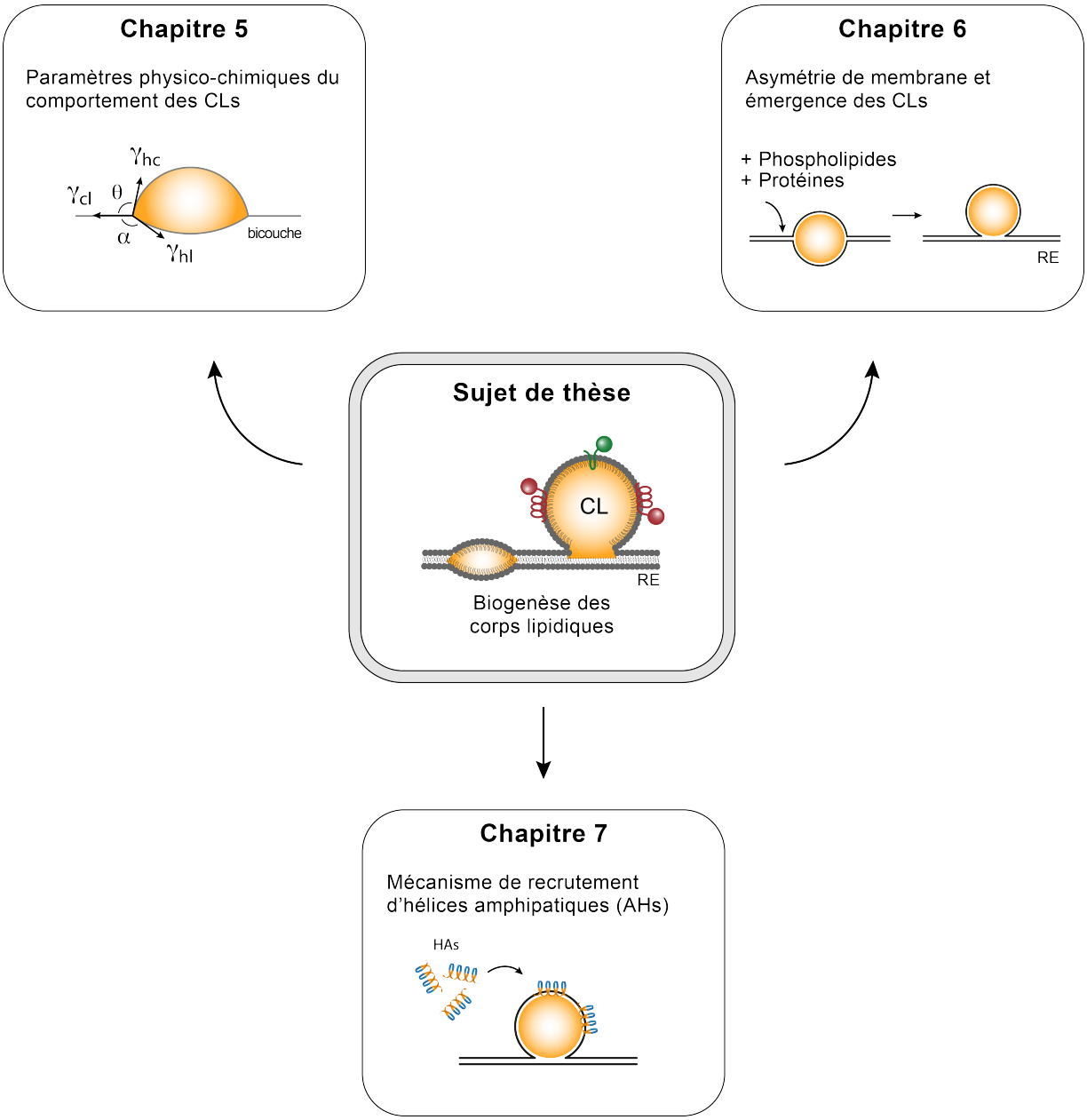

Chapitre 5 :

Émergence des CLs et physique du mouillage

Une asymétrie de tension de surface régule la direction de bourgeonnement des CLs

Travaux publiés dans Biophysical Journal

Les CLs sont des organelles dont la formation et la régulation sont cruciales pour le bon fonctionnement du métabolisme énergétique de la cellule. Pour mener à bien leurs fonctions, les CLs sont principalement formés à partir du réticulum endoplasmique dans le cytoplasme de la cellule [145,146]. Les mécanismes contrôlant cette formation directionnelle sont encore très peu connus. Cependant, comme il en était question dans les premiers chapitres de ce manuscrit, les CLs peuvent être considérés comme une émulsion intracellulaire et la physique de la matière molle, qui décrit les phénomènes d'émulsification, constitue un angle d'attaque prometteur pour éclairer les mécanismes de la formation directionnelle des CLs. Nous avons donc décidé d'utiliser les outils de cette physique pour identifier les paramètres biophysiques contrôlant la biogenèse directionnelle des CLs, dans le but de mieux appréhender les leviers protéiques que la cellule pourrait utiliser pour moduler ce bourgeonnement directionnel.

De manière à pouvoir moduler précisément les paramètres biophysiques contrôlant la formation des CLs, nous avons développé un système minimal *in vitro* reproduisant la topologie de la bicouche du RE avec un CL incorporé entre ses deux feuillets. Ce système, que nous avons baptisé DEV (Droplet Embeded Vesicule), est produit par la mise en contact d'une émulsion d'huile dans l'eau avec des vésicules géantes unilamellaires. On peut ainsi contrôler finement la composition physico-chimique de la bicouche et les tensions de surface du système de manière à isoler les paramètres clés modulant le bourgeonnement directionnel des CLs.

Grâce à ce système modèle, nous avons obtenu les principaux résultats expérimentaux suivants :

- La forme d'un CL inséré entre les deux feuillets d'une bicouche est déterminée par un équilibre de tension de surface.

- La direction de bourgeonnement d'un CL en formation est déterminée par une asymétrie de tension de surface entre ses deux monocouches.
- Une haute tension de bicouche réprime l'asymétrie de tension nécessaire à l'émergence d'un CL.

Ces résultats montrent que la forme et la position du CL artificiel par rapport à la bicouche sont déterminées par l'équilibre des tensions de surfaces de la bicouche et des deux monocouches du CL, à la manière d'un système de mouillage à trois phases. Ce résultat est valable indépendamment de la composition de la bicouche et du type d'huile utilisé et pour des CLs ayant des tailles supérieures à 20 nm, taille limite à partir de laquelle les effets de courbure deviennent négligeables. Concrètement, une haute tension de bicouche étale le CL dans la membrane, lui donnant une forme de lentille, alors qu'une diminution de tension favorise la formation d'un CL sphérique. Le bourgeonnement du CL hors de la bicouche est contrôlé par une asymétrie de tension entre les deux monocouches du CL : le CL émerge du côté présentant la plus faible tension de surface.

Dans la cellule, nos résultats suggèrent que, pour garantir une formation majoritaire des CLs dans le cytoplasme, il soit nécessaire de maintenir la tension de la monocouche cytoplasmique plus basse que celle de la monocouche luminale. Il est très probable que ces tensions soient modulées par la cellule de manière à contrôler la direction de formation des CLs. Nous proposons que cette asymétrie de tension puisse être imposée de manière purement mécanique ou par le maintien d'une asymétrie de composition protéique et/ou phospholipidique entre les deux monocouches. Par exemple, la cellule pourrait potentiellement adapter la composition phospholipidique de son RE à l'aide d'enzymes agissant sur les phospholipides, ou favoriser l'insertion spécifique de protéines d'un côté du RE.

Nos résultats soulignent comment la cellule pourrait exploiter des principes bien connus de la physique du mouillage pour extraire les molécules huileuses de son RE en formant des CLs à travers un processus d'émulsification original. Ceci permet de proposer des pistes pour rechercher les protéines impliquées dans la régulation de la formation directionnelle des CLs et ouvre la porte à une meilleure compréhension des mécanismes de sécrétion des lipides.

L'ensemble de cette étude a fait l'objet d'un article publié dans Biophysical Journal qui compose le chapitre suivant de cette thèse.

Biophysical Journal
Article

Biophysical Society

An Asymmetry in Monolayer Tension Regulates Lipid Droplet Budding Direction

Aymeric Chorlay[1] and Abdou Rachid Thiam[1,*]
[1]Laboratoire de Physique Statistique, Ecole Normale Supérieure, PSL Research University, Sorbonne Université, UPMC Université Paris 06, Université Paris Diderot, CNRS, Paris, France

ABSTRACT Cells store excess energy in the form of neutral lipids that are synthesized and encapsulated within the endoplasmic reticulum intermonolayer space. The lipids next demix to form lipid droplets (LDs), which, surprisingly, bud off mostly toward the cytosol. This directional LD formation is critical to energy metabolism, but its mechanism remains poorly understood. Here, we reconstituted the LD formation topology by embedding artificial LDs into the intermonolayer space of bilayer vesicles. We provide experimental evidence that the droplet behavior in the membrane is recapitulated by the physics of three-phase wetting systems, dictated by the equilibrium of surface tensions. We thereupon determined that slight tension asymmetries between the membrane monolayers regulate the droplet budding side. A differential regulation of lipid or protein composition around a forming LD can generate a monolayer tension asymmetry that will determine the LD budding side. Our results offer, to our knowledge, new insights on how the proteins might regulate LD formation side by generating a monolayer tension asymmetry.

INTRODUCTION

Biological membranes are made up of two adhering phospholipid monolayers that form a bilayer. The properties of this bilayer are crucial for various biological mechanisms and rely strongly on bilayer lipid composition. This is illustrated by the difference in membrane composition between cellular organelles (1), which perform different tasks. For example, as compared to other organelle membranes, the plasma membrane is enriched in lipid surfactants such as cholesterol or specific charged phospholipids (2). The endoplasmic reticulum (ER) membrane can instead particularly contain neutral lipids, which are oily molecules, or fat, localized at the interstice between the two monolayers composing the membrane (3) (Fig. 1 *A*). This happens typically in energy-rich conditions under which neutral lipids such as triglycerides, sterol or retinyl esters, or squalene are produced by enzymes directly inside the ER intermonolayer membrane (4). These lipids can affect the ER membrane properties, disrupt it, and mediate protein unfolding and ER stress (5,6). However, at a certain concentration, the neutral lipids probably demix, forming a lipid lens within the bilayer (Fig. 1 *A*), which further grows by accumulating lipids (7,8). In cells, this phenomenon presumably drives the removal of neutral lipids from the ER bilayer, packaging them into organelles called oil bodies or lipid droplets (LDs) (9).

LDs are oil droplets covered by a phospholipid monolayer containing proteins; they constitute a newly identified class of organelles whose formation and regulation are critical for cellular energy metabolism (10,11). LDs bud off from the ER bilayer membrane and, remarkably, mainly toward the cytosol (12,13). The mechanisms responsible for the packaging of neutral lipids into droplets and LD directional budding are still weakly understood. However, LDs can be seen as the disperse phase of an intracellular oil-in-water emulsion (7,14), and therefore, LD formation can be considered as an emulsification mechanism of oil-in-water droplets from the ER bilayer. Soft-matter physics, which describes such typical phenomena, should thus enable a better comprehension of the mechanism of LD directional formation (7). We decided to take advantage of such knowledge to identify the biophysical parameters governing LD directional formation and shed light on how proteins might regulate cytosolic LD biogenesis (15).

Studying the biophysics of LD budding requires knowledge of the behavior of oil molecules in a bilayer. It is now possible to acquire such knowledge by various in vitro model systems based on giant unilamellar vesicles (GUVs) made in the presence of oils. This is the case, for example, when GUVs are prepared using

Submitted September 26, 2017, and accepted for publication December 11, 2017.

*Correspondence: thiam@lps.ens.fr

Editor: Markus Deserno.
https://doi.org/10.1016/j.bpj.2017.12.014

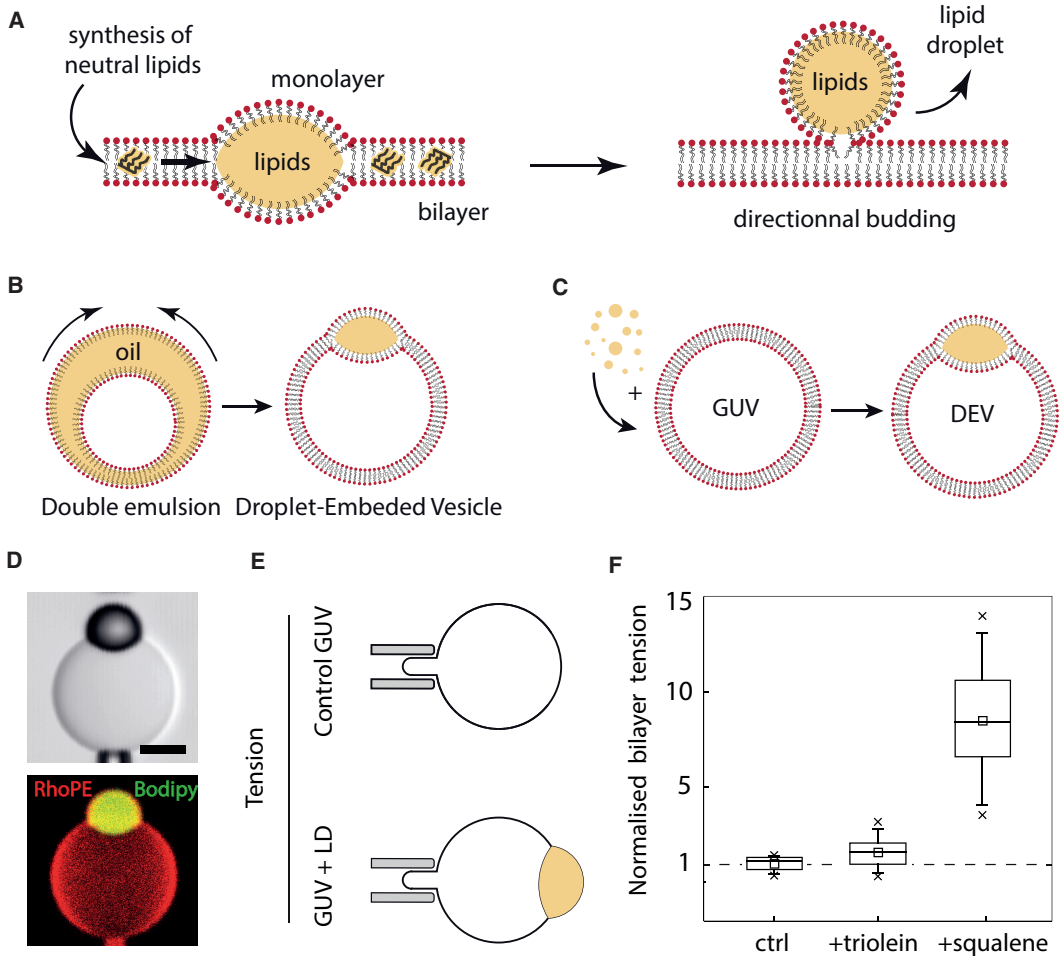

FIGURE 1 The presence of neutral lipids increases bilayer surface tension. (*A*) Schematic description of LD formation steps. (*B*) The oil film of a water-in-oil-in-water double emulsion (made by microfluidics, see (14) for more detail) spontaneously collapses to form a GUV embedded with an LD. (*C*) GUVs are mixed with artificial LDs that are incorporated into the intermonolayer space of the GUVs to form a GUV embedded with an LD, termed DEVs. (*D*) Reconstitution of an artificial LD (Bodipy stained) embedded in the intermonolayer space of a PC (dioleoylphosphatidylcholine) GUV using the technique described in (*B*). Rhodamine-PE (0.5% w/w to PC) is used to visualize the membranes by fluorescence. Scale bars, 10 μm. (*E*) Microaspiration is used to measure bilayer tension of a GUV in the presence and absence of an LD. Micrographs of the experiments are shown in Fig. S1. (*F*) Bilayer tensions of a different set of GUVs normalized by the average GUV tension without an LD (3.10–2 mN/m): control and embedded LDs of triolein and squalene. $N = 10$, 9, and 11, respectively. To see this figure in color, go online.

water-in-oil-in-water double emulsions (Fig. 1 *B*) or inverted emulsion methods (16,17). In these situations, a large oil film is first generated between two monolayers before it collapses into an oil droplet (Fig. 1 *B*). The resulting system is a vesicle embedded with an LD. Recently, we have developed an alternative system in which we first make GUVs by electroformation and afterward incorporate oil droplets directly within the intermonolayer space (18,19) (Fig. 1 *C*)—we term this system droplet-embedded vesicles (DEVs). DEVs offer minimal systems mimicking the topology of an LD forming in the ER bilayer; their surface tensions or membrane physical chemistry can be finely modulated to isolate relevant parameters controlling LD directional budding.

We hypothesized that the DEV topology is a three-phase system in which the equilibrium between surface tensions dictates droplet shape (20,21). We here bring the tensions into play and show that, regardless of the physical chemistry of the membrane, their equilibrium indeed follows a three-phase wetting theory, i.e., the shape of a droplet, described by the angle it forms with the bilayer, is dictated by the balance of surface tensions (7). We suggest that the budding of the model LDs corresponds to a full dewetting situation, i.e., generation of a spherical droplet sharing a neck with the bilayer (Fig. 1 *A*). The exclusive formation of droplets on one side of the membrane requires keeping an imbalance of surface tensions between the two monolayers enclosing the droplet. Such tension imbalance can arise from a

mechanically imposed difference of tensions between the monolayer leaflets and/or an asymmetry in protein or phospholipid composition dynamically generated by the action of enzymes. Our results thus bring new insights, to our knowledge, on how proteins might act in cells to modulate the formation of cytosolic LDs.

MATERIALS AND METHODS

GUV preparation

Unless stated otherwise, all GUVs were 99.5% 1,2-dioleoyl-*sn*-glycero-3-phosphocholine (DOPC) and 0.5% (w/w) Rhodamine-DOPE. GUVs were prepared by electroformation (19). Phospholipids and mixtures thereof in chloroform at 0.5 μM were dried on an indium-tin-oxide-coated glass plate. The lipid film was desiccated for 1 h. The chamber was sealed with another indium-tin-oxide-coated glass plate. The lipids were then rehydrated with a sucrose solution (275 $\pm$ 15 mOsm). Electroformation is performed using 100 Hz alternating-current voltage at 1.0–1.4 Vpp and maintained for at least 1 h. This low voltage was used to avoid hydrolysis of water and dissolution of the titanium ions on the glass plate. GUVs were either stored in the chamber at 4°C overnight or directly collected with a Pasteur pipette.

Buffer HKM composition

Unless mentioned, experiments were performed in a buffer of 50 mM Hepes, 120 mM Kacetate, and 1 mM MgCl2 (in Milli-Q water) at pH 7.4 and 275 $\pm$ 15 mOsm.

Incorporation of droplets into GUV membranes to make DEVs

To prepare GUVs embedded with artificial LDs, 5 μL of the oil was added to 45 μL of HKM buffer. The mixture was sonicated for 1 min. GUVs were then incubated with the artificial LDs for 5 min under gentle mixing. The GUV-LD mixture was then placed on a glass coverslip, pretreated with 10% (w/w) bovine serum albumin (BSA), and washed three times with buffer.

Micromanipulation and surface tension measurements by micro aspiration

Micropipettes were made from capillaries drawn out with a Sutter Instruments (Novato, CA) pipette puller. They were used to manipulate the LD-embedded GUVs to get a side view of the system. The pipettes were incubated for 30 min in a 5% BSA solution before use, to prevent droplets and membranes from adhering to the glass.

Additionally, surface tensions were measured and modulated using the same pipettes. As shown in (Fig. 1 *D*), the micromanipulation of the external LD monolayer (and bilayer) enables the measurement and modulation of surface tension (γ). Using Laplace's law and the measurement of the pipette inner diameter, droplet diameter, and suction pressure, the surface tension of the interface can be determined (19) as

$$\gamma = \frac{\Delta P\mathrm{suc}}{2\left(\frac{1}{Rp} - \frac{1}{Rd}\right)},$$

where ΔPsuc, Rp, and Rd are the suction pressure, the pipette radius, and the droplet (or GUV) radius.

The suction was carried out using a syringe. The resulting pressure was measured with a pressure transducer (DP103, Validyne Engineering, Northridge, CA), the output voltage of which was monitored with a digital voltmeter. The pressure transducer (range 55 kPa) was calibrated before the experiments were performed.

Reagents

Glyceryl trioleate (triolein) (T7140) and squalene (S3626) were from Sigma Aldrich (St. Louis, MO). Phospholipids used were DOPC, rhodamine-1,2-dioleoyl-*sn*-glycero-3-phosphoethanolamine (rhodamine-DOPE), and lysophosphatidylcholine (LysoPC) (18:1) from Avanti Polar Lipids (Alabaster, AL). Bodipy (D3922, Molecular Probes, Eugene, OR) was used at 1:100 of a 10 mg/mL stock concentration. BSA 98% (A7906-100G) and sucrose 99.5% (59378- 500G) were purchased from Sigma-Aldrich.

Equipment

All micrographs were made on a laser scanning microscope (LSM 800, Carl Zeiss, Oberkochen, Germany). Glass coverslips (24 $\times$ 36 mm #0) were from Menzel Glaser (Braunschweig, Germany). Micropipettes made from capillaries (1.0 OD $\times$ 0.58 ID $\times$ 150 L (mm); 30-0017 GC100-15b, Harvard Apparatus, Holliston, MA) were used with a micropipette puller (model P-2000, Sutter Instruments). Micromanipulation was achieved using TransferMan 4r (Eppendorf, Hamburg, Germany). The pressure measurement unit was provided by Validyne Engineering (DP103).

RESULTS

The presence of neutral lipids increases bilayer surface tension

We generated dioleoylphosphatidylcholine (PC) GUVs of low tension by electroformation and mixed part of them with triolein or squalene (Fig. 1, *C* and *D*), which are biological oils synthesized in different cell types (10). We measured with microaspiration techniques the bilayer tension of each sample and found that GUVs mixed with oil, i.e., forming DEVs, systematically had a significantly higher bilayer surface tension than control GUVs (Fig. 1, *E* and *F*). This is likely due to the localization of oil molecules into the intermonolayer space of the bilayer. The subsequent increase of surface tension probably arises from different contributions. This increase might originate from the higher energy cost of the interaction between the acyl chains of phospholipids and oil molecules, as compared to the interaction between facing phospholipids in a pure bilayer. In addition, the accumulation of oil molecules in the bilayer tends to make the membrane similar to two phospholipid-covered oil-water interfaces, which have higher surface tension (1–30 mN/m (18,19,22)) than pure bilayer membranes (0.001–1 mN/m (23–25)).

We also noted that for the same phospholipid composition, i.e., PC, triolein and squalene differently increased the bilayer tension (Fig. 1 *F*), which probably reflects the difference in affinity of the oils with phospholipids and/or surrounding water phase. Changing the membrane phospholipid composition would also change the relative tension variation (18). In conclusion, our results show that the presence of neutral lipids in a bilayer increases surface tension.

Thus, as compared to classical bilayer organelles, the ER bilayer might acquire higher surface tensions because of the presence of neutral lipids. Packaging neutral lipids into LDs would make it possible to reduce tension, maintain ER membrane integrity, and avoid bilayer stress.

The balance of tensions determines droplet shape in a bilayer

We recently found that decreasing the bilayer tension favors the removal of neutral lipids from the bilayer and their packaging into spherical droplets (18). Here, we experimentally observed that the shape of the droplet indeed depends on the bilayer tension, which was mechanically varied (Fig. 2 *A*). A spherical droplet was obtained at lower bilayer tension; a higher bilayer tension led to a droplet having a lense-like shape. We previously assumed that the droplet shape is determined by the equilibrium between the various tensions (Fig. 2 *B*), as is the case for three-phase wetting situations (20,26). Such equilibrium would yield

$$\gamma_{\mathrm{int}}\ \sin(\alpha)\ =\ \gamma_{\mathrm{ext}}\ \sin(\theta) \tag{1}$$

and

$$\gamma_{\mathrm{b}}\ =\ -\gamma_{\mathrm{int}}\ \cos(\alpha)\ -\ \gamma_{\mathrm{ext}}\ \cos(\theta), \tag{2}$$

where γ represents surface tension and α and θ are the different angles formed between the bilayer and monolayers (Fig. 2 *B*). This assumption is valid only when the membrane bending contribution, given by its bending modulus, κ, can be neglected. This condition is satisfied when the droplet size is $>(\kappa/\gamma)^{1/2} \sim 20$ nm, when taking $\kappa \sim 10 k_{\mathrm{B}}T$ and $\gamma \sim 1$ mN/m, which are typical values for a phospholipid monolayer (18,22,27). The size of cellular LDs is well above 50 nm (28), which implies that surface tensions might be at some level the main physical parameters that determine the formation of spherical LDs.

If the balance of tensions determines the droplet shape, the membrane physical chemistry should not be directly

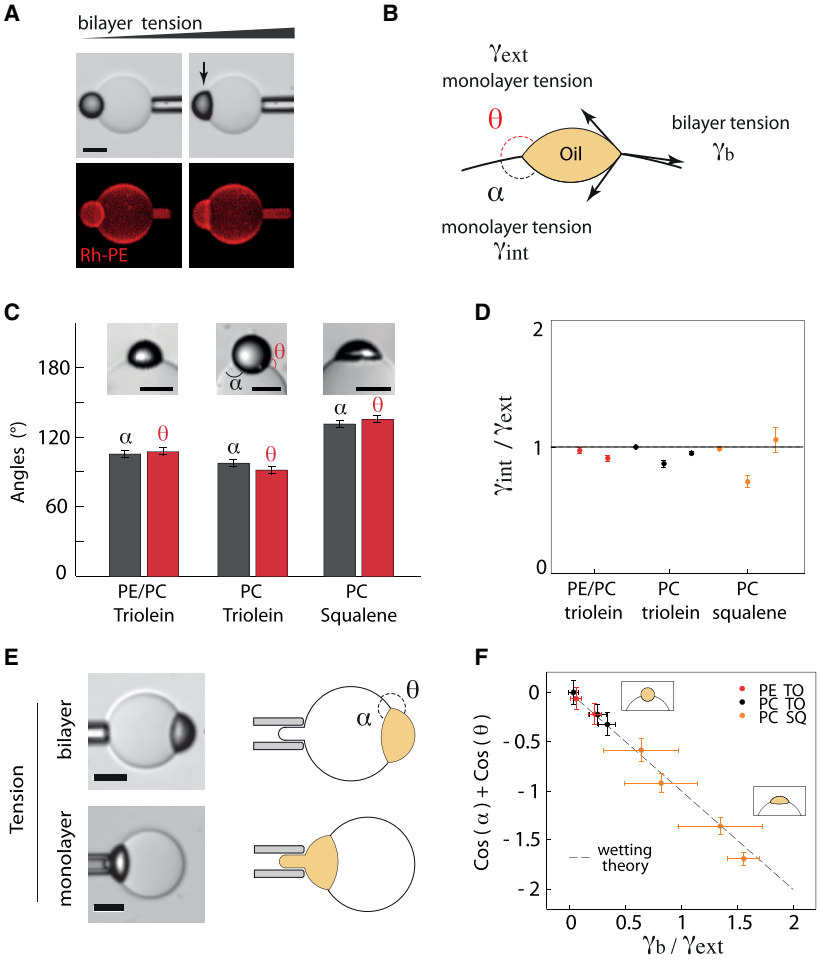

FIGURE 2 The equilibrium of tensions determines droplet shape in a bilayer according to a wetting theory. (*A*) A triolein LD embedded in a PC GUV spreads in the bilayer when tension is increased by the microaspiration technique. Scale bars, 10 μm. (*B*) Illustration of an LD embedded in a bilayer, showing the biophysical parameters controlling its shape: external and internal monolayer tension, and bilayer tension. The two angles α and θ describe the shape and position of the LD. (*C*) Angles α and θ correspond to different oil droplet (triolein or squalene) and membrane compositions (PE/PC 40:60 or PC 100%). Scale bars, 10 μm. (*D*) Ratios of internal to external surface tension corresponding to the angles in (*B*), calculated using the equilibrium-of-tensions law described by Eq. 1. Eight measurements of different physical chemistry conditions were probed with varying phospholipid/oil compositions. (*E*) Method of measurement of the external monolayer and bilayer tensions using micropipettes. The suction by the micropipette is correlated to the surface tension through the Laplace law. (*F*) Experimental α and θ sum of cosine is displayed as a function of the ratio of bilayer to monolayer tensions, corresponding to the experimental conditions in (*D*). The wetting theory prediction from Eq. 3 is displayed as a dashed line. To see this figure in color, go online.

involved. We thus studied different phospholipid and oil compositions. Using electroformation, we made PC/PE and PC GUVs, to vary the membrane composition, and embedded them with triolein oil droplets to make DEVs. We also embedded trioelin and squalene droplets in PC GUVs to change the neutral lipid oil composition instead of phospholipids. We observed that the embedded droplets adopted different shapes (Fig. 2 *C*). For all lipid conditions, however, the droplets were often positioned in the middle of the bilayer, i.e., $\alpha = \theta$ (Fig. 2 *C*). This would imply from Eq. 1 that the inner and outer monolayers of these droplets have the same tension (Fig. 2 *D*), which is plausible, as no asymmetry was introduced during GUV formation. Thus, by assuming that $\gamma_{int} = \gamma_{ext}$, Eq. 2 can be written simply as

$$\gamma_b/\gamma_{ext} = -(\cos(\alpha) + \cos(\theta)). \quad (3)$$

Experimentally, we can measure γ_b and γ_{ext} by micropipette aspiration, and the angles, which are geometrical parameters (Fig. 2 *E*). We observed that all lipid conditions follow Eq. 3 (see Fig. 2 *F*). This result provides evidence that the balance between the monolayer and bilayer tensions exclusively determines the droplet shape in the bilayer.

Modeling the role of surface tensions in droplet shape and budding direction

Considering that the droplet shape is exclusively determined by surface tensions, we developed a basic model (Supporting Material, Text S1) that allowed us to draw a phase diagram describing the behavior of a droplet in a bilayer. The droplet is subjected to two monolayer tensions that pull on the contact line to make it spherical, and to the bilayer tension, which pulls in the opposite direction to flatten it (Fig. 2 *B*). When the bilayer tension is substantially higher than the monolayer tensions, the droplet tends to adopt a lens-like shape (Fig. 3 *A*). In the extreme case, when $\gamma_b - \gamma_{int} - \gamma_{ext} \geq 0$, which can be rewritten as

$$\gamma_{int}/\gamma_{ext} \leq \gamma_b/\gamma_{ext} - 1, \quad (4)$$

oil molecules contained in the droplet are entirely spread in the bilayer (Fig. 3 *A*, *pink region*).

For a given bilayer tension, if the external monolayer surface tension of the droplet is higher than the internal tension, the pressure of the external bulk fluid will push the droplet inside the membrane due to the Laplace effect. If, instead, the inner monolayer surface tension is higher, the luminal pressure will be higher than the bulk pressure and will push the droplet to the outside. In the extreme situations where the droplet fully buds internally or externally, the tensions follow $(\gamma_{ext} - \gamma_{int}) - \gamma_b \geq 0$ and $(\gamma_{int} - \gamma_{ext}) - \gamma_b \geq 0$, respectively, which can be rewritten as

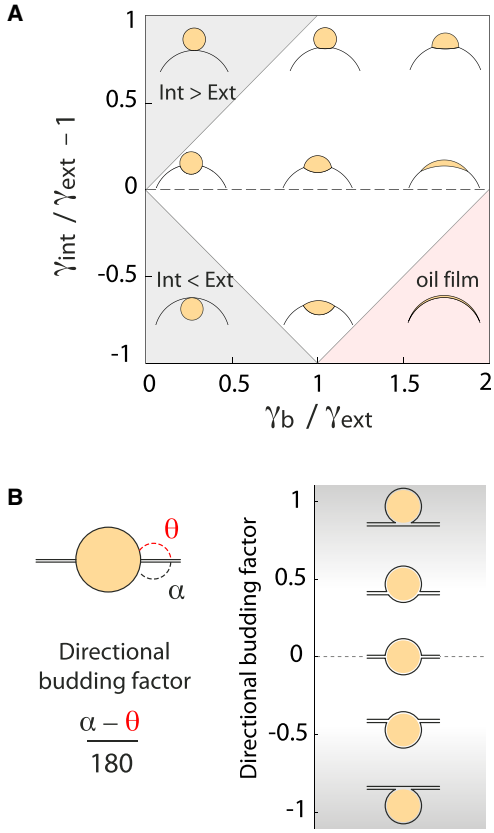

FIGURE 3 Modeling of the role of surface tensions on LD shape and budding direction. (*A*) The competition between the three different surface tensions (bilayer, external monolayer, and internal monolayer tensions) determines LD shape in the bilayer. The phase diagram shows simulated LD shape and position according to the competition between bilayer and external monolayer tensions, and the ratio between external and internal monolayer tensions (see Supporting Material, Text S2). High bilayer tensions flatten the LD and imbalance between internal and external tension dictates the budding direction. The top gray region corresponds to full external budding, low bilayer tensions, and internal tensions larger than external tensions; the bottom gray region corresponds to full internal budding, low bilayer tensions, and internal tensions smaller than external tensions. The pink region corresponds to full spreading of the oil film in the bilayer (unstable condition). (*B*) Directional budding factor describing the position of the LD relative to the bilayer and corresponding LD positions, here displayed at low bilayer tension (spherical LD). To see this figure in color, go online.

$$\gamma_{int}/\gamma_{ext} \leq 1 - \gamma_b/\gamma_{ext} \quad (5)$$

and

$$\gamma_{int}/\gamma_{ext} \geq 1 + \gamma_b/\gamma_{ext}. \quad (6)$$

Equations 4, 5, and 6 delineate the regions of the phase diagram, showing the different shape and budding direction of the droplets (Fig. 3 *A*). This phase diagram was also numerically calculated (unpublished data) using a

mathematical model that takes into account a GUV bilayer containing an LD (Supporting Material, Text S1).

In summary, the diagram recapitulates that the imbalance between the monolayer tensions determines the position of the droplet with respect to the bilayer, and that the droplet is pushed toward the side with the lower monolayer surface tension. The droplet can be fully budded on either the inside of the membrane (Fig. 3 *A*, *lower gray region*) or the outside (Fig. 3 *A*, *upper gray region*), or can remain in the bilayer, with varying degrees of contact with the interior and exterior (Fig. 3 *A*). When the monolayer tensions are equal, the LD lies in the middle of the bilayer, except for very low bilayer tension ($\gamma_b/\gamma_{ext} < \sim 0.2$), for which effective line tensions can theoretically promote the spontaneous budding of the droplet (27) but would not control the budding direction.

An asymmetry in monolayer tension determines LD budding direction

A currently unanswered question regarding the mechanism of LD biogenesis is how LD exclusive formation in the cytosol is achieved. This is an important question for lipid metabolism because lipid fluxes strongly rely on the accessibility of LDs to cytosolic proteins. Our analysis of the role of tensions in LD shape and position suggests that controlling the LD budding side or direction is possible by constantly maintaining a tension asymmetry between the monolayer leaflets (Fig. 3 *A*). Surface tensions are generally controlled mechanically or chemically by the presence of surfactants, which can be lipids or proteins. We probed these predictions in our DEV system.

We prepared PC GUVs and incorporated them with LDs. We used microaspiration to modulate surface tensions in the resulting DEV system. We can modulate and measure both bilayer and external monolayer tensions, separately or concurrently, by pulling on their respective membranes (Fig. 2 *E*). The tension of the inner monolayer can be inferred from the droplet shape (Supporting Material, Text S2).

At the outset, the LDs were centered in the bilayer. To characterize the droplet position, we defined the directional budding factor as the relative angle or position shift of the LD between the inside and outside of the membrane (see Fig. 3 *B*). Initially, the directional budding factor was close to 0 (Fig. 4, *A* and *B*). We increased the outer monolayer tension and observed that the LD was displaced into the GUV lumen (Fig. 4 *A*, *arrow*; Fig. S2 *C arrow*); the directional budding factor was consequently largely negative (Fig. 4 *B*). Measurement of the tension values confirmed that an asymmetry of monolayer tension was maintained (Fig. 4 *C*; Fig. S2, *C–E*). The final set of surface tensions is consistent with the droplet shape predicted by the phase diagram (Fig. S2 *A*). These observations show that physically maintaining a tension asymmetry can enable control over the droplet budding side.

In cells, the surface tension of the cytosolic monolayer of a forming LD can be modulated, for example, by the asymmetrical insertion or action of proteins such as perilipins or complex protein I (19,29). Proteins might also modulate the phospholipid monolayer composition to generate an asymmetry of tension. This is the case of phospholipases, for example, which mainly act on the cytosolic face of LDs.

We probed the effect of the phospholiphase A2 (PLA2), which is involved in cellular LD formation, by transforming phospholipids into lysophospholipids (18,30). We made GUVs containing LDs and added PLA2 enzyme to the external bulk solution (Fig. S4, *A* and *B*), which makes lysophospholipids only on the external monolayer a priori; the conversion of PC to Lyso-PC on GUVs by PLA2 has been proven using thin-layer chromatography in our previous work (18). Over time, we observed dynamic changes of shape and position of the droplet in the bilayer. The droplet moved toward the interior of the GUV, suggesting an increase of the external monolayer tension. This tension increase likely arose from the replacement of PC by Lyso-PC

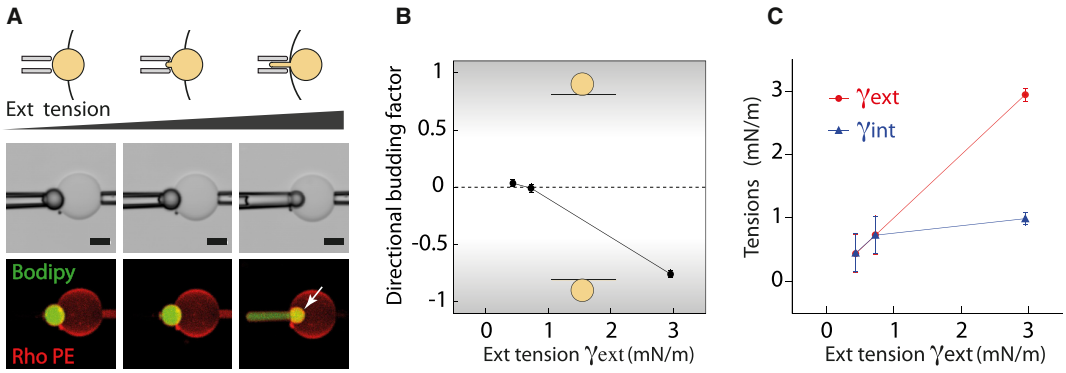

FIGURE 4 Asymmetry between monolayer tensions determines droplet budding direction. (*A*) A triolein LD embedded in a GUV. Increasing the external monolayer tension with a micropipette causes the internalization of the LD. Scale bars, 10 μm. (A similar experiment with a squalene LD and the bilayer tension kept constant is shown in Fig. S2, *C–E*). (*B*) The directional budding factor drastically decreases due to the internalization of the LD. (*C*) Throughout the internalization process, the internal tension remains roughly constant as external tension is increased. To see this figure in color, go online.

in the external monolayer. Substituting PC with Lyso-PC in the monolayer introduces more phospholipid packing defects on the external monolayer, which results in an increase of surface tension. Indeed, a fully packed PC monolayer on a triolein droplet has a tension of ~0.6 mN/m, whereas a pure Lyso-PC monolayer has a higher tension, >2 mN/m (18). It is worth noting that these monolayer tension values are much higher than bilayer tensions, which are usually well below 1 mN/m. Consequently, we think that spontaneous curvatures, which mediate bilayer deformation, would have a smaller impact on the monolayer deformation because of the high monolayer tension values. Our results thus suggest that keeping an asymmetry of phospholipid type around a forming LD gives rise to asymmetric monolayer tensions and might regulate the side of LD budding.

High bilayer tensions repress the effect of tension asymmetry on the droplet budding direction

According to the phase diagram (Fig. 3 *A*), LD directional formation is essentially controlled by an asymmetry in monolayer tension. However, the diagram also suggests that a low bilayer tension is necessary to facilitate the budding step (18,27) by decreasing the required monolayer tension asymmetry (Fig. 3 *A*). Consequently, increasing the bilayer tension should repress budding and, considering the phase diagram, reduce the effect of monolayer tension asymmetry on the droplet directional formation. We experimentally tested this prediction.

We embedded an LD in a GUV bilayer and introduced a slight tension asymmetry by increasing its external tension (see droplet tongue suctioned into the micropipette (Fig. 5 *A*)). This caused the droplet to bulge into the GUV lumen (Fig. 5 *A*, *arrow*). While maintaining the suction on the external monolayer, we pulled on the bilayer to increase its tension (Fig. 5 *A*). This operation repressed the internalization, equilibrated the monolayer tensions, and recentered the droplet in the middle of the bilayer (Fig. 5, *B* and *C*). This observation confirmed that increasing the bilayer tension reduces the asymmetry of monolayer tensions. All together, our results predict that having a higher surface tension on the luminal monolayer of an LD, along with a low ER bilayer tension, will guarantee budding in the cytosol (Fig. 6 *A*). Finely tuning ER molecular composition in the cell can enable the meeting of such requirements.

DISCUSSION

We have experimentally demonstrated that the shape and position in a bilayer of a reconstituted LD are determined by the equilibrium between the tensions of the bilayer and two monolayers enclosing the droplet, as in three-phase wetting systems; this result is valid when droplet size is >20 nm. Our result thus highlights how a cell might exploit well-known physical concepts of wetting processes to exclude fat from membranes and mediate an emulsification process mediating LD formation. Concretely, high bilayer surface tension leads to disperse neutral lipids in the membrane. Decreasing the bilayer tension enables packaging of the neutral lipids into spherical droplets (Figs. 2 *A*, 3 *A*, and 6 *A*) (18,27). The budding direction is determined by the tension asymmetry between the monolayers; budding happens toward the side of lower monolayer tension

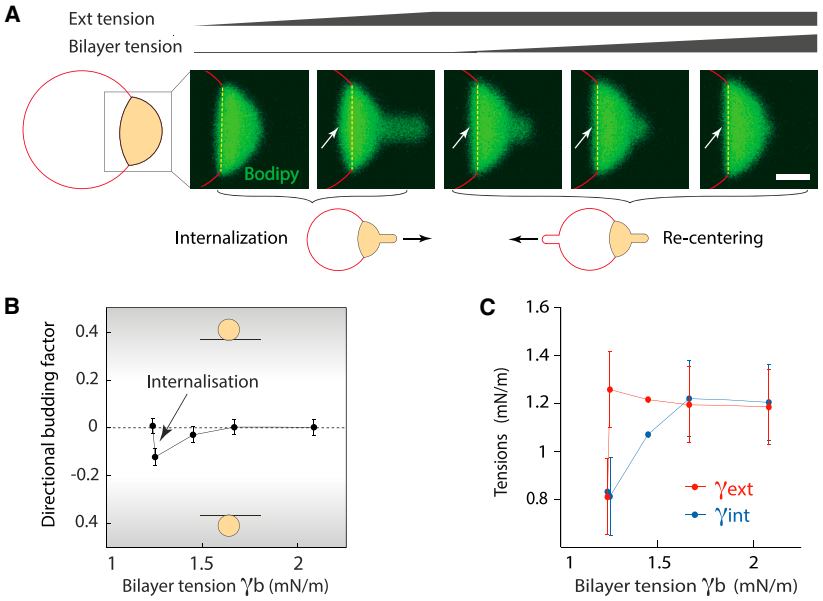

FIGURE 5 High bilayer tensions repress the effect of tension asymmetry on directional budding. (*A*) An artificial LD is slightly internalized by an increase of its external tension. Then, increasing the bilayer tension recenters the LD. Scale bars, 10 μm (full pictures are shown in Fig. S3 *A*). (*B*) Increase of external over internal tension diminishes the directional budding factor. An increase in bilayer tension recenters the LD and thus brings the directional budding factor back to zero. (*C*) Internal and external monolayer tensions are plotted as a function of bilayer tension. The asymmetrization of monolayer tension is suppressed by increasing bilayer tension. These tensions are in part calculated as described in Text S2 in the Supporting Material, with angles displayed in Fig. S3 *B*. To see this figure in color, go online.

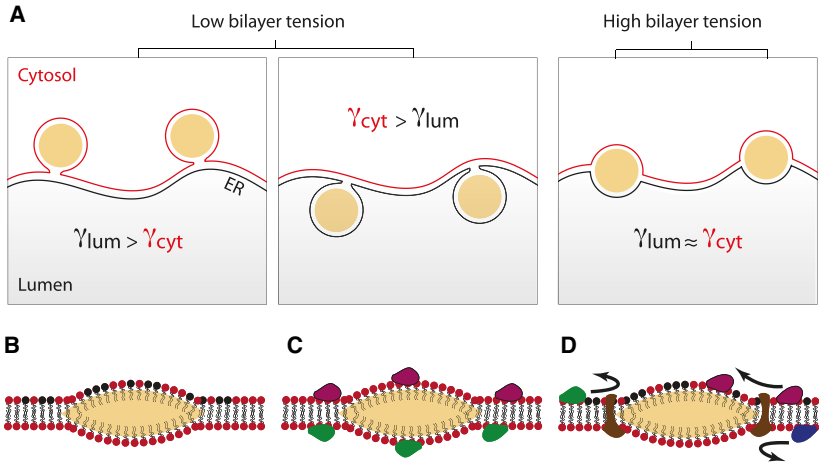

FIGURE 6 Model for the role of surface tensions and excess of phospholipids in LD position and contact with different cell compartments. (*A*) At high bilayer tensions, LDs are centered and spread in the middle of the bilayer. Lowering the tension allows budding of the droplets toward the side with the lower monolayer tension. (*B*) Asymmetry in phospholipid composition between the two sides of the bilayer. (*C*) Asymmetry of protein repartition on the two sides of the bilayer. (*D*) Transmembrane proteins that might regulate the protein and phospholipid asymmetry. To see this figure in color, go online.

(Fig. 6 *A*). These various tensions are very likely modulated in cells to control cytosolic LD formation. For example, altering ER phospholipid composition, and potentially shape, by the action of phospholipid remodeling enzymes and/or shaping proteins, modulates ER bilayer surface tension and LD formation (18,30,31). To guarantee LD exclusive formation in the cytosol, a constant lower tension of the cytosolic over the luminal monolayer should be maintained around forming LDs. Questions to address are how and which proteins modulate tensions of the cytosolic and luminal monolayers to guarantee LD formation toward the cytosol.

Proteins might regulate monolayer surface tensions by different means. A first class of proteins can directly bind LDs from the cytosol, or the ER membrane or its lumen, and generate an asymmetry in monolayer tensions. This can be achieved by locally creating an asymmetry in protein and lipid composition between the monolayer leaflets (Fig. 6, *B* and *C*), as different lipid and protein compositions proffer different monolayer tensions (18,19,22,32). Such action could be mediated by lipid remodeling enzymes such as phospholipases, lipin, or diacylglycerol-acyltransferase (30,33,34). Other proteins binding LDs can physically modulate the monolayer tension (Fig. 6 *C*). In the cytosol, this might be the case for perilipin proteins, or the complex protein I machinery that mechanically deforms the LD surface (19,29). Whether these proteins affect LD budding direction is currently not known.

There is a second class of proteins that do not bind LDs but can affect their budding directionality. These are ER-resident transmembrane proteins encompassing the fat-storage-inducing transmembrane protein 2 and seipin, which are the two main ER-resident proteins so far identified as key regulators of LD formation (35). However, only fat-storage-inducing transmembrane protein 2 has been shown so far to be critical for LD budding directionality (28). These proteins localize at LD-ER junctions or rims and could regulate the surface tensions of the cytosolic and luminal monolayers to generate the required asymmetry. Such asymmetry could be achieved by modulating phospholipids and proteins localizing on both monolayers (Fig. 6 *D*).

The budding of LDs toward the cytosol is critical for cellular metabolism because proteins regulating LDs are mainly present in the cytosol. The degree of contact of LDs with the cytosol will determine to what extent LDs are accessible to cytosolic and ER luminal proteins (36,37). Our results highlight the potential role of tensions in regulating the amount of LD surface accessible to these proteins. Since LDs within a single cell are different, based on their protein content, it is plausible that surface tensions are dynamically modulated to enable the formation of different LDs. This might explain the existence of LD subsets that are more exposed to the ER lumen (37,38). These LDs would potentially be implicated in specific metabolic pathways, such as in the biogenesis of lipoproteins or lipoviral particles (39,40). Indeed, these LDs are more accessible, for example, to the microsomal triglyceride transfer protein, which needs to access triglycerides for the biogenesis of apolipoprotein B (36,37,40). Our results suggest that these LD subsets would have a particularly high surface tension on their cytosolic leaflet, caused, for example, by the action of proteins such as complex protein I (19,29,41).

In conclusion, our findings suggest that the cytosolic LD biogenesis mechanism might simply arise from a phase-separation mechanism described by three-phase wetting systems. The physics of such systems is well documented. Establishing it in the context of LD formation enables us to make good projections on the role of proteins in regulating the direction of LD formation. We thereby bring important insights into the mechanisms of cytosolic LD formation and accessibility to

proteins and pave the way for a better understanding of LD function and mechanisms of lipid secretion. Reaching such a level of comprehension will have major implications for the diagnosis and treatment of metabolic disorders.

SUPPORTING MATERIAL

Supporting Materials and Methods and six figures are available at http://www.biophysj.org/biophysj/supplemental/S0006-3495(17)35094-4.

AUTHOR CONTRIBUTIONS

A.R.T. conceived the project and A.C. conducted experimental work. A.C. and A.R.T. analyzed data. A.R.T. wrote the manuscript with feedback from A.C.

ACKNOWLEDGMENTS

We thank Drs. Lionel Forêt and Kalthoum Ben M'barek for their critical reading of the manuscript and helpful discussions. We also thank all the members of the group for comments and critical discussions, especially Kamran Ramji for editing the manuscript.

This work was supported by the ATIP-Avenir program, the Programme Emergence de la Ville de Paris, a Paris Sciences et Lettres installation grant, and NANODROP project supported by the ANR to A.R.T. The EDPIF program supports A.C.

REFERENCES

1. van Meer, G., D. R. Voelker, and G. W. Feigenson. 2008. Membrane lipids: where they are and how they behave. *Nat. Rev. Mol. Cell Biol.* 9:112–124.
2. van Meer, G., and A. I. de Kroon. 2011. Lipid map of the mammalian cell. *J. Cell Sci.* 124:5–8.
3. Murphy, D. J., and J. Vance. 1999. Mechanisms of lipid-body formation. *Trends Biochem. Sci.* 24:109–115.
4. Buhman, K. K., H. C. Chen, and R. V. Farese, Jr. 2001. The enzymes of neutral lipid synthesis. *J. Biol. Chem.* 276:40369–40372.
5. Holthuis, J. C., and A. K. Menon. 2014. Lipid landscapes and pipelines in membrane homeostasis. *Nature.* 510:48–57.
6. Volmer, R., and D. Ron. 2015. Lipid-dependent regulation of the unfolded protein response. *Curr. Opin. Cell Biol.* 33:67–73.
7. Thiam, A. R., and L. Forêt. 2016. The physics of lipid droplet nucleation, growth and budding. *Biochim. Biophys. Acta.* 1861 (8 Pt A):715–722.
8. Pol, A., S. P. Gross, and R. G. Parton. 2014. Review: biogenesis of the multifunctional lipid droplet: lipids, proteins, and sites. *J. Cell Biol.* 204:635–646.
9. Martin, S., and R. G. Parton. 2006. Lipid droplets: a unified view of a dynamic organelle. *Nat. Rev. Mol. Cell Biol.* 7:373–378.
10. Walther, T. C., and R. V. Farese, Jr. 2012. Lipid droplets and cellular lipid metabolism. *Annu. Rev. Biochem.* 81:687–714.
11. Fujimoto, T., Y. Ohsaki, …, Y. Shinohara. 2008. Lipid droplets: a classic organelle with new outfits. *Histochem. Cell Biol.* 130:263–279.
12. Ohsaki, Y., M. Suzuki, and T. Fujimoto. 2014. Open questions in lipid droplet biology. *Chem. Biol.* 21:86–96.
13. Ohsaki, Y., J. Cheng, …, T. Fujimoto. 2009. Biogenesis of cytoplasmic lipid droplets: from the lipid ester globule in the membrane to the visible structure. *Biochim. Biophys. Acta.* 1791:399–407.
14. Thiam, A. R., R. V. Farese, Jr., and T. C. Walther. 2013. The biophysics and cell biology of lipid droplets. *Nat. Rev. Mol. Cell Biol.* 14:775–786.
15. Joshi, A. S., H. Zhang, and W. A. Prinz. 2017. Organelle biogenesis in the endoplasmic reticulum. *Nat. Cell Biol.* 19:876–882.
16. Arriaga, L. R., S. S. Datta, …, D. A. Weitz. 2014. Ultrathin shell double emulsion templated giant unilamellar lipid vesicles with controlled microdomain formation. *Small.* 10:950–956.
17. Pautot, S., B. J. Frisken, and D. Weitz. 2003. Production of unilamellar vesicles using an inverted emulsion. *Langmuir.* 19:2870–2879.
18. Ben M'barek, K., D. Ajjaji, …, A. R. Thiam. 2017. ER membrane phospholipids and surface tension control cellular lipid droplet formation. *Dev. Cell.* 41:591–604.e7.
19. Thiam, A. R., B. Antonny, …, F. Pincet. 2013. COPI buds 60-nm lipid droplets from reconstituted water-phospholipid-triacylglyceride interfaces, suggesting a tension clamp function. *Proc. Natl. Acad. Sci. USA.* 110:13244–13249.
20. Kusumaatmaja, H., and R. Lipowsky. 2011. Droplet-induced budding transitions of membranes. *Soft Matter.* 7:6914–6919.
21. Roux, A., and R. Loewith. 2017. Tensing up for lipid droplet formation. *Dev. Cell.* 41:571–572.
22. Thiam, A. R., and F. Pincet. 2015. The energy of COPI for budding membranes. *PLoS One.* 10:e0133757.
23. Morris, C. E., and U. Homann. 2001. Cell surface area regulation and membrane tension. *J. Membr. Biol.* 179:79–102.
24. Upadhyaya, A., and M. P. Sheetz. 2004. Tension in tubulovesicular networks of Golgi and endoplasmic reticulum membranes. *Biophys. J.* 86:2923–2928.
25. Shi, Z., and T. Baumgart. 2015. Membrane tension and peripheral protein density mediate membrane shape transitions. *Nat. Commun.* 6:5974.
26. Neeson, M. J., R. F. Tabor, …, D. Y. Chan. 2012. Compound sessile drops. *Soft Matter.* 8:11042–11050.
27. Deslandes, F., A. R. Thiam, and L. Forêt. 2017. Lipid droplets can spontaneously bud off from a symmetric bilayer. *Biophys. J.* 113:15–18.
28. Choudhary, V., N. Ojha, …, W. A. Prinz. 2015. A conserved family of proteins facilitates nascent lipid droplet budding from the ER. *J. Cell Biol.* 211:261–271.
29. Wilfling, F., A. R. Thiam, …, T. C. Walther. 2014. Arf1/COPI machinery acts directly on lipid droplets and enables their connection to the ER for protein targeting. *Elife.* 3:e01607.
30. Gubern, A., J. Casas, …, E. Claro. 2008. Group IVA phospholipase A2 is necessary for the biogenesis of lipid droplets. *J. Biol. Chem.* 283:27369–27382.
31. Klemm, R. W., J. P. Norton, …, H. Y. Mak. 2013. A conserved role for atlastin GTPases in regulating lipid droplet size. *Cell Reports.* 3:1465–1475.
32. Small, D. M., L. Wang, and M. A. Mitsche. 2009. The adsorption of biological peptides and proteins at the oil/water interface. A potentially important but largely unexplored field. *J. Lipid Res.* 50 (*Suppl*):S329–S334.
33. Andersson, L., P. Boström, …, S. O. Olofsson. 2006. PLD1 and ERK2 regulate cytosolic lipid droplet formation. *J. Cell Sci.* 119:2246–2257.
34. Adeyo, O., P. J. Horn, …, J. M. Goodman. 2011. The yeast lipin orthologue Pah1p is important for biogenesis of lipid droplets. *J. Cell Biol.* 192:1043–1055.
35. Chen, X., and J. M. Goodman. 2017. The collaborative work of droplet assembly. *Biochim. Biophys. Acta.* 1862 (10 Pt B):1205–1211.

36. Mishra, S., R. Khaddaj, …, R. Schneiter. 2016. Mature lipid droplets are accessible to ER luminal proteins. *J. Cell Sci.* 129:3803–3815.

37. Ohsaki, Y., J. Cheng, …, T. Fujimoto. 2008. Lipid droplets are arrested in the ER membrane by tight binding of lipidated apolipoprotein B-100. *J. Cell Sci.* 121:2415–2422.

38. Thiam, A. R., and M. Beller. 2017. The why, when and how of lipid droplet diversity. *J. Cell Sci.* 130:315–324.

39. Paul, D., V. Madan, and R. Bartenschlager. 2014. Hepatitis C virus RNA replication and assembly: living on the fat of the land. *Cell Host Microbe.* 16:569–579.

40. Sturley, S. L., and M. M. Hussain. 2012. Lipid droplet formation on opposing sides of the endoplasmic reticulum. *J. Lipid Res.* 53:1800–1810.

41. Beller, M., C. Sztalryd, …, B. Oliver. 2008. COPI complex is a regulator of lipid homeostasis. *PLoS Biol.* 6:e292.

A Tension Asymmetry Between Monolayers Regulates the Budding Direction of Reconstituted Lipid Droplets

Aymeric Chorlay[1], Abdou Rachid Thiam[1,*]

[1] Laboratoire de Physique Statistique, Ecole Normale Supérieure, PSL Research University, Sorbonne Université, UPMC Université Paris 06, Université Paris Diderot, CNRS, Paris, France

Supporting Material

Figures S1

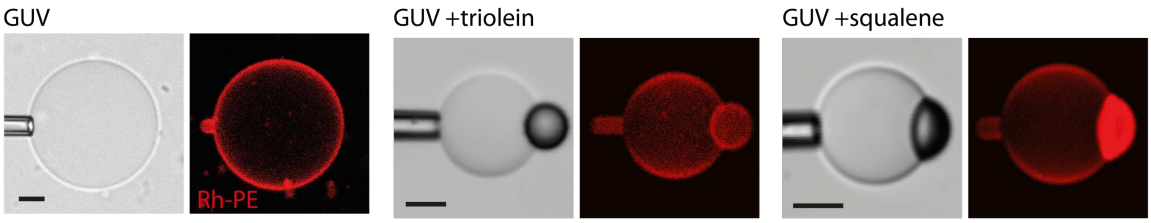

Supplementary Figure S1 | Illustration of micro-aspiration measurement of the bilayer surface tension of PC GUV, PC GUV embedded with a triolein LD and PC GUV embedded with squalene LD. Scale bar is 10 µm.

Figures S2

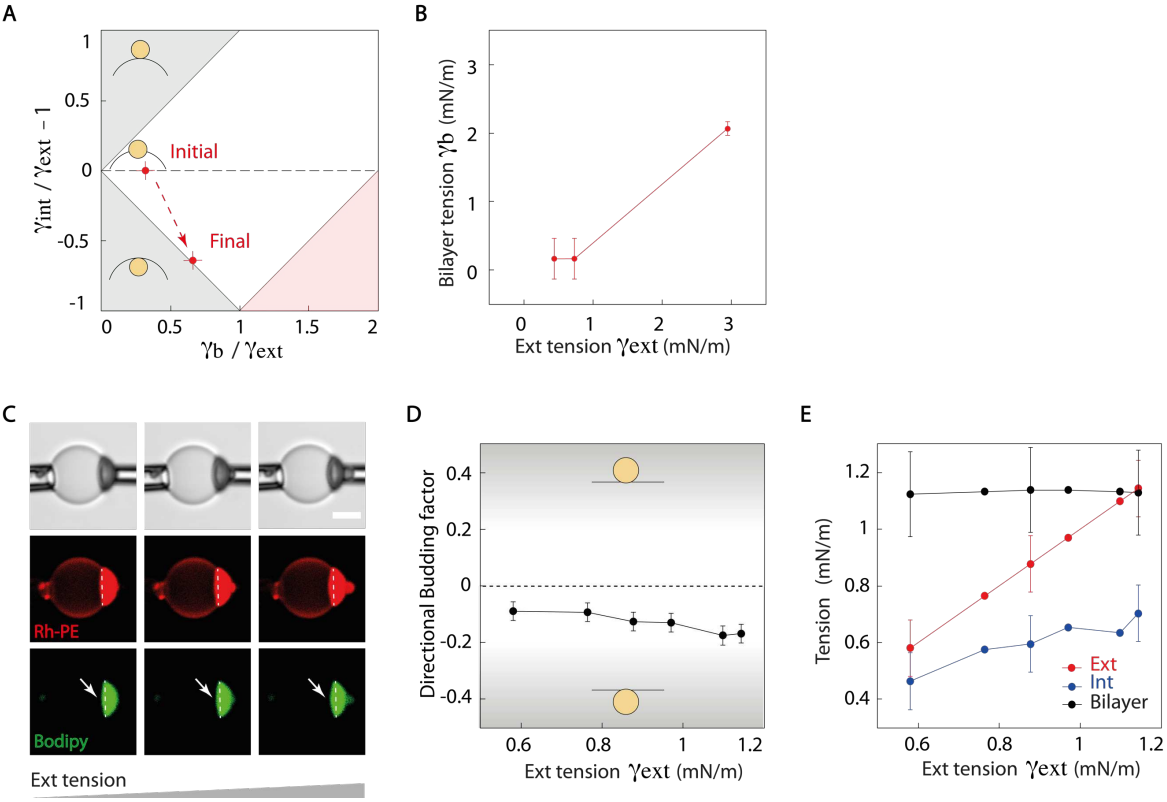

Supplementary Figure S2 | A) Initial and final states of the LD shape from the Fig. 4A, indicated on the phase diagram of Fig.3A. **B**) Bilayer tension corresponding to the experiment shown in Fig. 4A, calculated using the technique describe in supplementary text 2 **C)** Squalene LD embedded in a GUV.

External monolayer tension in increased with right micropipette and bilayer tension is kept constant with the left micropipette. The LD tends to internalized (arrow). Scale bar is 10 µm. **D)** Corresponding Directional budding factor as a function of the external tension. **E)** Evolution of the three tensions as the external tension is increased. Bilayer tension is kept constant.

Figures S3

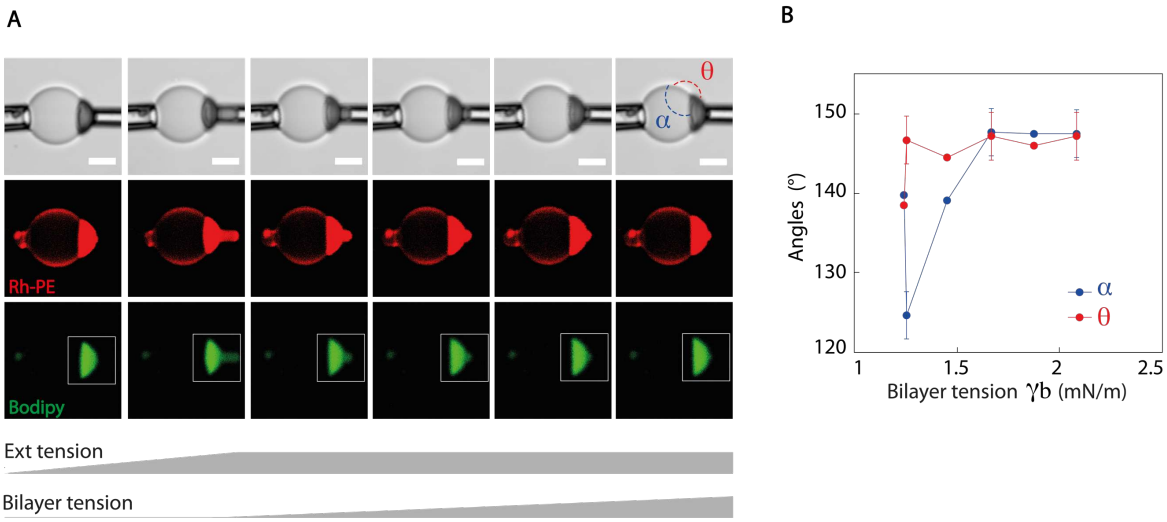

Supplementary Figure S3 | A) Full frame view of the experiment shown in (Fig. 5A). Scale bar is 10 µm **B)** Corresponding angles alpha and theta plotted as a function of the bilayer tension.

Figures S4

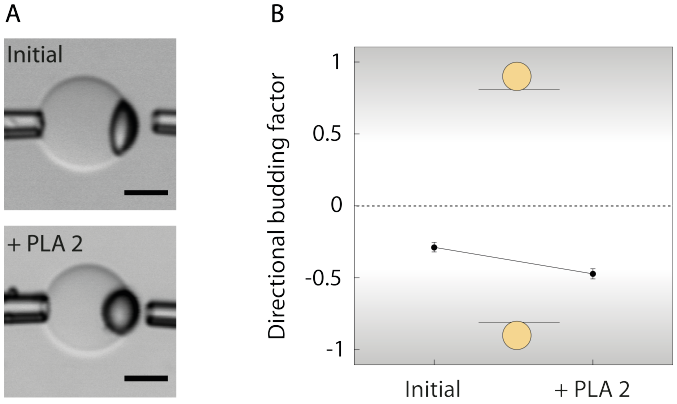

Supplementary Figure S4 | A) PLA2 enzyme is added to the external medium of a PC/PA (70/30) GUV embedding a triolein LD. (PA: dioleoylphosphatidic acid**)** PA was added to increase the bilayer tension and obtain droplets that were not readily budded, which often occurred with pure PC. The evolution of the droplet is observed over time. Scale bar is 10 µm. **B)** Decreasing directional budding factor showing a asymetrization of the LD position.

Supplementary text 1 | Determination of the shape and position of an LD in a GUV bilayer.

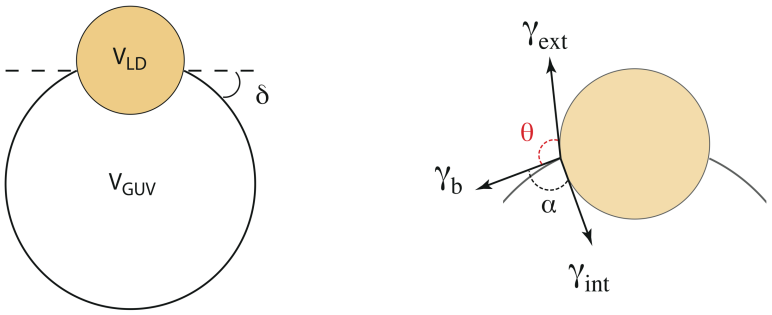

Considering that the lipid droplet's shape is driven by the equilibrium of the three surface tensions (bilayer γ_b, external monolayer γ_{ext} and internal monolayer γ_{int}) (Eq. 1), can be projected on the bilayer axis and lead to (Eq. 2).

$$\overrightarrow{\gamma_b} + \overrightarrow{\gamma_{int}} + \overrightarrow{\gamma_{ext}} = \vec{0} \qquad (1)$$

$$\begin{aligned} \gamma_b &= -\gamma_{int}\cos(\alpha) - \gamma_{ext}\cos(\theta) \\ \gamma_{ext}\sin(\theta) &= \gamma_{int}\sin(\alpha) \end{aligned} \qquad (2)$$

Moreover, the conserved volume of the LD and the GUV gives two other equations (Eq. 3,4):

$$V_{LD} = \frac{4\,\Pi Ro^3}{3}\left(\frac{2-\cos(\theta-\delta)^3+3\cos(\theta-\delta)}{\sin(\theta-\delta)^3} + \frac{2-\cos(\alpha-\delta)^3+3\cos(\alpha-\delta)}{\sin(\alpha-\delta)^3}\right) \qquad (3)$$

$$V_{GUV} = \frac{4\,\Pi Ro^3}{3}\left(\frac{2-\cos(\delta)^3+3\cos(\delta)}{\sin(\delta)^3} - \frac{2-\cos(\alpha-\delta)^3+3\cos(\alpha-\delta)}{\sin(\alpha-\delta)^3}\right) \qquad (4)$$

In order to determine the shape of the droplet, we only need three parameters: alpha, theta and delta, as a function of the tensions γ_b, γ_{int} and γ_{ext}.

Rearranging these equations leads to a set of 3 equations (Eq. 5,6,7) that can be solved numerically. The following equations (5, 6) Gives alpha and theta:

$$\cos(\theta) = \frac{{\gamma_{int}}^2 - {\gamma_{ext}}^2 - {\gamma_b}^2}{2\,\gamma_b\,\gamma_{ext}} \qquad (5)$$

$$\cos(\alpha) = \frac{{\gamma_{ext}}^2 - {\gamma_{int}}^2 - {\gamma_b}^2}{2\,\gamma_b\,\gamma_{int}} \qquad (6)$$

The last parameter delta is determined numerically, keeping the volumes constant (Eq. 7):

$$\frac{V_{LD}}{V_{GUV}} = \frac{\frac{2-\cos(\theta-\delta)^3+3\cos(\theta-\delta)}{\sin(\theta-\delta)^3} + \frac{2-\cos(\alpha-\delta)^3+3\cos(\alpha-\delta)}{\sin(\alpha-\delta)^3}}{\frac{2-\cos(\delta)^3+3\cos(\delta)}{\sin(\delta)^3} - \frac{2-\cos(\alpha-\delta)^3+3\cos(\alpha-\delta)}{\sin(\alpha-\delta)^3}} \qquad (7)$$

The profiles of the embedded LDs displayed in (Fig. 4B) are obtained using this mathematical model.

Supplementary text 2 | Determination of surface tensions.

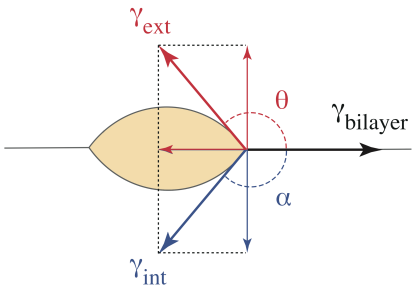

Given that the LD shape is driven by surface tension, the following equation describes the link between the bilayer tension γ_b, the external tension γ_{ext}, and the internal tension γ_{int}:

$$\gamma_b = -\gamma_{int}\cos(\alpha) - \gamma_{ext}\cos(\theta) \quad (1)$$

$$\gamma_{ext}\sin(\theta) = \gamma_{int}\sin(\alpha) \quad (2)$$

Measuring one of the tensions and the two angles (θ and α) allows us to determine the two other tensions using the two former equations. For example, knowing alpha, theta, and the external tension enable the determination of the bilayer tension by $\gamma_b = -(\gamma_{ext}\mathrm{cotan}(\alpha)\sin(\theta) + \cos(\theta))$, and γ_{int} through equation (2).

Chapitre 6 :

Formation des CLs et asymétrie de membrane du RE

Une asymétrie membranaire impose la directionnalité de l'émergence des corps lipidiques à partir du réticulum endoplasmique.

Travaux publiés dans Developmental CELL

La plupart des CLs émergent dans le cytoplasme de la cellule, ce qui est essentiel pour le métabolisme cellulaire car c'est dans le cytoplasme que l'on retrouve la plupart des protéines qui régulent l'utilisation des lipides neutres stockés dans les CLs. Les CLs interagissent aussi directement avec presque toutes les organelles cytoplasmiques, échangeant avec elles lipides et protéines [10]. Un contrôle précis de la direction d'émergence des CLs est donc crucial, mais les facteurs contrôlant cette directionnalité sont pour l'instant très peu compris [30].

Comme la plupart des CLs émergent dans le cytoplasme, de nombreux phospholipides, provenant sûrement du feuillet cytoplasmique, sont utilisés pour recouvrir la surface des CLs en formation [14]. Pour maintenir l'intégrité du RE, il semble alors nécessaire que les phospholipides du feuillet cytoplasmique consommés par la formation des CLs soient remplacés par de nouveaux phospholipides. Ceci semble indiquer qu'il existe des liens étroits entre la biogenèse des CLs et l'homéostasie du RE par l'intermédiaire de flux de lipides [64,147–149] et que ces derniers jouent un rôle prépondérant pour assurer une formation efficace des CLs.

Au cours du précédent chapitre, nous avons mis en avant que l'émergence d'un CL artificiel était principalement contrôlée par un déséquilibre de tension entre ses monocouches. En s'appuyant sur ces résultats, les travaux suivants chercheront donc à comprendre comment la cellule peut imposer une formation unidirectionnelle des CLs tout en garantissant l'intégrité de son RE.

Pour répondre à cette question, j'ai ai commencé à explorer *in vitro* (DEV) les facteurs permettant une formation unidirectionnelle des CLs. Cette approche m'a permis de distinguer des leviers utilisables par la cellule pour contrôler la directionnalité de formation des CLs. Pour vérifier la validité de ces résultats aux petites échelles inaccessibles à l'expérience, j'ai conçu les protocoles d'expériences *in silico* qui ont été realisé par un expert du domaine. J'ai ensuite voulu tester la pertinence de ces résultats et les implications qu'ils pouvaient avoir *in vivo* en travaillant avec des collaborateurs. Ces derniers ont réalisé les expériences qui nous semblaient les plus appropriées sur des cellules de levure et des cellules de drosophiles. Le choix des levures a été fait car ce sont des cellules simples qui présentent un réticulum plus facilement caractérisable. J'ai ensuite analysé et traité toutes les données en interne et réalisé des expériences complémentaires *in vitro* (DEV) pour corroborer nos conclusions. Ce travail a ainsi abouti aux principaux résultats expérimentaux suivants :

- L'insertion de protéines provoque l'émergence de CLs artificiels incorporés dans une bicouche.
- Les CLs artificiels incorporés dans une bicouche émergent du coté de la membrane présentant un excès de phospholipides.
- La courbure de la bicouche facilite le bourgeonnement des CLs artificiels mais un apport de phospholipides est nécessaire à l'émergence complète de la bicouche.
- La production forcée de CLs dans des cellules de levures (saccharomyces cerevisiae) est concomitante avec l'apparition d'une morphologie aberrante du RE.
- L'émergence correcte des CLs est favorisée par la synthèse de phospholipides chez la levure.
- Les CLs restent plus en contact avec le RE dans des cellules de drosophiles présentant une activité réduite de CCT1 (enzyme participant à la synthèse des phospholipides).
- Sans apport de nouveaux phospholipides, les CLs artificiels émergent des deux cotés de la bicouche (extérieur et lumen)

Ces résultats montrent que les CLs émergent du coté de la bicouche présentant la meilleure couverture, de phospholipides ou de protéines, c'est-à-dire du côté du feuillet ayant la densité la plus élevée et donc la tension la plus basse. Dans la cellule, cela suggère que, durant les épisodes de formation des CLs, le feuillet cytoplasmique du RE devrait, au moins de manière transitoire, présenter une densité de phospholipides plus importante que son feuillet luminal. Cela semble aussi indiquer que certaines protéines pourraient par leur recrutement sur le feuillet cytoplasmique, améliorer sa couverture et ainsi aider l'émergence des CLs. Il faut aussi noter que les zones courbées du RE favorisent la formation des CLs dans le cytoplasme, mais que sans ajout de phospholipides sur le feuillet externe, une émergence totale est exclue.
D'autre part, la production de nombreux CLs dans le cytoplasme prélève de nombreux phospholipides au feuillet cytoplasmique du RE. Nos données suggèrent que sans remplacement constant de ces phospholipides, la couverture phospholipidique du feuillet va diminuer, ce qui aura pour effet de favoriser l'émergence de CLs du côté luminal du RE. Il semble donc nécessaire de fournir de nouveaux phospholipides au feuillet cytoplasmique, de

manière à assurer la formation de CLs vers le cytoplasme. Nous avons en effet observé que dans les cellules ayant une capacité limitée à produire des phospholipides, le RE avait une morphologie aberrante et que les CLs étaient plus fréquemment en contact avec le lumen du RE.
De nombreux mécanismes pourraient permettre le remplacement des phospholipides absorbés par la monocouche des CLs en formation. On peut par exemple penser aux enzymes de la synthèse de phospholipides *de novo* (Kennedy pathway) qui sont en effet importantes pour l'émergence des CLs [55,147,148], ou à l'action de certaines flipases [150] qui pourraient transférer des phospholipides vers le feuillet cytosolique du RE.

Pour résumer, nos données suggèrent que la membrane du RE subit un remodelage asymétrique des feuillets de sa bicouche pendant les périodes de lipogenèse, de manière à assurer la formation des CLs dans le cytoplasme de la cellule, ce qui est essentiel pour que les CLs puissent assurer leurs fonctions.

L'ensemble de cette étude a fait l'objet d'un article publié dans Developmental CELL qui constitue le chapitre suivant de cette thèse.

Article

Developmental Cell

Membrane Asymmetry Imposes Directionality on Lipid Droplet Emergence from the ER

Graphical Abstract

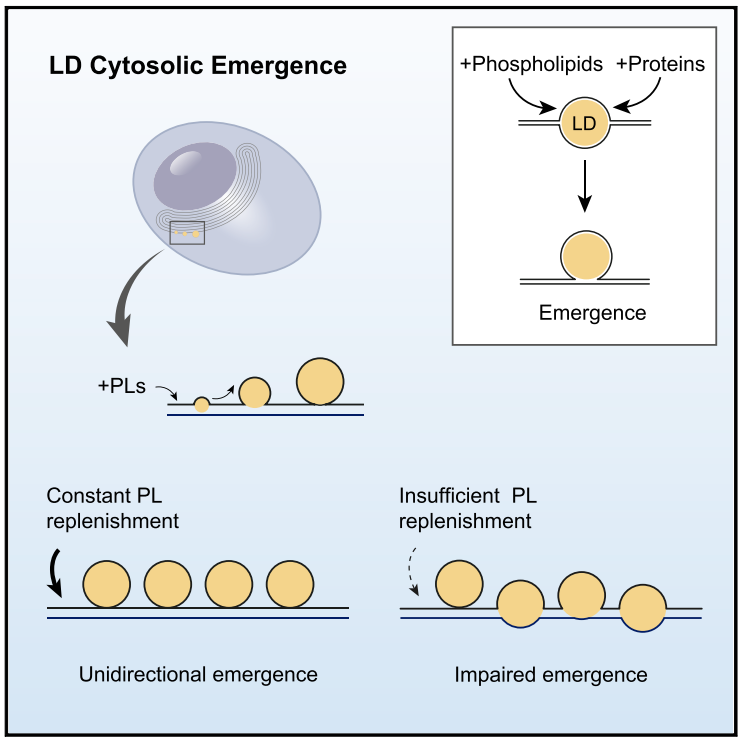

Authors

Aymeric Chorlay, Luca Monticelli, Joana Veríssimo Ferreira, ..., Mathias Beller, Pedro Carvalho, Abdou Rachid Thiam

Correspondence

thiam@ens.fr

In Brief

Lipid droplets bud from the ER into the cytosol. This directionality is crucial to lipid metabolism, but its underlying mechanism is elusive. Chorlay et al. provide evidence that it is mediated by membrane asymmetries in phospholipids and proteins. Excess phospholipids on the ER cytosolic leaflet guarantees proper lipid droplet emergence.

Highlights

- Emergence of LDs from the ER into the cytosol is facilitated by phospholipid synthesis
- Membrane imbalance in phospholipid density regulates the emergence side of model LDs
- Model LDs emerge on the side with the higher monolayer surface coverage
- Asymmetric membrane insertion of proteins regulates the emergence side of model LDs

Chorlay et al., 2019, Developmental Cell *50*, 1–18
July 1, 2019
https://doi.org/10.1016/j.devcel.2019.05.003

CellPress

Please cite this article in press as: Chorlay et al., Membrane Asymmetry Imposes Directionality on Lipid Droplet Emergence from the ER, Developmental Cell (2019), https://doi.org/10.1016/j.devcel.2019.05.003

Developmental Cell
Article

Membrane Asymmetry Imposes Directionality on Lipid Droplet Emergence from the ER

Aymeric Chorlay,[1] Luca Monticelli,[2] Joana Veríssimo Ferreira,[3] Kalthoum Ben M'barek,[1] Dalila Ajjaji,[1] Sihui Wang,[3] Errin Johnson,[3] Rainer Beck,[4] Mohyeddine Omrane,[1] Mathias Beller,[5] Pedro Carvalho,[3] and Abdou Rachid Thiam[1,6,*]

[1]Laboratoire de Physique de l'Ecole Normale Supérieure, ENS, Université PSL, CNRSSorbonne Université, Université Paris-Diderot, Sorbonne Paris Cité, Paris, France
[2]Laboratory of Molecular Microbiology and Structural Biochemistry, UMR5086 CNRS and University of Lyon, Lyon 69367, France
[3]Sir William Dunn School of Pathology, University of Oxford, Oxford, UK
[4]Heidelberg University Biochemistry Center, Heidelberg, Germany
[5]Institute for Mathematical Modeling of Biological Systems, Systems Biology of Lipid Metabolism, Heinrich Heine University, Düsseldorf, Germany
[6]Lead Contact
*Correspondence: thiam@ens.fr
https://doi.org/10.1016/j.devcel.2019.05.003

SUMMARY

During energy bursts, neutral lipids fabricated within the ER bilayer demix to form lipid droplets (LDs). LDs bud off mainly in the cytosol where they regulate metabolism and multiple biological processes. They indeed become accessible to most enzymes and can interact with other organelles. How such directional emergence is achieved remains elusive. Here, we found that this directionality is controlled by an asymmetry in monolayer surface coverage. Model LDs emerge on the membrane leaflet of higher coverage, which is improved by the insertion of proteins and phospholipids. In cells, continuous LD emergence on the cytosol would require a constant refill of phospholipids to the ER cytosolic leaflet. Consistent with this model, cells deficient in phospholipids present an increased number of LDs exposed to the ER lumen and compensate by remodeling ER shape. Our results reveal an active cooperation between phospholipids and proteins to extract LDs from ER.

INTRODUCTION

The endoplasmic reticulum (ER) is the cellular factory of lipids and membrane proteins, which are subsequently distributed to other organelles (Schwarz and Blower, 2016). This anabolic function of the ER is essential for maintaining organelle and cellular homeostasis, particularly when cells enter energy storage regimes. In these periods, excess energy is converted into neutral lipids, which upon synthesis are stored in ER-derived organelles called lipid droplets (LDs), also referred to as oil bodies or lipid bodies for plants (Martin and Parton, 2006; Murphy and Vance, 1999). The core of these droplets contains neutral lipids and is covered by a phospholipid monolayer derived from the ER bilayer, likely from its cytoplasmic leaflet (Fujimoto and Parton, 2011). Therefore, it seems essential to replenish the ER with new phospholipids to keep its integrity and proper function during lipogenesis. This is consistent with the trigger of *de novo* phospholipid synthesis by the activation of sterol regulatory element-binding protein genes in response to lipogenesis (Walker et al., 2011; Krahmer et al., 2011; Aitchison et al., 2015). These concordant events reveal a close relationship between LD biogenesis and ER homeostasis through phospholipid production (Lagace and Ridgway, 2013; Aitchison et al., 2015; Vevea et al., 2015; Ben M'barek et al., 2017) the consequences on LD biogenesis under conditions of limited phospholipid supply are poorly understood.

LDs also play important roles in several other biological processes, such as viral infections, embryonic development, and neurodegeneration (Welte, 2015). These functions are tightly related to how LDs are formed (Pol et al., 2014; Thiam and Beller, 2017; Henne et al., 2018). Neutral lipids synthesized in the ER at low concentration are likely dispersed and mobile in the space between the membrane leaflets. At elevated levels, these lipids can spontaneously demix to nucleate a lipid lens (Khandelia et al., 2010; Ben M'barek et al., 2017). The lens grows by accumulating more lipids and eventually forms a spherical LD that buds off or emerges from the bilayer (Thiam and Forêt, 2016; Pol et al., 2014; Choudhary et al., 2018). Throughout these steps toward LD maturation, proteins are dynamically targeted to the LD surface to control the LD function: they target LDs from the cytosol (Londos et al., 1995), the ER membrane (Wilfling et al., 2013, 2014; Jacquier et al., 2011), or possibly the ER lumen (Ohsaki et al., 2009). The amount of LD surface area that is in contact with the lumen and the cytosol will reflect the LD proteome and subsequent function. Most findings so far suggest that the surface of the majority of mature LDs is almost entirely exposed to the cytosol.

The emergence of LDs in the cytosol is crucial for metabolism because most regulatory proteins and enzymes that release lipids from LDs reside in the cytosol. LDs interact with nearly all cytoplasmic organelles to trade lipids and proteins (Olzmann and Carvalho, 2019). Also, they serve as a reservoir for certain

proteins such as histones during fly development (Welte, 2015) or aggregation-prone proteins that are targeted for degradation (Vevea et al., 2015). Finally, as most proteins involved in lipid secretion reside in the ER lumen, abnormal accessibility of LDs to ER luminal proteins will likely alter the secretion of very low-density lipoproteins (Ohsaki et al., 2009).

Factors controlling the directionality of LD budding are still poorly understood (Henne et al., 2018). Seipin is an integral ER protein that forms a scaffold around emerging LDs and is important for proper LD morphology (Yan et al., 2018; Sui et al., 2018). However, the depletion of Seipin does not hamper the trafficking of proteins residing on the cytosolic face of the ER, such as GPAT4, ADRP, or LiveDrop, to the LD surface (Salo et al., 2016; Wang et al., 2016). This suggests that LDs still bud toward the cytosol in the absence of Seipin, which is therefore not essential to controlling the directionality of LD budding. In contrast, depletion of fat storage-inducing transmembrane protein 2 (FIT2) results in the budding defects of an LD population (Choudhary et al., 2015). FIT2 is another integral ER membrane protein, which possibly has lipid-phosphate phosphatase activity on the ER luminal side (Becuwe et al., 2018; Hayes et al., 2017). It would transform phospholipids into diacylglycerol, which are molecules soluble in the neutral lipid phase (Thiam and Pincet, 2015). FIT2 activity would thus result in depleting phospholipids from the ER luminal leaflet. Thereupon, FIT2 generates at least transient membrane asymmetries that may determine the directionality of LD budding. Such contribution of FIT2 is appealing as a droplet in a bilayer has equivalent chances to emerge on both sides of the bilayer, unless a symmetry breaking is introduced (Chorlay and Thiam, 2018; Thiam and Forêt, 2016).

An asymmetry in phospholipid composition of the ER membrane can indeed control the directionality of LD emergence. For example, the recruitment of positively curved lipids, i.e., with bulky hydrophilic head, onto one of the monolayer leaflets will favor LD emergence toward this leaflet (Choudhary et al., 2018; Chorlay and Thiam, 2018; Zanghellini et al., 2010). Another source of asymmetry possibly modulating the direction of LD formation is membrane curvature. Curved membranes have a higher pressure in their concave region. Thus, when an LD forms, the internal pressure would tend to push the LD outside the lumen (Thiam and Forêt, 2016). The basic tubular structure of the ER membrane could hence modulate the direction of LD budding. Whether membrane curvature determines the directionality of LD emergence is not fully understood. Finally, another possible asymmetry is between the LD monolayer surface tensions (Chorlay and Thiam, 2018), which reflects an asymmetry in the surface coverage between the cytosolic and luminal monolayers surrounding LDs. Soon after nascent LDs appear in the ER (with a diameter over ~30 nm), the LD monolayer surface tension should indeed dominate spontaneous curvature and bending effects and control LD shape. In this size range, we previously worked with macroscopic model LDs and identified that an asymmetry in monolayer surface tension is sufficient to control the emergence of an artificial LD (Chorlay and Thiam, 2018).

Here, we test the hypothesis that monolayer surface-tension asymmetry is sufficient to guarantee that newly made and growing LDs become fully exposed to the cytosol. We investigate the presence of imbalances in monolayer surface tension and how they contribute to LD emergence. We find that artificial LDs, herein referred to as aLDs, emerge toward the membrane monolayer side offering better phospholipid surface coverage, i.e., having the higher phospholipid surface density and hence the lower surface tension. The monolayer coverage is also improved by the insertion of proteins; the strong binding of proteins to the aLD monolayer promotes retention of the droplet into the protein-containing reservoir. Our data support the hypothesis that systematic LD emergence toward the cytosol requires a phospholipid refill to the cytosolic leaflet of the ER membrane. Such refill ensures a good coverage (low surface tension) of this monolayer is kept. In cells experiencing a limited capacity of phospholipid supply, we observe an aberrant ER morphology concomitant with an increase in the number of LDs in large contact with the ER lumen.

RESULTS

Oil-water surface tension is diminished by covering the interface between the two liquids. In the context of LD biogenesis, the system presents two oil-water interfaces: between the neutral lipid phase and the cytosol and between the neutral lipids and the ER lumen. An asymmetry in the coverage between these interfaces will yield an asymmetry in surface tension. A monolayer surface coverage is improved by the adsorption of surfactants, which, in cells, are mainly proteins and lipids (Figure 1A). Our model predicts that the recruitment of these membrane constituents to one of the monolayers can improve this monolayer surface coating and be sufficient to promote emergence of the droplet. To test our prediction, we used the droplet-embedded vesicle system (DEV), consisting of giant unilamellar vesicles (GUVs) in which an aLD is incorporated between the leaflets of the bilayer (Figure 1B) (Chorlay and Thiam, 2018; Ben M'barek et al., 2017), mimicking the topology of an LD in the ER bilayer. We characterized the degree of emergence of an aLD from the bilayer by comparing the inner and outer surface areas of the droplet (Figure 1C). The asymmetry in the monolayer coverage, and more precisely in surface tension, is reflected by the angles formed by the droplet with the bilayer (Chorlay and Thiam, 2018), which defines the coverage asymmetry parameter (Figure 1C; STAR Methods: Determination of shape and position).

Insertion of Proteins Promotes Emergence of LDs from a Bilayer

Our model predicts that the insertion of a protein into a monolayer leaflet of an ER-enclosed LD will affect the direction of LD emergence. We tested the effect of different proteins on DEVs made with 1,2-dioleoyl-sn-glycero-3-phosphocholine (here referred to as PC) and containing triolein oil, which is the major cellular neutral lipid.

We started with Arf1, which regulates lipid metabolism and binds to cellular LDs from the cytosol (Wilfling et al., 2014; Guo et al., 2008; Thiam et al., 2013a). Arf1 uses an N-terminal myristoyl group and an N-terminal amphipathic helix to bind to membranes. These motifs are shielded within Arf1 when the protein is soluble in the cytosol and deployed when Arf1 is activated by a guanine nucleotide exchange factor and in the presence of GTP (Antonny et al., 1997); the nucleotide exchange is also promoted by reducing Mg^{2+} concentration down to the μM level by

Please cite this article in press as: Chorlay et al., Membrane Asymmetry Imposes Directionality on Lipid Droplet Emergence from the ER, Developmental Cell (2019), https://doi.org/10.1016/j.devcel.2019.05.003

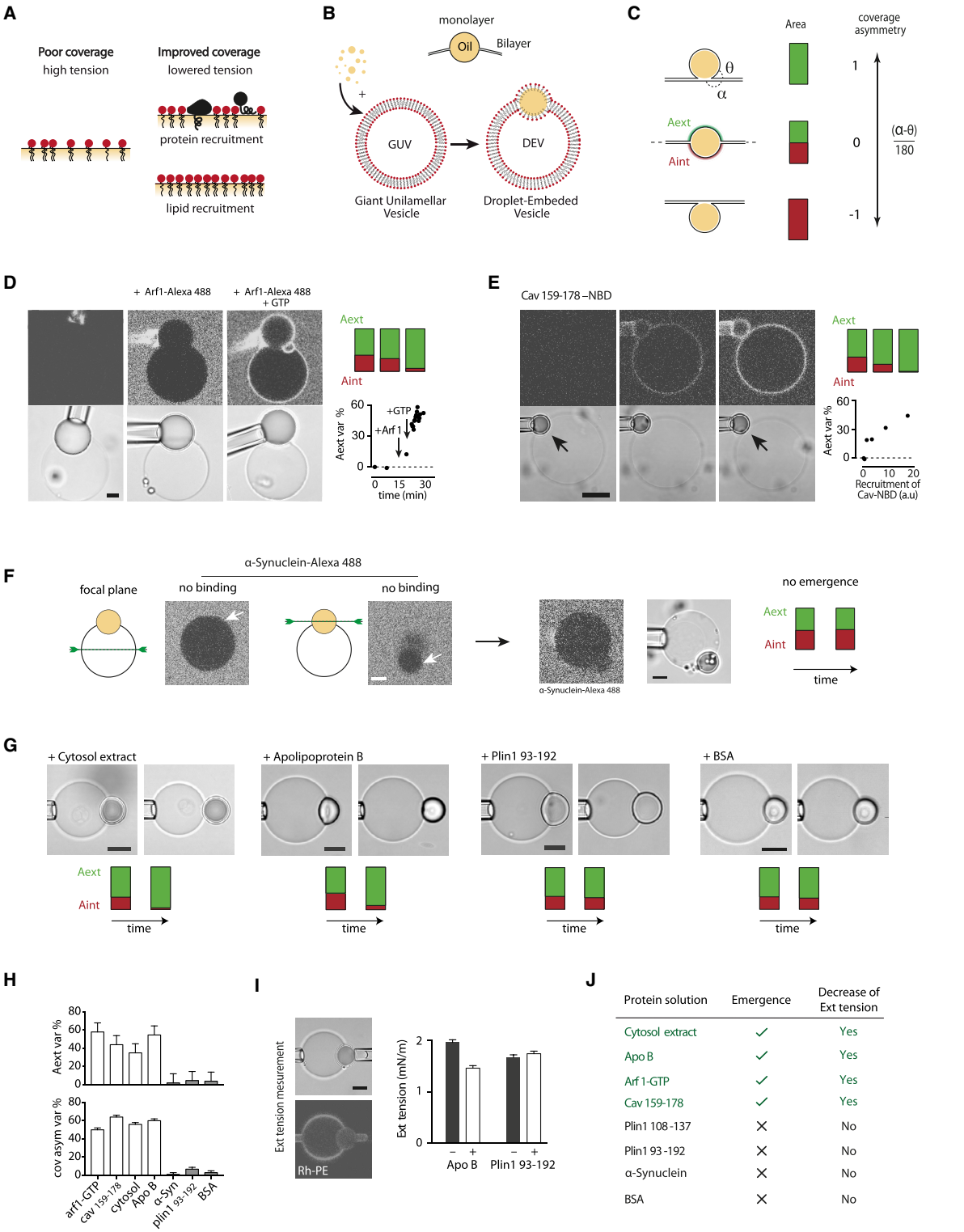

(legend on next page)

chelating it with EDTA (Bigay et al., 2003). We can thus dynamically switch on binding and record the impact on aLD emergence. When we added Arf1-Alexa488 and EDTA to DEVs, we observed no protein recruitment, as expected (Figures 1D and S1A). Only when GTP was subsequently added, Arf1 was recruited to the membranes (Figures 1D and S1A). Recruitment of Arf1 was concomitant to the full emergence of the artificial LD to the protein solution (Figures 1D and S1B). Following Arf1 binding, the droplet outer area increased and its inner area decreased (Figure 1D). Consistent with this observation, the outer monolayer coverage was improved (Figure 1H), supporting the fact that binding induced aLD emergence by improving the monolayer coverage.

Most proteins use amphipathic helices (AHs) to associate with the LD surface. The presence of highly hydrophobic residues such as phenylalanine, tyrosine, or tryptophan, on the hydrophobic face of AHs increases membrane association. We used an AH peptide from caveolin 1 (Cav aa159-178 with an NBD tag), which binds to LDs and targets other proteins to cellular LDs (Ostermeyer et al., 2001; Kassan et al., 2013). This peptide is particularly rich in hydrophobic amino acids (Figure S1E). When it was added to DEVs, we observed an increase of the peptide signal on the DEV membrane (Figure 1E). This binding was concomitant with the emergence of the droplet into the protein solution (Figure 1E), and the improvement of the external monolayer coverage.

We next worked with an AH that lacks highly hydrophobic residues. We chose alpha-Synuclein-Alexa488, which is localized to the surface of LDs (Cole et al., 2002) but which binds *in vitro* only to droplet monolayers with poor phospholipid coating (Thiam et al., 2013a) (Figures S1C and S1F). Here, alpha-Synuclein failed to bind DEVs and the droplets did not emerge (Figure 1F); the inner and outer droplet areas remained constant and no improvement of the external monolayer coverage was detected (Figures 1F and 1H). These results suggest that only AH-containing proteins that are able to strongly associate with monolayers can promote LD emergence.

We finally investigated the effect of perilipins (Plins), which are major LD-associated proteins. Plins bind to LDs in part by using an 11-mer AH repeat (Brasaemle, 2007). To test whether this domain alone can mediate LD emergence, we examined the effect of the Plin1 11-mer AH repeat, Plin1 93–192 (Rowe et al., 2016), and a fragment of this domain also displaying an AH motif, Plin1 108–137 (Figure S1E). We found that these peptides did not enable aLD emergence (Figures 1G, 1J, and S1D). The failure of these peptides in promoting emergence is probably due to inefficient binding to a droplet monolayer, which is continuous with a phospholipid bilayer reservoir (see below). Compared to Cav 159–178 AH, the Plin fragments are less dense in hydrophobic residues (Figure S1E), which could explain (at least partly) their inefficient binding (Prévost et al., 2018). Alternatively, this Plin domain might simply require specific lipids or membrane curvature for binding; other domains of the full-length protein, or protein partners, are required to achieve the strong membrane association of the full-length protein (Ajjaji et al., 2019).

Since many proteins target LDs from the cytosol, we decided to put artificial DEVs in contact with a cytosolic extract from hepatocyte cells. We observed systematic outbound emergence of the droplets into the cytosolic medium (Figures 1G and S1D). This experimental condition closely mimics the cytosolic emergence of cellular LDs mediated by cytosolic components. Note the small decrease of the GUV size because of water evaporation (Figure 1G); this decrease only affects the bilayer tension and does not introduce membrane asymmetry (Chorlay and Thiam, 2018).

Figure 1. The Insertion of Proteins Promotes Artificial LD Emergence

(A) The surface tension of an oil-water interface is decreased by improving the surface coverage with surfactants, such as proteins and phospholipids.

(B) Top: schematic of an artificial LD (aLD) embedded in a bilayer as during LD formation. Bottom: principle of the droplet-embedded vesicle (DEV) system, made by an aLD incorporated into the intermonolayer space of a giant unilamellar vesicle (GUV).

(C) LD emergence is characterized by the fraction of its external and internal surface areas. The imbalance of monolayer tension between the interior and exterior, reflecting the asymmetry in surface coverage, defines the coverage of the asymmetry parameter (see STAR Methods).

(D) Arf1 binding to DEVs promotes artificial LD extraction. Left: a PC DEV with a triolein droplet is made and Arf1-Alexa488 added to the external medium. Arf1 DEV-recruitment occurred only with the subsequent addition of GTP. The artificial LD emerged toward the exterior upon Arf1 binding. The glass pipette was used for softly maintaining the DEV under the observatory region during injection; the pipette was motionless and images were rotated for visualization. Top right: external and internal surface areas corresponding to the pictures shown on the left. Bottom right: corresponding time course displaying the protein recruitment effect on the external Area ("Aext var" represent the external area variation). Arf1 recruitment on the bilayer and droplet surface is displayed in Figure S1A. Additional images of fully emerged aLDs following Arf1 binding are displayed in Figure S1B. Scale bar, 10 μm.

(E) The fragment of caveolin 159–178, used in the Hpos construct, which targets LDs (Kassan et al., 2013), bound to DEVs and promoted aLD extraction. Left: Cav 159–178-NBD was added to the medium of a PC DEV containing triolein droplets. The artificial LD emerged toward the exterior upon Cav159-178-NBD binding. The glass pipette was used for softly maintaining the DEV under the observatory region during injection. Top right: external and internal surface areas corresponding to the pictures shown on the left. Bottom right: effect of Cav 159–178-NBD recruitment on artificial LD external Area. ("Aext var" represent the external area variation). Scale bar, 10 μm.

(F) Alpha-Synuclein did not bind to PC DEV (left), even after 30 min (right), and the artificial LD did not emerge. Arrows point to the GUV and droplet interface. The external area did not vary. Scale bars, 10 μm.

(G) A cytosolic extract from Huh7.5 cells and apolipoprotein B promoted artificial LD emergence from DEVs, while Plin1 93–192 or BSA did not. Corresponding external and internal surface areas variation are shown below each condition. For fluorescence confocal micrographs see Figure S1D. For each of these conditions, external area variation and coverage asymmetry is displayed over time in Figure S1D. Scale bars, 10 μm.

(H) The induced effects of the proteins on the aLD external surface area variation (top) and coverage asymmetry (bottom) are displayed. Error bars are measurement precision.

(I) The external monolayer tension of the artificial LD is measured by microaspiration technique (left images—fluorescent signal is rhodamine-PE (Rh-PE)), before and after addition of apolipoprotein B and Plin1 93–192. A decrease of tension was measured when apolipoprotein B was added, while tension remained constant with Plin1 93–192. Scale bar, 10 μm; error bars are measurement precision.

(J) Summary of the effect of the protein solutions on aLD emergence and membrane coverage asymmetry (decrease of external surface tension).

See also Figure S1.

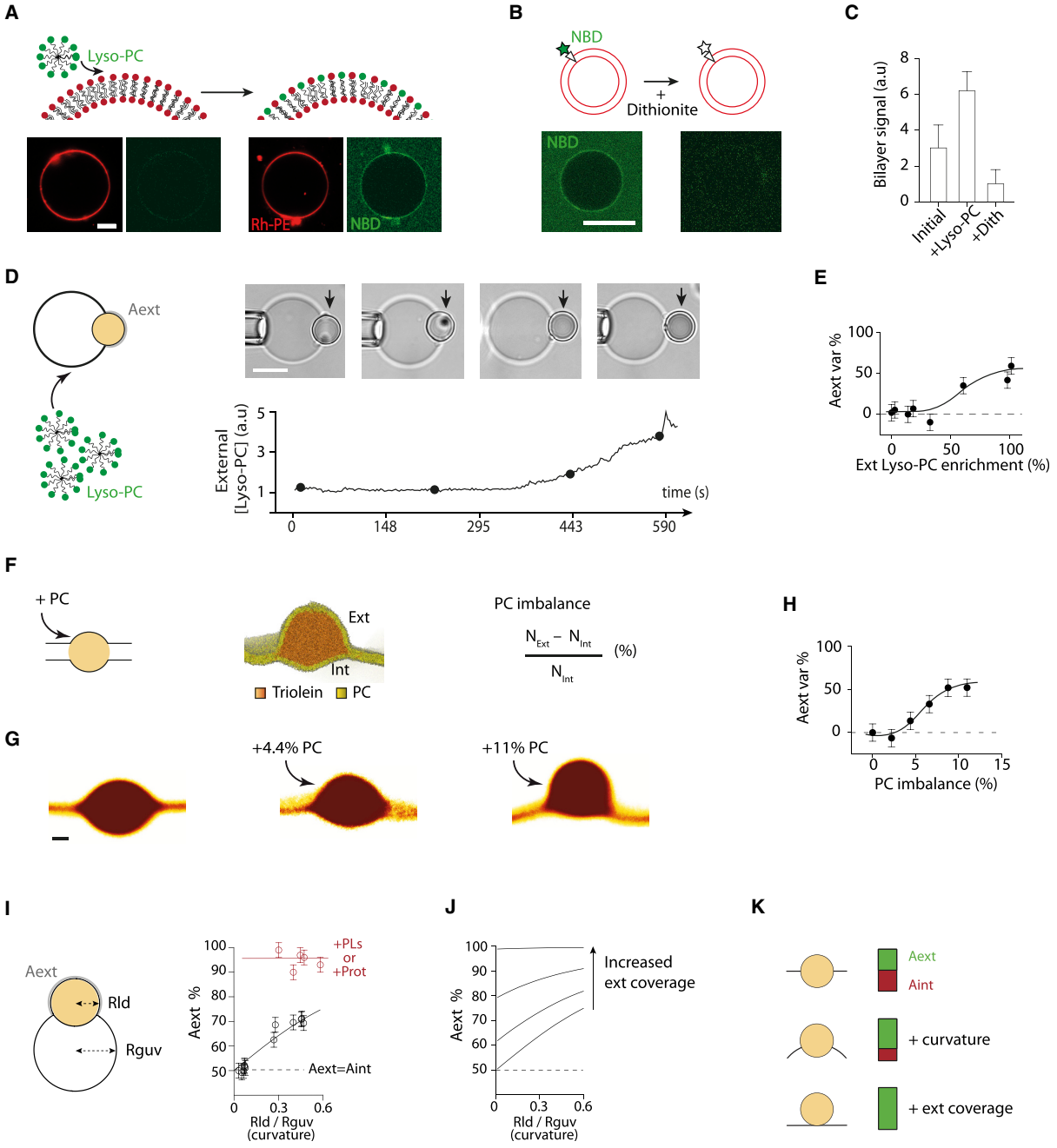

Figure 2. Artificial LDs Emerge toward the Monolayer Bearing Excess Phospholipids

(A) A Lyso-PC micellar solution containing NBD-PE (1% w/w to lyso-PC) was added to GUVs marked by Rhodamine-PE (Rh-PE) (0.5% w/w to PC). Lyso-PC molecules, reported by NBD, are recruited to the external GUV surface see arrows (and Figures S2B and S2C). Scale bar, 10 μm.

(B) Determination of the location of recruited lyso-PC molecules by following NBD-PE signal. Dithionite, an NBD quencher, is added to the external solution. The NBD signal disappears entirely, suggesting that lyso-PC enrichment occurred only on the external leaflet. Scale bar, 10 μm.

(C) Relative NBD signal on the bilayer displayed for different GUVs: before any treatment, after Lyso-PC micelle addition, and after dithionite treatment. Data are represented as mean ±SD.

(D) A Lyso-PC micellar solution containing NBD-PE was added to a DEV. When the NBD concentration around the DEV increased (see example in Figure S2B), the embedded droplet emerged toward the exterior. Scale bar, 10 μm.

(E) The droplet external area variation in (D) is displayed as function of the Lyso-PC enrichement on the DEV, which is reported by the NBD-PE signal. Error bars are measurement precision.

(F) Simulated situation with increasing the number of PC molecules in the external leaflet of a bilayer containing a 35 nm-sized triolein droplet.

(legend continued on next page)

To further challenge our hypothesis, we tested the effect of the addition of apolipoprotein B (ApoB) on LD emergence. ApoB is localized in the ER lumen where it was shown to retain LDs following lipid accumulation (Ohsaki et al., 2008). Here, we indeed found that the addition of ApoB promoted aLD emergence (Figures 1G and S1D) toward the ApoB-containing medium. In cells, ApoB would thus promote the emergence of LDs into the ER lumen. As a control, we finally also tested for an effect of bovine serum albumin, which is not an LD protein and observed no emergence (Figure 1F).

These observations support our hypothesis that the insertion of proteins in an LD monolayer promotes LD emergence by decreasing the monolayer surface tension, through improving its surface coverage. To confirm the link between protein binding and surface tension, for selected examples, we measured the changes in surface tension upon addition of the protein using the micropipette aspiration technique (Figure 1G). Upon addition of ApoB (which improved the monolayer coverage and induced aLD emergence) (Figures 1H and S1D), we observed a decrease in the surface tension of the external monolayer (Figure 1I); on the contrary, in the case of Plin1 93–192 (or proteins which did not induce budding), no change in the external tension was measured (Figure 1I). Emergence of aLDs induced by protein binding is therefore mediated by the decrease in monolayer tension (Figure 1J).

In summary, the asymmetric insertion of proteins to an aLD surface promotes emergence toward the protein-enriched monolayer. This emergence results from a decrease of this monolayer surface tension due to an improvement of its surface coverage. In cells, controlling LD emergence would require regulating the access of proteins to the luminal and cytosolic sides of nascent LDs. Overexpression of proteins that strongly bind to LDs from these compartments will affect LD emergence.

Lipid Droplets Emerge toward the Membrane Monolayer Side Bearing an Excess of Phospholipids

Monolayer surface coverage can also be improved by increasing the surface density of phospholipids (Figure 1A). Phospholipids can be expected to be more effective than proteins at decreasing tension, by virtue of their higher flexibility and ability to form well-packed interfaces. For example, we measured the minimal surface tension reachable in a monolayer made of PC and found that it is lower than that obtained with ApoB, or with previously studied proteins (Figure S2A). This analysis suggests that the monolayer coverage can be improved more effectively by adding phospholipids than by inserting proteins. The addition of phospholipids could thus be more effective at promoting LD emergence.

We decided to asymmetrically increase the number of phospholipids in DEVs, for which the outer monolayer is more accessible. However, increasing the number of PC molecules by direct supply is difficult because PC forms in solution relatively stable and non-fusogenic bilayer structures. Instead, we chose to test the addition of Lyso-PC because it forms micelles, which spontaneously adsorb onto membranes. To prove this idea, we first made Lyso-PC micelles containing fluorescent NBD-PE (1%, w/w) and added them to PC GUVs (Figure 2A). Over time, after the micelles arrived in the vicinity of the GUVs, the phospholipids were recruited to the membrane as reported by the increase of the NBD signal (Figures 2A, 2C, and S2B). To know whether the phospholipids were only recruited to the external monolayer, we added dithionite to the bulk solution. Dithionite quenches the NBD signal and can only access the outer leaflet of the GUV, as it does not cross the membrane (Laouini et al., 2012). After few minutes, the NDB signal disappeared completely (Figures 2B, 2C, and S2C), supporting that phospholipids were mainly recruited to the external GUV monolayer. We hence decided to use this technique to increase the number of phospholipids in the outer monolayer of DEVs.

We took DEVs in which the aLD monolayers had no asymmetry in phospholipid composition. We next added Lyso-PC micelles to increase the number of phospholipids in the outer monolayer surface. We systematically observed that the aLDs emerged toward the outside (Figures 2D and 2E), exactly as with the insertion of proteins. This observation confirmed that the aLD emergence happens on the monolayer with the better surface coverage, mediated here by a phospholipid supply from the bulk solution.

It is worth noting that Lyso-PC has a positive spontaneous curvature, which, in principle, can have an effect on LD emergence at nanometric scales, as recently proposed (Choudhary et al., 2018). However, in our macroscopic scale (Figure 2D), spontaneous curvature effects should be dominated by surface tension (Thiam and Forêt, 2016). We hypothesize that the aLD emergence observed here is not due to Lyso-PC positive curvature but to its ability to improve the external monolayer surface coverage. To demonstrate that the asymmetry in monolayer phospholipid coverage is the main factor that mediates emergence, we used molecular dynamics simulations. Compared to experiments, in simulations it is much easier to increase or decrease the amount of phospholipid selectively in each leaflet. We performed simulations of phospholipid bilayers exclusively made of PC (~75 nm lateral size) and bearing a ~35 nm-sized triolein droplet (Figure 2F); note that PC has a slightly negative spontaneous curvature (Zimmerberg and Kozlov, 2006), opposite to the pronounced positive curvature of Lyso-PC. Starting

(G) Examples of cross sections of multiple merged snapshots of the results for different PC imbalances (0%, 4.4%, and 11% PC excess in upper leaflet). See Figure S2D for more examples. Scale bar, 7 nm.

(H) The aLD external area variation in (G) shows the externalization of the droplet with increased PC imbalance. Related to Figure S2D. Error bars are measurement precision.

(I) The external area fraction of aLDs in a DEV is displayed against the aLD radius over the GUV radius (Rld/Rguv), which takes into account the bilayer curvature. Red, values for experiments where phospholipids or proteins (that bound were added to the external medium) and black, no addition of materials. Error bars are measurement precision.

(J) Simulated relative aLD external area versus Rld/Rguv with varying the coverage asymmetry (0, 0.2, 0.6, and 0.98).

(K) On a flat and finite bilayer a large droplet will be in the middle of the bilayer, with external and internal areas being equal (top); curvature of the bilayer will induce only partial emergence (middle); providing phospholipids to increase the coverage asymmetry alone (bottom) is sufficient to promote full emergence.

See also Figure S2.

from a completely symmetric system (equal number of PC molecules on both leaflets), we performed simulations with an increasing phospholipid imbalance, up to 11% excess of PC molecules in the upper monolayer (Figures 2G and S2D). We observed that a 4% imbalance in the phospholipid count is sufficient to induce a significant asymmetry in droplet shape. The asymmetry grows as the lipid imbalance increases, and it causes the aLD to emerge toward the PC-enriched monolayer (Figures 2G, 2H, and S2D). These results show that LDs can emerge from the ER bilayer simply by maintaining an excess of phospholipids on one monolayer side, without using phospholipids with positive spontaneous curvature, which fully agrees with our *in vitro* data (Figures 2A–2E).

It is important to note that generation of high membrane coverage asymmetry cannot be maintained in the bilayer, as it would otherwise destabilize the membrane both *in vitro* and *in silico*. Instead, the surplus of phospholipids is absorbed by the increasing surface of the emerging droplet. This process is almost instantaneous as it happens in much less than a second, based on our previous work (Chorlay and Thiam, 2018). During LD budding *in vivo*, possible lipid flipping, which happens over minutes (Pomorski and Menon, 2006) would probably not be fast enough to reset the bilayer symmetry (see STAR Methods: Time scale of LD emergence).

Membrane Curvature Facilitates Lipid Droplet Budding but a Supplement of Phospholipids Remains Essential to Guarantee Full Emergence

The ER consists of relatively flat cisternae and high curvature tubules, with diameters in the range of 30–100 nm (West et al., 2011). The DEV system does not fully capture the shape nor the scale of such tubules; also, because of the large size of DEVs, the effect of membrane rigidity on LD shape is supposed to be negligible. Nonetheless, by conserving droplet-to-membrane aspect ratios, our DEV system can be seen as an upscale of a section of an LD forming on a tube (Figure 2I, left). We thus decided to use it to explore possible contributions of bilayer membrane curvature on LD emergence.

We made DEVs presenting various droplet-to-GUV aspect ratios by varying the aLD and GUV sizes. For each case, we measured the fraction of the droplet area exposed to the exterior (A_{ext}). This surface fraction was represented against the ratio of the droplet-to-GUV size (Figure 2I), which merely represents the curvature of the GUV bilayer membrane relative to the droplet. Droplets that were small relative to the GUV size were equally exposed to both membrane sides, $A_{ext} = A_{int} = 50\%$ (Figure 2I, lower black circles). In contrast, larger droplets had an external area larger than the inner area, $A_{ext} > 50\%$, indicating that they emerged more toward the exterior (Figure 2I, upper black circles). These results suggest that membrane curvature favors the outward emergence of large droplets. However, we never observed full emergence of large droplets in the DEVs, i.e., $A_{ext} = 100\%$, unless phospholipids or proteins were added to the external leaflet (Figure 2I, red circles). This suggests that curvature promotes outward budding, but the addition of phospholipids to the external leaflet is necessary to guarantee full emergence.

To further understand our data, we used a basic theoretical model computing the balance of forces acting on a droplet in a bilayer (Chorlay and Thiam, 2018) (STAR Methods: Determination of shape and position). This model fitted well with our experimental data (Figure 2I, black line), which confirmed that the effect of phospholipid surface density is stronger than the effect of curvature in determining the direction of emergence (Figures 2J, 2K, S2E, and S2F). It is worth noting that if no phospholipid is added in the system, the externalization of growing droplets would induce stretching of the external monolayer. This monolayer, not supplemented with phospholipids, would reach a lower coverage (higher surface tension) than the inner one, which, in turn, would promote inward budding (Figure S2G). In this situation, the droplets will tend to remain in contact with the lumen despite the effect of curvature.

In conclusion, our data suggest that when an LD forms and grows, the ER membrane curvature helps to preset the direction of emergence of the LD, i.e., in the cytosol. However, the supplement of phospholipids, and eventually of proteins, to the cytosolic monolayer would be required and be more efficient at promoting the full emergence of the LD into the cytosol. In case of phospholipid deficiency on this leaflet, droplets would fail to properly emerge and remain in contact with the ER lumen (Figure S2G).

Altogether, our results in Figures 1 and 2 suggest that in close systems, i.e., where there is no excess or addition of phospholipids or proteins, the droplet emergence essentially follows leaflet asymmetry. Emergence occurs toward the monolayer with the better surface coverage, which is improved by the insertion of proteins and phospholipids. In open systems, such as in cells, the order of events is not known, so asymmetry in leaflet coverage may be induced by multiple events. In any case, our *in vitro* observations predict that LD exclusive formation into the cytosol requires a regulation of phospholipid density and protein binding in of each monolayer.

Stimulated LD Production in *Saccharomyces cerevisiae* Cells by Oleic Acid Is Associated with Aberrant ER Morphology

Under basal conditions, the ER cytosolic side probably has enough proteins and phospholipids to impose directionality on LD budding. However, during high lipogenesis regimes, the demands for LD surface coating may become limiting. The emergence of many LDs will deplete phospholipids from the cytosolic leaflet of the ER membrane. In this case, if phospholipids are not present in large excess, quickly replenished, or replaced by other surfactant molecules (e.g., proteins), LD emergence (Figure S2G) and ER morphology could both be affected.

We considered cellular model systems in which the ER membrane surface can be easily visualized and characterized. We chose to work with the *Saccharomyces cerevisiae* cells because most of their ER surface is essentially composed of two domains, the cortical and nuclear ER (West et al., 2011). The total apparent surface of these two-ER domains can be approximately determined by considering them as spherical surfaces, which is an overestimation of the ER surface based on quantifications from 3D ultrastructure imaging (Wei et al., 2012). We reasoned that if too many LDs were to form in these cells, they would mobilize phospholipids from the ER cytosolic leaflet and the ER membrane might find a way to compensate for this asymmetric usage of phospholipids.

Please cite this article in press as: Chorlay et al., Membrane Asymmetry Imposes Directionality on Lipid Droplet Emergence from the ER, Developmental Cell (2019), https://doi.org/10.1016/j.devcel.2019.05.003

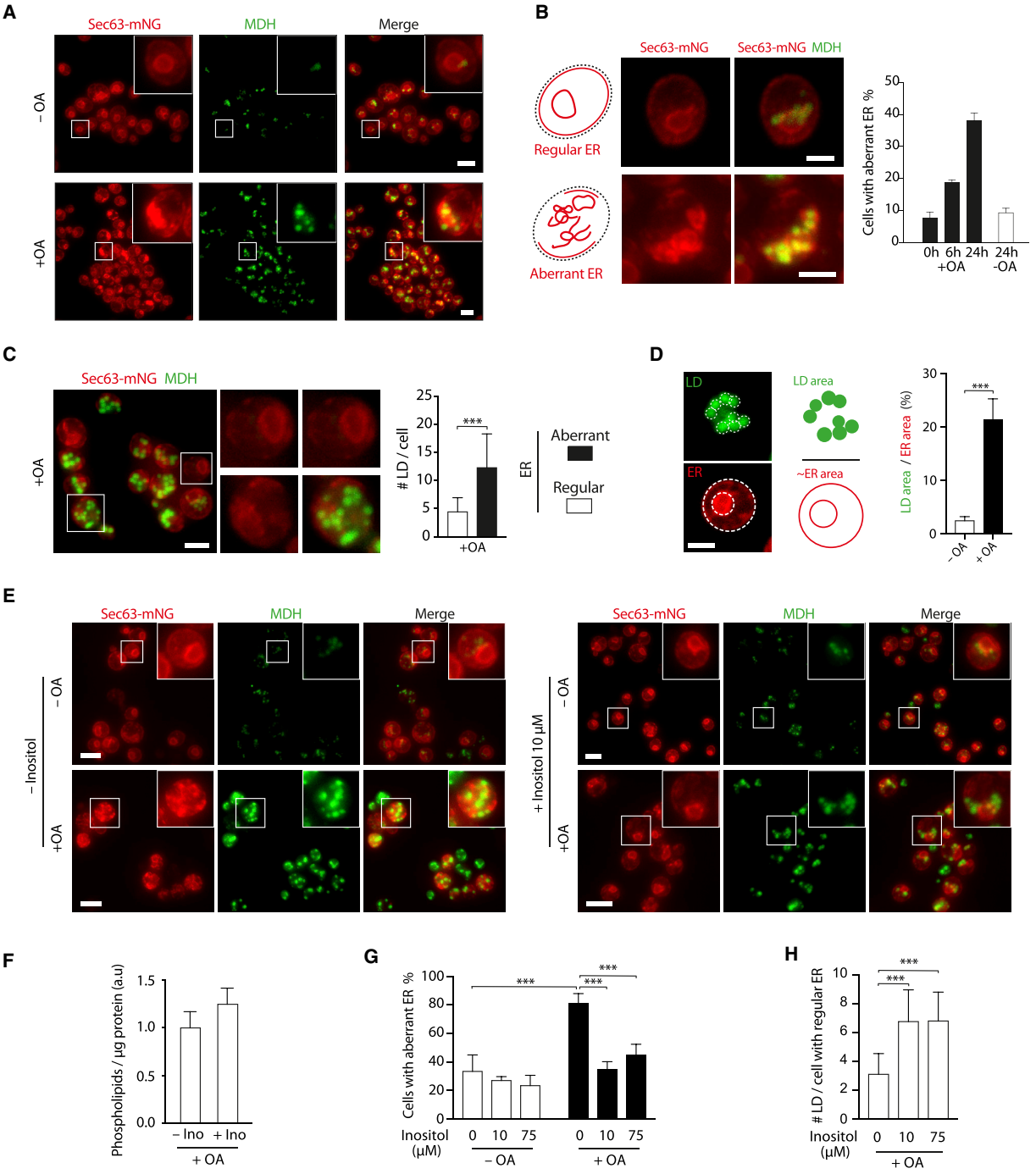

Figure 3. Boosted LD Formation Is Concomitant with Remodeled ER Morphology

(A) Representative images of wild-type (WT) *Saccharomyces cerevisiae* cells in stationary phase, imaged after 24 h, with or without treatment with oleic acid (OA). The ER marker protein, Sec63, was endogenously tagged with monomeric NeonGreen (Sec63-mNG) and LDs were labeled by monodansylpentane (MDH). Images shown represent z projection of different confocal planes. Scale bar, 5 µm.

(B) Left: schematics and representative images of cells with regular or aberrant ER. An image is shown for each situation. Images shown represent z projection of different confocal planes (shown in Figure S3F) Scale bar, 2 µm. Right: Quantification of the number of cells with aberrant ER, 0, 6, and 24 h after OA treatment of cells in log phase. Control cells with no OA addition are shown at 24 h time point. n > 200 cells/condition (ntotal = 1,276). Data are represented as mean ±SD. See Figures S3A–S3C for other tested conditions.

(legend continued on next page)

Yeast strains expressing the ER marker protein Sec63 at endogenous levels, tagged with the monomeric fluorescent protein neon green (Sec63-mNG), were grown in oleate-containing media (0.1%) for 6 to 24h, in order to produce numerous and big enough LDs to quantify by fluorescence (LDs were stained by monodansylpentane, MDH). Under these conditions, we observed increased numbers of cells with aberrant ER membranes, as compared to non-oleate loaded cells (Figures 3A and 3B). Unusual ER membrane signals appeared in the cytoplasm in the form of lumps or threads. The cortical ER, which seemed to be discontinuous or disappeared, was more affected than the nuclear ER, which was sometimes shrunk or distorted (Figures 3B and S3F). These phenotypes were observed irrespective of whether LD production was stimulated during exponential or stationary phases (Figures S3A and S3D). Interestingly, cells with aberrant ER very often contained larger numbers of LDs (Figures 3C and S3E), suggestive of a link between the LD number, or total LD surface, and ER morphology defects. By estimating the amount of total LD surface over the cortical and nuclear ER surface, we found that this ratio was less than 2% in most cells cultured in regular media (no oleate) (Figure 3D)—consistent with values from tomogram reconstitution data of *Saccharomyces cerevisiae* cells (Wei et al., 2012; West et al., 2011). In contrast, in cells grown in oleate-containing media, this ratio was more than 22% (Figure 3D).

Assuming that the LDs were all formed toward the cytosol in the oleate-loaded cells, the ER membrane would be depleted of 22% in phospholipids on its cytosolic leaflet, which would generate a huge asymmetry on the membrane. Indeed, a pure bilayer can only withstand an asymmetry of less than 1% in phospholipids (Segrest et al., 2015; Farge and Devaux, 1992). Otherwise, the membrane will undergo spontaneous reshaping to release the stress created by this asymmetry (Segrest et al., 2015; Farge and Devaux, 1992). With the potential membrane asymmetry of 22% induced by LD formation, such spontaneous membrane reshaping mechanism could explain, at least in part, the observed loss of the normal ER morphology.

Phospholipids may be refilled to the ER cytosolic leaflet during the formation of LDs in non-fed cells, through the activity of scramblases (Pomorski and Menon, 2016). In contrast, the fed cells were probably challenged beyond their capacity of phospholipid supply for covering the LDs. Thus, they would likely respond to this demand by remodeling their ER membrane. Consistent with this analysis, cells fed under our working conditions were previously reported to reach a ~1.3-fold increase of their total phospholipid (Grillitsch et al., 2011). Our quantifications from thin-layer chromatography showed that the total phospholipid level barely changed (Figure S3G). Overall, these observations suggest that LD formation in oleate feeding conditions, the phospholipid levels were not sufficient to overcome the demand.

We reasoned that increasing phospholipid production under lipogenic conditions would rescue the aberrant ER phenotype. In yeast, inositol is a major component regulating phospholipid biosynthesis (Carman and Henry, 1989). It is a precursor of the synthesis of PI, a main lipid of yeast ER membranes. The enzymes executing PI synthesis are located on the cytosolic membrane side of the ER (Carman and Henry, 1989). The addition of inositol to yeast cells led to a 5-fold increase in PI as well as overall cellular phospholipid levels (Gaspar et al., 2006) (Figure S3H); only PC levels were slightly decreased, as reported before (Gaspar et al., 2006) (Figure S3H). We cultured yeast cells in the presence of oleate and inositol and quantified the amount of total phospholipid per microgram of proteins. The overall phospholipid level was increased by ~30% (Figure 3F) and we found a significant increase of PI (Figure S3H). Interestingly, we found that the addition of inositol rescued the aberrant ER phenotype (Figures 3E and 3G). In this condition, we also noticed that cells presenting a normal ER morphology tolerated a higher number of LDs than the control cells, i.e., without inositol addition but in the presence of oleic acid (OA) (Figure 3H). Based on our model, these observations suggest that the cells treated with inositol, which induced an increase in total phospholipids, were better set with phospholipids to cover the total surface of generated LDs. This overall rescue of the aberrant ER phenotype is probably mediated by the presence on the ER cytosolic monolayer of additional phospholipids, probably PI (Figure S3H), which contributed to the coverage of the LDs.

Finally, we tried to accentuate the aberrant ER phenotype, by aiming at decreasing the number of phospholipids available in the cell. We deleted the choline-phosphate cytidylyltransferase gene (PCT1), the rate-limiting enzyme in the Kennedy pathway of PC biosynthesis (Dowd et al., 2001). However, no striking differences were observed between WT and pct1Δ, except at 6 h after OA treatment where pct1Δ cells showed a stronger increase of aberrant ER frequency (Figure S3D). This is probably because the large asymmetric phospholipid usage introduced by the numerous LDs formed was already too strong, and therefore no further ER membrane reorganization could be induced. As an alternative, the contribution of PCT1 to PC synthesis under our working condition could be smaller than pathways involving e.g., Cho2 and Opi3.

(C) Cells with the aberrant ER phenotype statistically contained more LDs than cells with a normal ER. t test ($p < 0.0001$), n = 140 cells, data are represented as mean ±SD. Similar results for *pct1*Δ are presented in Figure S3E. Scale bar, 5 μm.

(D) Left: illustrative image showing the measuring principle of total LD area and cortical and nuclear ER surface. Scale bar, 2 μm. Right, quantification of the total LD over ER area at 24 h in stationary phase with and without oleate. t test show a significant difference ($p < 0.0001$); n = 10 cells. Data are represented as mean ±SD.

(E) Left: representative images of cells in stationary phase, imaged after 24 h, with or without with (OA). Right: the cells were additionally treated with 10 μM inositol. Scale bars, 5 μm.

(F) Total amount of phospholipids/μg of proteins in the presence of OA, with and without inositol treatment. Quantification of thin-layer chromatography (Figure S3H). Experiment was repeated three times. Data are represented as mean ±SD.

(G) Quantification of the number of cells with aberrant ER at 24 h for various inositol concentrations, with and without OA treatment (conditions displayed in E). n > 200 cells/condition (ntotal = 1,979). t test show significative diferences with ($p < 0.001$). Data are represented as mean ±SD.

(H) Cells presenting a normal ER statistically bear more LDs in inositol treatment. n = 30 cells ($p < 0.0001$), data are represented as mean ±SD.

See also Figure S3.

Please cite this article in press as: Chorlay et al., Membrane Asymmetry Imposes Directionality on Lipid Droplet Emergence from the ER, Developmental Cell (2019), https://doi.org/10.1016/j.devcel.2019.05.003

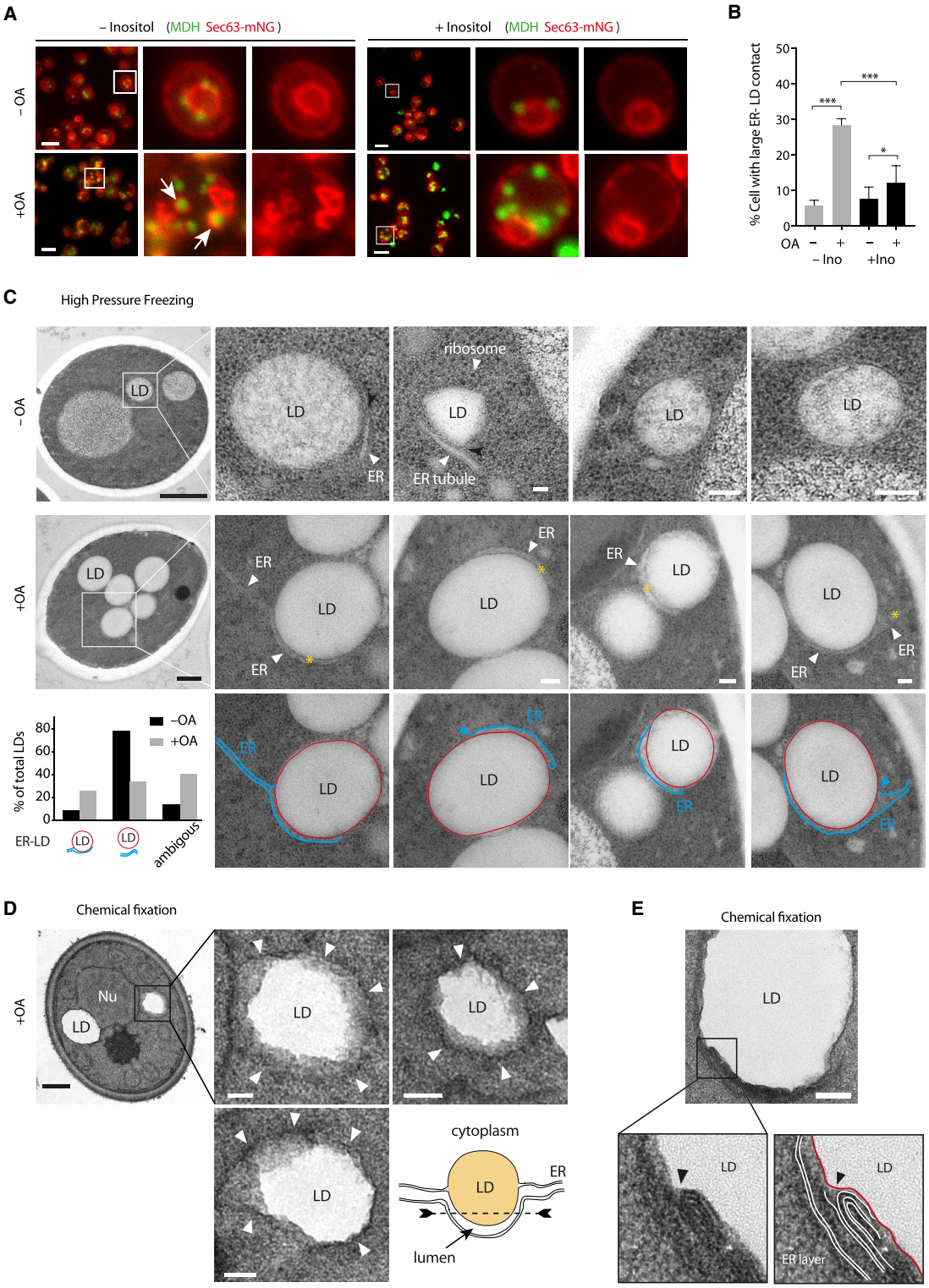

Figure 4. LD Proper Emergence in *Saccharomyces cerevisiae* Is Facilitated by Phospholipid Production

(A) *Saccharomyces cerevisiae* cells in logarithmic growth phase treated with OA show LDs with large contact zones with the ER membrane (white arrows). Less LD-ER contact zones were observed after inositol treatment, as in non-oleated cells. Sec63-mNG marks ER and LD are MDH stained. Scale bar, 5 μm.

(legend continued on next page)

In summary, the formation of multiple LDs correlated with the appearance of an aberrant ER membrane. This phenotype was rescued by the addition of inositol, which led to an increase in phospholipid levels. These results show that increasing phospholipid levels during lipogenesis ensures the formation of multiple LDs in the cytosol and keeping the ER morphology intact.

Proper LD Emergence Is Facilitated by Phospholipid Synthesis in Yeast Cells

The formation of multiple LDs depletes phospholipids from the cytosolic leaflet of the ER membrane. If the ER cannot meet this phospholipid demand on the cytosolic monolayer its luminal monolayer could become better covered with phospholipids, at least transiently. Therefore, we expect that in such conditions some LDs fail to fully emerge in the cytosol and instead, remain in contact with the ER lumen.

In the yeast cells fed with oleate to stimulate LD production, we observed increased numbers of LDs sharing large contacts with the ER membrane marker (Figure 4A, left and Figure 4B). This phenotype was much more pronounced in cells with an aberrant ER. In these cells, the ER sometimes adopted a cup shape structure, which embedded the LD or surrounded the LD on the observed plane (Figure 4A, arrows). This phenotype was more pronounced in *pct1Δ* cells (Figure S4A). Note that these LDs were not in the nucleus, which remained intact in most cases (Figures 4A, S4A, and S4B). These data support a failure in LD emergence in the cytosol, which would be consistent with our model of the need of phospholipid refill on the cytosolic monolayer for proper LD emergence (Figure 2). In fact, by the addition of inositol, which increased phospholipid levels and reduced the aberrant ER phenotype (Figures 3E–3G), we found that the fraction of LDs which were in large contact with the ER membrane was significantly decreased (Figure 4A, right and Figure 4B).

To visualize the topology of the ER-associated LDs, we performed electron microscopy (EM) imaging of high-pressure frozen (HPF) cells. In control (non-oleate-loaded) cells, most LDs were not in large contact with the ER (Figure 4C, top). Even though the ER membrane was sometimes close to LDs in these cells, there was a perfectly distinguishable free space between the two organelles (Figure 4C, top, black arrowhead). In oleate-loaded cells, which developed an aberrant ER phenotype, LDs were larger than in control cells and were often molded by ER membranes (Figure 4C). The ER lumen, marked by a membrane region devoid of ribosomes, seemed to be in contact with the LDs. In some cases, the focal section enabled us to catch structures that looked like an unzipping of the ER bilayer at the LD edge (see Figure 4C, blue arrowhead). These phenotypes might look like mere membrane wrapping phenomena but rather could be the signature of a defect in LD emergence, as theoretically predicted (Figure S2G). This conclusion is consistent with previous studies, performed exactly under our working conditions, which showed that the LDs were accessible to proteins expressed in the ER lumen, by both fluorescence and EM imaging (Mishra et al., 2016). To better visualize the membrane, we opted for a chemical fixation of the cells instead of HPF. With this method, membranes were better labeled and darker (Figure 4D, white arrowhead and Figure S4C). This approach enabled us to identify section planes where LDs were in contact with the ER lumen in oleate-loaded cells, as previously seen in yeast cells lacking FIT2 (Choudhary et al., 2015, 2018). On other focal sections, we also observed phenotypes where the ER membrane formed stacks on a portion of the LDs (Figures 4E and S4D), and sometimes we could catch what seemed to be an unzipping of the membrane at the LD edge (Figure 4E, black arrowhead).

LDs Remain More in Contact with the ER in *Drosophila* Cells with Reduced CCT1 Activity

We decided to test our model in a different cell type by manipulating phospholipid levels. We worked with *Drosophila* Kc167 cells because the synthesis of PC in these cells essentially happens through the Kennedy pathway. Contrary to PCT1 inhibition in yeast, PC level in *Drosophila* cells is markedly reduced by inhibiting the rate-limiting enzyme in PC synthesis, the choline-phosphate cytidylyltransferase enzyme 1 (CCT1) (Krahmer et al., 2011; Aitchison et al., 2015). Cells expressing the GFP-tagged ER marker Sec61β were treated with dsRNA targeting the CCT1 encoding transcript (Figure S5A) and then they were fed with oleate. We observed an increase in the number of large LDs (Figures S5C and S5D), a signature of PC deficiency in CCT1 depletion (Krahmer et al., 2011; Aitchison et al., 2015). As compared to yeast cells, in the fly cells the ER formed a complex 3D network, which was a limitation to properly characterize ER membrane morphology and to quantify the LD-to-ER surface ratio. Nonetheless, by using super-resolution structured illumination microscopy, in the CCT1-depleted cells, we found LD phenotypes similar to the ones found in yeast (Figures 4A, 4C, 4D, S4A, and S4C): as compared to WT control cells, many LDs were much more often in close contact with the ER membrane marker (Figure 5A), as visualized through z stacks. For many LDs, there were focal planes where the ER membrane marker protein was extremely close to the LD surface (Figure 5A,

(B) Quantification of the number of cells presenting large ER-LD contact (with or without inositol (10 μM)): ER-LD contact is considered large if more than half of the LD surface is in contact with the ER membrane. N >110 cells for each condition; $p < 0.0001$, $p < 0.0001$, and $p < 0.01$; Data are represented as mean ±SD.
(C) WT cells high-pressure cryofixed are observed by electron microscopy (EM) with and without OA treatment. Insets show different LDs in each condition. ER is indicated by white arrowheads. Dark dots are ribosomes. Ribosome free zones (yellow stars) are in close contact with LD in OA treatment conditions. Red lines delineate LD surface, blue lines indicate ER bilayer, and blue arrowheads indicate points where the ER seems to unzip around the LD in some focal planes. Scale bars, 500 nm (full view) and 100 nm (inset). Quantification of ER-LD contact is performed on N=120 LDs: on the section planes, the ER-LD contacts are either large, not visible or ambiguous.
(D) Cells are treated with OA and chemically fixed and observed using EM. Examples of section plans where LDs appear to be in contact with the ER lumen (white arrows) are shown. Schematic diagram describing the plausible topology of the EM images. Quantification of ER-LD contact is shown in Figure S4C. Scale bar, 500 nm (full view) and 100 nm (inset).
(E) Example of a section plan where ER membranes are recruited around an LD. The ER bilayer seems to unzip at the edge of the LD (in the inset, the ER membrane is drawn in white and the LD surface in red). Scale bar is 500 nm. Related to Figures S4C and S4D.
See also Figure S4.

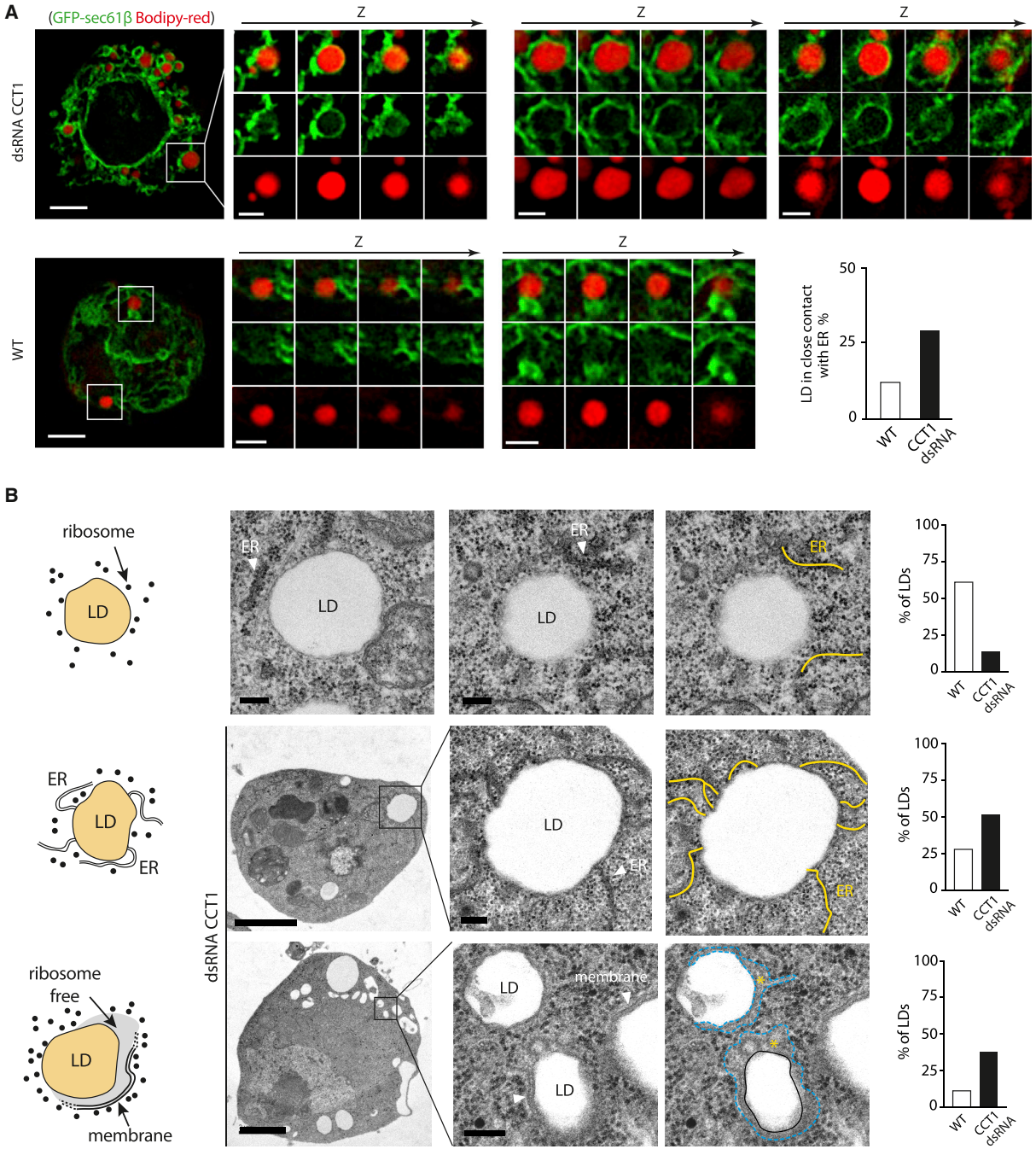

Figure 5. Drosophila Cells with Decreased CCT1 Display Increased ER-LD Contacts

(A) *Drosophila* cells were depleted of CCT1 by dsRNA. LDs are induced by oleate and stained by BODIPY558/568; GFP-sec61β marks the ER. Top: representative confocal image of dsRNA CCT1 cells. Insets show z stacks of LDs in close contact with the ER membrane marker. Bottom left: representative WT control with z stacks of example LDs. The ER-LD contact was less pronounced. Bottom right: dsRNA CCT1 cells present a higher number of LDs in close contact with the ER (quantification made for N =150 in each condition). Scale bar, 2 μm and 200 nm (inset). See Figure S5B for additional z stacks.

(B) WT and CCT1 depleted Drosophila cells treated with OA were fixed by glutaraldehyde and observed by electro-microscopy following contrastation with uranyl acetate and lead. In the section plane, three different LD-ER interactions are defined: top, LDs with no visible contact with ER; middle, LDs with multiple contact point with ER membrane; and bottom, LDs in large contact, with a noticeable ribosome free zone delineated by the ER membrane. Frequency of these phenotypes in WT and dsRNA CCT1 cells is shown on the right with an average of fifteen LDs each. More Illustrative EM images are presented in Figure S5E. Scale bar, 2 μm and 200 nm for zoomed insets. See also Figure S5.

see right examples) and was reminiscent of what an LD-associated protein signal would look like. This observation revealed that these LDs were in close contact with the ER lumen. We next performed EM imaging and found that CCT1 depletion led to significantly more ER-connected LDs (Figure 5B). We also found another significant phenotype where the LDs had regions devoid of ribosomes and delineated by membranes, which were probably the ER. This phenotype is reminiscent of the one observed in yeast (Figure 4C), where LDs are probably in contact with the ER lumen.

Model LDs Equally Emerge on Both Membrane Sides If Phospholipids Are Not Replenished

To further understand the ER-associated LD phenotypes, we opted for the DEV set-up to mimic the absence of a phospholipid refilling mechanism to the cytosolic monolayer, under conditions where many LDs are generated. We made PC DEVs with many small and symmetrically positioned artificial LDs (Figure 6A). Under these conditions, the aLD-to-bilayer surface ratio was ~2% (Figure 6A), close to LD-to-ER surface ratios in yeast (Figure 3D). We then decreased the DEV tension, by deflating them with a hypertonic buffer added to the aqueous medium, to promote spontaneous emergence of the droplets (Deslandes et al., 2017; Chorlay and Thiam, 2018). By following droplets of the same DEV, we observed that they fully emerged, interestingly, into both sides of the bilayer (Figures 6B, 6C, S6A, and S6B). These results were highly reproducible and the budding events into the internal and external sides were statistically equal (Figure 6D).

This even distribution of emerged artificial LDs across the bilayer probably arose from a compensatory mechanism of surface expansion (Figure S6C). The external and internal monolayers of the bilayer had initially approximately the same phospholipid coverage. When an artificial LD emerged, e.g., toward the exterior, it expanded the external leaflet surface area, while the amount of phospholipids remained constant on the time scale of droplet budding (because flip-flop rates are extremely slow for PC (Tieleman and Marrink, 2006; Nakano et al., 2009)). Expansion of the external leaflet reduced this monolayer phospholipid coverage as compared to the internal monolayer; therefore, emergence of the second droplet was favored toward the opposite leaflet (Figure S6C). Emergence of the second droplet re-equilibrate the surface coverage between the two monolayers and so on and so forth. This feedback mechanism can explain the increased number of LDs that stayed in contact with the ER lumen (Figures 4 and 5): in ER membranes unable to provide enough phospholipids to the cytoplasmic monolayer, the emergence of an LD population into the cytosol will tend to expose of the rest of the LDs to the lumen.

To fully prove this emergence feedback mechanism, we made a PC DEV with one large artificial LD (Figure 6E), with a droplet-to-bilayer surface of 22% (Figure 6F), close to the situation where many LDs are formed in yeast cells (Figure 3D). The aLD was symmetrically positioned in the bilayer (Figures 6E and 6G). With a micropipette, we suctioned out a small portion of the droplet and removed it, which mimics emergence from the ER of a given total aLD volume or surface (Figures 6E and S6D). This operation removed phospholipids from the outer monolayer, reducing its coverage as compared to the inner one. As expected, the remaining total aLD volume becomes more exposed toward the side with the better phospholipid coverage, i.e., the luminal side (Figures 6E and 6G). Emergence to the luminal side was evident after slightly decreasing the bilayer tension or internal pressure (previously increased by the ablation step) (Figures 6E, 6G, and 6H); note that simply decreasing this tension or pressure without the induced phospholipid coverage asymmetry was not solely sufficient to induce such emergence (Figure S6H). A cross section of a 3D visualization of the final system demonstrating the internal emergence is shown in Figures 6H and S6F. In conclusion, this experiment is evidence that in the absence of phospholipid replenishment, the budding of a droplet population toward the membrane side will promote the emergence of the rest of the droplets to the opposite side.

Finally, we estimated that the difference in monolayer coverage that induced the aLD internal emergence was about 9%, corresponding to an imbalance of monolayer surface tension of less than 8% (Figures 6I and S6G). Because our experimental condition reproduced LD/ER surface ratios found in yeast cells boosted with LDs, our findings suggest that maintaining an excess of around 9% of phospholipids on the cytosolic monolayers of the ER is sufficient to guarantee proper LD formation in the cytosol during high lipogenesis regimes.

DISCUSSION

In the present work, we show that LDs bud off and emerge toward the membrane side with higher monolayer leaflet coverage. LDs rapidly absorb this asymmetry by emerging on the side of higher coverage. Because *in vivo* LDs mainly emerge to the cytosol, our results suggest that during lipogenesis, the cytosolic monolayer coverage should transiently be kept higher than the luminal monolayer coverage. We shed light on the mechanisms that maintain such tension imbalances.

The strong adsorption of proteins from the cytosol improves the coverage of the monolayer surface by masking possible phospholipid packing defects of the monolayer (Bacle et al., 2017; Prévost et al., 2018; Thiam et al., 2013b). Thereupon, adsorbed proteins lower the surface tension of the cytosolic monolayer and imposes LD emergence in the cytosol (Figure 7A). This directional emergence could be also mediated by ER-embedded proteins that target LDs. Most of these proteins are indeed strongly attached to the LD cytosolic monolayer by using AHs and/or hairpin motifs (Kassan et al., 2013; Pol et al., 2014; Wilfling et al., 2013; Jacquier et al., 2013; Huang and Huang, 2017).

More generally, the strong binding of any protein to the monolayer of a nascent LD will tend to retain the LD into this monolayer compartment (Figure 7B). Thus, proteins that would strongly bind LDs from the cytosol and the ER lumen would compete for LD emergence. Depending on the binding affinity of these proteins, an LD could be trapped in the ER membrane with various degrees of contact with the ER lumen and the cytosol (Figure 7B). This probably explains how in hepatocytes ApoB100 retains some mature LDs in the ER lumen because of its irreversible binding to the LD surface (Figure S1F). In these cells, ApoB binds only to some LDs to possibly make them accessible to ER luminal proteins, which is important for the secretion of very low-density lipoprotein (Ohsaki et al., 2008, 2009). Similarly, LD retention in the ER lumen is also likely caused by the overexpression of Perilipin constructs targeted to the ER

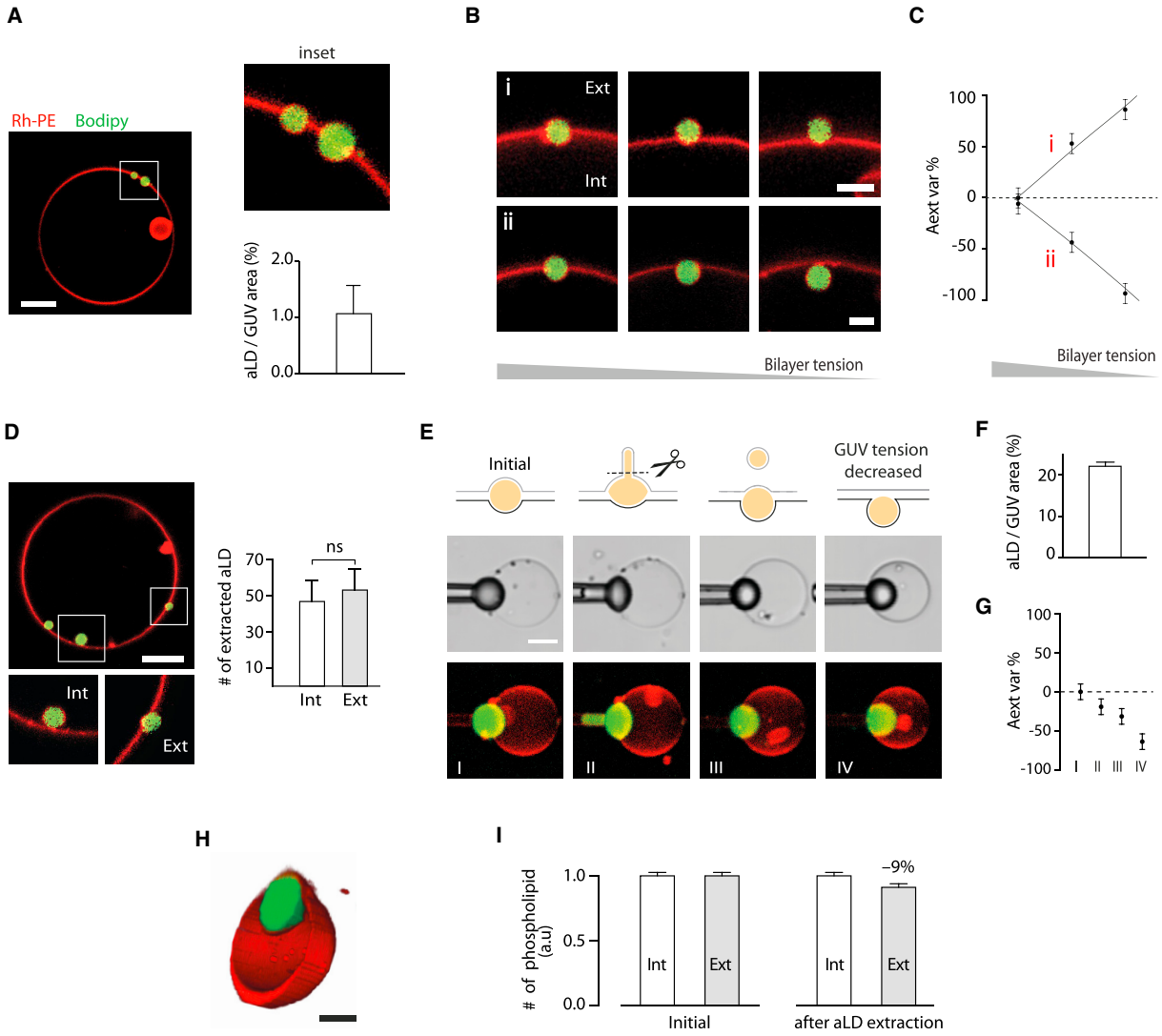

Figure 6. Artificial LDs Equally Emerge on Both Sides of a Same Bilayer with Fixed Phospholipid Number

(A) Example of a confocal image of DEV with small artificial LDs; the DEV contains other aLDs, which were not visible in the shown confocal plane. Bodipy stained the droplet and Rhodamine-PE (Rh-PE) labeled the membranes. The inset is zoomed. The graph shows the quantification of the total artificial LDs surface over the GUV bilayer apparent area (See Figure S6B). Scale bar, 10 μm. Error bar is the measurement precision.

(B) Example of two LDs in the same DEV that emerge on different directions upon decreasing the DEV bilayer tension. Scale Bar, 2.5 μm. An extremely deflated GUV with aLDs emerged on both bilayer side is shown in Figure S6A).

(C) The external area variation ("Aext var") is shown for the two aLDs that emerged on different directions in (B). Error bar is the measurement precision.

(D) Example and quantification of the number of aLDs that emerged in the interior and exterior of DEVs. Scale bar, 10 μm. t test showed ns difference; N = 100. Data are represented as mean ± SD.

(E) Mimic of the budding of a total lipid droplet number (or aLD total surface) from a bilayer. The aLD of a DEV is suctioned on the exterior and ablated (see Figure S6D) to mimic emergence of a certain LD volume, or surface, from the bilayer. The remaining artificial LD is displaced in the bilayer lumen. Deflating the DEV to reduce its surface tension led to almost complete exposing the remained artificial LD into the lumen (full data see Figure S6E). Scale bar, 10 μm.

(F) Quantification of the total aLD surface over the GUV bilayer initial apparent area. Error bar is the measurement precision.

(G) The aLD external area variation corresponding to (E). Error bar is the measurement precision.

(H) 3D reconstitution of the inward emerged aLD (see Figure S6F). Scale bar, 10 μm.

(I) Quantification, based on the ablated aLD surface, of the relative change in the phospholipid number between the internal and external monolayers. Figure S6G shows the related external and internal monolayer tension generated. Error bar is the measurement precision.

See also Figure S6.

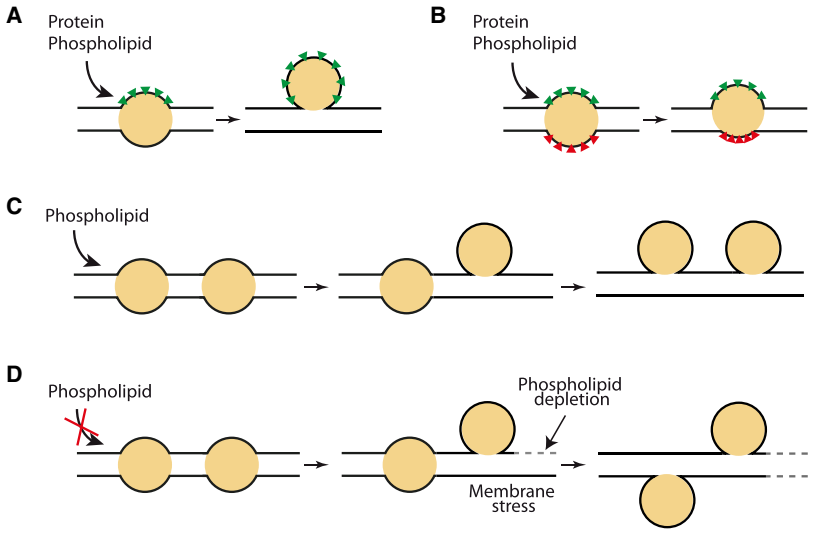

Figure 7. Proposed Model for the Impact of Proteins and Phospholipids on LD Emergence

(A) Recruitment of both proteins and phospholipids to one monolayer promotes LD emergence toward this monolayer side.

(B) A balance of strongly inserted proteins will position an LD in the bilayer with various degree of contact to the surrounding aqueous phases.

(C) Continuous injection of phospholipid on the upper monolayer promotes LD emergence to the upper side.

(D) Lack of a monolayer phospholipid excess, or supply, induces LD equal emergence to both membrane sides, membrane stress, and reorganization.

lumen. Indeed, in such cases LDs become accessible to ER luminal proteins (Mishra et al., 2016). Thus, the overexpression or downregulation of any protein that is able to tightly bind to the LD surface will affect LD emergence (Figure 7B). For LDs to fully emerge into the cytosol, proteins with high affinity for an LD surface should not get access to LD from the ER lumen. One possible way to fence out proteins, especially those coming from the luminal side, is provided by some specific proteins localized to LD biogenesis sites such as Seipin (Wang et al., 2016; Chen and Goodman, 2017; Thiam and Beller, 2017; Grippa et al., 2015).

The release of multiple ER-derived LDs into the cytosol will reduce the number of phospholipids in the ER cytosolic leaflet. Hence, this leaflet needs to be refilled to guarantee that all LDs bud in the same direction while preserving ER morphology (Figure 7C). Otherwise, chances are that LDs get in large contact within the ER lumen (Figure 7D). In *Saccharomyces cerevisiae* and *Drosophila* cells deficient in PCT1 and CCT1 enzymes respectively, or in phospholipids, many LDs indeed failed to fully emerge in the cytosol.

Excess phospholipids on the cytosolic monolayer will make the ER asymmetric, at least under lipogenesis conditions during which phospholipid synthesis is triggered on the cytosolic ER leaflet (Lagace and Ridgway, 2013; Walker et al., 2011; Van Meer et al., 2008). Thus, the idea that the ER has a symmetric membrane needs to be reconsidered. During lipogenesis conditions, the ER may actually display regions where an asymmetry in phospholipid type and density is generated for controlling the LD emergence side. For example, early lipidomic studies of ER-derived microsomes from rat liver have shown that the ER outer leaflet is more enriched in PC and less in phosphatidylethanolamine (Higgins and Dawson, 1977). Also, phospholipids are provided in an asymmetric fashion by the fusion with the ER of retrograde transport vesicles. These vesicles are derived from the Golgi that is asymmetrical in lipid composition (Van Meer et al., 2008) and have more and different phospholipids on their outer monolayer. Finally, the exclusive phosphate phosphatase activity of FIT2 in the ER luminal membrane side suggests at least a transient asymmetry of the membrane in phosphatidic acid.

Regarding the asymmetry in phospholipid density, various mechanisms can enable the refill of the cytosolic leaflet with phospholipids. *De novo* phospholipid biosynthesis is probably the primary mechanism fulfilling such need (Lagace and Ridgway, 2013; Van Meer et al., 2008). Enzymes of the Kennedy pathway for *de novo* PC biosynthesis are indeed important for LD emergence (Lagace and Ridgway, 2013; Krahmer et al., 2011; Aitchison et al., 2015) (Figures 5 and S4A). Alternatively, ER-embedded flippases (Bishop and Bell, 1985) might transfer phospholipids from the ER luminal to the cytosolic monolayer to control LD emergence. The unselective insertion of proteins into the ER cytosolic monolayer may also increase the phospholipid density in this monolayer (Segrest et al., 2015). Finally, FIT2 is also a potential factor promoting ER membrane asymmetry in phospholipid density. By its presumable phosphate phosphatase activity in the ER luminal monolayer (Becuwe et al., 2018; Hayes et al., 2017), FIT2 may convert phospholipids of this monolayer into diacylglycerols. These molecules are soluble in the neutral lipid phases and will be released from the luminal monolayer into the lipid phase; next, they could be reconverted into phospholipids on the cytosolic monolayer. Hence, FIT2 activity would result in a net phospholipid transfer from the ER luminal leaflet to the cytosolic one. Such action would maintain LD emergence toward the cytosol.

Finally, membrane curvature may also help LD emergence (Figures 2I–2K). However, the emergence of LDs in the cytosol will deplete the cytosolic monolayer of phospholipids, unless these are refilled. This would introduce an asymmetry in monolayer phospholipid coverage that would favor inward emergence. These antagonist effects would perturb the tubular membrane topology and later formed LDs would remain in contact with the ER lumen. This situation will induce phenotypes where growing LDs, which are more exposed to the lumen, become tightly opposed to the ER membrane. Hence, the often-reported ER-wrapped phenotype may be a signature of a defect in LD emergence.

In conclusion, our findings bring insights on mechanisms of cytosolic LD biogenesis and their link with ER morphology and phospholipid biosynthesis. Our data support the hypothesis that the ER membrane undergoes dynamic asymmetrical remodeling during lipogenesis periods, so as to guarantee LD

formation in the cytosol, which is critical for the LD proteome and subsequent biological functions.

STAR★METHODS

Detailed methods are provided in the online version of this paper and include the following:

- KEY RESOURCES TABLE
- CONTACT FOR REAGENT AND RESOURCE SHARING
- EXPERIMENTAL MODEL AND SUBJECT DETAILS
  - Yeast Strain and Culture Media Conditions
  - Huh7.5 Culture and Media Conditions
  - *Drosophila* Kc167 Culture Media Conditions
- METHOD DETAILS
  - DEV Preparation: GUVs + LDs
  - Determination of the Degree of LD Emergence in the DEV Experimental System
  - Determination of the Coverage Asymmetry
  - Determination of the Shape and Position of an LD in a GUV Bilayer
  - Proteins Production and Purification
  - Protein Enrichment of the DEV External Leaflet
  - Micromanipulation & Surface Tension Measurements by Micro Aspiration
  - Pendent Droplet Interfacial Tension Measurements
  - Triolein-Protein Surface Tension Measurement
  - Triolein-Phospholipid Surface Tension Measurement
  - Lyso-PC Enrichment to the GUV External Leaflet
  - Molecular Dynamics (MD) Simulations
  - Time Scale of LD Emergence and Phospholipid Flipping
  - Lipid Droplet Induction and Fluorescence Microscopy of Yeast Cells
  - Electron Microscopy Experiments in Yeast Cells
  - Thin Layer Chromatography and Lipid Detection
  - dsRNAs Construction for Drosophila Experiments
  - Structured Illumination Microscopy of Drosophila Experiments
  - qPCR Confirmation of CCT1 Knock-Down in Drosophila Experiments
  - Electron Microscopy Experiments of Drosophila Cells
  - Modulation of GUVs Bilayer Tension Using Osmotic Pressure
  - Calculation of the Amount of Removed Phospholipids
- QUANTIFICATION AND STATISTICAL ANALYSIS
  - Quantification Methods in Yeast
  - Quantification in Drosophila cells
  - Statistical Analysis
- DATA AND SOFTWARE AVAILABILITY

SUPPLEMENTAL INFORMATION

Supplemental Information can be found online at https://doi.org/10.1016/j.devcel.2019.05.003.

ACKNOWLEDGMENTS

We are thankful to Dr. David Savage and Bruno Antonny for the kind gift of proteins, Alisa Gahlen and Elisabeth John for technical support, and Astrid Schauss and Felix Babatz from the CECAD Imaging Facility for EM imaging. We thank all the group members for their valuable comments and critical discussions. This work was supported the ANR-NanoDrop to A.R.T. and L.M., ANR-LDEN, ANR-Mobil, ANR-18-CE11-0012-01, and Paris Sciences et Lettres to A.R.T.

AUTHOR CONTRIBUTIONS

A.C. and A.R.T. designed the research and experiments and quantified all data. A.C. performed all *in vitro* experiments, with the help of K.B.M. and M.O., and D.A. performed the lipid analysis. S.W., J.F., E.J., and P.C. performed the yeast and the electron microscopy experiments. M.B. did the studies in *Drosophila* cells, and L.M. performed the molecular dynamics studies. R.B. purified proteins and helped on the elaboration of *in vitro* experiments. A.R.T. wrote the manuscript and all the authors reviewed and edited it.

DECLARATION OF INTERESTS

The authors declare no competing interests.

Received: April 26, 2018
Revised: January 11, 2019
Accepted: May 2, 2019
Published: May 30, 2019

REFERENCES

Aitchison, A.J., Arsenault, D.J., and Ridgway, N.D. (2015). Nuclear-localized CTP:phosphocholine cytidylyltransferase alpha regulates phosphatidylcholine synthesis required for lipid droplet biogenesis. Mol. Biol. Cell *26*, 2927–2938.

Ajjaji, D., Mbarek, K.B., Mimmack, M.L., England, C., Herscovitz, H., Dong, L., Kay, R.G., Patel, S., Saudek, V., Small, D.M., et al. (2019). Dual binding motifs underpin the hierarchical association of perilipins1-3 with lipid droplets. Mol. Biol. Cell *30*, 703–716.

Antonny, B., Beraud-Dufour, S., Chardin, P., and Chabre, M. (1997). N-terminal hydrophobic residues of the G-protein ADP-ribosylation factor-1 insert into membrane phospholipids upon GDP to GTP exchange. Biochemistry *36*, 4675–4684.

Bacle, A., Gautier, R., Jackson, C.L., Fuchs, P.F.J., and Vanni, S. (2017). Interdigitation between triglycerides and lipids modulates surface properties of lipid droplets. Biophys. J. *112*, 1417–1430.

Beck, R., Sun, Z., Adolf, F., Rutz, C., Bassler, J., Wild, K., Sinning, I., Hurt, E., Brügger, B., Béthune, J., et al. (2008). Membrane curvature induced by Arf1-GTP is essential for vesicle formation. Proc. Natl. Acad. Sci. USA *105*, 11731–11736.

Becuwe, M., Bond, L.M., Mejhert, N., Boland, S., Elliott, S.D., Cicconet, M., Liu, X.N., Graham, M.M., Walther, T.C., and Farese, R.V. (2018). FIT2 is a lipid phosphate phosphatase crucial for endoplasmic reticulum homeostasis. bioRxiv.

Ben M'barek, K., Ajjaji, D., Chorlay, A., Vanni, S., Forêt, L., and Thiam, A.R. (2017). ER membrane phospholipids and surface tension control cellular lipid droplet formation. Dev. Cell *41*, 591–604.e7.

Bigay, J., Gounon, P., Robineau, S., and Antonny, B. (2003). Lipid packing sensed by ArfGAP1 couples COPI coat disassembly to membrane bilayer curvature. Nature *426*, 563–566.

Bishop, W.R., and Bell, R.M. (1985). Assembly of the endoplasmic reticulum phospholipid bilayer: the phosphatidylcholine transporter. Cell *42*, 51–60.

Brasaemle, D.L. (2007). Thematic review series: adipocyte biology. The perilipin family of structural lipid droplet proteins: stabilization of lipid droplets and control of lipolysis. J. Lipid Res. *48*, 2547–2559.

Carman, G.M., and Henry, S.A. (1989). Phospholipid biosynthesis in yeast. Annu. Rev. Biochem. *58*, 635–669.

Chen, X., and Goodman, J.M. (2017). The collaborative work of droplet assembly. Biochim. Biophys. Acta Mol. Cell Biol. Lipids *1862*, 1205–1211.

Chorlay, A., and Thiam, A.R. (2018). An asymmetry in monolayer tension regulates lipid droplet budding direction. Biophys. J. *114*, 631–640.

Choudhary, V., Golani, G., Joshi, A.S., Cottier, S., Schneiter, R., Prinz, W.A., and Kozlov, M.M. (2018). Architecture of lipid droplets in endoplasmic reticulum is determined by phospholipid intrinsic curvature. Curr. Biol. *28*, 915–926.e9.

Choudhary, V., Ojha, N., Golden, A., and Prinz, W.A. (2015). A conserved family of proteins facilitates nascent lipid droplet budding from the ER. J. Cell Biol. *211*, 261–271.

Cole, N.B., Murphy, D.D., Grider, T., Rueter, S., Brasaemle, D., and Nussbaum, R.L. (2002). Lipid droplet binding and oligomerization properties of the Parkinson's disease protein alpha-synuclein. J. Biol. Chem. *277*, 6344–6352.

Copic, A., Antoine-Bally, S., Gimenez-Andres, M., La Torre Garay, C., Antonny, B., Manni, M., Pagnotta, S., Guihot, J., and Jackson, C. (2018). A giant amphipathic helix from a perilipin that is adapted for coating lipid droplets. Nature Communications *9*, https://doi.org/10.1038/s41467-018-03717-8.

Deslandes, F., Thiam, A.R., and Forêt, L. (2017). Lipid droplets can spontaneously bud off from a symmetric bilayer. Biophys. J. *113*, 15–18.

Dowd, S.R., Bier, M.E., and Patton-Vogt, J.L. (2001). Turnover of phosphatidylcholine in Saccharomyces cerevisiae. J. Biol. Chem. *276*, 3756–3763.

Farge, E., and Devaux, P.F. (1992). Shape changes of giant liposomes induced by an asymmetric transmembrane distribution of phospholipids. Biophys. J. *61*, 347–357.

Fujimoto, T., and Parton, R.G. (2011). Not just fat: the structure and function of the lipid droplet. Cold Spring Harb. Perspect. Biol. *3*, a004838.

Gaspar, M.L., Aregullin, M.A., Jesch, S.A., and Henry, S.A. (2006). Inositol induces a profound alteration in the pattern and rate of synthesis and turnover of membrane lipids in Saccharomyces cerevisiae. J. Biol. Chem. *281*, 22773–22785.

Griesbauer, J., Wixforth, A., and Schneider, M.F. (2009). Wave propagation in lipid monolayers. Biophys. J. *97*, 2710–2716.

Grillitsch, K., Connerth, M., Köfeler, H., Arrey, T.N., Rietschel, B., Wagner, B., Karas, M., and Daum, G. (2011). Lipid particles/droplets of the yeast Saccharomyces cerevisiae revisited: lipidome meets proteome. Biochim. Biophys. Acta *1811*, 1165–1176.

Grippa, A., Buxó, L., Mora, G., Funaya, C., Idrissi, F.Z., Mancuso, F., Gomez, R., Muntanyà, J., Sabidó, E., and Carvalho, P. (2015). The seipin complex Fld1/Ldb16 stabilizes ER-lipid droplet contact sites. J. Cell Biol. *211*, 829–844.

Guo, Y., Walther, T.C., Rao, M., Stuurman, N., Goshima, G., Terayama, K., Wong, J.S., Vale, R.D., Walter, P., and Farese, R.V. (2008). Functional genomic screen reveals genes involved in lipid-droplet formation and utilization. Nature *453*, 657–661.

Hayes, M.J., Choudhary, V., Ojha, N., Shin, J.J., Han, G.S., Carman, G.M., Loewen, C.J., Prinz, W.A., and Levine, T.P. (2017). Fat storage-inducing transmembrane (FIT or FITM) proteins are related to lipid phosphatase/phosphotransferase enzymes. Microb. Cell *5*, 88–103.

Henne, W.M., Reese, M.L., and Goodman, J.M. (2018). The assembly of lipid droplets and their roles in challenged cells. EMBO J. *37*.

Higgins, J.A., and Dawson, R.M.C. (1977). Asymmetry of the phospholipid bilayer of rat liver endoplasmic reticulum. Biochim. Biophys. Acta *470*, 342–356.

Huang, C.Y., and Huang, A.H.C. (2017). Unique motifs and length of hairpin in oleosin target the cytosolic side of endoplasmic reticulum and budding lipid droplet. Plant Physiol. *174*, 2248–2260.

Jacquier, N., Choudhary, V., Mari, M., Toulmay, A., Reggiori, F., and Schneiter, R. (2011). Lipid droplets are functionally connected to the endoplasmic reticulum in Saccharomyces cerevisiae. J. Cell Sci. *124*, 2424–2437.

Jacquier, N., Mishra, S., Choudhary, V., and Schneiter, R. (2013). Expression of oleosin and perilipins in yeast promotes formation of lipid droplets from the endoplasmic reticulum. J. Cell Sci. *126*, 5198–5209.

Kassan, A., Herms, A., Fernández-Vidal, A., Bosch, M., Schieber, N.L., Reddy, B.J., Fajardo, A., Gelabert-Baldrich, M., Tebar, F., Enrich, C., et al. (2013). Acyl-CoA synthetase 3 promotes lipid droplet biogenesis in ER microdomains. J. Cell Biol. *203*, 985–1001.

Khandelia, H., Duelund, L., Pakkanen, K.I., and Ipsen, J.H. (2010). Triglyceride blisters in lipid bilayers: implications for lipid droplet biogenesis and the mobile lipid signal in cancer cell membranes. PLoS One *5*, e12811.

Krahmer, N., Guo, Y., Wilfling, F., Hilger, M., Lingrell, S., Heger, K., Newman, H.W., Schmidt-Supprian, M., Vance, D.E., Mann, M., et al. (2011). Phosphatidylcholine synthesis for lipid droplet expansion is mediated by localized activation of CTP:phosphocholine cytidylyltransferase. Cell Metab. *14*, 504–515.

Lagace, T.A., and Ridgway, N.D. (2013). The role of phospholipids in the biological activity and structure of the endoplasmic reticulum. Biochim. Biophys. Acta *1833*, 2499–2510.

Laouini, A., Jaafar-Maalej, C., Limayem-Blouza, I., Sfar, S., Charcosset, C., and Fessi, H. (2012). Preparation, characterization and applications of liposomes: state of the art. J. Colloid Sci. Biotechnol. *1*, 147–168.

Londos, C., Brasaemle, D.L., Gruia-Gray, J., Servetnick, D.A., Schultz, C.J., Levin, D.M., and Kimmel, A.R. (1995). Perilipin: unique proteins associated with intracellular neutral lipid droplets in adipocytes and steroidogenic cells. Biochem. Soc. Trans. *23*, 611–615.

Martin, S., and Parton, R.G. (2006). Lipid droplets: a unified view of a dynamic organelle. Nat. Rev. Mol. Cell Biol. *7*, 373–378.

Mishra, S., Khaddaj, R., Cottier, S., Stradalova, V., Jacob, C., and Schneiter, R. (2016). Mature lipid droplets are accessible to ER luminal proteins. J. Cell Sci. *129*, 3803–3815.

Murphy, D.J., and Vance, J. (1999). Mechanisms of lipid-body formation. Trends Biochem. Sci. *24*, 109–115.

Nakano, M., Fukuda, M., Kudo, T., Matsuzaki, N., Azuma, T., Sekine, K., Endo, H., and Handa, T. (2009). Flip-flop of phospholipids in vesicles: kinetic analysis with time-resolved small-angle neutron scattering. J. Phys. Chem. B *113*, 6745–6748.

Ohsaki, Y., Cheng, J., Suzuki, M., Fujita, A., and Fujimoto, T. (2008). Lipid droplets are arrested in the ER membrane by tight binding of lipidated apolipoprotein B-100. J. Cell Sci. *121*, 2415–2422.

Ohsaki, Y., Cheng, J., Suzuki, M., Shinohara, Y., Fujita, A., and Fujimoto, T. (2009). Biogenesis of cytoplasmic lipid droplets: from the lipid ester globule in the membrane to the visible structure. Biochim. Biophys. Acta *1791*, 399–407.

Olzmann, J.A., and Carvalho, P. (2019). Dynamics and functions of lipid droplets. Nat. Rev. Mol. Cell Biol. *20*, 137–155.

Ostermeyer, A.G., Paci, J.M., Zeng, Y., Lublin, D.M., Munro, S., and Brown, D.A. (2001). Accumulation of caveolin in the endoplasmic reticulum redirects the protein to lipid storage droplets. J. Cell Biol. *152*, 1071–1078.

Pol, A., Gross, S.P., and Parton, R.G. (2014). Review: biogenesis of the multifunctional lipid droplet: lipids, proteins, and sites. J. Cell Biol. *204*, 635–646.

Pomorski, T., and Menon, A.K. (2006). Lipid flippases and their biological functions. Cell. Mol. Life Sci. *63*, 2908–2921.

Pomorski, T.G., and Menon, A.K. (2016). Lipid somersaults: uncovering the mechanisms of protein-mediated lipid flipping. Prog. Lipid Res. *64*, 69–84.

Prévost, C., Sharp, M.E., Kory, N., Lin, Q., Voth, G.A., Farese, R.V., and Walther, T.C. (2018). Mechanism and determinants of amphipathic helix-containing protein targeting to lipid droplets. Dev. Cell *44*, 73–86.e4.

Rajan, A., and Perrimon, N. (2012). Drosophila cytokine unpaired 2 regulates physiological homeostasis by remotely controlling insulin secretion. Cell. *151*, 123–137.

Rowe, E.R., Mimmack, M.L., Barbosa, A.D., Haider, A., Isaac, I., Ouberai, M.M., Thiam, A.R., Patel, S., Saudek, V., Siniossoglou, S., et al. (2016). Conserved amphipathic helices mediate lipid droplet targeting of perilipins 1-3. J. Biol. Chem. *291*, 6664–6678.

Salo, V.T., Belevich, I., Li, S., Karhinen, L., Vihinen, H., Vigouroux, C., Magré, J., Thiele, C., Hölttä-Vuori, M., Jokitalo, E., and Ikonen, E. (2016). Seipin regulates ER-lipid droplet contacts and cargo delivery. EMBO J. *35*, 2699–2716.

Schwarz, D.S., and Blower, M.D. (2016). The endoplasmic reticulum: structure, function and response to cellular signaling. Cell. Mol. Life Sci. *73*, 79–94.

Segrest, J.P., Jones, M.K., Catte, A., Manchekar, M., Datta, G., Zhang, L., Zhang, R., Li, L., Patterson, J.C., Palgunachari, M.N., et al. (2015). Surface density-induced pleating of a lipid monolayer drives nascent high-density lipoprotein assembly. Structure *23*, 1214–1226.

Sui, X., Arlt, H., Brock, K.P., Lai, Z.W., Dimaio, F., Marks, D.S., Liao, M., Farese, R.V., and Walther, T.C. (2018). Cryo-electron microscopy structure of the lipid droplet-formation protein seipin. J. Cell Biol. *217*, 4080–4091.

Thiam, A.R., Antonny, B., Wang, J., Delacotte, J., Wilfling, F., Walther, T.C., Beck, R., Rothman, J.E., and Pincet, F. (2013a). COPI buds 60-nm lipid droplets from reconstituted water-phospholipid-triacylglyceride interfaces, suggesting a tension clamp function. Proc. Natl. Acad. Sci. USA *110*, 13244–13249.

Thiam, A.R., and Beller, M. (2017). The why, when and how of lipid droplet diversity. J. Cell Sci. *130*, 315–324.

Thiam, A.R., Farese, R.V., Jr., and Walther, T.C. (2013b). The biophysics and cell biology of lipid droplets. Nat. Rev. Mol. Cell Biol. *14*, 775–786.

Thiam, A.R., and Forêt, L. (2016). The physics of lipid droplet nucleation, growth and budding. Biochim. Biophys. Acta *1861*, 715–722.

Thiam, A.R., and Pincet, F. (2015). The energy of COPI for budding membranes. PLOS ONE *10*, e0133757.

Tieleman, D.P., and Marrink, S.J. (2006). Lipids out of equilibrium: energetics of desorption and pore mediated flip-flop. J. Am. Chem. Soc. *128*, 12462–12467.

Van Meer, G., Voelker, D.R., and Feigenson, G.W. (2008). Membrane lipids: where they are and how they behave. Nat. Rev. Mol. Cell Biol. *9*, 112–124.

Vevea, J.D., Garcia, E.J., Chan, R.B., Zhou, B.W., Schultz, M., Di Paolo, G., Mccaffery, J.M., and Pon, L.A. (2015). Role for lipid droplet biogenesis and microlipophagy in adaptation to lipid imbalance in yeast. Dev. Cell *35*, 584–599.

Walker, A.K., Jacobs, R.L., Watts, J.L., Rottiers, V., Jiang, K., Finnegan, D.M., Shioda, T., Hansen, M., Yang, F., Niebergall, L.J., et al. (2011). A conserved SREBP-1/phosphatidylcholine feedback circuit regulates lipogenesis in metazoans. Cell *147*, 840–852.

Wang, H., Becuwe, M., Housden, B.E., Chitraju, C., Porras, A.J., Graham, M.M., Liu, X.N., Thiam, A.R., Savage, D.B., Agarwal, A.K., et al. (2016). Seipin is required for converting nascent to mature lipid droplets. Elife *5*, e16582.

Wang, S., Idrissi, F.Z., Hermansson, M., Grippa, A., Ejsing, C.S., and Carvalho, P. (2018). Seipin and the membrane-shaping protein Pex30 cooperate in organelle budding from the endoplasmic reticulum. Nat. Commun. *9*, 2939.

Wei, D., Jacobs, S., Modla, S., Zhang, S., Young, C.L., Cirino, R., Caplan, J., and Czymmek, K. (2012). High-resolution three-dimensional reconstruction of a whole yeast cell using focused-ion beam scanning electron microscopy. BioTechniques *53*, 41–48.

Welte, M.A. (2015). Expanding roles for lipid droplets. Curr. Biol. *25*, R470–R481.

West, M., Zurek, N., Hoenger, A., and Voeltz, G.K. (2011). A 3D analysis of yeast ER structure reveals how ER domains are organized by membrane curvature. J. Cell Biol. *193*, 333–346.

Wilfling, F., Thiam, A.R., Olarte, M.-J., Wang, J., Beck, R., Gould, T.J., Allgeyer, E.S., Pincet, F., Bewersdorf, J., and Farese, R.V. (2014). Arf1/COPI machinery acts directly on lipid droplets and enables their connection to the ER for protein targeting. Elife *3*, e01607.

Wilfling, F., Wang, H., Haas, J.T., Krahmer, N., Gould, T.J., Uchida, A., Cheng, J.X., Graham, M., Christiano, R., Fröhlich, F., et al. (2013). Triacylglycerol synthesis enzymes mediate lipid droplet growth by relocalizing from the ER to lipid droplets. Dev. Cell *24*, 384–399.

Yan, R., Qian, H., Lukmantara, I., Gao, M., Du, X., Yan, N., and Yang, H. (2018). Human seipin binds anionic phospholipids. Dev. Cell *47*, 248–256.e4.

Zanghellini, J., Wodlei, F., and von Grünberg, H.H. (2010). Phospholipid demixing and the birth of a lipid droplet. J. Theor. Biol. *264*, 952–961.

Zimmerberg, J., and Kozlov, M.M. (2006). How proteins produce cellular membrane curvature. Nat. Rev. Mol. Cell Biol. *7*, 9–19.

Please cite this article in press as: Chorlay et al., Membrane Asymmetry Imposes Directionality on Lipid Droplet Emergence from the ER, Developmental Cell (2019), https://doi.org/10.1016/j.devcel.2019.05.003

STAR★METHODS

KEY RESOURCES TABLE

REAGENT or RESOURCE	SOURCE	IDENTIFIER
Chemicals, Peptides, and Recombinant Proteins		
Phospholipids (DOPC, Rhodamine-DOPE, LysoPC (18:1))	Avanti Polar Lipids	https://avantilipids.com/
Triolein	Sigma Aldrich	T7140
Bovine Serum Albumin (BSA)	Sigma Aldrich	A7906-100G
Dithionite	Sigma Aldrich	71699-250G
Apolipoprotein B from human plasma	Sigma Aldrich	SRP6302
Plin1 108-137, Purity 96.83% (NBD-PPEKIASELKDTISTRLRSARNSISVPIAS)	ProteoGenix, France	https://www.proteogenix.science/
CAV fragment 159-178, Purity 96.83% (NBD-LFEAVGKIFSNVRINLQKEI)	Peptide 2.0, USA	https://www.peptide2.com/
Alpha-Synuclein	Bruno Antonny's lab, IPMC CNRS	N/A
Plin1 fragment 93-192	Pr. David Savage (Cambridge Metabolic Research Laboratories, UK).	N/A
Fluorescently labeled Arf1	This study, see Method Details	N/A
Monodansyl pentane (MDH)	Abgent	SM1000a
Oleic acid	Sigma Aldrich	O1008-1G
Inositol	Sigma	I5125-50G
Yeast nitrogen base with ammonium sulfate	MP Biomedicals	4027-522
Yeast nitrogen base with ammonium sulfate, without inositol	MP Biomedicals	4027-412
CSM-HIS-LEU-TRP-URA	MP Biomedicals	4550-022
Bacto yeast extract	BD	212750
Bactopeptone	BD	211677-500G
Fluorescently labeled C12 fatty acid	Thermo Fisher / Molecular Probes	D3835
Fatty acid free Bovine Serum Albumin (BSA)	Sigma Aldrich	A8806
Oleic acid	Calbiochem	4954
Experimental Models: Cell Lines		
S. cerevisiae: (BY4741) *MATa ura3Δ0his3Δ1leu2Δ0met15Δ0* SEC63-mNeonGreen-HIS	This paper	yPC10613
S. cerevisiae: (BY4741) *MATa ura3Δ0his3Δ1leu2Δ0met15Δ0pct1::KAN* SEC63-mNeonGreen-HIS	This paper	yPC10672
Human hepatocytes Huh7.5	Apath Missouri	APC 49
Drosophila Kc167	Harvard RNAi screening center	https://fgr.hms.harvard.edu
Oligonucleotides		
CCT1_RNAi_fwd: gtaatacgactcactataggATCGGAAGTTCAGGATCAGC	Harvard RNAi Screening Center	DRSC08157
CCT1_RNAi_rev: gtaatacgactcactataggCCCGCTGAAGAATTGCTG	Harvard RNAi Screening Center	DRSC08157
CCT1_RNAi_fwd: gtaatacgactcactataggGATGGCCACCTCATCGATAC	Harvard RNAi Screening Center	DRSC27869
CCT1_RNAi_rev: gtaatacgactcactataggCTTTGTGAGATGGTGCGTGT	Harvard RNAi Screening Center	DRSC27869
rp49_fwd: ATCGGTTACGGATCGAACAA	(Rajan et al., 2012)	N/A
rp49_rev: GACAATCTCCTTGCGCTTCT	(Rajan et al., 2012)	N/A

(*Continued on next page*)

Continued

REAGENT or RESOURCE	SOURCE	IDENTIFIER
CCT1_qPCR_fwd: GGAAGCGGACCTACGAGATA	(Copic et al., 2018)	N/A
CCT1_qPCR_rev: GTGCCCTGATCCTGAACTT	(Copic et al., 2018)	N/A
Recombinant DNA		
pA-GFP-W-sec61ß	Tobias Walther's laboratory, Harvard Medical School	N/A
Software and Algorithms		
Matlab R2016a	Licence of the École Normale Supérieure	https://fr.mathworks.com
Fiji	Online	https://imagej.net/Fiji
Adobe illustrator CS4	Licence of the École Normale Supérieure	N/A
GraphPad Prism 7.0a	Licence of the École Normale Supérieure	https://graphpad.com/scientific-software/prism/
GROMACS v5.1.4	Online	http://www.gromacs.org/

CONTACT FOR REAGENT AND RESOURCE SHARING

Further information and requests for reagents may be directed to and will be fulfilled by the Lead Contact, Abdou Rachid Thiam (thiam@ens.fr).

EXPERIMENTAL MODEL AND SUBJECT DETAILS

Yeast Strain and Culture Media Conditions

Saccharomyces cerevisiae cell strains used in the experiments are yPC10613 (*MATa ura3Δ0his3Δ1leu2Δ0met15Δ0* SEC63-mNeonGreen-HIS) and yPC10672 (*MATa ura3Δ0his3Δ1leu2Δ0met15Δ0pct1::KAN* SEC63-mNeonGreen-HIS). Cells were grown at 30°C in YPD liquid medium (1% yeast extract, 2% peptone, 2% glucose).

Huh7.5 Culture and Media Conditions

Huh7.5 were maintained in Dulbecco's modified Eagle's medium (DMEM) supplemented with 10% heat inactivated fetal bovine serum (Life Technologies), 0.1 gL-1 sodium pyruvate (Life Technologies) and 1% penicillin-streptomycin (Life Technologies). The cells were cultured at 37°C under a 5% CO2 atmosphere.

Drosophila Kc167 Culture Media Conditions

Drosophila Kc167 cells were grown in Schneider's Drosophila medium with L-Glutamine including 10% heat inactivated fetal calf serum (medium and serum from PAN Biotech, Aidenbach, Germany) with Penicillin/Streptomycin.

METHOD DETAILS

DEV Preparation: GUVs + LDs

Unless mentioned, *in vitro* experiments were performed in the following HKM buffer: 50 mM Hepes, 120 mM Kacetate, and 1 mM MgCl2 (in Milli-Q water) at pH 7.4 and 275±15 mOsm.

All GUVs were 99.5 % DOPC 0.5% (w/w) Rhodamine-DOPE. GUVs were prepared by electro-formation (Thiam et al., 2013a). Phospholipids and mixtures thereof in chloroform at 0.5 μM were dried on an indium tin oxide (ITO) coated glass plate. The lipid film was desiccated for 1 h. The chamber was sealed with another ITO coated glass plate. The lipids were then rehydrated with a sucrose solution (275+-15 mOsm). Electro-formation is performed using 100 Hz AC voltage at 1.0 to 1.4 Vpp and maintained for at least 1 h. This low voltage was used to avoid hydrolysis of water and dissolution of the titanium ions on the glass plate. GUVs were either stored in the chamber at 4°C overnight or directly collected with a Pasteur pipette.

To prepare the artificial lipid droplets (aLDs), 5 μL of the oil was added to 45 μL of HKM buffer. The mixture was sonicated. The diameter of the resulting droplets is on the order of a few hundred nanometers. To make DEV, GUVs were then incubated with the LDs for 5 min. The GUV-LD mixture was then placed on a glass coverslip pretreated with 10 % (w/w) BSA and washed three times with buffer.

Determination of the Degree of LD Emergence in the DEV Experimental System

We characterized the degree of emergence of the aLD from the bilayer by comparing the inner and outer surface areas of the droplets (Figure 1C). This was assessed by considering the inner and outer surfaces of the LD as spherical caps. All micrographs of *in vitro* systems were made on a Carl ZEISS LSM 800. Glass coverslips: Menzel Glaser (24x36mm #0).

Determination of the Coverage Asymmetry

The asymmetry in the monolayer coverage, is directly related to the surface tension asymmetry which is reflected by the angles formed by the droplet with the bilayer (α and θ, see Figure 1C). More precisely we defined "coverage asymmetry" parameter as $(\alpha - \theta)/180$.

If the two LD monolayers present the same coverage, i.e. the same surface tension, α and θ are equal, and "coverage asymmetry" parameter is 0. When the external coverage is increased, i.e. external surface tension decreases, α increases, and θ diminishes (Chorlay and Thiam, 2018, STAR Methods: Determination of the shape and position of an LD in a GUV bilayer). This results in an increasing of the "coverage asymmetry" parameter. In the limit of a drastic improvement of the external monolayer coverage, provoking a full emergence of the LD, θ is equal to zero, α to 180 degrees and the "coverage asymmetry" parameter is equal to 1. O the opposite configuration, i.e. strong improvement of the external monolayer coverage, If the LD would emerge in the opposite direction, and the "coverage asymmetry" parameter would the be -1.

Determination of the Shape and Position of an LD in a GUV Bilayer

(adapted from Chorlay and Thiam Biophysical Journal 2018)

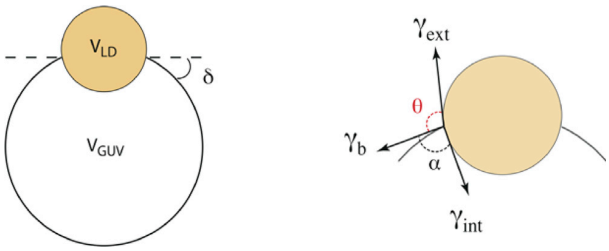

Considering that the aLD's shape is driven by the equilibrium of the three surface tensions (bilayer γ_b, external monolayer γ_{ext} and internal monolayer γ_{int}) (Equation 1), can be projected on the bilayer axis and lead to (Equation 2).

$$\overrightarrow{\gamma_b} + \overrightarrow{\gamma_{int}} + \overrightarrow{\gamma_{ext}} = \overrightarrow{0} \quad \text{(Equation 1)}$$

$$\gamma_b = -\gamma_{int}\cos(\alpha) - \gamma_{ext}\cos(\theta) \quad \text{(Equation 2)}$$

$$\gamma_{ext}\sin(\theta) = \gamma_{int}\sin(\alpha)$$

Moreover, the conserved volume of the LD and the GUV gives two other equations (Equations 3 and 4):

$$V_{LD} = \frac{4\,\Pi Ro^3}{3}\left(\frac{2-\cos(\theta-\delta)^3+3\cos(\theta-\delta)}{\sin(\theta-\delta)^3}+\frac{2-\cos(\alpha-\delta)^3+3\cos(\alpha-\delta)}{\sin(\alpha-\delta)^3}\right) \quad \text{(Equation 3)}$$

$$V_{GUV} = \frac{4\,\Pi Ro^3}{3}\left(\frac{2-\cos(\delta)^3+3\cos(\delta)}{\sin(\delta)^3}-\frac{2-\cos(\alpha-\delta)^3+3\cos(\alpha-\delta)}{\sin(\alpha-\delta)^3}\right) \quad \text{(Equation 4)}$$

In order to determine the shape of the droplet, we only need three parameters: alpha, theta and delta, as a function of the tensions γ_b, γ_{int} and γ_{ext}.

Rearranging these equations leads to a set of 3 equations (Equations 5, 6, and 7) that can be solved numerically.

The following equations (Equations 5 and 6) Gives alpha and theta:

$$\cos(\theta) = \frac{\gamma_{int}^2 - \gamma_{ext}^2 - \gamma_b^2}{2\,\gamma_b\,\gamma_{ext}} \quad \text{(Equation 5)}$$

$$\cos(\alpha) = \frac{\gamma_{ext}^2 - \gamma_{int}^2 - \gamma_b^2}{2\,\gamma_b\,\gamma_{int}} \quad \text{(Equation 6)}$$

The last parameter delta is determined numerically, keeping the volumes constant (Equation 7):

$$\frac{V_{LD}}{V_{GUV}} = \frac{\frac{2-\cos(\theta-\delta)^3+3\cos(\theta-\delta)}{\sin(\theta-\delta)^3} + \frac{2-\cos(\alpha-\delta)^3+3\cos(\alpha-\delta)}{\sin(\alpha-\delta)^3}}{\frac{2-\cos(\delta)^3+3\cos(\delta)}{\sin(\delta)^3} - \frac{2-\cos(\alpha-\delta)^3+3\cos(\alpha-\delta)}{\sin(\alpha-\delta)^3}} \quad \text{(Equation 7)}$$

The simulation displayed in Figures 2I and 2J are obtain using this mathematical model and varying the Vld/Vguv parameter.

Proteins Production and Purification

Cytosol extract was obtained from hepatocyte Huh7.5 cells: confluent monolayers of Huh7.5 cells were placed on ice, washed twice with ice-cold PBS at pH 7.4, and then incubated with 10 mM Tris/HCl, pH 7.4 buffer for 5 minutes on ice. The cells were scraped into a homogenization buffer comprising 10 mM Tris/HCl, 1 mM EGTA, 0.5 mM EDTA and 0.25 M sucrose, pH 7.4, which also contained Complete TM protease inhibitors. The cells were homogenized by twenty in/out passages within a syringe fin needle. The homogenate was transferred to ultracentrifugation tube (2 ml) and were centrifuged for 1 h at 100 000 G at 4°C. The resulting supernatant was used as a cytosol extract.

Fluorescently labeled Arf1 was generated using an Arf1-variant in which the single cysteine residue of Arf1 was replaced with serine, and the C-terminal lysine was replaced with cysteine, yielding Arf1- C159S-K181C. Published work has demonstrated that exchanging the C-terminal lysine of the small GTPase with a Cys- residue, and subsequent fluorescent labeling (using thiol-reactive dyes on Cys181), does not inhibit Arf1-function (Beck et al., 2008). In short, human Arf1- C159S-K181C and yeast N-myristoyltransferase were coexpressed in Escherichia coli supplied with BSA-loaded myristate. Cell lysates were subjected to 35% ammonium sulfate, and the precipitate, enriched in myristoylated Arf1, was further purified by DEAE-ion exchange. Eluted fractions of interest were concentrated in spin-column filters with a 10-kD cutoff (Millipore), and fluorescently labeled using Cy3-maleimide (GE Healtcare) according to the manufacturer's protocol. To remove excess dye, samples were purified by gel filtration using a Superdex 75 column (GE Healthcare).

Protein Enrichment of the DEV External Leaflet

A DEV hold by a glass micropipette is observed by confocal microscopy. 5 μL of protein solution is injected in the 100 μL bulk phase of the DEV solution. The resulting effective concentrations were respectively: Arf1 (1μM); CAV159-178 (5μM); Alpha-Synuclein (5.5μM); ApolipoproteinB (0.1 μM); Plin1 fragment 93-192 (4.7μM); BSA (75μM); The DEV is then followed for ~ 40 min. Solutions were injected at similar spots from the pipette.

Micromanipulation & Surface Tension Measurements by Micro Aspiration

Micro-pipettes were made from capillaries drawn out with a Sutter Instruments pipette-puller. They were used to manipulate the LD-embedded GUVs in order to get a side view of the system. The pipettes were incubated for 30 min in a 5% bovine serum albumin solution (BSA) before use, in order to prevent droplets and membranes from adhering to the glass.

Additionally, surface tensions were measured and modulated using the same pipettes. As shown in (Figure 1I), the micromanipulation of the external LD monolayer enables the measurement of the eternal monolayer surface tension. Using Laplace's law, and the measurement of the pipette inner diameter, droplet diameter, and suction pressure, the surface tension of the interface can be determined:

$$\gamma = \frac{\Delta Psuc}{2\left(\frac{1}{Rp} - \frac{1}{Rd}\right)},$$

where ΔPsuc, Rp and Rd are the suction pressure, the pipette radius and the droplet external radius.

The suction was carried out using a syringe. The resulting pressure was measured with a pressure transducer (DP103 provided by Validyne Eng. Corp, USA), the output voltage of which was monitored with a digital voltmeter. The pressure transducer (range 55 kPa) was calibrated prior to the experiments. Micro-pipettes made from capillaries (1.0oDx0.58iDx150Lmm 30-0017 GC100-15b Harvard Apparatus) with micropipette puller (Sutter instrument model P-2000). Micromanipulation (Eppendorf TransferMan® 4r). Pressure measurement unit (DP103 provided by Validyne eng. corp, USA).

Pendent Droplet Interfacial Tension Measurements

A pendent droplet tensiometer designed by Teclis Instruments (Longessaigne, France) was used to measure the interfacial tension of oil/water interfaces. All experiments were conducted at room temperature. To create triolein/buffer interfaces, triolein drops (from 5 to 16.0μL) were formed at the tip of a J-needle submerged in 5 mL of HKM buffer.

Triolein-Protein Surface Tension Measurement

5 μl of the solution containing the proteins is added to the bulk buffer while the tension of a triolein/buffer interface is measured. The resulting concentrations of proteins were: Alphaalpha-Synuclein (0.1μM); BSA (1.5μM); ApolipoproteinB (2nM); Plin1 108-137 (1μM);

Plin1 fragment 93-192 (0.09μM). When tension stabilizes, the interface is compressed. The tension at maximum coverage was determined when wrinkles appeared on the surface of the droplet. If no wrinkles were observed, the compression was stopped, the max packing tension was determined after waiting for the relaxation and re-stabilization of the tension.

Triolein-Phospholipid Surface Tension Measurement

To create phospholipid monolayers at the interface, phospholipids were dissolved in the triolein (0.01% w/w). After forming a droplet, the PLs relocate at the interface. The Droplet is then compressed until a tension plateau is reached. This plateau of tension is the tension corresponding to the maximum PL coverage, and evoked as the minimal tension reachable.

Lyso-PC Enrichment to the GUV External Leaflet

A micellar solution of lyso-PC (18:1) in HKM at 10x the CMC is prepared by desiccating the phospholipids dissolved in chloroform and rehydrating them in HKM buffer. In order to get a fluorescent signal, 1% (w/w) of NBD-PE is added to the lyso-PC. The resulting solution is then vortexed and sonicated for 5 min, three times. 5 to 20 μL of this micellar solution is then directly added to the 100 μL GUVs solution already placed under the microscope. This system is then observed with and without LDs embedded in the GUVs.

Molecular Dynamics (MD) Simulations

We built lipid bilayer systems consisting of dioleoylphosphatidylcholine (DOPC) containing triolein (TO) lenses starting from a homogeneous distribution of TO in a DOPC bilayer. All systems featured the same number of TO molecules (7500) and a variable number of DOPC lipids, starting from a symmetric system with 9072 DOPC molecules per monolayer and reducing progressively the number of DOPC molecules in one leaflet, in steps of 100 lipids, to reach a maximum imbalance of 1000 lipids (11% imbalance). For each system, we carried out molecular dynamics (MD) simulations of at least 2 μs, and used the final snapshot as a starting point to build the subsequent stage. The reference symmetric system (9072 lipids in each bilayer) was simulated for 30 μs, and the final system with 11% imbalance was simulated for 10 μs. All systems were simulated at the coarse-grained level, using the MARTINI force field (v2.0, lipid version 2015-06 except for triolein, optimized specifically for the present work).

All simulations were carried out with GROMACS v5.1.4, using a leap-frog stochastic dynamics integrator (sd option in GROMACS), with a time step of 20 fs. Non-bonded interactions were calculated with a cutoff of 1.1 nm, using a Verlet neighborlist scheme (Verlet buffer tolerance of 10^{-6} kJ mol^{-1} ps^{-1} per atom); electrostatic interactions were calculated with a dielectric constant of 15 and shifted from 0 nm, Lennard-Jones were shifted from 0.9 nm. All simulations were run at constant temperature (300 K) and pressure using semi-isotropic pressure coupling (Parrinello-Rahman barostat, time constant of 20 ps, 1 bar in xy and z dimensions), resulting in overall zero surface tension in the system.

Time Scale of LD Emergence and Phospholipid Flipping

In a bilayer containing a lipid droplet, any asymmetry in monolayer coverage is spontaneously absorbed (below a second) by the repositioning of the LD in the bilayer (i.e. its emergence). Indeed, micro-manipulation experiments showed that it is a mechanical equilibrium that is reached quicker than we can see ($\Delta t < 40$ms, from our imaging frame rate) (Chorlay and Thiam, 2018).

An asymmetry can be generating in ER by inserting phospholipids on the outer leaflet. This excess of phospholipids has thus to be detected by a LD for emerging. To assess the time scale of this event, let's consider a 1 m long ER and a speed of propagation of the lateral pressure (i.e. phospholipid density) on a monolayer of 1 m/s, despite it has been estimated around 100 m/s (Griesbauer et al., 2009). In this setting, a LD will sense a fabricated PL in few 10 ms. Consequently the increase of the lateral pressure induced by this new phospholipid will be instantaneously detected by the droplet, which will therefore emerge on this side of higher lateral pressure.

Based on these above points, the time frame to rectify a bilayer asymmetry by the re-positioning of a lipid droplet is in the tenth ms range. This time is much smaller than the flip-flop time of a phospholipid in a bilayer which is in the order of minutes as reported in vitro and in vivo (Pomorski and Menon, 2006), which could rectify the asymmetry.

Altogether, if an asymmetry is created between a bilayer leaflets, a lipid droplet will almost instantaneously expend toward the denser monolayer side and absorb the asymmetry. The more asymmetry created the more the droplet will bulge toward the monolayer with excess phospholipids. The flipping of phospholipids will not be fast enough to rectify the asymmetry between the leaflets.

Lipid Droplet Induction and Fluorescence Microscopy of Yeast Cells

Yeast cells grown as described in the EXPERIMENTAL MODEL AND SUBJECT DETAILS section. For LD induction, cells were grown to exponential growth phase, pelleted, and resuspended in YPD + 0.1% oleic acid (Sigma, #O1008) where indicated. In inositol supplementated experiments, cells were grown in synthetic media lacking inositol, in presence (0.1%) or absence of oleate. After 18h growth, cells were harvested by centrifugation and each culture was resuspended and diluted in the same media in presence of absence of 75μM of inositol.

Cells were imaged at 0h, 6h and 24h upon inositol addition. Similar timepoints were collected for lipid analysis. Fluorescence microscopy was performed at room temperature using the Zeiss Cell Observer HS equipped with a CMOS camera (Hamamatsu ORCA-Flash4.0), controlled by 3i Slidebook6.0 software. A Plan-APOCHROMAT 100x 1.4 objective was used. mNeonGreen and MDH signals were detected using the GFP and DAPI filters respectively, at 600ms exposure.

Electron Microscopy Experiments in Yeast Cells

Yeast cells grown as described above were subjected to high pressure freezing and processed as described in (Wang et al., 2018). Alternatively, 10 ODs of exponentially growing cells were subjected to chemical fixation in 1% glutaraldehyde, 0.2% PFA in 40mM potassium phosphate pH 7 for 12-16h at 4C. Fixed cells were further processed as described in (Choudhary et al., 2015). All grids were imaged in a FEI Tecnai 12 TEM operated at 120 kV using a Gatan OneView digital camera.

Thin Layer Chromatography and Lipid Detection

Lipids were extracted and separated on silica TLC plates (Merck) either in chloroform/methanol/acetone/acetic acid/water (100:20:40:20:10) for phospholipids or in petroleum ether/diethyl ether/acetic acid (90:10:1) for neutral lipids, and detected by iodine vapor staining. Bands were identified by comparison with standards. The quantification of the bands were done using Fiji.

dsRNAs Construction for Drosophila Experiments

dsRNAs targeting CCT1 were prepared according to standard procedures (e.g. Beller et al. PLoS 2008). In brief, we amplified targeting sequences pre-computed from the Drosophila RNAi screening center (www.flyrnai.org) from genomic DNA using oligonucleotides fused to a T7 RNA polymerase promotor (lower case in the oligonucleotide sequences). For CCT1 we used the oligonucleotides corresponding to DRSC08157: fwd: gtaatacgactcactataggATCGGAAGTTCAGGATCAGC, rev: gtaatacgactcactataggCCCGCTGA AGAATTGCTG, or DRSC27869: fwd: gtaatacgactcactataggGATGGCCACCTCATCGATAC, rev: gtaatacgactcactataggCTTTGT GAGATGGTGCGTGT

Following PCR amplification we performed an *in vitro* transcription reaction with the TranscriptAid T7 High Yield Transcription Kit (Thermo Fisher Scientific) or the HiScribe T7 High Yield RNA Synthesis Kit (New England Bioloabs) and purified the dsRNA molecules using the Qiagen RNeasy Mini Kit according to the manufacturer's instructions. The dsRNA was stored at -80°C until use.

Structured Illumination Microscopy of Drosophila Experiments

For the targeting experiment analyzed by structured illumination microscopy we seeded 1 mL of 2.5 x 10[5] cells/mL Drosophila Kc167 cells in wells of 12-well tissue culture plates (Sarstedt, Numbrecht, Germany). Cells were imaged using a Zeiss Elyra structured illumination microscope and a Plan-Apochromat 63x/1.4 oil objective with Z-stacks. Cells were grown in Schneider's Drosophila medium with L-Glutamine including 10% heat inactivated fetal calf serum (medium and serum from PAN Biotech, Aidenbach, Germany) with Penicillin/Streptomycin. Following a 6 to 8 hours recovery phase we transfected the cells with 500 ng of the GFP-tagged Sec61beta expression construct (expression is driven by an actin promotor; kind gift from Tobias Walther) and 500 ng of the respective dsRNA or a water only control using the Effectene transfection reagent from Qiagen (Hilden, Germany) according to the manufacturer's instructions. After three days the cells were serum starved overnight (serum free medium with 0.2% fatty acid free bovine serum albumin) to deplete the cells of already existing LDs. On the next day, the cells were resuspended and transferred to high precision cover slips and allowed to adhere for one hour. Subsequently, the medium was replaced with medium containing 600 μM oleic acid containing 1 μg/mL BODIPY558/568 labeled C12 fatty acids (Thermo/Molecular probes) and incubated for six hours. Subsequently the cells were fixed with 4% paraformaldehyde and embedded in Mowiol containing antifades.

qPCR Confirmation of CCT1 Knock-Down in Drosophila Experiments

We isolated RNA from the frozen cells using the rNeasy Mini Kit (Qiagen). qPCR was performed according to standard procedures with oligos for rp49 (fwd: ATCGGTTACGGATCGAACAA, rev: GACAATCTCCTTGCGCTTCT) and CCT1 (fwd: GGAAGCGGACCTAC GAGATA and rev: GTGCCCTGATCCTGAACTT).

Electron Microscopy Experiments of Drosophila Cells

We added 30 μg of dsRNA or water only as a control to 6-well plates. Subsequently, we added 1 mL of 2 x 10[5] cells/mL Drosophila Kc167 cells in serum free Schneider's Drosophila medium. After 45 min incubation, we added 3 mL of complete Schneider's medium and incubated for four days to allow for knock-down of the target by RNA interference. Subsequently, we added 600 μM OA to the cells and incubated for six hours. Cells from one well per sample were washed with PBS and frozen at -80°C to allow later RNA extraction for qPCR analysis. Cells from a second well of each sample were washed with 0.1 M phosphate buffer and afterwards fixed with 2.5 % glutaraldehyde in 0.1 M phosphate buffer for 30 min. After another wash with 0.1 M phosphate buffer and the cells were mixed with 3 % low melting agar in PBS. Agar was cut into small 1 mm square blocks, washed three times with 0.1 M sodium cacodylate buffer before incubation in 1 % osmium, 10 mg/mL potassium ferrocyanide in 0.1 M sodium cacodylate buffer, followed by three more washed in the cacodylate buffer and an ethanol dehydration series. After 100 % ethanol was added, there were two more washes with epon:ethanol (1:1) and epon:ethanol (3:1), respectively. Subsequently, the blocks were incubated with fresh epon at 4°C over night, and two more hours at room temperature, followed by curing at 60°C for 48 to 72 hours. Ultrathin sections (70 μm) were cut from the blocks using an ultramicrotome (Leica, UC7) and stained with 1.5% uranyl acetate for 20 min and Reynolds lead citrate solution for 3 min. Electron micrographs were recorded with a JEM-2100 Plus Transmission Electron Microscope (JEOL) operating at 80 kV with a Camera OneView 4k 32 bit (Gatan) and the software DigitalMicrograph (Gatan).

Modulation of GUVs Bilayer Tension Using Osmotic Pressure

GUV membranes are water-permeable, thus an osmolarity difference between the lumen and the exterior of the GUV results in a deflation or swelling of the GUV. This increases or decreases the bilayer tension. It is then possible to increase the bilayer tension osmotically with a hypotonic external buffer (e.g. adding MQ water to the HKM buffer surrounding the GUV; standard procedure is 10 μL of MQ water added to the 100 μL of HKM buffer). The bilayer tension can be decreased using a hypertonic external buffer (5 μL of 1M NaCl solution added to the 100 μL of HKM buffer).

Calculation of the Amount of Removed Phospholipids

When mechanically depleting the external leaflet of the GUV-LD system (see Figure 6E), we remove a portion of the PLs by ablating a part of the external monolayer. Assuming that the repartition of the PLs is homogenous on the leaflets, the number of PLs removed from the external leaflet is proportional to the ablated area of leaflet. Then the percentage of removed PLs can be calculated by: area of the removed tongue over total external leaflet area. The internal leaflet remains intact, so the number of PLs on this leaflet is constant.

QUANTIFICATION AND STATISTICAL ANALYSIS

Quantification Methods in Yeast

Aberrant ER: Yeast cells were enumerated according to their ER morphology using a Z projection of Z-stack images. If the cortical and nuclear ER were clearly defined, the cell was considered regular, if unusual ER membrane signals appeared in the cytoplasm, forming of lumps or threads, the cell was considered as aberrant.

Number of LD in Aberrant /Regular cells: Two sets of cells were selected according to the morphology of their ER (see above). Ambiguous cells were discarded. In these two populations the number of LD was quantified in approximately 40 cells in each subset.

LD in large contact with the ER: the proportion of cells presenting at least one event of LD presenting a close contact with ER (on half of its surface or more) was quantified over the total number of cell.

Quantification in Drosophila cells

LD in close contact with the ER: the number of LD surrounded or more than semi surrounded in the ER is quantified over the total number of LD in the cells.

LD size distribution: After preforming a Z projection with the Z-stack images of the LD and a thresholding, a Matlab program calculated the surface of the individual LDs. The statistics on the LD radius was maid (considering the LD as spherically shaped).

Statistical Analysis

The statistical comparisons where made using a non-parametric t-test (GraphPad Prism 7.0a; *** indicates $p < 0.0001$ ** indicates $p < 0,001$ * indicates $p < 0.01$). Unless mentioned, all values shown in the text and figures are mean ± S.D.

DATA AND SOFTWARE AVAILABILITY

All simulations were carried out with GROMACS v5.1.4.

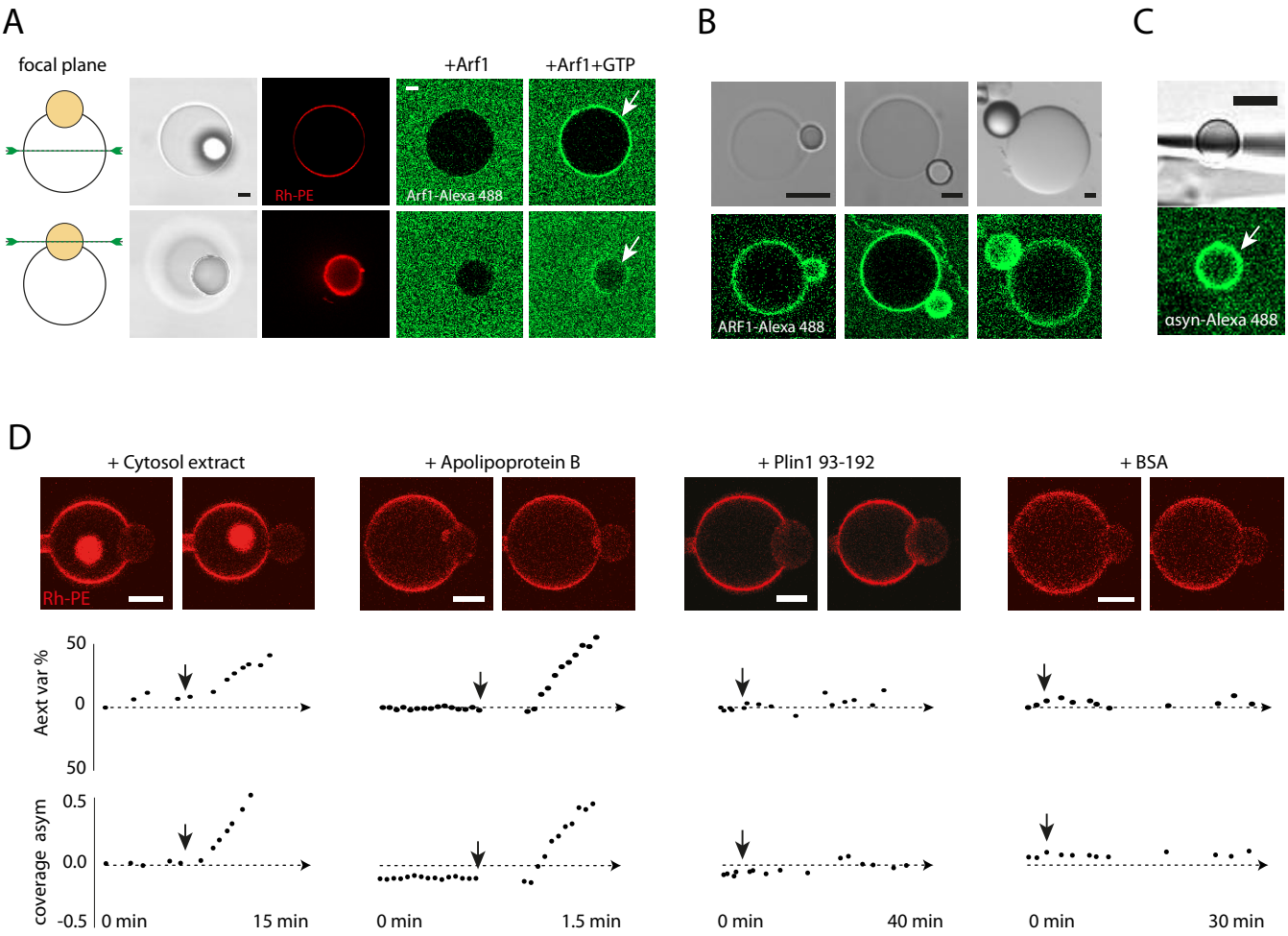

E

Protein fragment	Sequence
Cav 159-178	NBD-L**F**EAVGKI**F**SNVRINLQKEI
Plin1 108-137	NBD-PPEKIASELKDTISTRLRSARNSISVPIAS
Plin1 93-192	RGLDHLEEKIPALQ**Y**PPEKIASELKDTISTRLRSARNSISVPIASTSDKVLGAALAGCELA**W**GV ARDTAE**F**AANTRAGRLASGGADLALGSIEKVVE**Y**LL
α-Synuclein	Alexa488-MDV**F**MKGLSKAKEGVVAAAEKTKQGVAEAAGKTKEGVL**Y**VGSKTKEGVVHGVATVAEKTK EQVTNVGGAVVTGVTAVAQKTVEGAGSIAAATG**F**VKKDQLGKNEEGAPQEGILEDMPVDP DNEA**Y**EMPSEEG**Y**QD**Y**EPEA

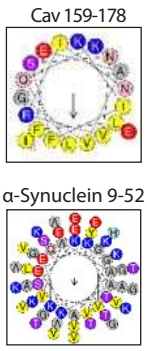

F

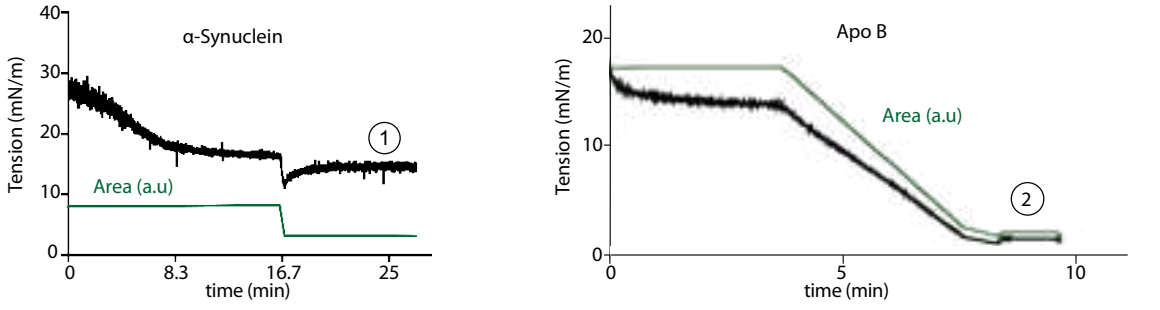

Supplementary Figure S1 | Membrane binding characteristics of the different proteins assessed for LD emergence capacity, related to Figure 1

A) PC DEV with a triolein droplet stained with Rhodamine-PE. Arf1-Alexa488 added to the external medium. Arf1 recruits on the bilayer and the droplet when GTP is added to the external medium. Arrows point to the GUV and droplet interface. Scale bars is 5 μm.

B) Side views of PC DEV with a triolein droplet after incubation with Arf1-Alexa488 + GTP for 20 min. Droplets emerged towards the exterior. Scale bars are 5 μm.

C) Bare triolein droplet after 20 min incubation with Alpha-Synuclein-Alexa488. Alpha-Synuclein-Alexa488 is recruited on the droplet surface. Scale bars is 5 μm.

D) Fluorescence Confocal images of condition displayed in Figure 1G. Red is phospholipids marked with Rhodamine-PE. Scale bars are 10 μm. For each of these conditions, artificial LD external area variation and coverage asymmetry are displayed over time. Arrows indicate proteins injection time.

E) Left: sequences of the proteins fragments used in the Figure 1 experiment; highly hydrophobic residues are highlighted in bold. Right: examples of helix wheels, Cav 159-178 fragment and Alpha-Synuclein 9-52 helix.

F) Droplet surface tension measurement by a droplet tensiometer method (see star methods). A Pure triolein droplet was formed in a buffer phase. Protein solutions were next added to the bulk buffer phase, which was agitated by using a magnetic bead (Left: Alpha-Synuclein; Right: Apolipoprotein B). After waiting for an equilibrium of tension, the droplet surface is decreased and then kept constant. Two different behavior are observed: 1- tension relaxes (Alpha-Synuclein), suggesting ejection of the protein by lateral compression; 2- tension stays constant (Apolipoprotein B), meaning that the protein is strongly bound to the interface; in the latter case the proteins formed a rigid coat that mechanically retained the interface (images not shown). Thus, binding of Apolipoprotein B can mechanically retain a nascent LD into the protein-containing region. Green curves are the droplet surface area (a.u.).

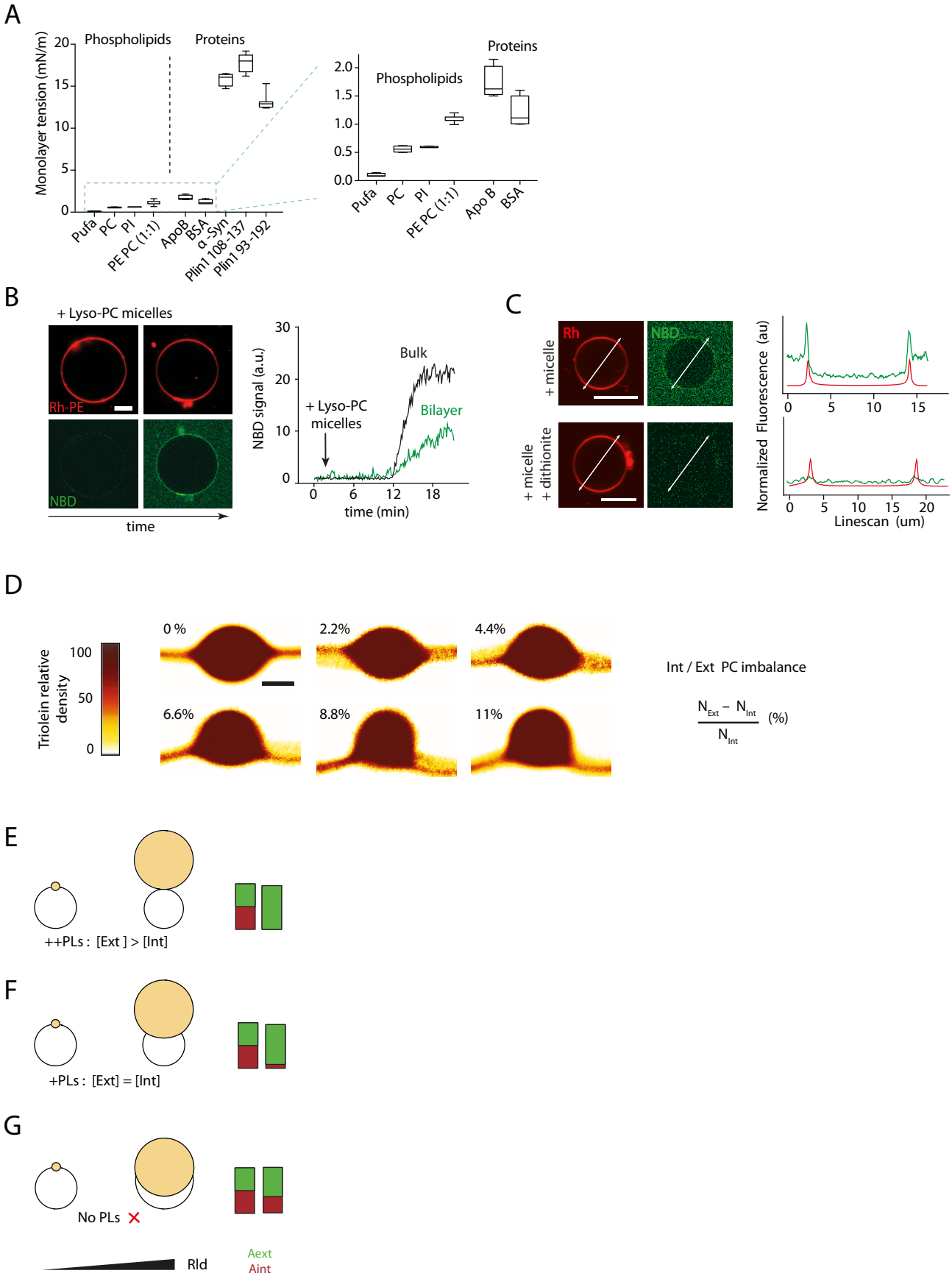
A
Monolayer tension (mN/m)
Phospholipids
Proteins
Pufa
PC
PI
PE PC (1:1)
ApoB
BSA
α-Syn
Plin1 108-137
Plin1 93-192
Apo B
B
+ Lyso-PC micelles
Rh-PE
NBD
time
NBD signal (a.u.)
Bulk
Bilayer
+ Lyso-PC micelles
time (min)
C
Rh
NBD
+ micelle
+ micelle + dithionite
Normalized Fluorescence (au)
Linescan (um)
D
Triolein relative density
0 %
2.2%
4.4%
6.6%
8.8%
11%
Int / Ext PC imbalance
(%)
E
++PLs : [Ext] > [Int]
F
+PLs : [Ext] = [Int]
G
No PLs
Rld
Aext
Aint

Supplementary Figure S2 | Maintaining an excess of phospholipids and proteins on one monolayer leaflet enables to decrease tension and favors LD full emergence, related to Figure 2

A) Minimal surface tensions of triolein/buffer interface covered by different phospholipids or proteins. These minimal monolayer surface tensions are measured at maximum monolayer packing or pressure, obtained by reducing the volume of the triolein-in-buffer drop (see for example in Figure S1F) (Pufa stands for C18:0 C22:4 polyunsaturated phosphatidylcholine).

B) NBD signal in bulk and on the surface of the GUV over time. After addition, the micellar solution diffuses to reach a GUV. The signal in the GUV vicinity increases which leads to rapid increase of the bilayer signal, meaning lyso-PC recruitment. Scale bar is 10 µm.

C) Linescans through GUVs corresponding to Figure 2B: GUV after Lyso-PC micelles treatment, GUV after Lyso-PC micelles treatment and Dithionite treatment. Red channel: rhodamine-PE marking the GUV membrane, green channel: NBD-PE marking the Lyso-PC micelles. The micelle treatment increases the NBD signal outside of the GUV and fluorescence is recruited on the bilayer. The dithionite treatment quenches all NBD fluorescence. Scale bars are 10 µm.

D) Average density distribution of triolein molecules embedded in the PC bilayer for 0%, 2.2%, 4.4%, 6.6%, 8.8%, 11% PC excess in external leaflet corresponding to Figure 2G,H . Colors heat map give an insight of the probability of triolein molecule presence. Scale bar is 15 nm.

E), Simulated profile showing the plausible behavior of a growing LD where exterior phospholipid coverage is increase during LD growth. This results in a full emergence of the LD.

F), Simulated profile showing the plausible behavior of a growing LD where phospholipids are added to maintain a constant coverage on both monolayers. The LD tends to emerge due to curvature effects. The LD remains always in contact with the interior.

G) Simulated profile showing the plausible behavior of a growing LD. Here no phospholipids are added during growth. Increasing the aLD radius (Rld) expands external monolayer (see Figure 2I,J). This results in a decrease of phospholipid coverage concomitant with an increase of external tension that prevents LD emergence.

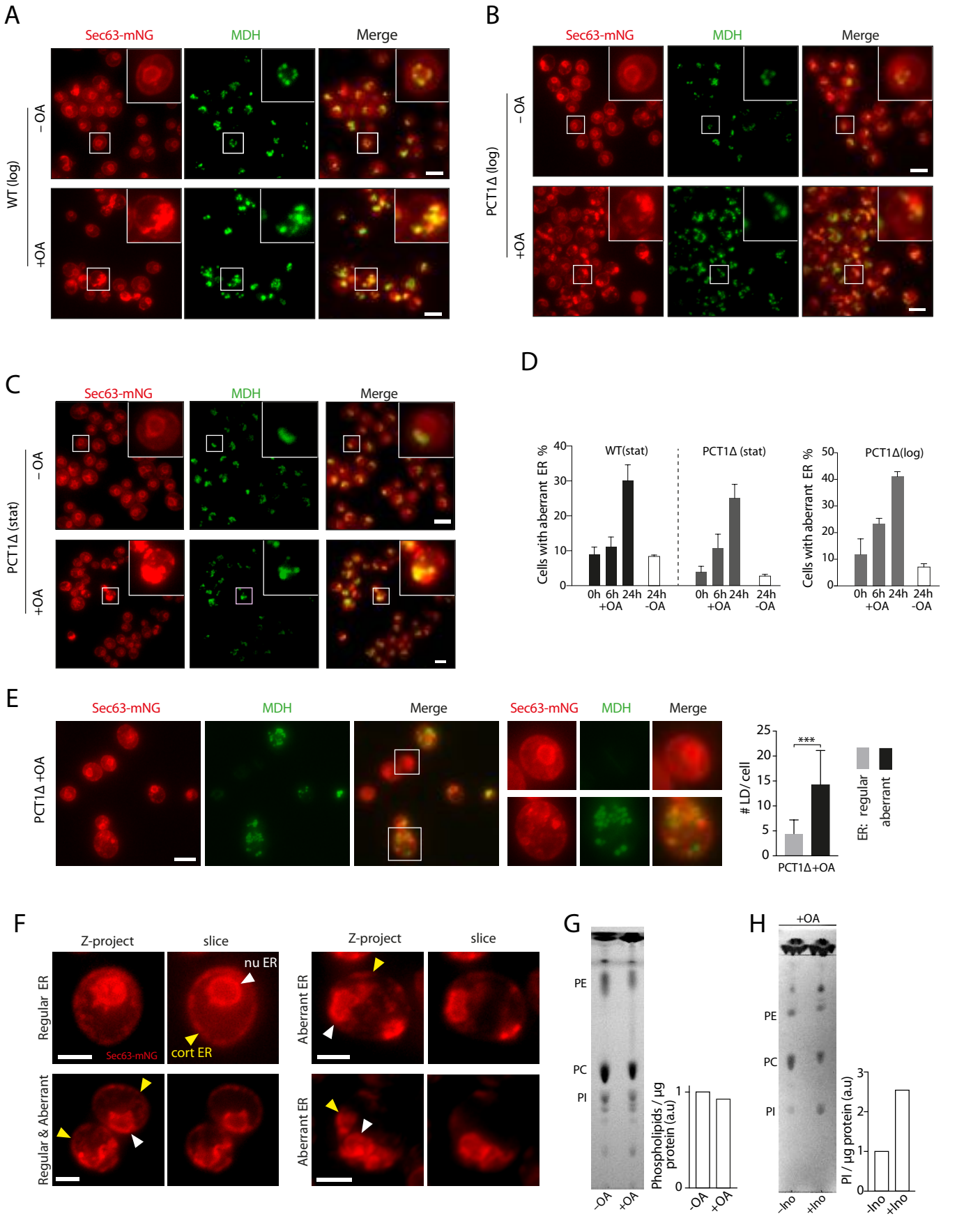
A
Sec63-mNG
MDH
Merge
WT (log)
– OA
+OA
B
PCT1Δ (log)
C
PCT1Δ (stat)
D
Cells with aberrant ER %
WT(stat)
PCT1Δ (stat)
PCT1Δ(log)
0h 6h 24h +OA
24h -OA
E
PCT1Δ +OA
LD/ cell
***
ER: regular aberrant
F
Z-project
slice
Regular ER
Aberrant ER
Regular & Aberrant
nu ER
cort ER
Sec63-mNG
G
PE
PC
PI
Phospholipids / µg protein (a.u)
-OA
+OA
H
+OA
PI / µg protein (a.u)
-Ino
+Ino

Supplementary Figure S3 | Excess LD formation in *Saccharomyces cerevisiae* cells under logarithmic or exponential phases is associated with ER remodeling, related to Figure 3

A) *Saccharomyces cerevisiae* cells cultured in the presence or not of OA (Oleate) from logarithmic growth phase are imaged at 24 h. The ER marker protein, Sec63, was endogenously tagged with monomeric NeonGreen (Sec63-mNG), and LDs were labeled by monodansylpentane (MDH). Images shown represent z-projection of different planes. Scale bars, 5 μm.

B) PCT1-depleted (*pct1*Δ) *Saccharomyces cerevisiae* cells cultured in the presence or not of OA to logarithmic growth phase are imaged at 24 h. The ER marker protein, Sec63, was endogenously tagged with monomeric NeonGreen (Sec63-mNG), and LDs were labeled by the neutral lipid dye, MDH. Images shown represent z-projection of different planes. Scale bars, 5 μm.

C) PCT1-depleted (*pct1*Δ) *Saccharomyces cerevisiae* cells cultured to stationary phase, imaged after 24 h with or without treatment with oleic acid (OA). Sec63-mNG marked the ER and LDs were stained by MDH. Images shown represent z-projection of different stacks. Scale bars, 5 μm.

D) Corresponding quantification of the number of cells with aberrant ER, 0 h, 6 h and 24 h after OA treatment. Control cells with no OA addition are shown at 24 h time point. N=1300 cells for both *pct1*Δ and WT. Data are represented as mean ±SD.

E) Left: PCT1-deleted *Saccharomyces cerevisiae* cells cultured to stationary phase, after 24h treated with oleic acid (OA). Sec63-mNG marks ER and LD are MDH labeled. Scale bars, 5 μm. Right: Aberrant-ER cells statistically contained more LDs than cells with normal ER. t-test ($p<0.0001$), N = 140 cells, Data are represented as mean ±SD.

F) *Saccharomyces cerevisiae* cells cultured to stationary phase with OA. Phenotypes of regular and aberrant ER are shown displaying Z projection and slice image. ER is Sec63-mNG marked. Yellow arrowheads indicate Cortical ER, white arrowheads indicate nuclear ER. Scale bar are 2 μm.

G) Thin layer chromatography (TLC) experiment: Total amount of Phospholipids/μg of proteins in *Saccharomyces cerevisiae* treated with or without OA. Quantification is shown on the right. Protein concentration in lysate: –OA:2,9μg/mL; +OA: 2,8μg/mL.

H), Thin layer chromatography (TLC) experiment performed with cellular extract of WT cells cultured to stationary phase, after 24h in presence of OA and with or without inositol treatment. Protein concentration in lysate: –inositol: 2,7μg/mL; +Inositiol: 2,4μg/mL. Quantification of PI (Phosphatidylinositol) is shown on the right.

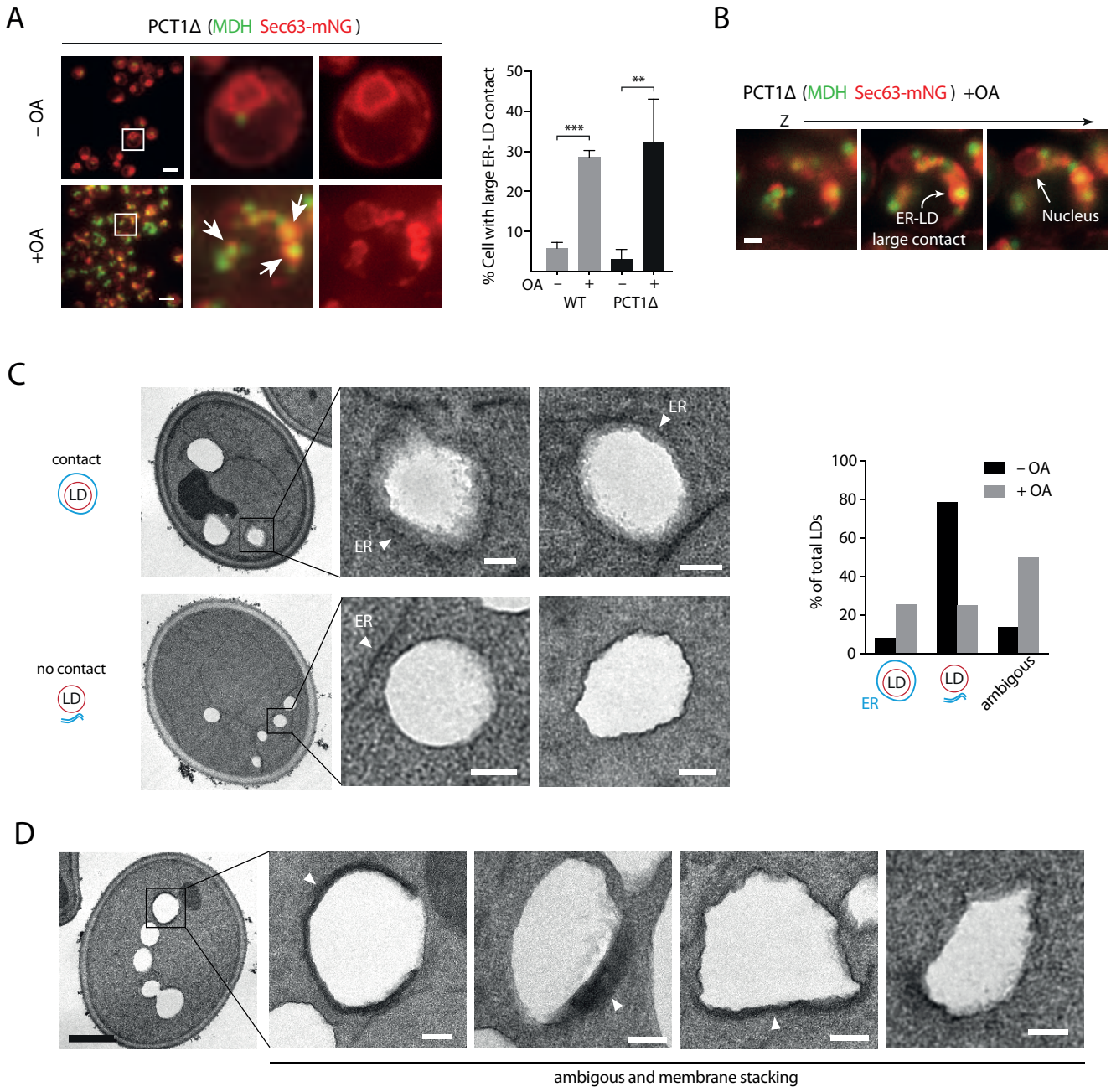
A
PCT1Δ (MDH Sec63-mNG)
– OA
+OA
% Cell with large ER-LD contact
50
40
30
20
10
***
**
OA – + – +
WT
PCT1Δ
B
PCT1Δ (MDH Sec63-mNG) +OA
Z
ER-LD
large contact
Nucleus
C
contact
LD
no contact
LD
ER
ER
ER
% of total LDs
100
80
60
40
20
0
– OA
+ OA
LD
ER
LD
ambigous
D
ambigous and membrane stacking

Supplementary Figure S4 | Complementary microscopy images showing LDs retained in the ER in *Saccharomyces cerevisiae* cells, related to Figure 4

A) PCT1-depleted *Saccharomyces cerevisiae* cells cultured from logarithmic growth phase with and without oleate (OA) treatment. Cells treated with OA show LDs with large ER contact zones (see arrows). Sec63-mNG marks ER and LD are MDH stained. Scale bar is 5 µm. Quantification with WT control is shown on the left. N >100 cells for each condition; Data are represented as mean ±SD.

B) Z-stack corresponding to Z projection displayed in A (PCT1-depleted +OA). Arrows indicates nucleus and large ER-LD contact zone. Scale bar is 1 µm.

C) Left: EM, chemically fixated WT *Saccharomyces cerevisiae* cells treated with OA showing examples of LDs with ER surrounding them (contact) and LDs presenting no apparent ER contact (no contact). Scale bar are 200 nm. Right: quantification of ER-LD contact with and without OA treatment corresponding to condition shown on the left and in Figure 4D. N= 200 LDs. Right: example of categories quantified on the left (contact, no contact and ambiguous).

D) EM, chemically fixated WT *Saccharomyces cerevisiae* cells treated with OA presenting LDs with ambiguous ER contact and unusual membrane stacking surrounding them (see white arrowheads). These phenotypes are not seen in cells without OA treatment. Scale bar are 200 nm.

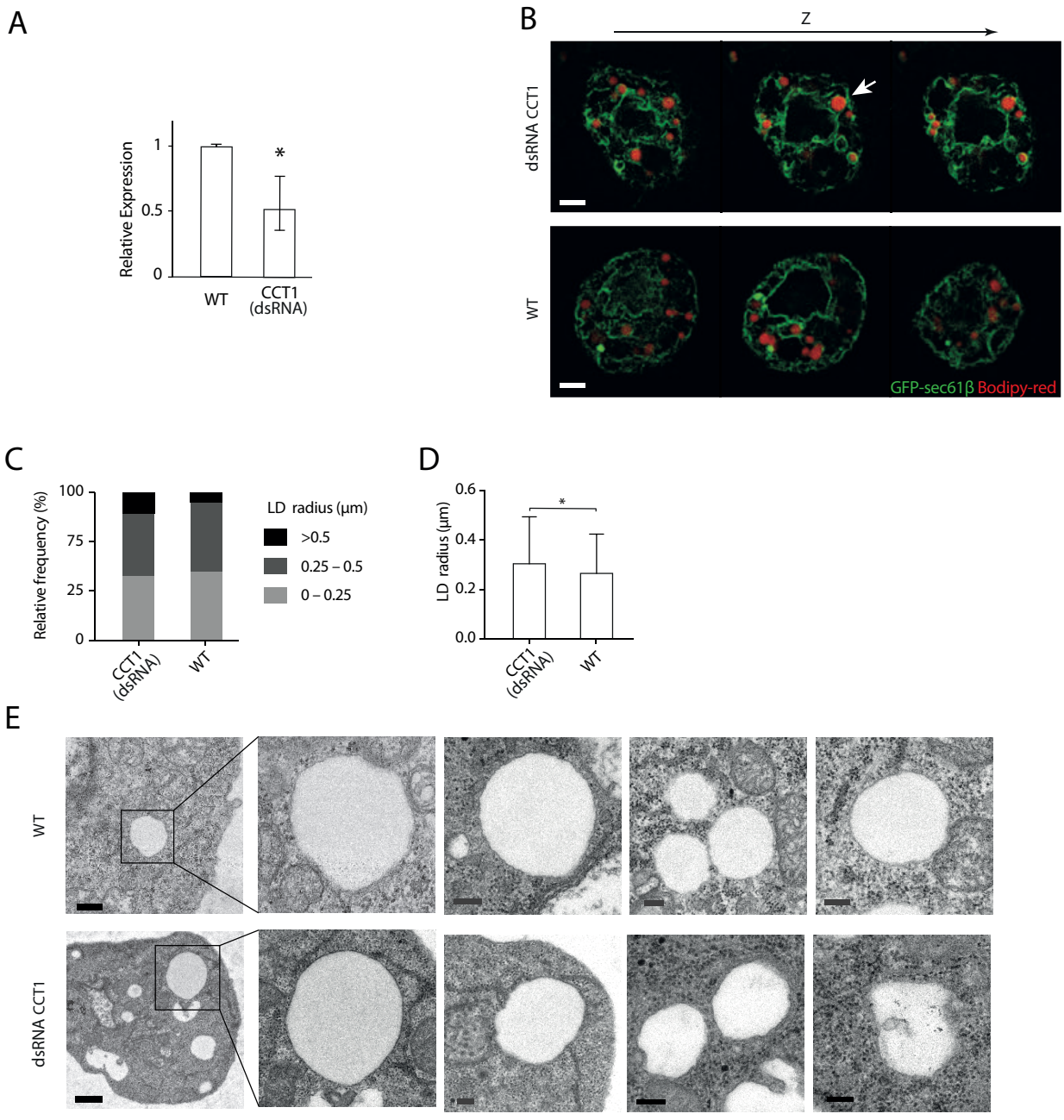
A
Relative Expression
1
0.5
0
*
WT
CCT1
(dsRNA)
B
Z
dsRNA CCT1
WT
GFP-sec61β Bodipy-red
C
Relative frequency (%)
100
75
25
0
LD radius (μm)
>0.5
0.25 – 0.5
0 – 0.25
CCT1
(dsRNA)
WT
D
LD radius (μm)
0.6
0.4
0.2
0.0
*
CCT1
(dsRNA)
WT
E
WT
dsRNA CCT1

Supplementary Figure S5 | Complementary microscopy images showing LDs retained in the ER in *Drosophila* cells, related to Figure 5

A) Quantification of the relative expression of CCT1 in WT and dsRNA CCT1 cells. P-value 0.034 by a permutation test. Data are represented as mean ±SD.

B) Additional z stacks images of Drosophila cells depleted from CCT1 by dsRNA. WT is shown as a control. LDs are induced by oleate and labeled by BODIPY558/568 and GFP-sec61β marks the ER. Arrow points to examples of LDs in close contact with ER. Scale bar is 2 μm.

C) LD radius frequency distribution of droplets smaller than 0.25μm, between 0.25μm and 0.5μm and above 0.5μm displayed for CCT1 depleted and WT Drosophila cells.

D) LD radius of CCT1 depleted and WT Drosophila cells. t-test show ns difference between CCT1 condition and significant difference between depleted cells and WT (p=0.0172). Data are represented as mean ±SD.

E) Example of EM images of LDs in WT and CCT1 depleted cells used for quantification in Figure 5B. Scale bars are 1 μm and 200 nm for the insets.

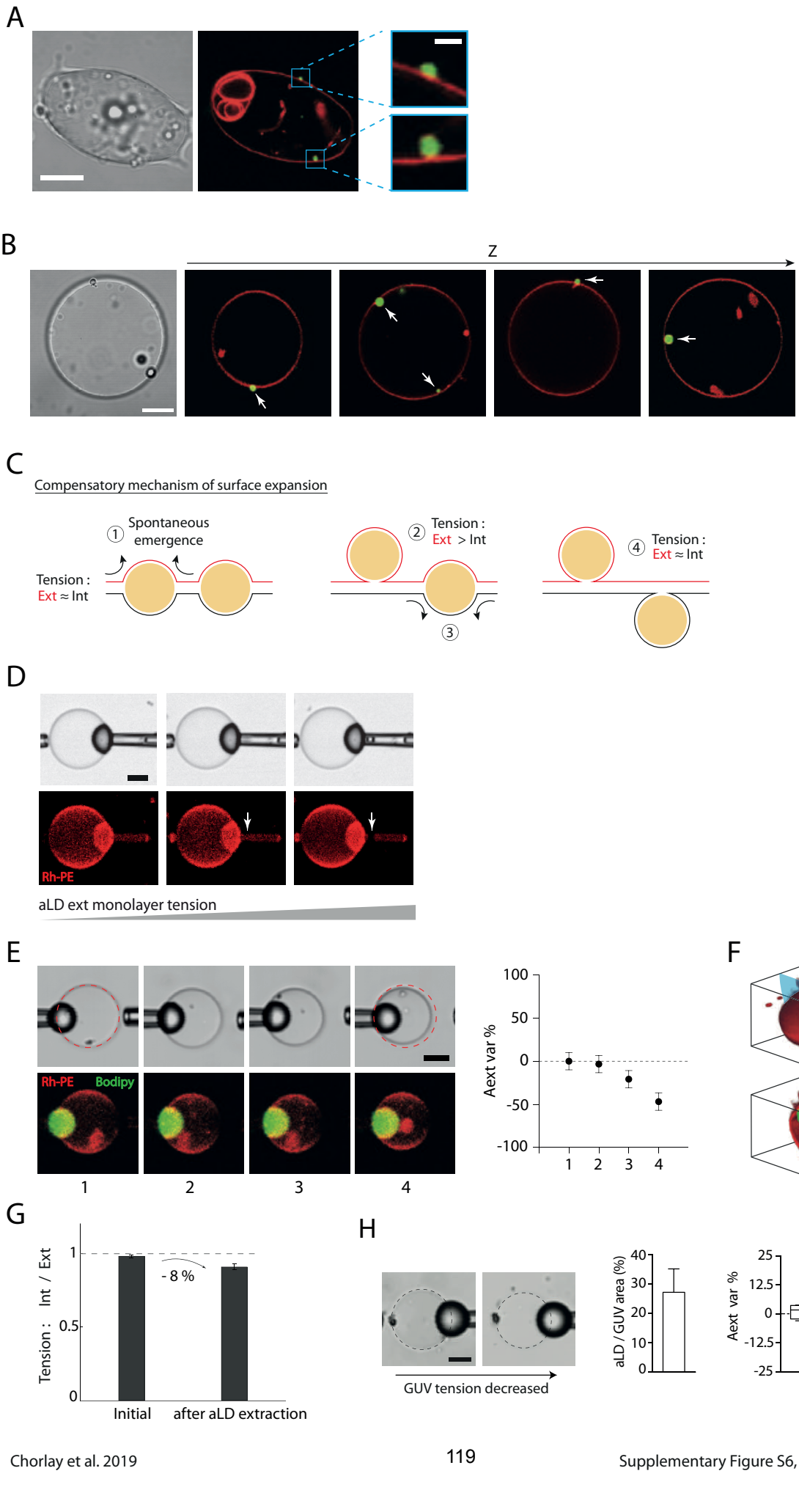
A
B
z
C
Compensatory mechanism of surface expansion
1 Spontaneous emergence
Tension : Ext ≈ Int
2 Tension : Ext > Int
3
4 Tension : Ext ≈ Int
D
Rh-PE
aLD ext monolayer tension
E
Rh-PE Bodipy
1
2
3
4
Aext var %
100
50
0
-50
-100
F
G
Tension : Int / Ext
1
0.5
0
- 8 %
Initial
after aLD extraction
H
GUV tension decreased
aLD / GUV area (%)
40
30
20
10
0
Aext var %
25
12.5
0
-12.5
-25

Supplementary Figure S6 | Detailed examples and model for the compensatory mechanism of the leaflet mismatch by LD emergence, related to Figure 6

A) Non-spherical GUV after strong osmotic deflation (very low bilayer tension) showing externally and internally budded LDs on the same bilayer. Scale bar is 10 µm and 2,5 µm in the inset.

B) Z slices of a GUV with multiple small LDs emerged towards the interior and exterior of the GUV (see arrows). Scale bar is 10 µm.

C) Predicted emergence steps of LDs in a single GUV: (1) at low bilayer tensions spontaneous emergence of an LD, for instance, on the external side of the bilayer; (2) the increase of the external leaflet surface area causes an increase of the external monolayer tension because the amount of phospholipid is constant; (3) the next LD will consequently bud on the opposite side of the bilayer; (4) the internal and external tensions tend to re-equilibrate.

D) Example of the scission of oil tongue describing the ablation of an artificial LD part (Figure 6E). Scale bar is 10 µm.

E) Time lapse of the osmotic deflation of Figure 5E experiment and corresponding LD external area variation showing the internal emergence of the aLD (trapped). Error bars are measurement precision. Scale bar is 10 µm.

F) 3D reconstruction of the final state after osmotic deflation (up) and cross section of the same system. The red cylinder in the background is the glass micropipette. Scale bar is 10 µm.

G) Variation of internal over external monolayer tensions ratio, before and after ablation of an artificial LD piece.

H) Left: A DEV with a ratio of artificial LD/GUV area (middle) close to the one in (Figure 6E) is deflated by osmotic choc. No significant external or internal area variation is observed after osmotic deflation; N = 10. Scale bar is 10 µm. Data are represented as mean ±SD.

Chapitre 7 :

Lipides neutres et recrutement d'hélices amphipathiques

Les lipides neutres modulent l'affinité des hélices amphipathiques pour les gouttes lipidiques.

Travaux publié dans Journal of Cell Biology

Les CLs forment une émulsion intracellulaire d'huile dans l'eau dont la phase huileuse est composée de lipides neutres de différentes natures selon le type de cellule et l'état métabolique [151]. Ce noyau de lipides neutres est stabilisé par une monocouche de phospholipides qui joue un rôle important dans le recrutement des protéines à la surface des CLs. La présence de ces protéines régule directement la fonction biologique et donc le futur des CLs au sein de la cellule [44].
De nombreuses protéines ciblent la surface des CLs à l'aide d'hélices amphipathiques (HAs), qui sont aussi capables d'ancrer des protéines à la surface de bicouches de phospholipides. Cependant, de nombreuses protéines possédant des motifs d'HAs sont capables d'interagir sélectivement avec la monocouche de phospholipides des CLs. Plus encore, il semble que certaines d'entre elles sont à même de cibler spécifiquement des sous-groupes de CLs qui peuvent par exemple différer de par la composition en lipides neutres de leur noyau[41,54,152,153]. On ne connaît cependant pas comment cette spécificité de recrutement est rendue possible.

Les HAs sont des domaines protéiques en forme d'hélice dont l'agencement particulier des acides aminés permet de former une partie hydrophobe et une partie hydrophile. Ce sont donc des motifs qui ont un pouvoir surfactant, c'est-à-dire que leur absorption sur une interface réduit son énergie de surface. Ainsi il a été avancé que les défauts de couverture dans la monocouche de phospholipides exposent le cœur hydrophobe des CLs, favorisant le recrutement des HAs à leur surface [125,154,155]. Cependant, aucune caractérisation expérimentale des défauts de couverture à la surface des CLs n'a encore été menée à ce jour et leur contribution dans le recrutement sélectif des HAs reste encore largement méconnue.

Le travail présenté dans ce chapitre essaie d'apporter des éléments de compréhension pour éclairer le rôle des phospholipides et des lipides neutres dans le recrutement des HAs à la surface des CLs. Au cours de cette étude, nous avons obtenu les résultats expérimentaux suivants :

- Les HAs sont recrutées différemment à la surface de CLs artificiels ne présentant pas les mêmes compositions de lipides neutres dans leur noyau.
- La densité de défauts de couverture de la monocouche de phospholipides, recouvrant la surface de CLs artificiels émergeant d'une bicouche, est indépendante de la composition du cœur de lipides neutres.
- Les HAs interagissent de manière différente avec les CLs artificiels selon la composition en lipides neutres de ces derniers, et ce indépendamment du niveau de couverture en phospholipides.
- Le type de phospholipides module le recrutement spécifique des HAs à la surface de CLs artificiels.

Ces résultats montrent que, pour une densité de phospholipides donnée, le recrutement des HAs à la surface de CLs artificiels dépend de la composition en lipides neutres. Ceci indique que la densité de défauts de couverture dans la monocouche de phospholipides n'est pas le seul régulateur de la liaison des HAs et que les lipides neutres ont une contribution majeure. Plus précisément, nos données suggèrent que la densité de la monocouche de phospholipides est un levier de régulation secondaire qui module l'accessibilité des HAs aux lipides neutres sous-jacents.

Concrètement, nous proposons le modèle suivant : l'affinité avec les lipides neutres est fixée par la composition des acides aminés hydrophobes de l'HA. Pour une forte affinité, le niveau de recrutement ne sera que faiblement influencé par les défauts de couverture de la monocouche. Pour une faible affinité, de nombreux défauts de couverture seront nécessaires pour atteindre un recrutement similaire. Ainsi la densité de défauts de couverture devient un facteur déterminant pour les HAs présentant une plus faible affinité pour les lipides neutres.

Nos derniers résultats expérimentaux semblent indiquer que cette approche peut être généralisée pour décrire les paramètres influençant le recrutement des HAs sur les bicouches, le rôle des lipides neutres étant remplacé par celui des chaînes carbonées qui composent l'intérieur de la bicouche. Nos données mettent donc en avant la contribution sous-évaluée des lipides neutres dans le contrôle du recrutement des HAs à la surface des CLs.

L'ensemble de cette étude a fait l'objet d'un article publié dans Journal of Cell Biology qui constitue le prochain chapitre de cette thèse.

JCB Journal of Cell Biology

ARTICLE

Neutral lipids regulate amphipathic helix affinity for model lipid droplets

Aymeric Chorlay and Abdou Rachid Thiam

Cellular lipid droplets (LDs) have a neutral lipid core shielded from the aqueous environment by a phospholipid monolayer containing proteins. These proteins define the biological functions of LDs, and most of them bear amphipathic helices (AH), which can selectively target to LDs, or to LD subsets. How such binding preference happens remains poorly understood. Here, we found that artificial LDs made of different neutral lipids but presenting equal phospholipid packing densities differentially recruit AHs. Varying the phospholipid density shifts the binding levels, but the differential recruitment is unchanged. We found that the binding level of AHs is defined by their interaction preference with neutral lipids and ability to decrease surface tension. The phospholipid packing level regulates mainly the amount of neutral lipid accessible. Therefore, it is the hydrophobic nature of the phospholipid packing voids that controls the binding level of AHs. Our data bring us a major step closer to understanding the binding selectivity of AHs to lipid membranes.

Introduction

Lipid droplets (LDs) are intracellular oil-in-water emulsion droplets, present in almost all organisms and playing diverse biological functions (Olzmann and Carvalho, 2019; Thiam and Beller, 2017; Welte, 2015). They primarily function to maintain cellular energy balance (Walther and Farese, 2012) but are also implicated in several other mechanisms such as protein quality control or lipid stress response (Bersuker and Olzmann, 2017; Shyu et al., 2018). The oil core of LDs is made of neutral lipids whose composition varies between cell types and metabolic conditions (Walther and Farese, 2012). Triacylglycerols and sterol esters (SEs) are the most abundant neutral lipids stored in LDs, but other neutral lipids can be found. For instance, retinol esters, a storage form of vitamin A, are abundant in liver hepatic stellate cells (Blaner et al., 2009); acylceramides, storage forms of ceramides, are made in liver cells under high-fat diet conditions (Senkal et al., 2017); squalene (SQ) or wax oils are also present in many cell types, e.g., skin or plant cells (Spanova and Daum, 2011).

Most neutral lipids are fabricated at the ER bilayer and encapsulated within the bilayer leaflets. When their concentration reaches a threshold, they condense into spherical LDs, which further emerge in the cytosol (Chorlay et al., 2019; Henne et al., 2018; Thiam and Forêt, 2016; Walther et al., 2017). LDs are covered by a single phospholipid (PL) monolayer embedded with proteins, which determine most LD biological functions (Kory et al., 2016). Many of these proteins bind to LDs by using amphipathic helix (AH) domains, motifs that are also capable of targeting bilayer membranes (Bigay and Antonny, 2012; Kory et al., 2016; Thiam and Dugail, 2019). However, despite the fact that bilayer surfaces are much more abundant in cells, many AH-containing proteins achieve to selectively target to the monolayer surface of LDs. Even within a single cell, proteins containing different AHs can preferentially bind to LD subsets, for example made of different neutral lipids (Hsieh et al., 2012; Straub et al., 2008; Thiam and Beller, 2017; Wolins et al., 2006). This occurs for instance with Perilipins (1–5), major LD proteins that bear AH motifs and can preferentially localize to triglyceride or cholesterol ester LDs (Hsieh et al., 2012; Straub et al., 2008), or with the lecithin retinol acyl transferase, whose N terminus AH seem to more strongly associate with retinol palmitate than with triolein (TO) droplets (Molenaar et al., 2019).

Decreasing the PL packing density at the monolayer surface of LDs accentuates the contact between hydrophobic and hydrophilic phases, which is favorable for the binding of AHs (Čopič et al., 2018; Prévost et al., 2018; Thiam et al., 2013a). Indeed, AHs are basically surfactants, and their adsorption to hydrophobic–hydrophilic interfaces is favorable for reducing interfacial energies (Thiam and Dugail, 2019). Currently, there is no experimental determination of the PL packing level at the surface of LDs, nor clear understanding of its contribution to the

Laboratoire de Physique de l'Ecole Normale Supérieure, ENS, Université PSL, Centre National de la Recherche Scientifique, Sorbonne Université, Université de Paris, Paris, France.

Correspondence to Abdou Rachid Thiam: thiam@ens.fr.

binding of AHs. In the case of lipid bilayer, the presence of PL packing defects, or voids, favors the binding of many AHs, by proffering access to the hydrophobic acyl chain core of the bilayer (Bigay and Antonny, 2012; Vanni et al., 2014). In the case of LDs, the situation is different in the sense that AHs have to expose their hydrophobic moieties to neutral lipids. Thus, the nature of the interactions between the hydrophobic amino acids of an AH with neutral lipids could be a major driving force for the targeting of AHs to LDs.

Here, we investigate the contribution of PLs and neutral lipids to the binding of AHs to artificial LDs (aLDs). We find that AHs do not equally bind to the oil/water interface of aLDs made of different neutral lipids but present similar PL packing densities. We subsequently unveil that the chemistry of the neutral lipid has a major contribution to the binding of AHs to LDs. The density of the PL monolayer regulates mainly the amount of neutral lipids accessible to the AHs. These findings highlight that the hydrophobic nature of the packing voids within a PL layer is determinant to the recruitment of AHs.

Results

The binding of AHs to model bilayer-connected LDs depends on the neutral lipid composition

We employed the droplet-embedded vesicle (DEV) system, which consists of aLDs embedded within the bilayer leaflets of a giant vesicle (Chorlay and Thiam, 2018), here made of dioleoylphosphatidylcholine, which is referred to as PC (Fig. 1 A). This topology mimics an LD emerging from the ER membrane, with the bilayer behaving as a PL reservoir to the aLD. DEVs were generated with different neutral lipids: SQ, TO, or TO supplemented with ∼25% (wt/wt) SE (TO-SE), which was around the maximum solubility of SE in TO at room temperature.

We first wondered whether the neutral lipid type affects the surface tension of spherical aLDs emerging from the bilayer. By using a microaspiration technique, we measured this tension (Fig. 1 B) and found it respectively of 0.58 mN/m for SQ, 1.63 mN/m for TO, and 1.84 mN/m for TO-SE (Fig. 1 C). These values are comparable to the surface tension of LDs isolated from mammalian or fly cells (Ben M'barek et al., 2017). SQ aLDs had a lower interfacial tension than TO-containing aLDs. Supplementing TO with 25% SE was sufficient to slightly increase surface tension; pure SE-LDs can be expected to have an even higher surface tension. These results suggest that LDs may emerge from the ER bilayer with different interfacial energies with respect to their neutral lipid content. This interfacial energy could be further reduced by the recruitment of amphipathic molecules such as AHs (Chorlay et al., 2019). Thus, we hypothesized that AHs would be differently recruited to the surface of emerging aLDs made of different neutral lipids.

We studied the recruitment of fluorescently labeled AH peptides derived from proteins reported to bind to LDs. Several AHs were considered so as to cover as much as possible diverse amino acid features. We used an NBD-tagged AH sequence from caveolin 1 (Cav aa159–178, termed Cav1-AH) which was used to target hydrophobic peptides to the surface of cellular LDs (Kassan et al., 2013); a rhodamine-tagged AH sequence from Arfgap1, which is a PL packing sensor (Bigay et al., 2005) also found on LDs (Gannon et al., 2014); a short NBD-tagged AH in the 11-mer repeat sequence of Plin1 (Plin1_108-137; Ajjaji et al., 2019; Rowe et al., 2016), which is the major LD protein in adipocytes (Brasaemle, 2007; Fig. S1 C); and finally, a rhodamine-tagged AH of the nonstructural protein 5 of the hepatitis C virus, which binds to LDs during viral replication (Shi et al., 2002). As the larger difference in surface tension was measured between SQ and TO (Fig. 1 C), we focused on the binding of the peptides to aLDs made of these two neutral lipids. This strategy would a priori enable better discrimination of the role of the neutral lipid type in recruitment.

The peptides were added to the external medium of the DEVs (Fig. 1 D). To quantify binding, we defined the "droplet enrichment index," which is the peptide signal on the droplet normalized by the one on the bilayer, corrected by an optical factor (β) that accounts for the optical index mismatch between the oil droplet and the external water phase (Fig. 1 D and Fig. S2). Cav1-AH, Arfgap1-AH, and NS5A-AH were recruited much more to TO than to SQ aLDs (Fig. 1, E–I; and Fig. S1 B), proving that the neutral lipid content impacts the recruitment level of an AH. On the contrary, Plin1_108-137-AH barely bound to TO or SQ aLD (Fig. 1 I and Fig. S1 C), showing the importance of amino acid composition on AH LD binding. Membrane binding is particularly favored by bulky hydrophobic residues (Prévost et al., 2018; Wimley and White, 1993), such as tryptophan or phenylalanine, which are present in Cav1-AH, Arfgap1-AH, and NS5A but not Plin1_108-137-AH (Fig. 1, E and G; and Fig. S1, B and C). NS5A-AH, for instance, bears the larger number of bulky hydrophobic residues and was more strongly recruited to both neutral lipids than other AHs. However, the presence of hydrophobic bulky residues is not mandatory to guarantee stable binding. Indeed, when we mutated the two phenylalanines of Cav1-AH into leucine (F2L,F8L), the binding efficiency onto TO aLDs was similar to that of the wild-type AH (Fig. 1 J and Fig. S1 D). The presence of opposite charges on the hydrophilic face of the AH might have promoted lateral AH–AH interaction and stabilized binding, as proposed for Plin4 (Čopič et al., 2018). On the contrary, when we put a charge in the hydrophobic face of the AH, by mutating the valine into arginine (V5R), we lost binding to the aLDs (Fig. 1 J and Fig. S1 D). Finally, Arf1 protein binds to membranes and to LDs (Guo et al., 2008; Thiam et al., 2013a) with an AH dense in tryptophan and phenylalanine, in combination with a myristoylated acyl chain. In the presence of GTP and EDTA, to activate Arf1 binding (Antonny et al., 1997), the recruitment to TO aLDs was much higher than for other AHs, and much more than to SQ aLDs (Fig. S1 E).

To further validate our observation on the influence of the oil type on peptide recruitment, we used dodecane, which is a nonphysiological oil whose measured oil/buffer interfacial tension (31.8 mN/m) was between SQ and TO (23.7 mN/m and 34.1 mN/m, respectively). We found that both Cav1-AH and Arfgap1-AH were enriched to dodecane aLDs at intermediate levels between SQ and TO (Fig. S1 A).

Altogether, these results indicate that the neutral lipid composition impacts the recruitment level of AHs to aLDs connected to a bilayer. Here, the recruitment of the AHs was more

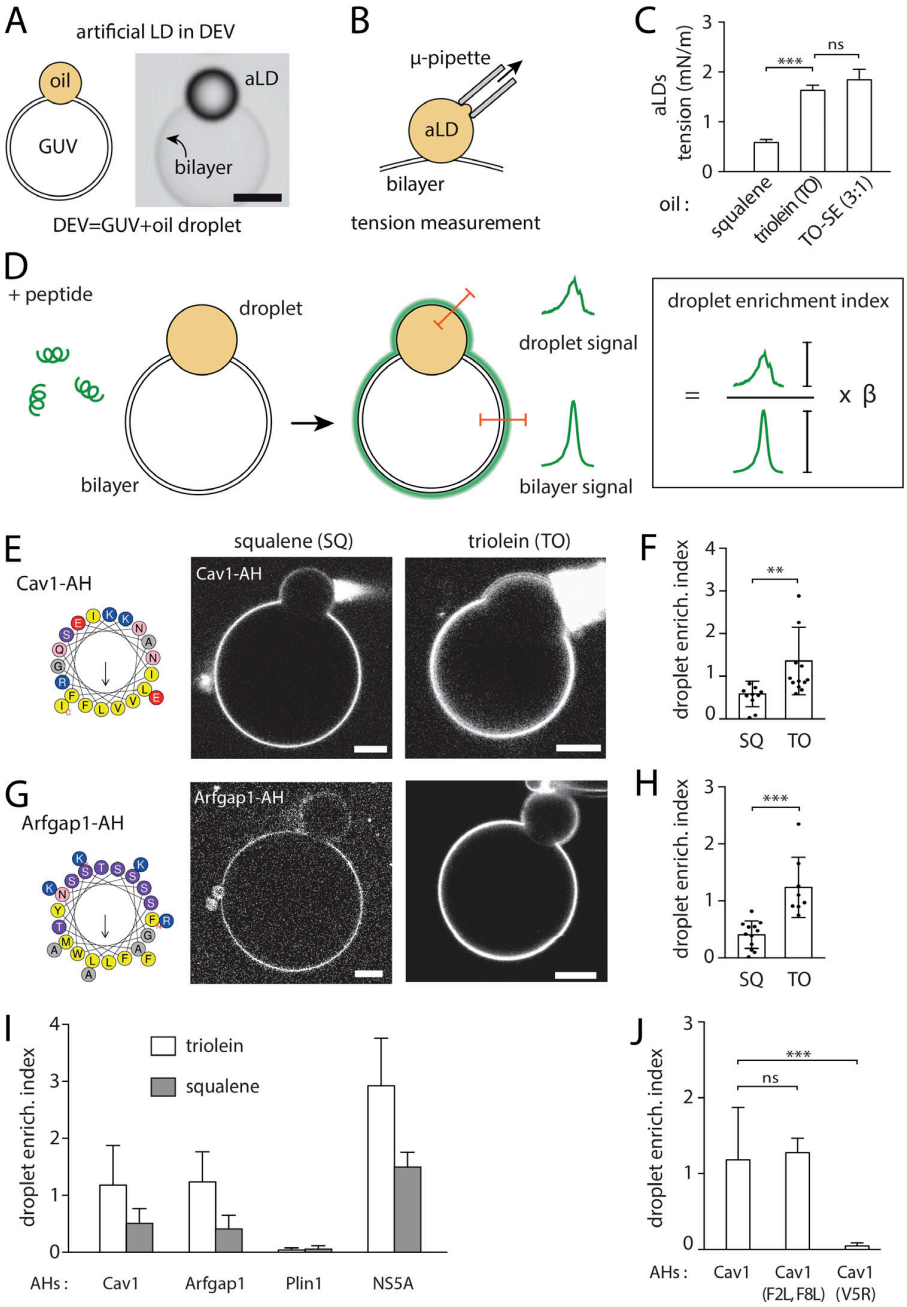

Figure 1. **AHs differentially bind to aLDs emerging from a bilayer and made of different neutral lipids. (A)** Diagram of an aLD incorporated in the inter-monolayer space of a GUV bilayer, forming the DEV system. Example of a DEV is shown on the right. Scale bar, 5 µm. **(B)** Surface tension of an aLD in a DEV is measured using the micropipette aspiration technique. **(C)** Surface tension of aLDs in DEV made using SQ, TO, and TO mixed with 25% of SE. **(D)** A solution of fluorescently tagged peptide is added to a DEV. The peptide is recruited to the DEV interfaces. Fluorescent signal is quantified on the aLD and the GUV bilayer. We calculated a droplet enrichment index by taking the ratio between droplet signal and GUV bilayer signal and multiply it by an optical correction factor (β); see Fig. S2. **(E)** Cav1-AH tagged with NBD is added to a DEV solution. Micrographs show Cav1-AH recruited to DEVs containing SQ or TO aLDs. Scale bars, 10 µm. See also Fig. S1 A. **(F)** Quantification of droplet enrichment index for both SQ and TO aLDs. TO droplets recruited more Cav1-AH as compared with SQ droplets. *t* test shows significant difference ($P < 0.001$). Data are represented as mean ± SD. **(G)** Arfgap1-AH tagged with rhodamine B is added to a DEV solution. Micrographs show Arfgap1-AH recruited to the DEV surface containing SQ or TO aLDs. Scale bars, 10 µm. See also Fig. S1 B. **(H)** Quantification of droplet enrichment index for both SQ and TO aLDs. TO droplets recruited more Arfgap1-AH as compared with SQ droplets. *t* test shows significant difference ($P < 0.0001$). Data are represented as mean ± SD. **(I)** Droplet enrichment index of AH from Caveolin 1 (Cav1), Arfgap1 (Arfgap1), and Perilipin 1 (Plin1). *t* test shows significant differences between TO and SQ with $P < 0.0001$ for all AH tested except for the AH from Perilipin 1. Data are represented as mean ± SD. See also Fig. S1, B, C, and E. **(J)** Droplet enrichment index for Cav1-AH and mutated versions: Cav1-AH(F2L,F8L), two phenylalanines mutated into leucine, Cav1-AH(V5R) by mutating the valine into arginine in the hydrophobic face. *t* test shows no significant difference between Cav1-AH and Cav1-AH(F2L,F8L) ($P = 0.71$) but shows significant differences between Cav1-AH and Cav1-AH(V5R) with $P < 0.0001$. Data are represented as mean ± SD. See also Fig. S1 D.

favorable to TO than SQ aLDs and also depended on the amphipathic sequence.

The PL packing density of the model bilayer-connected LDs is independent of the neutral lipid content

Arfgap1-AH is a PL packing sensor (Bigay et al., 2005) that is better bound to TO than to SQ aLDs (Fig. 1 I). We hence thought that aLDs connected to bilayers might present different PL packing levels according to their neutral lipid content. This would be consistent with the difference in surface tension and AH recruitment between TO and SQ. To quantify the PLs density, we made PC DEVs containing 1% of nickel PL (DGS NTA(Ni)), which covalently binds to histidine. Histidine-mCherry was added to the medium and recruited to DEVs by nickel lipids (Fig. 2 A and Fig. S3 I). The PL density at the aLD and the bilayer interfaces of the DEV was hence reported by mCherry signal.

DEVs were imaged at their lowest plane (Fig. 2 A), which yields a signal not reduced by the index mismatch between the water phase and the oil droplet (Fig. 2 B and Fig. S2). By measuring the aLD mCherry signal normalized to that of the bilayer, we found no significant difference between SQ, TO, and TO-SE (Fig. 2 C and Fig. S3, A and B). The average fluorescence ratio between the aLD and the bilayer was ∼0.87, below 1, suggesting that the PL density of the aLD monolayer was constant and lower than that of the bilayer: on average, for 100 PLs on the monolayer of the bilayer, there are ∼87 PLs on the monolayer of the droplet (Fig. 2 C, bottom). This finding indicates that the differential recruitment of the AHs between SQ and TO aLDs was not due to a difference in PL packing.

It is well known that the PL packing density correlates with the binding of AHs (Bigay et al., 2005; Čopič et al., 2018; Pranke et al., 2011; Prévost et al., 2018), but here it did not seem to explain the differential recruitment of the tested AHs. We thus sought an independent confirmation of this unanticipated finding of the unchanged PL density at the monolayer covering the different neutral lipids. We opted for a droplet tensiometer measurement, which is a complementary and nonfluorescence method, to our previous approach. We generated a neutral lipid-in-buffer droplet whose interface was decorated by PC, which was added from the aqueous phase in the form of liposomes (Fig. 2 D), and we measured the surface tension. We next performed droplet area oscillations by imposing blowing-shrinking cycles of the droplet volume. This manipulation enables to probe the rheology of the monolayer and to extract its elastic modulus (E). This modulus reflects the lateral interactions between PLs and is therefore linked to the PL monolayer density (Fainerman et al., 2002; Kralchevsky et al., 2008). The droplet was next shrunk to increase the PL density and the oscillation repeated, and so on and so forth (Fig. S4). These operations enabled to establish the dependence of the elastic modulus (E) against the monolayer lateral pressure (π; Fig. 2 E), which is directly linked to the area per PL through the isotherm of compression. A subsequent mathematical fitting of this curve by the Frumkin isotherm model (Kolev et al., 2002; Kralchevsky et al., 2008) enabled extraction of the area occupied by a PL at the neutral lipid–buffer interface (Fig. 2 F). For both TO and SQ, the experimental data points and the fitting curve followed a similar trend (Fig. 2 E), suggesting an equivalent PL density at the neutral lipid–buffer surface. At a surface pressure of ∼30 mN/m, corresponding to a surface tension of ∼1 mN/m, which is close to the one of aLDs (Fig. 1 C) and to that of cellular LDs (Ben M'barek et al., 2017), the area per PC lipid at the monolayer interface was found to be ∼78 Å^2 (Fig. 2 G). This area was identical for SQ and TO, and even for the nonphysiological dodecane oil (Fig. S3, C–F), with the precision of the measurement technique. Note that for a bilayer, the surface area of a PC molecule varies between 69.7 Å^2 and 74 Å^2 (Fig. 2 H; Kučerka et al., 2008; Reddy et al., 2012), based on the maximum bilayer area expansion (Fig. S3, G and H); this range of area is indeed slightly smaller than the 78 Å^2 area on the monolayer, and consistent with our previous findings with DEVs (Fig. 2 C).

In conclusion, our data reveal that the density of PC molecules on the monolayer of an aLD connected to a bilayer is independent of the tested neutral lipids and is ∼0.87 times smaller than the density in the bilayer (Fig. 2, C, G, and H).

AHs are differentially recruited to bare neutral lipid/buffer interfaces

Since the PL packing density was identical for SQ and TO aLDs, it did not explain the differential recruitment of the AHs (Fig. 1, E–I). Therefore, it was probably the nature of the interactions between the AH and the neutral lipid interface that was responsible for the differential binding observed in Fig. 1. To test this hypothesis, we produced simultaneously PL-free TO and SQ droplets in buffer (Fig. 3 A). We added Cav1-AH, Arfgap1-AH, or Plin1_108-137-AH to the buffer and measured their fluorescence signal at the surface of the droplets (Fig. 3 B). We observed a neat difference in recruitment: AHs were much more enriched to the TO-buffer than to the SQ-buffer interfaces. Note that the net recruitment was higher for Cav1-AH than for Plin1_108-137-AH (Fig. S5 H), as for the aLDs of DEVs (Fig. 1 I). Here, to appreciate the differential recruitment for each AH, the recruitment signal was normalized by the signal at the TO/buffer interface.

What makes an AH more favorably binding to a given neutral lipid/buffer interface? To provide hints to this question, we decided to map the binding efficiency for a variety of neutral lipid conditions and focused on Cav1-AH and Plin1_108-137, which had contrasted binding efficiencies (Fig. 1 I and Fig. 3 B). We started by mixing SQ and TO at different ratios, as binding of the AHs was highly different between these two neutral lipids. Increasing the SQ fraction decreased the binding of both peptides (Fig. S5 A), even though this decrease was a little bit more pronounced for Cav1-AH. In contrast, while 25% of SQ in TO strongly decreased the relative recruitment of both AHs (Fig. S5 A), the presence of 25% SE in TO did not alter this binding (Fig. 3 C and Fig. S5 B). In TO/diolein mixtures, Cav1-AH recruitment is decreased by diolein presence, while Plin1_108-137-AH recruitment remained intact (Fig. 3 C and Fig. S5 C). We next tested the effect of monoolein addition and, contrarily to diolein, found a strong decrease of binding for both AHs. This is probably because monoolein behaves more like a surfactant, which is recruited and protects the neutral lipid/buffer surface from AH recruitment (Fig. S5 D; Thiam et al., 2013b). We also compared the recruitment to TO and retinol palmitate, a major neutral

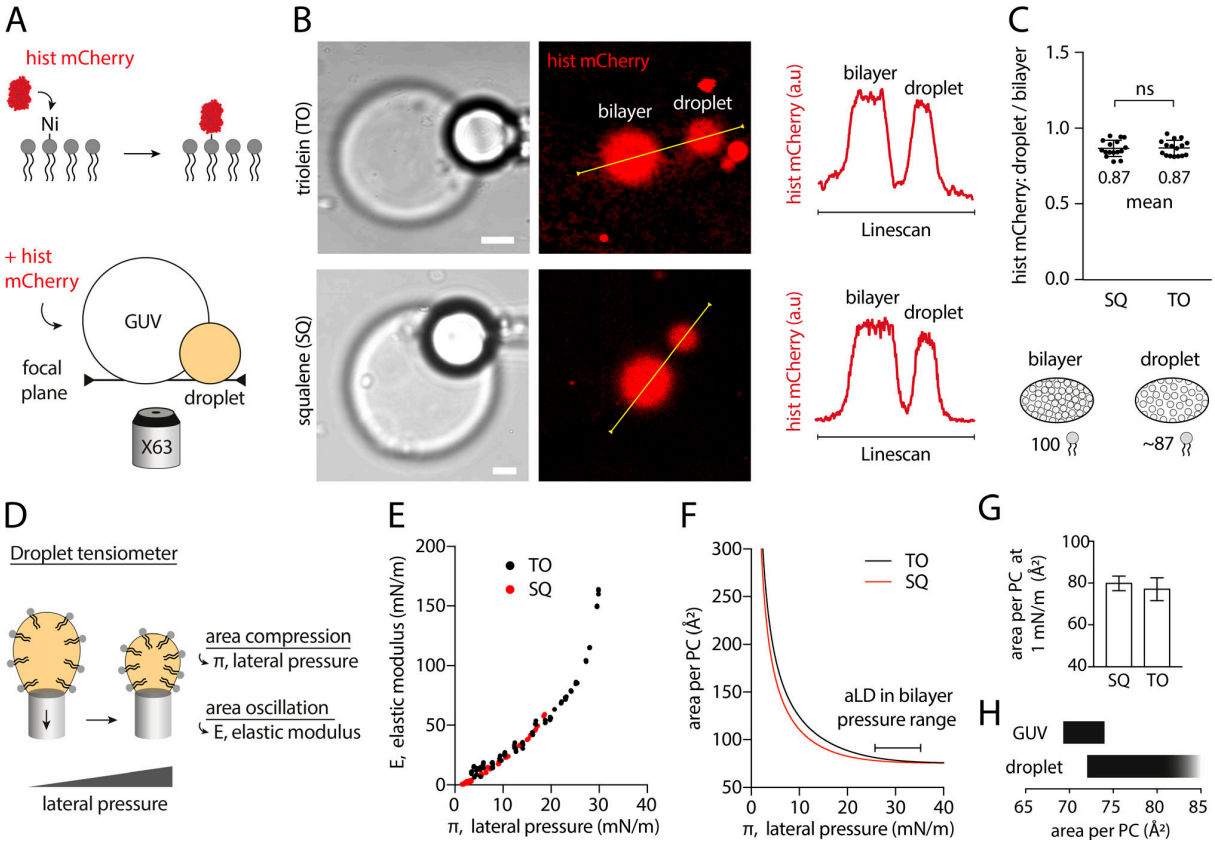

Figure 2. **The PL packing level is identical on aLDs emerging from a bilayer, independently of neutral lipid composition tested. (A)** Schematic diagram illustrating the method for measuring the relative PL density on DEVs. Top: fluorescent mCherry-histidine binds to nickel PLs (DGS-Ni-NTA). Bottom: mCherry-histidine is added to DEV system made with PC presenting 1% nickel PLs. After 10-min incubation with mCherry-histidine, the GUV membrane and aLD surface are visualized simultaneously at their apex (same focal plane). Control experiment without nickel lipid is shown in Fig. S3 I. **(B)** Representative confocal fluorescence images of mCherry-histidine marking PLs of DEV containing SQ or TO aLDs. Linescans allow for the quantification of fluorescence intensity on the GUV membrane and droplet surface. Scale bar, 5 µm. **(C)** Top: Quantification of the ratio between the droplet and bilayer fluorescence intensities for SQ and TO aLDs. *t* test shows no significant difference. Data are represented as mean ± SD. DEVs containing TO-SE aLDs were also imaged and quantified; they show no difference with TO and SQ (see Fig. S3, A and B). Bottom: Cartoon of the PC density on an aLD and a bilayer of a DEV: for an identical area, 100 PC molecules on the bilayer and ∼87 PC molecules on the aLD. **(D)** PC-covered oil droplet surface was characterized by using a droplet tensiometer method. PL lateral pressure (π) is increased by reducing the droplet surface area, and area oscillation enables measurement of the interface elastic modulus (E). **(E)** E-π isotherms for SQ and TO oil phase. **(F)** Area per PC molecule as function of the lateral pressure π at SQ and TO/buffer interface. Data are obtained by fitting the experimental E-π isotherms with a Frumkin theoretical model. Lateral pressure region typically encountered in DEV systems and in cellular LDs corresponds to the flat area around 30 mN/m. **(G)** Area per PC molecule on SQ and TO aLD, at 1 mN/m surface tension; see Fig. S3 E. 1 mN/m was chosen as the average surface tension of aLDs just emerging from a bilayer, and close to the surface tension of cellular LDs. Similar results for dodecane oil are displayed in Fig. S3, C–F. See Fig. S4 for raw data. **(H)** Area variation range of a PC molecule on a bilayer and a droplet monolayer.

lipid in hepatic stellate cell, and found much less recruitment to the latter for both AHs (Fig. 3 C and Fig. S5 E). More generally, we found that even nonphysiological oils were discriminated by these AHs (Fig. S5 F). Altogether, these results highlight two major points: the neutral lipid composition determines the binding level of AHs, and the ability of AHs to discriminate between neutral lipids relies on their amphipathic amino acid sequence. To further illustrate the latter, we thought that the point mutations done on Cav1-AH could be sufficient to alter its propensity to discriminate between SQ and TO. Indeed, we found that the F2L,F8L mutant surprisingly showed slightly more improved distinction between the neutral lipids, while the V5R mutant lost discernment (Fig. 3 D and Fig. S5 G).

The above experiments gave us enough source of variability to analyze for better understanding parameters controlling recruitment. One characteristic of recruitment is the minimization of interfacial energies. For example, bare TO/buffer surface tension was 34.1 mN/m, which is much higher than that of SQ/buffer, which was 23.7 mN/m. This higher tension for the TO interface could have favored the higher recruitment of the AHs, because of the higher energy cost for exposing TO than SQ to water molecules. Therefore, one predicts that surface tension correlates with recruitment. Thus, we represented the surface tension of all the tested neutral lipids and nonphysiological oils against the recruitment level of Cav1-AH or Plin1_108-137 (Fig. S5, I and J). For Cav1-AH, we found indeed that binding overall

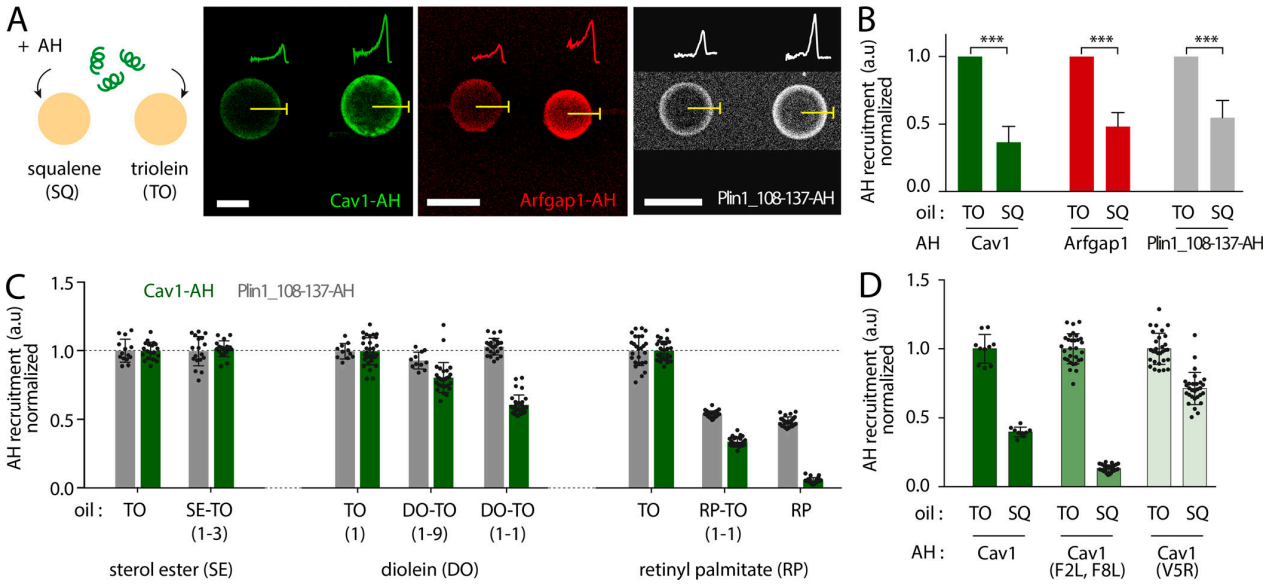

Figure 3. **AHs have differential affinities for neutral lipids. (A)** PL-free SQ and TO droplets are formed in buffer containing AHs (Cav1-AH, Arfgap1-AH, or Plin1_108-137-AH). Left: Representative confocal fluorescence images showing the recruitment level of the AHs are shown. The fluorescent signal is quantified on each droplet. Scale bar, 50 µm. **(B)** Quantification of the fluorescence intensity of Cav1-AH, Arfgap1-AH, and Plin1_108-137-AH at the surface of SQ and TO droplets, normalized by the fluorescence intensity on TO droplets for each AH. *t* test shows a significant difference between SQ and TO data ($P < 0.001$). Data are represented as mean ± SD. **(C)** Left: Quantification of the fluorescence intensity of Cav1-AH (green) and Plin1_108-137-AH (gray) at the surface of SE-TO (SE/TO, 1–3, wt/wt) and TO droplets, normalized by the fluorescence intensity on TO droplets. *t* test shows no significant difference between SE/TO (1/3) and TO data for both Cav1-AH and Plin1_108-137-AH ($P > 0.1$). Corresponding micrographs are shown in Fig. S5 B. Middle: Quantification of fluorescence intensity of Cav1-AH and Plin1_108-137-AH at the surface of TO and diolein-TO mixtures (DO/TO, 1/9, 1/1, vol/vol), normalized by the fluorescence intensity of TO droplets. *t* test shows a significant difference between DO/TO (1/1) and TO data for Cav1-AH ($P < 0.0001$) but shows no significant difference between DO/TO (1/1) and TO data for Plin1_108-137-AH ($P = 0.07$). Corresponding micrographs are shown in Fig. S5 C. Right: Quantification of fluorescence intensity of Cav1-AH and Plin1_108-137-AH at the surface of TO and RP/TO (1/1, 1/0), normalized by the fluorescence intensity of TO droplets. *t* test shows significant differences between RP and TO, and RP/TO (1/1) and TO, for both Cav1-AH and Plin1_108-137-AH ($P < 0.0001$). Corresponding micrographs are shown in Fig. S5 E. **(D)** Quantification of the fluorescence intensity of Cav1-AH (dark green), Cav1-AH(F2L,F8L) (green), and Cav1-AH(V5R) (light green) at the surface of SQ and TO droplets, normalized by the fluorescence intensity on TO droplets. Corresponding micrographs are shown in Fig. S5 G. *t* test shows significant differences between SQ and TO data for Cav1-AH, Cav1-AH(F2L,F8L), and Cav1-AH(V5R) ($P < 0.0001$). F-test of variance shows significant differences between SQ and TO data for both Cav1-AH and Cav1-AH(F2L,F8L) ($P = 0.0052$ and $P < 0.0001$, respectively) but no significative difference between SQ and TO for Cav1-AH(V5R) ($P = 0.8824$).

increased when the oil/buffer surface tension was higher (Fig. S5 I). However, within a given range of surface tensions, binding did not correlate with tension (Fig. S5 I). For Plin1_108-137, there was no correlation between the binding level and surface tension (Fig. S5 J). Altogether, these data suggest that the binding extent of an AH to a neutral lipid/buffer interface is driven by at least two contributions: a rough contribution of the ability of the AH to reduce the surface tension of the interface, and a fine-tuned contribution of the intrinsic interaction between the AH and the neutral lipid phase.

PLs control the accessibility of neutral lipids to AHs

During LD formation, the LD neutral lipid core is covered by a PL monolayer mainly deriving from the ER cytoplasmic leaflet. After emerging from the ER, LDs can grow or shrink, meaning that their PL monolayer density may vary, especially if they are physically disconnected from the ER membrane (Wilfling et al., 2014). Variation of the PL monolayer density will affect the accessibility of AHs to the oil-buffer interface. We hence wanted to understand the contribution of the PL packing density on AH binding level.

To characterize how the PL monolayer density modulates binding, we made neutral lipid-in-buffer aLDs with heterogeneous coverage in PC, to which 1% of Cy5-PE was added. Cy5 signal was hence a reporter for the PL density at each aLD surface (Fig. 4 A). We next added Cav1-AH into the solution and recorded its recruitment over time (Fig. 4 A). Recruitment to aLDs presenting a lower PL density was more pronounced in both TO and SQ (Fig. 4 A, right; and Fig. S6, A and B, right). However, for a given PL density, the plateau of maximum recruitment was higher for TO than for SQ (Fig. 4, B and C), consistent with our previous observations. This maximum recruitment was then reported for each PL density (Fig. 4 D). We found that increasing the PL density diminished binding to aLDs (Fig. 4 D, right) until a critical density above which the binding level became almost constant (Fig. 4 D, right, higher PL densities). We actually found that the relative recruitment level of the AH to SQ and TO droplets remained independent of the PL level (Fig. 4, D and E): at any PL density, the ratio of CAV1-AH signal between TO and SQ was almost constant, ~2.62 (Fig. S3 H). This result suggests that the PL packing density simply modulates the amount of accessible neutral lipids and does not have a

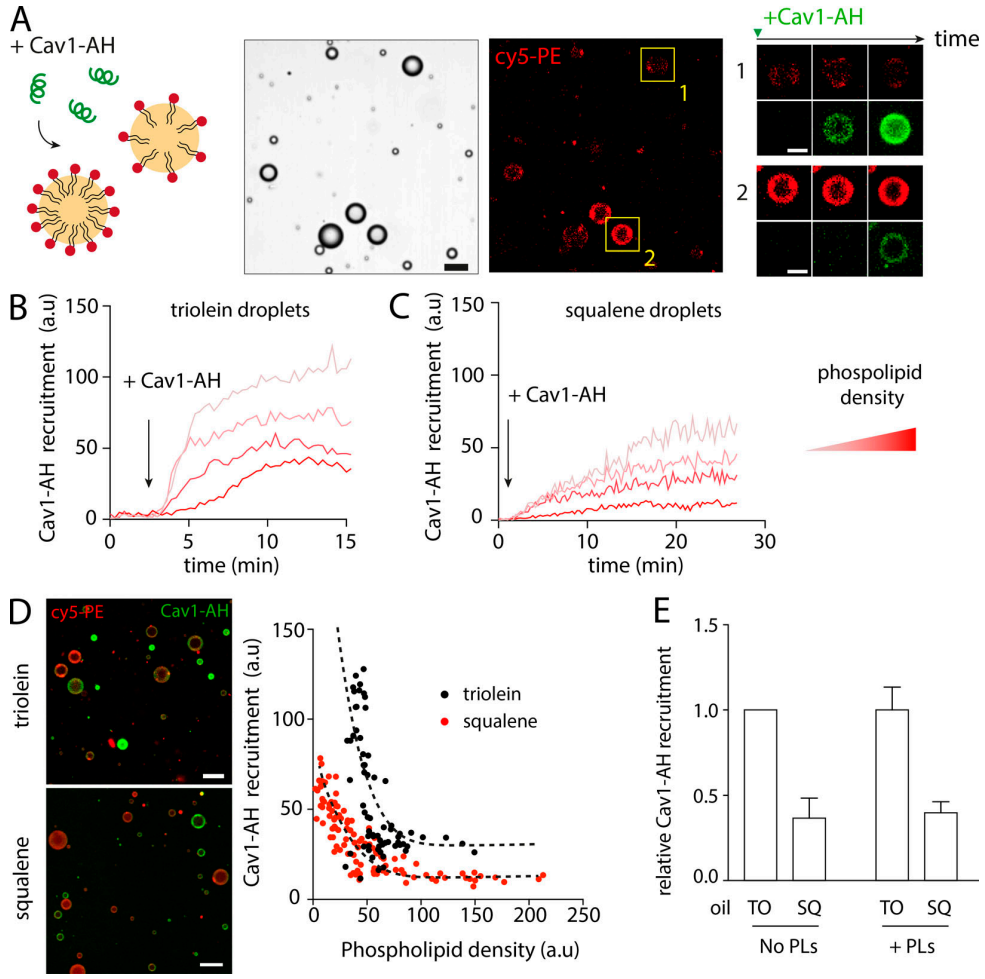

Figure 4. **PLs control the accessibility of neutral lipids to AHs. (A)** TO aLD with heterogeneous PL densities (DOPC:Cy5-DOPE; 99:1) were prepared in a buffer solution (see Cy5-DOPE channel, middle panel). NBD-tagged Cav1-AH was added to the bulk solution and the recruitment observed over time on aLDs presenting low (1) and high (2) PL density (right: time lapses of the droplets in yellow insets). Scale bars, 20 µm, and 10 µm for insets. **(B)** Cav1-AH recruitment over time to various TO droplets presenting different PL densities. Arrow indicates injection time of Cav1-AH to the bulk solution. The PL density evolves with red color darkness. Illustrative micrographs are shown in Fig. S6 A. **(C)** Cav1-AH recruitment over time on various SQ droplets presenting different PL densities. Arrow indicates injection time of Cav1-AH to the bulk solution. PL density varies with red color darkness. See Fig. S6 B for illustrative micrographs. Laser and microscope settings were identical for both SQ and TO experimental conditions. **(D)** Left: TO and SQ oil droplets supplemented with DOPC:Cy5-DOPE (99:1) were formed in buffer containing NBD tagged Cav1-AH. Droplets were imaged by confocal microscope after 30-min incubation time. Scale bar, 30 µm. Right: For both SQ and TO, cav1-AH recruitment over PL density shows a decrease as the PL density increases. Dashed lines are homothetical curve tendencies (with a factor of ∼2.62), indicating a constant relative recruitment between TO and SQ, independent of PL packing level. **(E)** Quantification of Cav1-AH recruitment on aLDs, with or without PLs at their surface. SQ over TO recruitment of Cav1-AH remains constant, independently of the presence of PLs at the droplet surface. Recruitment is normalized by the recruitment on TO droplets. For +PLs condition, Cav1-AH recruitment was averaged for a PL density around150 a.u. in D.

meaningful input in binding per se. These results reveal that the nature of the hydrophobic phase beneath a lipid layer is a major driving force to the binding of AHs (Fig. 5 A).

Based on all our above results, we propose a qualitative and illustrative phase diagram for the recruitment level of AHs based on their affinity to the lipid interface and the PL packing density (Fig. 5 B). The lipid interface could be either that of the neutral lipids or of the PL tails forming the intermonolayer space of a bilayer. A key feature of this diagram is that reaching a given binding level can be obtained by "slight" modulations of the interaction of the AH with the hydrophobic core, e.g., by a single mutation as seen with Cav1-AH in Fig. 1 J. In contrast, larger modulations of the PL packing density would be necessary to reach the same binding level by an AH of lower affinity. A good illustration of the latter point is Plin1_108-137-AH, which did not bind to aLDs connected to the bilayer (Fig. 1 I) but bound to isolated aLDs with ultra-loose PL packing (Fig. S1 F and Fig. S5 B).

PL acyl chain and shape modulate the recruitment of AHs to model LDs

PLs can have different membrane packing propensities and interactions with AHs. Hence, the PL nature could alter the

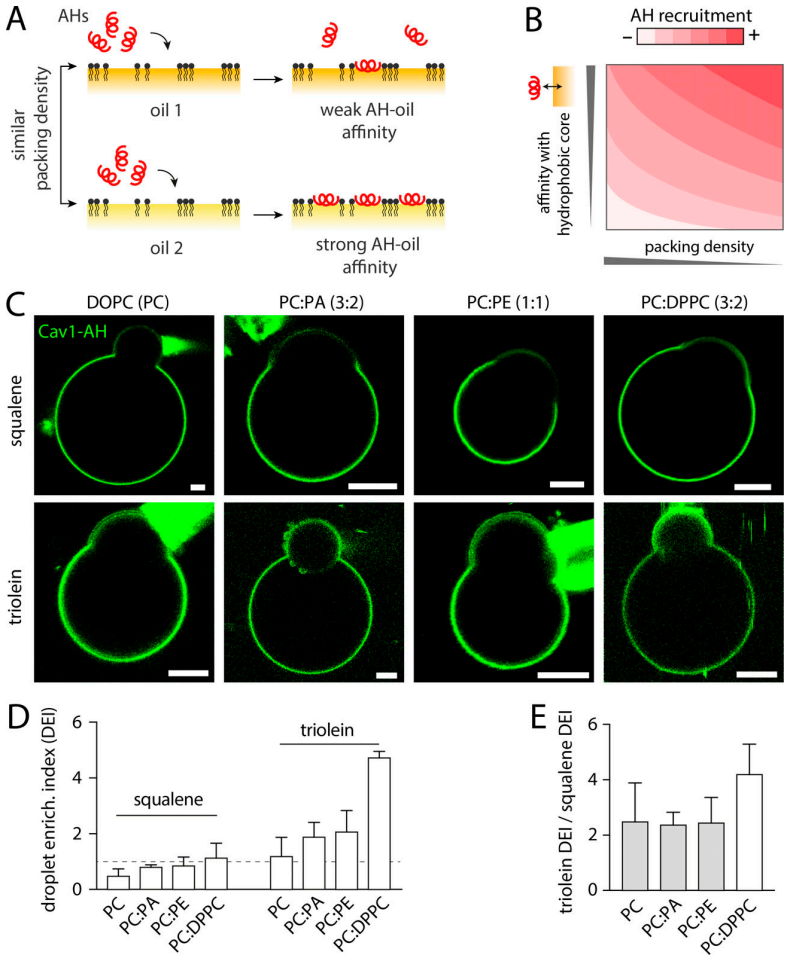

Figure 5. **PL acyl chain and shape regulates the preferential recruitment of AHs to aLDs. (A)** Illustration of the contribution of the neutral lipid type in AH recruitment. For a given PL packing level, an AH will be more recruited to the interface presenting the strongest AH-neutral lipid affinity. **(B)** Illustrative phase diagram showing the AH recruitment extent to the PL monolayer interface covering a hydrophobic region of a monolayer or a bilayer. This phase diagram takes into account the AH affinity for the hydrophobic region and PL packing density. **(C)** Representative confocal fluorescence images of DEVs made of SQ or TO and different PL composition, DOPC, DOPC-DOPA (3:2), DOPC-DOPE (1:1), DOPC-DPPC (3:2), and incubated with NBD tagged Cav1-AH. Scale bars, 5 µm. **(D)** Quantification of the droplet enrichment index for each condition shows a higher recruitment to TO than to SQ aLDs. Changing the PL composition of the DEV improves the recruitment, in PE, PA, and DPPC. **(E)** Ratio between the droplet enrichment index between TO and SQ droplets for a given DEV PL composition. The ratio is constant at ∼2 between DOPC, DOPC-DOPA, and DOPC-DOPE, which have the same acyl tails. With DPPC, which has saturate acyl chains, the ratio is doubled.

binding level of AHs to LDs. We made DEVs containing dioleoyl DOPC (1,2-dioleoyl-sn-glycero-3-phosphocholine), DOPC/DOPE (1:1), or DOPC/DOPA (3:2). DOPE and DOPA had the same dioleoyl acyl chain as DOPC. We added Cav1-AH (Fig. 5 C) and determined the droplet enrichment index for TO and SQ conditions (Fig. 5 D). As compared with DOPC, the presence of DOPE and DOPA improved the enrichment index on the aLD for both neutral lipids. This improvement can be ascribed to the ability of DOPE and DOPA to generate more PL packing defects, due to their negative spontaneous curvature (Bigay and Antonny, 2012; Thiam et al., 2013b). The induced defects were probably identical on the bilayer and the aLD surface, because the relative binding to TO and SQ was constant, around 2, independent of DOPC, DOPE, and DOPA (Fig. 5 E).

The droplet enrichment index quantifies the recruitment to the aLD relative to the bilayer membrane of the DEV. If the bilayer recruitment is decreased, this index can be enhanced, while the net binding to the aLD may not be increased. In DOPC, DOPA, and DOPE, which have the same dioleoyl acyl chain, the interaction of the AH with the hydrophobic region of the bilayer, i.e., the PL acyl chains, is conserved between these PLs. We thus changed the PL acyl chain composition by making DEV with a mixture of DOPC, which has one unsaturation on each acyl chain, and DPPC (1,2-dipalmitoyl-sn-glycero-3-phosphocholine), which is fully saturated, at a ratio of 3:2. Cav1-AH was then added to the medium (Fig. 5 C), and we observed that the droplet enrichment index was drastically increased as compared with DOPC DEVs (Fig. 5 D). In TO, binding was increased by more than four times than in DOPC alone, while for SQ it was only doubled. The ratio of the droplet enrichment factor between TO over SQ was consequently increased (Fig. 5 E). This higher enrichment to the aLD in DPPC was likely due to a diminished recruitment of the peptide to the bilayer.

Altogether, our above results illustrate how alteration of membrane PL composition can shift the relative AH recruitment to the droplet surface to a greater extent. This can partly explain how AHs may be more recruited to LDs instead of bilayers. However, in the above experiments, a PL mixture was used, and we cannot exclude the possibility of a PL sorting between the bilayer and the aLD, which would make interpretation of the data difficult.

Discussion

The binding of AHs to membranes is regulated by several factors including membrane charges, packing defects, curvature, etc.

(Bigay and Antonny, 2012). On LDs, the PL packing density is so far the only lipid parameter found to regulate the binding of AHs (Bacle et al., 2017; Prévost et al., 2018; Thiam et al., 2013a), which depends also on the nature of the amphipathic sequence (Čopič et al., 2018; Prévost et al., 2018). Despite this understanding, it is still unclear how AHs specifically bind to LDs or LD subsets.

Here, we bring experimental evidence supporting that the LD surface is always less dense in PLs than a bilayer. Compared with 100 PLs on average on a monolayer of a bilayer, an aLD monolayer can bear up to a maximum of ∼87 PLs. This maximum is reached when the aLD is connected to the bilayer, which behaves as a PL reservoir. Therefore, LDs are more preset to recruit AHs than bilayers. However, our data show that this is not the whole picture since the nature of the hydrophobic phase, to which an AH has to bind, plays a crucial role in the recruitment. This hydrophobic phase would be PL acyl chains for a bilayer and neutral lipids for LDs. Thus, in addition to the higher PL packing defects on LDs, a more favorable interaction of an AH with the interface of neutral lipids than with PL acyl chains will promote more AH recruitment to LDs.

AHs may preferentially bind to LD subsets containing specific neutral lipids (Hsieh et al., 2012; Straub et al., 2008), and could therefore favor specific oil compositions. This is would be consistent with our data indicating that AHs may have differential affinities with neutral lipids, or at least to their interface with water (Fig. 3). For instance, the N-terminal AH of the lecithin retinol acyl transferase binds more tightly to retinol palmitate than to TO/water surface (Molenaar et al., 2019). On the contrary, Cav1-AH bound better to TO than to retinol palmitate or SQ/water interfaces. Diacylglycerols decreased Cav1-AH recruitment to TO interface but not for Plin1_108-137 (Fig. 3 C). These results support that the amphipathic sequence is crucial to the interactions with neutral lipids, beyond decreasing interfacial tension. This is particularly well illustrated by the ability of Cav1-AH and its F2L,F8L mutant to distinguish well between TO and SQ interfaces, but not the V5R mutant (Fig. 3 D). The question is therefore how amino acids can discern hydrophobic regions. Bulky hydrophobic residues typically facilitate the binding to both bilayers and LDs (Prévost et al., 2018; Wimley and White, 1993), because of the energy cost of exposing these residues to water. Hence, increasing the number of hydrophobic residues would basically decrease tension and hence annihilate specificity, as seen, for example, for NS5A (Fig. 1 I), or for Plin4 or CTP:phosphocholine cytidylyltransferase α mutations (Čopič et al., 2018; Prévost et al., 2018). Instead, to reach binding specificity, there might be amphipathic sequences that are well-tuned in hydrophobicity to decrease the neutral lipid/water surface tension enough without binding to bilayers and designed with an optimal interaction with a given neutral lipid. This seems to be at least the case for the most abundant LD proteins, Perilipin 1–5, whose 11-mer repeat AH sequence lacks bulky hydrophobic residues but can specifically detect LD surface (Ajjaji et al., 2019; Brasaemle, 2007; Čopič et al., 2018; Rowe et al., 2016). For instance, Perilipin 3 seems to better bind to LDs in the presence of diacylglycerols (Skinner et al., 2009).

Finally, the neutral lipid/water surface is permissive to the binding of any AH-containing protein, because of the high energy cost of exposing oil molecules to water, which is decreased by the adsorption of any amphiphilic molecules. Although all AHs may associate with bare neutral lipid/water interfaces, increasing the PL packing density will at some point specifically prevent the binding of AHs of weaker affinity, while those of higher affinity will still bind. For example, Cav1-AH and Plin1_108-137 both bound to the bare TO/buffer interface (Fig. 3 B), but only Cav1-AH bound to aLDs connected to the bilayer (Fig. 1 I). In cells, additional regulatory means can control the recruitment of AHs (Kory et al., 2016; Thiam and Dugail, 2019). For example, crowding of the LD surface by strongly bound proteins, such as Perilipin 1, or hairpin-containing proteins, enables prevention of the nonspecific adsorption of soluble AH-containing proteins (Ajjaji et al., 2019; Kory et al., 2015). Interactions with PL headgroups may also facilitate AH recruitment specificity. A good illustration of such regulation is provided by α-synuclein-AH, a lipid packing sensor that also localizes to LDs (Outeiro and Lindquist, 2003). This AH has a poorly developed hydrophobic face that needs the presence of charged PLs to reveal its ability to target to membrane packing defects (Pranke et al., 2011). AH–AH interactions, or AH interactions with other LD proteins, may also improve the binding selectivity (Kory et al., 2016; Thiam and Dugail, 2019).

In conclusion, our data highlight an undervalued contribution of neutral lipids in controlling the binding of AHs to the surface of LDs. The PL packing density simply regulates the amount of exposed neutral lipids. which dictates the binding level of AHs. Clearly, the full picture of how AHs selectively bind to LDs in a cellular context remains not completely resolved yet, but our data bring us a major step closer to it.

Materials and methods

DEV preparation: giant unilamellar vesicles (GUVs) + LDs

Unless mentioned otherwise, experiments were performed in the following HKM buffer: 50 mM Hepes, 120 mM K acetate, and 1 mM $MgCl_2$ (in Milli-Q water) at pH 7.4 and 275 ± 15 mOsm.

GUVs were prepared by electro-formation (Thiam et al., 2013a). PLs and mixtures thereof in chloroform at 0.5 µM were dried on an indium tin oxide–coated glass plate. The lipid film was desiccated for 1 h. The chamber was sealed with another indium tin oxide–coated glass plate. The lipids were then rehydrated with a sucrose solution (275 ± 15 mOsm). Electroformation is performed using 100 Hz AC voltage at 1.0 to 1.4 Vpp and maintained for at least 1 h. This low voltage was used to avoid hydrolysis of water and dissolution of the titanium ions on the glass plate. GUVs were either stored in the chamber at 4°C overnight or directly collected with a Pasteur pipette.

GUVs composition for used PLs mixtures were as follows: DOPC GUVs were 100% DOPC. Nickel DOPC GUVs were 99% DOPC, 1% DGS NTA(Ni). DOPE-DOPC GUVs were 50% DOPE, 50% DOPC. DOPA-DOPC GUVs were 40% DOPA, 60% DOPC. DPPC-DOPC GUVs were 40% DPPC, 60% DOPC.

To prepare the aLDs, 5 µl of the oil (TO, SQ, or dodecane) was added to 45 µl of HKM buffer. The mixture was sonicated. The diameter of the resulting droplets is on the order of a few hundred nanometers. To make DEV, GUVs were then incubated

with the LDs for 5 min. The GUV-LD mixture was then placed on a glass coverslip pretreated with 10% (wt/wt) BSA and washed three times with buffer.

Confocal microscope images

All micrographs of DEV were made on a Carl Zeiss LSM 800 with a 63× oil immersion objective, and observed samples were held by glass coverslips (Menzel Glaser; 24 × 36 mm, no. 0). Micrographs of oil droplets were made on a Carl Zeiss LSM 800 with a 10× air objective.

Micromanipulation and surface tension measurements by microaspiration

Micropipettes were made from capillaries drawn out with a Sutter Instruments pipette puller. They were used to manipulate the LD-embedded GUVs in order to get a side view of the system. The pipettes were incubated for 30 min in a 5% BSA solution before use, in order to prevent droplets and membranes from adhering to the glass.

Additionally, surface tensions were measured using the same pipettes (Fig. 1 B). The micromanipulation of the external LD monolayer enables the measurement of the external monolayer surface tension. Using Laplace's law, and the measurement of the pipette inner diameter, droplet diameter, and suction pressure, the surface tension of the interface can be determined:

$$\gamma = \frac{\Delta Psuc}{2\left(\frac{1}{Rp} - \frac{1}{Rd}\right)},$$

where $\Delta Psuc$, Rp, and Rd are the suction pressure, the pipette radius, and the droplet external radius, respectively.

The suction was performed using a syringe. The resulting pressure was measured with a pressure transducer, the output voltage of which was monitored with a digital voltmeter. The pressure transducer (range, 55 kPa) was calibrated before the experiments. Micropipettes were made from capillaries (1.0 OD × 0.58 ID × 150 L mm 30–0017 GC100-15b; Harvard Apparatus) with a micropipette puller (Sutter Instrument model P-2000). The micromanipulators used were TransferMan 4r, purchased from Eppendorf. The pressure transducer used was DP103, provided by Validyne Engineering Corp.

Peptide and protein recruitment on the DEV and oil droplets

The DEVs were held by a glass micropipette and observed by confocal microscopy. 5 µl of peptide or protein solution was injected in the 100 µl bulk phase of the DEV solution. The resulting effective peptide concentrations were, respectively, Arf1 (1 µM); caveolin-AH aa159–178 (5 µM); Arfgap1-AH (3.6 µM); and Plin1 AH aa108–137 (50 µM). The DEV is then followed for ∼10 min. Solutions were injected at similar spots from a pipette. Note that for Arfgap1-AH, due to peptide solubility issues, the buffer pH was lowered to 5.5.

Tagging PL with histidine mCherry fluorescent protein

Nickel DOPC GUVs were produced by electro-formation with a mixture of 99% DOPC and 1% DGS-Ni-NTA (wt/wt). DEVs were made using these GUVs. 5 µl of a histidine mCherry at 2.2 µM stock solution was added to 100 µl of the DEV solution and homogenated for 5 min. The resulting solution was placed on a coverslip (pretreated with 10% [wt/wt] BSA and washed three times with buffer). After 5 min, the red fluorescent histidine polluting the coverslip in the observation zone was laser bleached. DEV were brought with a micromanipulator into the clean observation zone and imaged at the apex, i.e., at the coverslip upper surface.

Pendent droplet interface characterization and surface tension measurements

A pendent droplet tensiometer designed by Teclis Instruments was used to measure the interfacial tension of oil/water interfaces. All experiments were conducted at room temperature. To create oil-buffer interfaces, oil drops (from 5 to 16.0 µl) were formed at the tip of a J-needle submerged in 5 ml of HKM buffer.

Oil-buffer interface tension measurement

After forming an oil droplet, the surface tension of the interface is measured until it stabilizes to a plateau. This plateau of tension is the tension designated as the bare oil-buffer surface tension.

Oil-PL interface characterization

To create PL monolayers at the oil-water interface, 100 µl of DOPC liposomes solution were added to the 5-ml HKM buffer. After forming a droplet, the PLs relocate at the interface. Sinusoidal area oscillations are applied to the droplet for 10 cycles as the interfacial tension is recorded. This allows us to calculate the elastic modulus of the interface E (mN/m). Then the droplet is compressed in order to increase the lateral pressure (π) in the PL monolayer, and sinusoidal area oscillations are applied to the droplet for another 10 cycles. This method is reproduced for various lateral pressures, allowing us to build an elastic modulus (E) over lateral pressure (π) isotherm. This isotherm is then fitted using the theoretical Frumkin isotherm and enables us to get an estimation of the molecular area of PLs at the interface.

Frumkin isotherm model and molecular area extraction

The Frumkin isotherm model leads to the following expression of the elastic modulus of a PL monolayer (E) related to the lateral pressure of this same monolayer (π; Kolev et al., 2002):

$$\pi = -RT\,\Gamma_\infty\left[Ln\left(1-\frac{\Gamma}{\Gamma_\infty}\right) - \frac{h\,\Gamma^2}{RT\,\Gamma_\infty{}^2}\right],$$

$$E = RT\,\Gamma_\infty\left[1-\frac{\Gamma}{\Gamma_\infty\left(1-\frac{\Gamma}{\Gamma_\infty}\right)} + 2\frac{h\,\Gamma^2}{RT\,\Gamma_\infty{}^2}\right].$$

The parameters appearing in these two expressions are Γ, the molar PL surface density of the interface; Γ_∞, molar PL surface density extrapolated at the infinite compression; R, the perfect gas constant; T, the temperature; and h, the absorption enthalpy of PL at the oil buffer interface.

By modulating h and Γ_∞ to fit the experimental E-π curve obtained following the protocol described in Pendent droplet interface characterization..., it is then possible to get access to an estimation of the PL density at the interface Γ and to easily obtain the evolution of the molecular area of the PLs.

Oil in water PL-free droplet

To simultaneously observe a micrometric-size droplet constituted of different oil under the confocal microscope, we used two micropipettes, prefilled with two different oil types, and connected to syringes. The pipettes were introduced in a buffer medium placed under a confocal microscope. By pressing on the syringes, multiple droplets of two different compositions were formed in the observation field. The peptide was then added to the medium and peptide recruitment observed by fluorescence.

Oil in water droplet covered with PLs

DOPC PLs in chloroform were dried under argon and oil was added in such proportion to obtain a molar ratio of 0.1%. The mix was then sonicated for 10 min and 100 µl of HKM buffer was then added to 10 µl of oil and gently agitated to obtain the micron-size droplets observed under microscope.

GUV under osmotic shock

DOPC GUVs were produced by electro-formation with a mixture of 99% DOPC and 1% (wt/wt) rhodamine-DOPE (wt/wt). The resulting GUV solution was placed on a coverslip (pretreated with 10% [wt/wt] BSA and washed three times with buffer) and observed with a confocal microscope (10× objective). 20 µl Ultrapure Milli-Q water was added for 100 µl of the GUV solution. GUVs were then imaged over time. GUV radius was measured over time.

Surface tension of different oil-water interface

Surface tension of oil buffer interface was measured using pendent droplet tensiometer except for silicone oil (tension from Mazurek, 2007), PFOB (Astafyeva et al., 2015 and our measurement using pendent droplet tensiometer), and diolein-TO mix (Shimada and Ohashi, 2003).

Quantification and statistical analysis

Fluorescent signal quantification at GUV or aLD surface

To quantify the recruitment of the fluorescent peptides at the surface of LDs, we used the radial angle profile plugin of ImageJ software. This plugin measures the average signal intensity along the perimeter of concentric circles. It results in a plot of the intensity profile of a circular object for various positions relative to its center. We chose the maximum intensity profile as a measurement of recruited peptide density. The same method was used to quantify the PL density covering oil droplet.

Determination of the optical corrective parameter (β), related to Fig. S2

Due to experimental limitations, the DEVs used in this study were mainly imaged along their equatorial cross-section, an easier configuration when using micropipettes for manipulation. However, when measuring the fluorescence signal of aLDs at this equatorial level, we found a significant attenuation as compared with the signal measured at the apex of the droplet (Fig. S2 A). This is very likely due to the mismatch in optical index between the bulk water phase and the oil phase of the droplet (with 63× objective).

To investigate this attenuation effect, we imaged a single oil droplet homogeneously marked with histidine mCherry (Fig. S2 D). We noticed that the intensity of confocal fluorescence signal was varying along the z axis (Fig. S2 D, left). We quantified this signal modification with intensity-linescans at different z positions (see Fig. S2 D, right). The signal was maximum at the lower apex plane, i.e., bottom of the droplet, and almost dimmed just above the equatorial position (see third slice, Fig. S2 D). We reasonably assumed that this effect was due to the refraction of the laser light by the refractive index variation at the droplet–buffer interface. Indeed, when imaged at the lower apex, the light beam from the microscope objective is directly reflected back to the imaging system. On the contrary, when the droplet is imaged at or above the equatorial cross-section, part of the light has to pass through the oil phase of the droplet and is certainly disrupted by the optical index mismatch, leading to the observed signal attenuation (Fig. S2, A and D).

Therefore, the signal measured at the apex (not affected by the optical index mismatch) is to be considered as the correct measurement of the fluorescent signal on the droplet. On the contrary, to get the real signal on the droplet at the equatorial cross-section, the measured signal has to be corrected.

To quantify the signal attenuation at the equatorial cross-section, we imaged various DEV at the equatorial cross-section and the apex. We normalized the droplet signal by the bilayer signal (Fig. S2 B) and compared the normalized signal measured at the apex and the equatorial cross-section. We found an average of 2.67 times less signal at the equatorial cross-section as compared with the apex.

We thus defined a correcting optical parameter β as the apex normalized signal divided by the equatorial cross-section normalized signal (Fig. S2 C), which was therefore equal to 2.67. To properly evaluate the fluorescence on aLDs imaged at the equatorial cross-section, the measured signal then had to be multiplied by the optical parameter β = 2.67.

As some of the DEVs used in this study were made with SQ oil droplets, we performed similar experiments on such systems and found comparable results (Fig. S2 E). The fluorescence signal attenuation between apex (focal plane 1) and equatorial cross-section (focal plane 2) was found at 2.7 (Fig. S2 E, right), a value comparable to those obtained with TO droplets in Fig. S2 B.

Statistical analysis

The statistical comparisons were made using a nonparametric *t* test (GraphPad Prism 7.0a; ***, P < 0.0001; **, P < 0.001; *, P < 0.01). Unless mentioned, all values shown in the text and figures are mean ± SD.

Equipment and reagents

Equipment

Imaging was done using a Carl Zeiss LSM 800 microscope and a 63× objective. Glass coverslips were obtained from Menzel Glaser (24 × 36 mm, no. 0). Micropipettes were made from capillaries (1.0 OD × 0.58 ID × 150 L mm 30–0017 GC100-15b), purchased from Harvard Apparatus; they were stretched by using a micropipette puller from Sutter Instrument (model P-2000). Micromanipulators TransferMan 4r were purchased from Eppendorf. The pressure transducer used was DP103, provided by Validyne Engineering Corp. The pendent droplet tensiometer apparatus was from Teclis Instruments.

Chemical product list

Glyceryl trioleate (TO; T7140), dodecane (297879-1L), SQ (S3626), SE (C9253 1G), monoolein (1-oleoyl-rac-glycerol M7765), retinylpalmitate (RP; R3375), Hepes (54457–250-F), K acetate (P1190), $MgCl_2$ (M8266-100G), BSA 98% (A7906-100G), and sucrose 99.5% (59378-500G) were from Sigma-Aldrich. Perfluorooctyl bromide (AB104047, CAS: 423–55-2) was purchased from Abcr GmbH. Silicone oil (polydimethylsiloxane, 20cSt, ref 84543–290) was purchased from VWR Chemical. Dioleine (800811C, 10 mg dioleyl-sn-glycerol 18–1) was from Avanti Polar Lipids.

PLs, DOPC, DOPE, DOPA, DPPC, DGS-Ni-NTA, rhodamine-DOPE, and cy5-DOPE were from Avanti Polar Lipids.

Peptide and protein origin or production methods

Caveolin fragment tag with NBD refered to as Cav1-AH (fragment 159–178, purity 96.83%, NBD-LFEAVGKIFSNVRINLQKEI), corresponding mutant Cav1-AH(F2L,F8L) (purity 99.28% NBD-ahx-LLEAVGKILSNVRINLQKEI) and Cav1-AH(V5R) (purity 95.33% NBD-ahx-LFEARGKIFSNVRINLQKEI), and Arfgap1 modified fragment tagged with rhodamine refered to as Arfgap1-AH (fragment 199–223, purity 95.49%, rhodamineB-FLNSAMSSLYSGWSSFTTRAKKFAK) were synthesized by Peptide 2.0 (https://www.peptide2.com/).

Plin1 108–137, purity 96.83% (NBD-PPEKIASELKDTISTRLRSARNSISVPIAS), was purchased from ProteoGenix (https://www.proteogenix.science/fr/).

NS5A peptide (rhodamine-SGSWLRDVWDWVCTILTDFKNWLTSKLFPKL-CONH), which is the N-terminal AH of the nonstructural protein 5 of the hepatitis C virus, was provided by F. Penin, University of Lyon, Lyon, France.

Fluorescently labeled Arf1 was generated using an Arf1 variant in which the single cysteine residue of Arf1 was replaced with serine, and the C-terminal lysine was replaced with cysteine, yielding Arf1-C159S-K181C. Published work has demonstrated that exchanging the C-terminal lysine of the small GTPase with a Cys residue, and subsequent fluorescent labeling (using thiol-reactive dyes on Cys181) does not inhibit Arf1 function (Beck et al., 2008). In short, human Arf1-C159S-K181C and yeast N-myristoyltransferase were coexpressed in *Escherichia coli* supplied with BSA-loaded myristate. Cell lysates were subjected to 35% ammonium sulfate, and the precipitate, enriched in myristoylated Arf1, was further purified by DEAE-ion exchange. Eluted fractions of interest were concentrated in spin-column filters with a 10-kD cutoff (Millipore), and fluorescently labeled using Cy3-maleimide (GE Healtcare) according to the manufacturer's protocol. To remove excess dye, samples were purified by gel filtration using a Superdex 75 column (GE Healthcare).

Online supplemental material

Fig. S1 displays micrographs and quantification of various AHs recruitment on TO, dodecane, and SQ DEVs, related to Fig. 1. Fig. S2 describes the experimental determination of the optical correction factor β accounting for the optical index mismatch between the oil droplet and the external water phase. The methodology for determining the optical correction factor β accounting for the optical index mismatch between the oil droplet and the external water phase is described in the Materials and methods section. The figure is related to Fig. 2. Fig. S3 displays complementary experiments for the determination of the PL density in DEV by using tagged PLs and the pending droplet experiment. Dodecane and TO-SE oil mixtures are investigated. The figure is related to Fig. 2. Fig. S4 presents the pendent droplet experimental raw data used for the determination of the area per PL as a function of the lateral pressure. The figure is related to Fig. 2. Fig. S5 displays confocal micrographs corresponding to the quantification of recruitment of AHs to bare oil droplets of various oil compositions. The recruitment as a function of tension is presented. The figure is related to Fig. 3. Fig. S6 shows the recruitment time-lapse of Cav1-AH to TO and SQ droplets of various PL densities. The figure is related to Fig. 4.

Acknowledgments

We are thankful to all the group members for their valuable comments and critical discussions. We also thank Dr. Alain Cagna for helpful discussion and Dr. Alenka Copic for the critical read of the manuscript.

This work was supported by grants from the Agence Nationale de la Recherche (ANR-17-CE11-0003-NANODROP and ANR-18-CE11-0012-01-MOBIL), and by the Paris Sciences et Lettres to A.R. Thiam.

The authors declare no competing financial interests.

Author contributions: A.R. Thiam designed research. A. Chorlay performed experiments. A.R. Thiam and A. Chorlay analyzed data and wrote the manuscript.

Submitted: 15 July 2019
Revised: 14 December 2019
Accepted: 27 January 2020

References

Ajjaji, D., K. Ben M'barek, M.L. Mimmack, C. England, H. Herscovitz, L. Dong, R.G. Kay, S. Patel, V. Saudek, D.M. Small, et al. 2019. Dual binding motifs underpin the hierarchical association of perilipins1-3 with lipid droplets. *Mol. Biol. Cell.* 30:703–716. https://doi.org/10.1091/mbc.E18-08-0534

Antonny, B., S. Beraud-Dufour, P. Chardin, and M. Chabre. 1997. N-terminal hydrophobic residues of the G-protein ADP-ribosylation factor-1 insert into membrane phospholipids upon GDP to GTP exchange. *Biochemistry.* 36:4675–4684. https://doi.org/10.1021/bi962252b

Astafyeva, K., W. Urbach, N. Garroum, N. Taulier, and A.R. Thiam. 2015. Stability of C(12)E(j) Bilayers Probed with Adhesive Droplets. *Langmuir.* 31:6791–6796. https://doi.org/10.1021/acs.langmuir.5b00749

Bacle, A., R. Gautier, C.L. Jackson, P.F.J. Fuchs, and S. Vanni. 2017. Interdigitation between triglycerides and lipids modulates surface properties of lipid droplets. *Biophys. J.* 112:1417–1430. https://doi.org/10.1016/j.bpj.2017.02.032

Beck, R., Z. Sun, F. Adolf, C. Rutz, J. Bassler, K. Wild, I. Sinning, E. Hurt, B. Brügger, J. Béthune, and F. Wieland. 2008. Membrane curvature induced by Arf1-GTP is essential for vesicle formation. *Proc. Natl. Acad. Sci. USA.* 105:11731–11736. https://doi.org/10.1073/pnas.0805182105

Ben M'barek, K., D. Ajjaji, A. Chorlay, S. Vanni, L. Forêt, and A.R. Thiam. 2017. ER Membrane Phospholipids and Surface Tension Control Cellular Lipid Droplet Formation. *Dev. Cell.* 41:591–604.e7. https://doi.org/10.1016/j.devcel.2017.05.012

Bersuker, K., and J.A. Olzmann. 2017. Establishing the lipid droplet proteome: Mechanisms of lipid droplet protein targeting and degradation. *Biochim Biophys Acta Mol Cell Biol Lipids.* 1862(10 Pt B):1166–1177. https://doi.org/10.1016/j.bbalip.2017.06.006

Bigay, J., and B. Antonny. 2012. Curvature, lipid packing, and electrostatics of membrane organelles: defining cellular territories in determining specificity. *Dev. Cell.* 23:886–895. https://doi.org/10.1016/j.devcel.2012.10.009

Bigay, J., J.-F. Casella, G. Drin, B. Mesmin, and B. Antonny. 2005. ArfGAP1 responds to membrane curvature through the folding of a lipid packing sensor motif. *EMBO J.* 24:2244–2253. https://doi.org/10.1038/sj.emboj.7600714

Blaner, W.S., S.M. O'Byrne, N. Wongsiriroj, J. Kluwe, D.M. D'Ambrosio, H. Jiang, R.F. Schwabe, E.M. Hillman, R. Piantedosi, and J. Libien. 2009. Hepatic stellate cell lipid droplets: a specialized lipid droplet for retinoid storage. *Biochim. Biophys. Acta.* 1791:467–473. https://doi.org/10.1016/j.bbalip.2008.11.001

Brasaemle, D.L. 2007. Thematic review series: adipocyte biology. The perilipin family of structural lipid droplet proteins: stabilization of lipid droplets and control of lipolysis. *J. Lipid Res.* 48:2547–2559. https://doi.org/10.1194/jlr.R700014-JLR200

Chorlay, A., and A.R. Thiam. 2018. An asymmetry in monolayer tension regulates lipid droplet budding direction. *Biophysical journal.* 114(3): 631–640. https://doi.org/10.1016/j.bpj.2017.12.014

Chorlay, A., L. Monticelli, J. Veríssimo Ferreira, K. Ben M'barek, D. Ajjaji, S. Wang, E. Johnson, R. Beck, M. Omrane, M. Beller, et al. 2019. Membrane asymmetry imposes directionality on lipid droplet emergence from the ER. *Dev. Cell.* 50:25–42.e7. https://doi.org/10.1016/j.devcel.2019.05.003

Čopič, A., S. Antoine-Bally, M. Giménez-Andrés, C. La Torre Garay, B. Antonny, M.M. Manni, S. Pagnotta, J. Guihot, and C.L. Jackson. 2018. A giant amphipathic helix from a perilipin that is adapted for coating lipid droplets. *Nat. Commun.* 9:1332. https://doi.org/10.1038/s41467-018-03717-8

Fainerman, V.B., R. Miller, and V.I. Kovalchuk. 2002. Influence of the Compressibility of Adsorbed Layers on the Surface Dilational Elasticity. *Langmuir.* 18:7748–7752. https://doi.org/10.1021/la020024e

Gannon, J., J. Fernandez-Rodriguez, H. Alamri, S.B. Feng, F. Kalantari, S. Negi, A.H. Wong, A. Mazur, L. Asp, A. Fazel, et al. 2014. ARFGAP1 is dynamically associated with lipid droplets in hepatocytes. *PLoS One.* 9: e111309. https://doi.org/10.1371/journal.pone.0111309

Guo, Y., T.C. Walther, M. Rao, N. Stuurman, G. Goshima, K. Terayama, J.S. Wong, R.D. Vale, P. Walter, and R.V. Farese. 2008. Functional genomic screen reveals genes involved in lipid-droplet formation and utilization. *Nature.* 453:657–661. https://doi.org/10.1038/nature06928

Henne, W.M., M.L. Reese, and J.M. Goodman. 2018. The assembly of lipid droplets and their roles in challenged cells. *EMBO J.* 37:e98947. https://doi.org/10.15252/embj.201898947

Hsieh, K., Y.K. Lee, C. Londos, B.M. Raaka, K.T. Dalen, and A.R. Kimmel. 2012. Perilipin family members preferentially sequester to either triacylglycerol-specific or cholesteryl-ester-specific intracellular lipid storage droplets. *J. Cell Sci.* 125:4067–4076. https://doi.org/10.1242/jcs.104943

Kassan, A., A. Herms, A. Fernández-Vidal, M. Bosch, N.L. Schieber, B.J. Reddy, A. Fajardo, M. Gelabert-Baldrich, F. Tebar, C. Enrich, et al. 2013. Acyl-CoA synthetase 3 promotes lipid droplet biogenesis in ER microdomains. *J. Cell Biol.* 203:985–1001. https://doi.org/10.1083/jcb.201305142

Kolev, V.L., K.D. Danov, P.A. Kralchevsky, G. Broze, and A. Mehreteab. 2002. Comparison of the van der Waals and Frumkin adsorption isotherms for sodium dodecyl sulfate at various salt concentrations. *Langmuir.* 18: 9106–9109. https://doi.org/10.1021/la0259858

Kory, N., A.-R. Thiam, R.V. Farese Jr., and T.C. Walther. 2015. Protein crowding is a determinant of lipid droplet protein composition. *Dev. Cell.* 34:351–363. https://doi.org/10.1016/j.devcel.2015.06.007

Kory, N., R.V. Farese Jr., and T.C. Walther. 2016. Targeting fat: mechanisms of protein localization to lipid droplets. *Trends Cell Biol.* 26:535–546. https://doi.org/10.1016/j.tcb.2016.02.007

Kralchevsky, P.A., K.D. Danov, and N.D. Denkov. 2008. Chemical physics of colloid systems and interfaces. *In* Handbook of Surface and Colloid Chemistry. CRC Press, Boca Raton, FL. 204–384.

Kučerka, N., J.F. Nagle, J.N. Sachs, S.E. Feller, J. Pencer, A. Jackson, and J. Katsaras. 2008. Lipid bilayer structure determined by the simultaneous analysis of neutron and X-ray scattering data. *Biophys. J.* 95:2356–2367. https://doi.org/10.1529/biophysj.108.132662

Mazurek, M.H. 2007. Silicones. *In* Comprehensive Organometallic Chemistry III. D.M.P. Mingos, and R.H. Crabtree, editors. Elsevier Science, Amsterdam. 651–697. https://doi.org/10.1016/B0-08-045047-4/00052-2

Molenaar, M.R., T.A. Wassenaar, K.K. Yadav, A. Toulmay, M.C. Mari, L. Caillon, A. Chorlay, M.W. Haaker, R.W. Wubbolts, and M. Houweling. 2019. Lecithin: Retinol Acyl Transferase (LRAT) induces the formation of lipid droplets. *bioRxiv.* (preprint posted August 14, 2019). https://doi.org/10.1101/733931

Olzmann, J.A., and P. Carvalho. 2019. Dynamics and functions of lipid droplets. *Nat. Rev. Mol. Cell Biol.* 20:137–155. https://doi.org/10.1038/s41580-018-0085-z

Outeiro, T.F., and S. Lindquist. 2003. Yeast cells provide insight into alpha-synuclein biology and pathobiology. *Science.* 302:1772–1775. https://doi.org/10.1126/science.1090439

Pranke, I.M., V. Morello, J. Bigay, K. Gibson, J.-M. Verbavatz, B. Antonny, and C.L. Jackson. 2011. α-Synuclein and ALPS motifs are membrane curvature sensors whose contrasting chemistry mediates selective vesicle binding. *J. Cell Biol.* 194:89–103. https://doi.org/10.1083/jcb.201011118

Prévost, C., M.E. Sharp, N. Kory, Q. Lin, G.A. Voth, R.V. Farese Jr., and T.C. Walther. 2018. Mechanism and determinants of amphipathic helix-containing protein targeting to lipid droplets. *Dev. Cell.* 44:73–86.e4. https://doi.org/10.1016/j.devcel.2017.12.011

Reddy, A.S., D.T. Warshaviak, and M. Chachisvilis. 2012. Effect of membrane tension on the physical properties of DOPC lipid bilayer membrane. *Biochim. Biophys. Acta.* 1818:2271–2281. https://doi.org/10.1016/j.bbamem.2012.05.006

Rowe, E.R., M.L. Mimmack, A.D. Barbosa, A. Haider, I. Isaac, M.M. Ouberai, A.R. Thiam, S. Patel, V. Saudek, S. Siniossoglou, and D.B. Savage. 2016. Conserved amphipathic helices mediate lipid droplet targeting of perilipins 1–3. *J. Biol. Chem.* 291:6664–6678. https://doi.org/10.1074/jbc.M115.691048

Senkal, C.E., M.F. Salama, A.J. Snider, J.J. Allopenna, N.A. Rana, A. Koller, Y.A. Hannun, and L.M. Obeid. 2017. Ceramide is metabolized to acylceramide and stored in lipid droplets. *Cell Metab.* 25:686–697. https://doi.org/10.1016/j.cmet.2017.02.010

Shi, S.T., S.J. Polyak, H. Tu, D.R. Taylor, D.R. Gretch, and M.M. Lai. 2002. Hepatitis C virus NS5A colocalizes with the core protein on lipid droplets and interacts with apolipoproteins. *Virology.* 292:198–210. https://doi.org/10.1006/viro.2001.1225

Shimada, A., and K. Ohashi. 2003. Interfacial and emulsifying properties of diacylglycerol. *Food Sci. Technol. Res.* 9:142–147. https://doi.org/10.3136/fstr.9.142

Shyu, P. Jr., X.F.A. Wong, K. Crasta, and G. Thibault. 2018. Dropping in on lipid droplets: insights into cellular stress and cancer. *Biosci. Rep.* 38: BSR20180764. https://doi.org/10.1042/BSR20180764

Skinner, J.R., T.M. Shew, D.M. Schwartz, A. Tzekov, C.M. Lepus, N.A. Abumrad, and N.E. Wolins. 2009. Diacylglycerol enrichment of endoplasmic reticulum or lipid droplets recruits perilipin 3/TIP47 during lipid storage and mobilization. *J. Biol. Chem.* 284:30941–30948. https://doi.org/10.1074/jbc.M109.013995

Spanova, M., and G. Daum. 2011. Squalene–biochemistry, molecular biology, process biotechnology, and applications. *Eur. J. Lipid Sci. Technol.* 113: 1299–1320. https://doi.org/10.1002/ejlt.201100203

Straub, B.K., P. Stoeffel, H. Heid, R. Zimbelmann, and P. Schirmacher. 2008. Differential pattern of lipid droplet-associated proteins and de novo perilipin expression in hepatocyte steatogenesis. *Hepatology.* 47: 1936–1946. https://doi.org/10.1002/hep.22268

Thiam, A.R., and M. Beller. 2017. The why, when and how of lipid droplet diversity. *J. Cell Sci.* 130:315–324. https://doi.org/10.1242/jcs.192021

Thiam, A.R., and I. Dugail. 2019. Lipid droplet-membrane contact sites - from protein binding to function. *J. Cell Sci.* 132:jcs230169. https://doi.org/10.1242/jcs.230169

Thiam, A.R., and L. Forêt. 2016. The physics of lipid droplet nucleation, growth and budding. *Biochim. Biophys. Acta.* 1861(8, 8 Pt A):715–722. https://doi.org/10.1016/j.bbalip.2016.04.018

Thiam, A.R., B. Antonny, J. Wang, J. Delacotte, F. Wilfling, T.C. Walther, R. Beck, J.E. Rothman, and F. Pincet. 2013a. COPI buds 60-nm lipid droplets from reconstituted water-phospholipid-triacylglyceride interfaces, suggesting a tension clamp function. *Proc. Natl. Acad. Sci. USA.* 110:13244–13249. https://doi.org/10.1073/pnas.1307685110

Thiam, A.R., R.V. Farese Jr., and T.C. Walther. 2013b. The biophysics and cell biology of lipid droplets. *Nat. Rev. Mol. Cell Biol.* 14:775–786. https://doi.org/10.1038/nrm3699

Vanni, S., H. Hirose, H. Barelli, B. Antonny, and R. Gautier. 2014. A sub-nanometre view of how membrane curvature and composition modulate lipid packing and protein recruitment. *Nat. Commun.* 5:4916. https://doi.org/10.1038/ncomms5916

Walther, T.C., and R.V. Farese Jr. 2012. Lipid droplets and cellular lipid metabolism. *Annu. Rev. Biochem.* 81:687–714. https://doi.org/10.1146/annurev-biochem-061009-102430

Walther, T.C., J. Chung, and R.V. Farese Jr. 2017. Lipid droplet biogenesis. *Annu. Rev. Cell Dev. Biol.* 33:491–510. https://doi.org/10.1146/annurev-cellbio-100616-060608

Welte, M.A. 2015. Expanding roles for lipid droplets. *Curr. Biol.* 25:R470–R481. https://doi.org/10.1016/j.cub.2015.04.004

Wilfling, F., A.R. Thiam, M.-J. Olarte, J. Wang, R. Beck, T.J. Gould, E.S. Allgeyer, F. Pincet, J. Bewersdorf, R.V. Farese Jr., and T.C. Walther. 2014. Arf1/COPI machinery acts directly on lipid droplets and enables their connection to the ER for protein targeting. *eLife.* 3:e01607. https://doi.org/10.7554/eLife.01607

Wimley, W.C., and S.H. White. 1993. Membrane partitioning: distinguishing bilayer effects from the hydrophobic effect. *Biochemistry.* 32:6307–6312. https://doi.org/10.1021/bi00076a001

Wolins, N.E., D.L. Brasaemle, and P.E. Bickel. 2006. A proposed model of fat packaging by exchangeable lipid droplet proteins. *FEBS Lett.* 580:5484–5491. https://doi.org/10.1016/j.febslet.2006.08.040

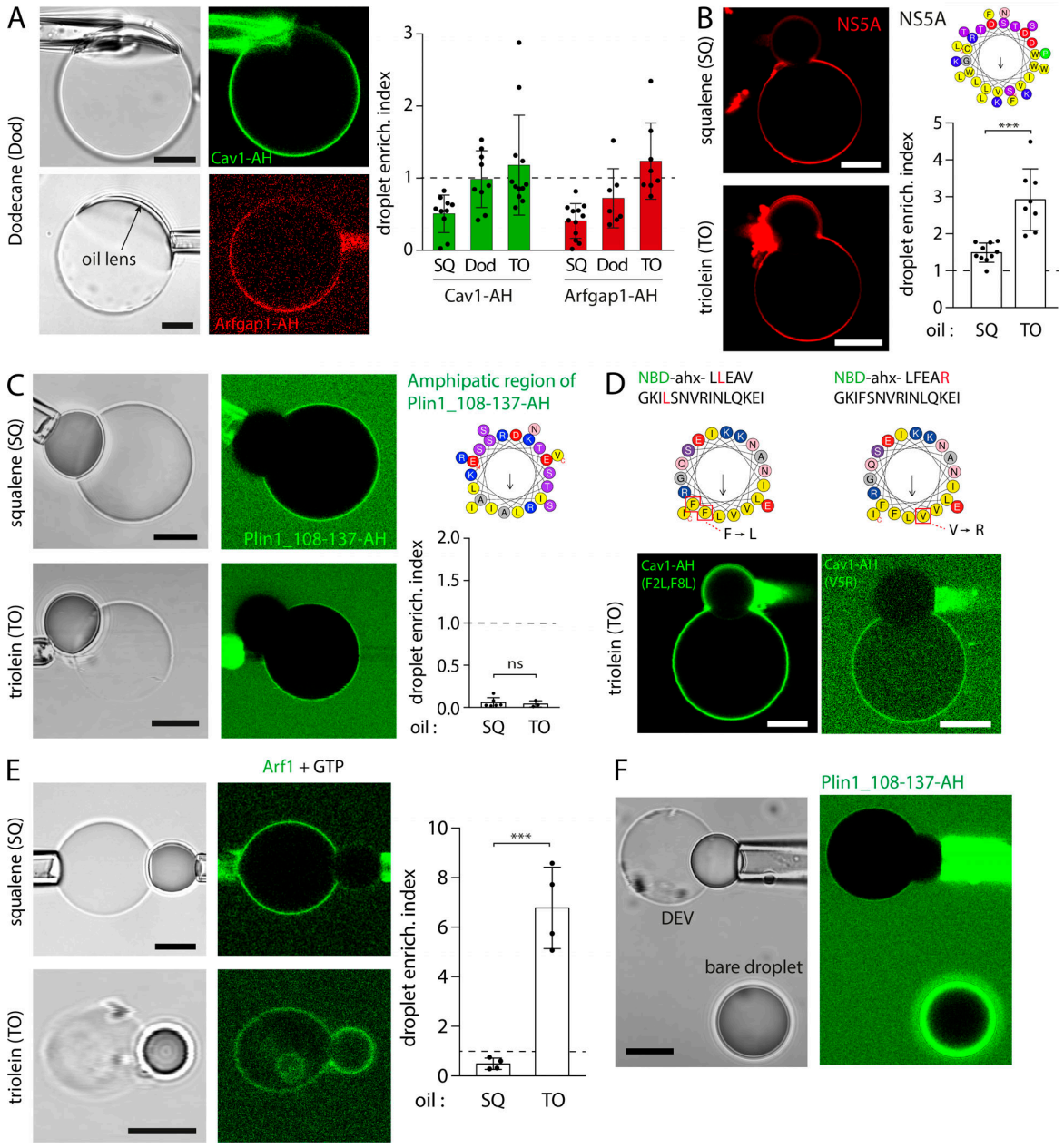

Figure S1. **Micrographs and quantification of various AHs recruitment on TO, dodecane, and SQ DEVs, related to Fig. 1. (A)** Left: DEV are produced using dodecane oil aLDs. Cav1-AH tagged with NBD and Arfgap1-AH tagged with rhodamine B recruitment to the dodecane interface is observed by confocal fluorescence microscopy. Scale bars, 10 µm. Right: Quantification of Cav1-AH and Arfgap1-AH droplet enrichment index for dodecane aLDs. SQ and TO droplet enrichment index are displayed for comparison. Data are represented as mean ± SD. Related to Fig. 1, E–H. **(B)** Left: A rhodamine-tagged NS5A-amphipatic helix (NS5A-AH) of the nonstructural protein 5 of the hepatitis C virus (see structure on the top right) is added to DEV solution. Micrographs show NS5A-AH recruited to DEVs containing SQ or TO aLDs. Scale bars, 10 µm. Bottom right: Quantification of droplet enrichment index for both SQ and TO aLDs. TO as compared with SQ recruited more Cav1-AH to the aLD. *t* test shows significant difference ($P < 0.001$). Data are represented as mean ± SD. **(C)** Left: Plin1 108–137 fragment (containing an AH region displayed on top right) tagged with NBD is added to a DEV solution. Micrographs show visible recruitment of Plin1(108–137)-AH to neither SQ nor TO aLDs. Scale bars, 10 µm. Bottom right: Quantification of Plin1(108–137)-AH droplet enrichment index for SQ an TO aLDs. Related to Fig. 1 I. **(D)** Top: Sequence and localization of mutated Cav1-AH: Cav1-AH(F2L,F8L) and Cav1-AH(V5R). Bottom: Cav1-AH(F2L,F8L) and Cav1-AH(V5R), tagged with NBD, are added to DEV solutions. Micrographs show recruitment of Cav1-AH(F2L,F8L) on TO aLDs but no recruitment of Cav1-AH(V5R). Scale bars, 10 µm. Related to quantification of Fig. 1 J. **(E)** Left: Arf1 full-length protein is added to a DEV solution containing GTP and EDTA. Micrographs show Arf1 recruited to the DEV surface containing SQ or TO aLDs. Scale bars, 10 µm. Right: Quantification of Arf1 droplet enrichment index for SQ and TO aLDs. TO aLDs recruited more Arf1 as compared with SQ droplets ($n = 1, 4$). **(F)** Plin1_108-137-AH, tagged with NBD, is added to a DEV solution (PC bilayer and TO-SE 3:1), which also contained bare TO-SE droplets, not covered by PC. Micrographs show no recruitment of Plin1(108–137)-AH on the aLD present in the DEV bilayer but strong recruitment to the bare droplet. Scale bar, 10 µm.

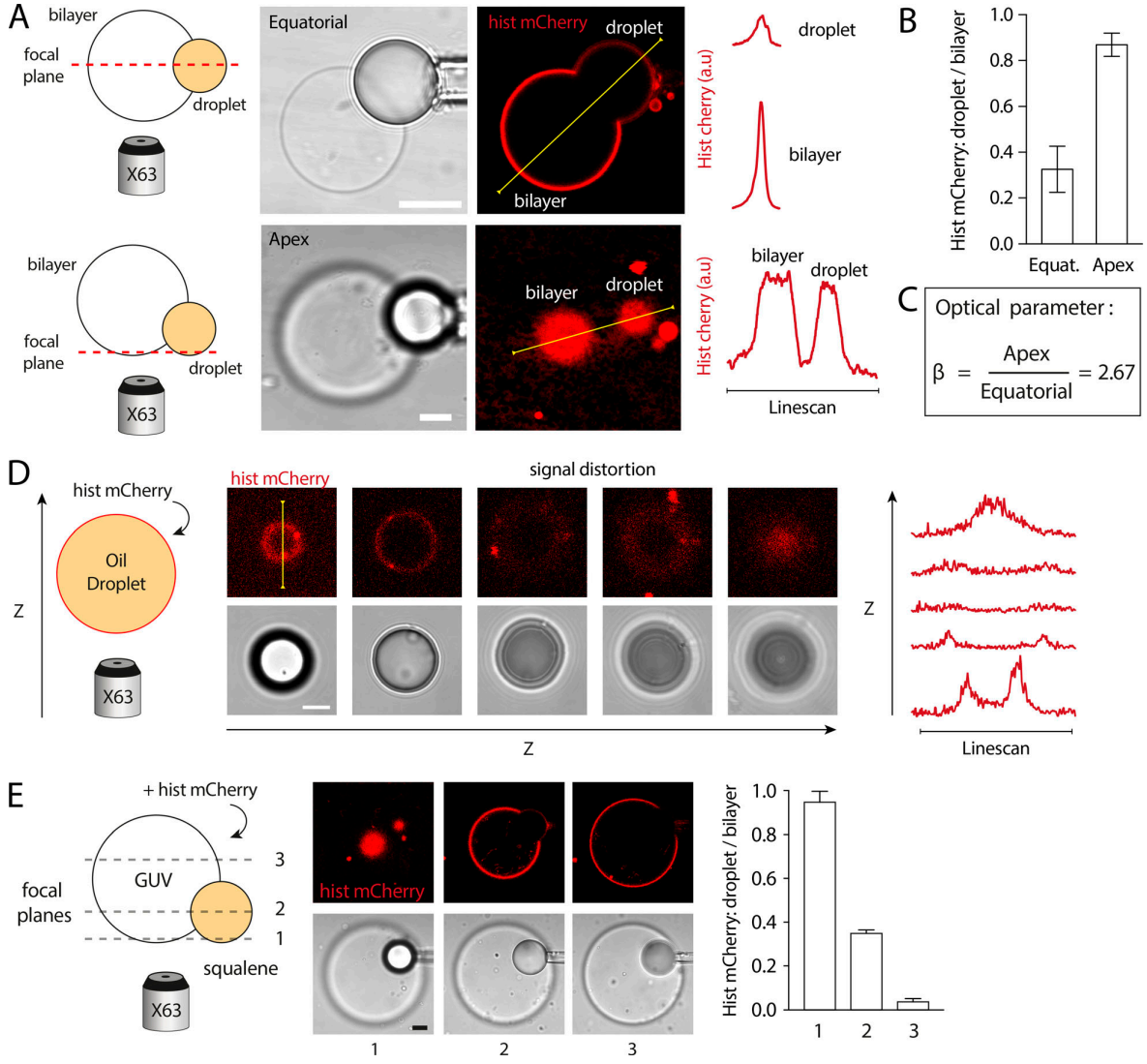

Figure S2. **Experimental determination of the optical correction factor (β) accounting for the optical index mismatch between the oil droplet and the external water phase, related to Materials and methods. (A)** DOPC:DGS-Ni-NTA (99:1) DEV embedding a TO aLD was tagged by histidine mCherry and observed at the equatorial cross section (up) and at its apex (bottom). Histidine mCherry fluorescence on the droplet and the bilayer was quantified at each cross-section. Scale bars, 5 µm. **(B)** Histidine mCherry fluorescence signal on the droplet normalized by signal on the bilayer quantified at each cross-section. Ratio at the equatorial cross-section shows significant attenuation (n > 15 DEVs quantified for each cross-section). **(C)** The correcting factor β is defined as the ratio of the signal at the apex of the droplet over the bilayer signal, divided by the droplet-bilayer signal ratio at the equatorial plane. The factor β was constant, equal to 2.67. **(D)** Left: TO droplet covered by a DOPC:DGS-Ni-NTA (99:1) PL mix was tagged by histidine mCherry and observed at different cross-sections. Right: Fluorescence signal was quantified, and revealed significant signal attenuation at the equatorial cross-section. Scale bar, 10 µm. **(E)** Left: DOPC:DGS-Ni-NTA (99:1) DEV embedding a SQ droplet was tagged by histidine mCherry and observed at different cross-sections. Right: Histidine mCherry fluorescence ratio between the droplet and the bilayer was quantified at each cross-section. Scale bar, 5 µm.

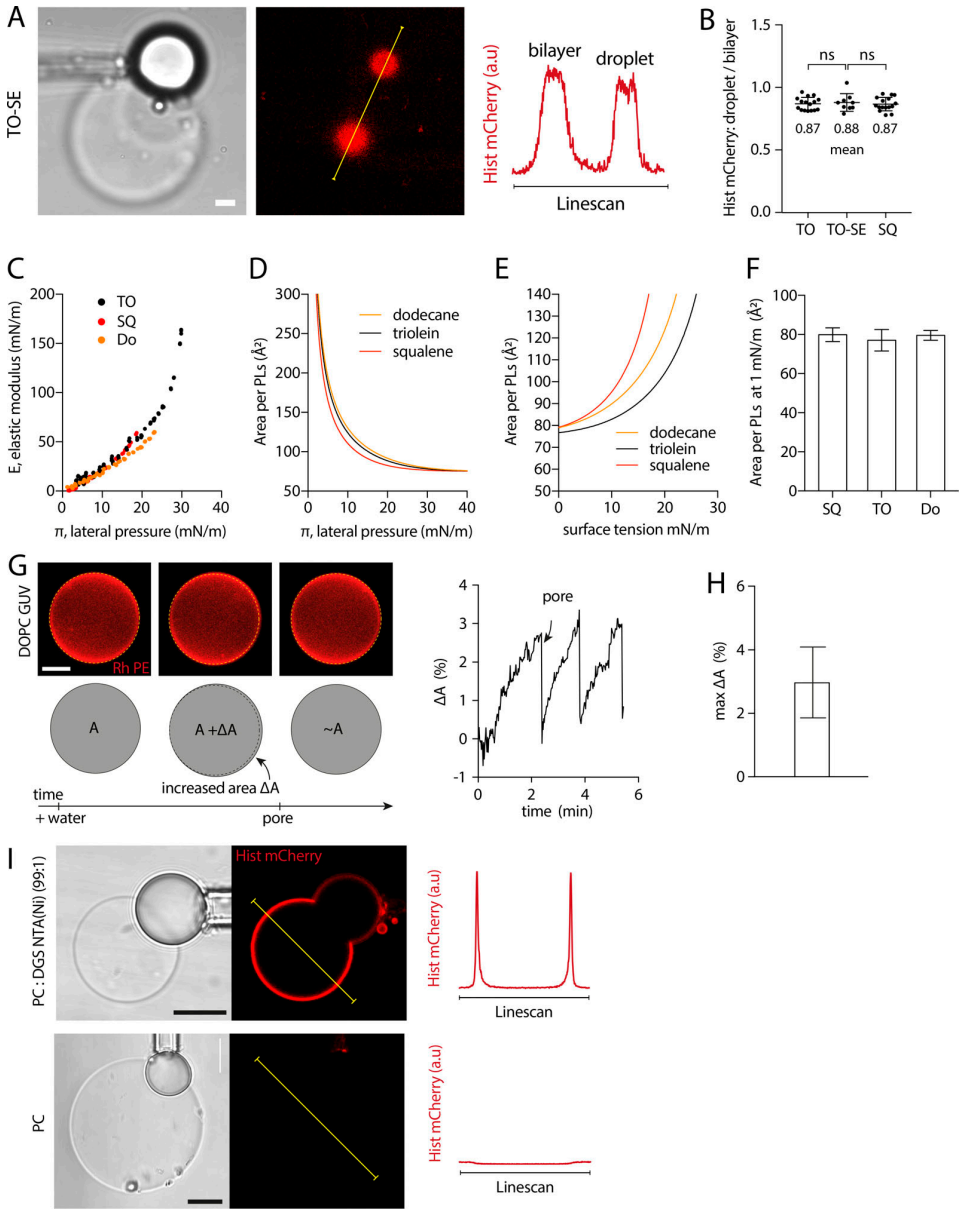

Figure S3. **Additional experimental determination of the PL density in DEV by using tagged PLs and the pending droplet experiment, related to Fig. 2. (A)** Representative confocal fluorescence images of mCherry-histidine marking PLs of a DEV containing TO-SE (3:1) aLDs. Linescans allow for quantification of fluorescence intensity on the bilayer and droplet surface. Scale bar, 5 µm. **(B)** Quantification of the ratio between the droplet and bilayer fluorescence intensity for TO, TO-SE, and SQ aLDs. *t* test shows no significant difference. Data are represented as mean ± SD. Related to Fig. 2, B and C. **(C)** PC-covered oil droplets were characterized using the pending droplet experiment. Resulting elastic modulus-lateral pressure (E-π) isotherms for SQ and TO and dodecane oil phases. See Fig. S4, A–C, for full data. Related to Fig. 2, D and E. **(D)** Area per PC molecule as a function of lateral pressure for SQ, dodecane, and TO oils; data obtained by fitting experimental E-π isotherms with a Frumkin theoretical model. See Fig. S4, A–C, for supporting data. Related to Fig. 2 F. **(E)** Area per PC molecule as a function of droplet surface tension for SQ, dodecane, and TO oils. Surface tension is obtained by subtracting the lateral pressure to bare oil buffer surface tension. Related to Fig. 2 G. **(F)** Area per PC molecule on SQ, dodecane, and TO droplets, at 1 mN/m surface tension. Surface tension of 1 mN/m was chosen as the average surface tension of aLDs in DEV. Related to Fig. 2 G. **(G)** Left: MQ water is added to the surrounding medium of a GUV (PC tagged with 1% Rhodamine-DOPE). The GUV swells because of the osmotic pressure imbalance, increasing its surface area by ΔA. The resulting increase of surface tension favors pore formation in the membrane. When a pore is formed, the internal solution is ejected and the GUV deflates, reducing both surface tension and surface area. At low tension, the pore is able to close, and the phenomenon can start again, resulting in a series of inflations-deflations of the GUV. Right: Quantification of GUV area variation (ΔA) after water addition to the external medium at time = 0 s. Arrows indicate an event of pore formation resulting in a quick decrease of ΔA. **(H)** Quantification of the GUV area variation before the pore formation (max ΔA), corresponding to the maximum area increase that the GUV membrane can endure. The average was found around 3% (GUV composition: PC 99%, rhodamine-DOPE 1%; data of 5 GUVs). **(I)** PC DEVs presenting TO aLDs were produced with and without DGS-Ni-NTA. After being incubated for 10 min with mCherry-histidine, DEV were imaged; mCherry-histidine was recruited only on DEV supplemented with DGS-Ni-NTA; see linescans on the left. Scale bars, 10 µm.

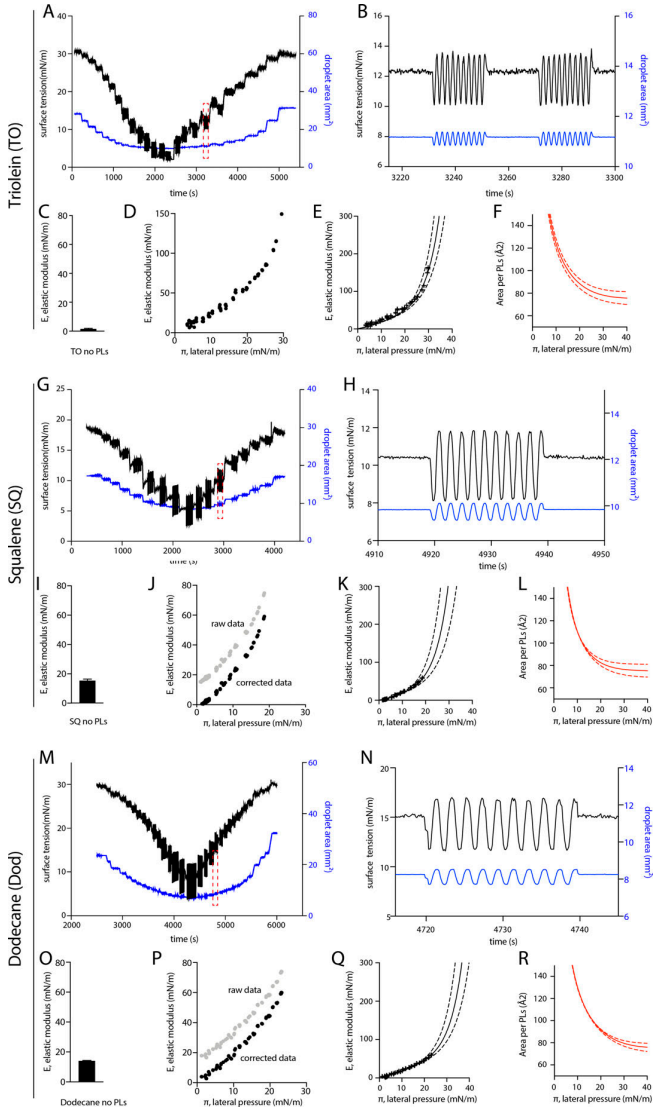

Figure S4. **Pending droplet experimental raw data used for the determination of the area per PL as a function of the lateral pressure, related to Fig. 2. (A)** Area and tension variation of a representative droplet tensiometer experiment using a TO droplet covered by DOPC PL (referred to below as PC). The droplet surface area was decreased and increased, and its surface tension was concomitantly measured. **(B)** Zoom-in: Sinusoidal area oscillations and resulting surface tension variation. Elastic modulus of the interface was calculated by the spectral analysis of the area oscillations and surface tension. **(C)** Elastic modulus (E) of bare TO-buffer interface. **(D)** The resulting elastic modulus against the lateral pressure (E-π) isotherm for TO oil covered by PC, determined from data presented in A. The lateral pressure (π) is calculated as the bare oil-buffer surface tension (s_0) minus the measured oil-PL-buffer surface tension (s): ($\pi = s_0$-s). **(E)** The E-π curve is fitted by a Frumkin theoretical isotherm. Dashed lines show error range on data fitting. **(F)** The resulting area per PC molecule as a function of the lateral pressure (π) on TO oil droplet, obtained by the Frumkin fitting model. **(G)** Area and tension variation of a representative droplet tensiometer experiment using a SQ droplet covered by DOPC PL (referred to below as PC). The droplet surface area was decreased and increased, and its surface tension was concomitantly measured. **(H)** Zoom-in: Sinusoidal area oscillations and resulting surface tension variation. Elastic modulus of the interface was calculated by the spectral analysis of the area oscillations and surface tension. **(I)** Elastic modulus (E) of bare SQ-buffer interface. **(J)** The resulting elastic modulus against the lateral pressure (E-π) isotherm for SQ oil covered by PC, determined from data presented in G. The lateral pressure (π) is calculated as the bare oil-buffer surface tension (s_0) minus the measured oil-PL-buffer surface tension (s): ($\pi = s_0$-s). **(K)** The E-π curve is fitted by a Frumkin theoretical isotherm. Dashed lines show error range on data fitting. **(L)** The resulting area per PC molecule as a function of the lateral pressure (π) on SQ oil droplet, obtained by the Frumkin fitting model. **(M)** Area and tension variation of a representative droplet tensiometer experiment using a dodecane droplet covered by DOPC PL (referred to below as PC). The droplet surface area was decreased and increased, and its surface tension was concomitantly measured. **(N)** Zoom-in: Sinusoidal area oscillations and resulting surface tension variation. Elastic modulus of the interface was calculated by the spectral analysis of the area oscillations and surface tension. **(O)** Elastic modulus (E) of bare dodecane-buffer interface. **(P)** The resulting elastic modulus against the lateral pressure (E-π) isotherm for dodecane oil covered by PC, determined from data presented in M. The lateral pressure (π) is calculated as the bare oil-buffer surface tension (s_0) minus the measured oil-PL-buffer surface tension (s): ($\pi = s_0$-s). **(Q)** The E-π curve is fitted by a Frumkin theoretical isotherm. Dashed lines show error range on data fitting. **(R)** The resulting area per PC molecule as a function of the lateral pressure (π) on dodecane oil droplet, obtained by the Frumkin fitting model.

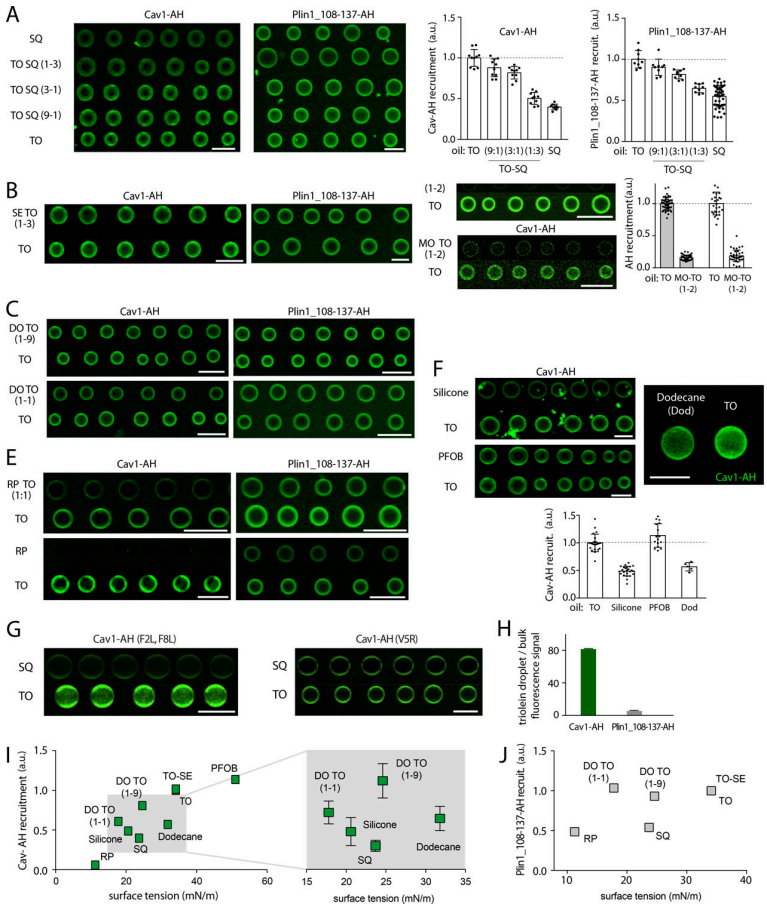

Figure S5. **Confocal micrographs corresponding to the quantification of recruitment of AHs to bare droplets of various oil compositions, related to Fig. 3. (A)** Left: PL-free SQ and TO, and mixtures thereof, TO-SQ (TO/SQ 1/9, 1/3, 3/1), are made in buffer containing Cav1-AH or Plin1_108-137-AH. Representative confocal fluorescence images showing the recruitment level of AHs are shown. The surface fluorescent signal is quantified on each droplet. Scale bar, 50 µm. Right: Corresponding quantification of the fluorescence intensity of Cav1-AH and Plin1_108-137-AH at the surface of droplets of SQ, and TO-SQ mixtures, normalized by the fluorescence intensity on TO droplets. Data are represented as mean ± SD. For Cav1-AH, *t* test shows significant differences between TO and TO/SQ (9/1), TO and TO/SQ (3/1), TO and TO/SQ (1/3), TO and SQ, with the respective P values P = 0.014, P = 0.0005, P < 0.0001, and P < 0.0001. For Plin1_108-137-AH, the *t* test shows no significant differences between TO and TO/SQ (9/1) but shows significant differences between TO and TO/SQ (3/1), TO and TO/SQ (1/3), TO and SQ, with the respective P values P = 0.063, P = 0.0003, P < 0.0001, and P < 0.0001. **(B)** PL-free SE-TO (SE/TO, 1/3) and TO are formed in buffer containing Cav1-AH or Plin1_108-137-AH. Representative confocal fluorescence images showing the recruitment level of AHs are presented. The surface fluorescent signal is quantified on each droplet. Scale bar, 50 µm. Related to Fig. 3 C. **(C)** PL-free droplets containing TO or diolein-TO mixtures (DO/TO, 1/9, 1/1, vol/vol) are formed in buffer in the presence of Cav1-AH or Plin1_108-137-AH. Representative confocal fluorescence images showing the recruitment level of AHs are presented. The surface fluorescent signal is quantified on each droplet. Scale bar, 50 µm. Related to Fig. 3 C. **(D)** Left: PL-free droplets of TO or monolein-TO mixture (MO-TO, 1/2, vol/vol) are formed in buffer containing AHs Cav1-AH or Plin1_108-137-AH. Representative confocal fluorescence images showing the recruitment level of AHs are presented. The surface fluorescent signal is quantified on each droplet. Scale bar, 50 µm. Right: Corresponding quantification of the fluorescence intensity of Cav1-AH and Plin1_108-137-AH at the surface of monolein-TO (1/2) and TO droplets, normalized by the fluorescence intensity of the TO droplet. *t* test shows significant differences between TO and MO-TO (1/2), for both Cav1-AH and Plin1(108–137)-AH (P < 0.0001). Data are represented as mean ± SD. **(E)** PL-free droplets of TO or RP/TO (1/1) are formed in buffer containing Cav1-AH or Plin1_108-137-AH. Representative confocal fluorescence images showing the recruitment level of AHs are presented. The surface fluorescent signal is quantified on each droplet. Scale bar, 50 µm. Related to Fig. 3 C. **(F)** Top: PL-free droplets of TO, silicone, perfluorooctylbromide (PFOB), or dodecane (Dod) are formed in buffer containing Cav1-AH. Representative confocal fluorescence images showing the recruitment level of AHs are presented. The surface fluorescent signal is quantified on each droplet. Scale bar, 50 µm. Bottom: Corresponding quantification of the fluorescence intensity of Cav1-AH and Plin1_108-137-AH at the surface of silicone, PFOB, Dod, and TO droplets, normalized by the fluorescence intensity on TO droplets. *t* test shows significant differences between TO and silicone oil, TO and PFOB, and TO and dodecane, with P values: P < 0.0001, P = 0.03, and P < 0.0001, respectively. Data are represented as mean ± SD. **(G)** PL-free droplets of SQ or TO droplets are formed in buffer containing Cav1-AH, Cav1-AH(F2L,F8L), or Cav1-AH(V5R). Representative confocal fluorescence images showing the recruitment level of these AHs are presented. The surface fluorescent signal is quantified on each droplet. Scale bar, 50 µm. Related to Fig. 3 D. **(H)** Net binding of Cav1-AH and Plin1_107-138-AH to bare TO-buffer interface. Quantification was done by determining the signal on the droplet divided by the signal in the bulk. **(I)** Cav1-AH recruitment to various PL-free oil droplets as a function of the oil-buffer surface tension. Cav1-AH recruitment values are normalized by the AH recruitment on TO droplets. The inset showcases data where there is no correlation between the surface tension and Cav1-AH recruitment level. **(J)** Plin1_108-137-AH recruitment to various PL-free oil droplets as a function of the oil-buffer surface tension. Plin1_108-137 recruitment values are normalized by the AH recruitment on TO droplets.

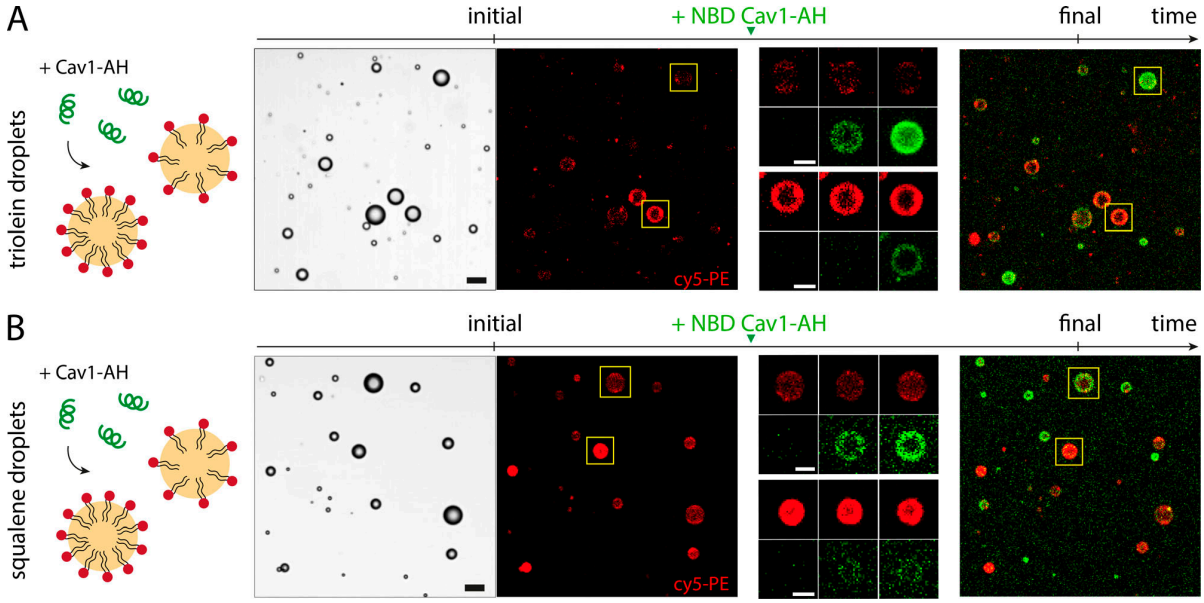

Figure S6. **Recruitment time-lapse of Cav1-AH to TO and SQ droplets of various PL densities, related to Fig. 4. (A)** TO aLD with heterogeneous PL densities (DOPC:Cy5-DOPE; 99:1) were prepared in a buffer solution (see Cy5-DOPE channel) and observed by confocal microscopy. NBD-tagged Cav1-AH was added to the bulk solution and recruitment observed over time on droplets presenting high and low PL density (see selected droplets depicted by yellow squares). After 20 min, droplets presenting the lower PL density had the higher NBD-tagged Cav1-AH signal (right merge image). Scale bar, 20 µm, and 10 µm for insets. Related to Fig. 4 B. **(B)** SQ aLD with heterogeneous PL densities (DOPC:Cy5-DOPE; 99:1) were prepared in a buffer solution (see Cy5-DOPE channel) and observed by confocal microscopy. NBD-tagged Cav1-AH was added to the bulk solution and recruitment observed over time on droplets presenting high and low PL density (see selected droplets depicted by yellow squares). After 20 min, droplets presenting the lower PL density presented the higher NBD-tagged Cav1-AH signal (right merge image). Note the weaker Cav1-AH signal on droplets as compared with TO droplets of Fig. S5 A. Microscope settings were identical in all Fig. S5 A experiments. Scale bars, 20 µm, and 10 µm for insets. Related to Fig. 4 C.

Conclusion

L'objectif de ce travail était d'apporter de nouvelles connaissances sur les mécanismes régissant la biogenèse des corps lipidiques, en privilégiant une approche physique des phénomènes.
De manière à mieux cerner la formation des corps lipidiques (CLs) à partir de la membrane du réticulum endoplasmique, nous souhaitions tout d'abord déterminer les paramètres physiques principaux contrôlant le comportement d'un CL en formation dans une bicouche de phospholipides.
Comme la plupart des CLs sont produits du même coté de la membrane du réticulum endoplasmique, nous nous sommes ensuite intéressés aux leviers physicochimiques que la cellule pourrait utiliser pour assurer cette formation unidirectionnelle, tout en caractérisant son influence sur l'homéostasie du RE.
Pour finir, nous voulions essayer de comprendre le mécanisme d'association entre les CLs et les hélices amphipathiques, domaines présents chez de nombreuses protéines recrutées sélectivement à la surface des CLs.

Pour répondre à ces questions, nous avons utilisé les outils de la physique de la matière molle et conçu un système *in vitro* mimant la topologie de la formation des CLs en cellule. Cette approche nous a permis de moduler finement les paramètres physico-chimiques du système et de mieux comprendre comment la cellule pouvait réguler la formation de ses CLs.

Au cours de cette étude, nous nous sommes rendus compte qu'un CL en formation dans la membrane du RE peut être décrit par un équilibre de tensions de surface. Plus précisément, la forme et la position du CL sont déterminées par un équilibre entre les tensions de surface de la bicouche et des deux monocouches du CL, à la manière d'un système de mouillage à trois phases. Une haute tension de bicouche tend à aplatir le CL, lui donnant une forme de lentille, des hautes tensions de monocouche tendent à former un CL sphérique. Pour voir le CL émerger de la bicouche, une asymétrie de tension entre ses deux monocouches est nécessaire : le CL émerge du coté où la tension est la plus basse. Ceci indique donc que la cellule devrait maintenir une tension plus basse sur l'une des monocouches des CLs en formation de manière à contrôler leur direction d'émergence. Ces résultats illustrent comment la cellule pourrait exploiter des concepts du mouillage pour débarrasser ses membranes de molécules huileuses et favoriser la formation de CLs.

Dans la cellule, la plupart des CLs émergent dans le cytoplasme. Comme nous l'avons observé grâce à notre système *in vitro*, cela implique que la tension de la monocouche

cytosolique des CLs en formation doit être maintenue plus basse. Nous avons donc recherché à savoir comment il était possible de remplir cette condition et nous avons montré que les CLs émergeaient du côté de la monocouche présentant le meilleur degré de couverture, qui peut être modulé, soit par la densité de phospholipides, soit par le recrutement de protéines surfactantes. Si une asymétrie de couverture est induite sur un CL en formation, cette asymétrie est rapidement absorbée par l'émergence du CL du côté présentant la plus grande couverture. Ces résultats suggèrent qu'*in vivo*, la monocouche cytoplasmique doit, au moins transitoirement, présenter une meilleure couverture que la monocouche luminale.
La formation de nombreux CLs dans le cytoplasme à partir du RE va cependant arracher une grande quantité de phopholipides au feuillet cytosolique du réticulum. Il sera donc nécessaire de remplacer ces phospholipides pour préserver la morphologie du réticulum et assurer la formation des futurs CLs dans le cytoplasme. En effet, s'ils ne sont pas remplacés, la couverture cytosolique sera inférieure à la couverture luminale et les CLs auront tendance à présenter des contacts importants avec le lumen du RE. Nos résultats suggèrent donc que le RE subit un remodelage dynamique et asymétrique de sa membrane durant les épisodes de lipogenèse, de manière à assurer une formation des CLs dans le cytoplasme, ce qui est essentiel au développement du protéome des CLs et donc à leurs fonctions biologiques ultérieures.

De nombreuses protéines ciblent la surface des CLs à l'aide d'hélices amphipathiques, motifs qui sont capables d'interagir avec la monocouche de phospholipides des CLs et qui semblent être capables de cibler spécifiquement des sous-groupes de CLs présentant une composition différente en lipides neutres. Afin d'étudier les paramètres contrôlant ce recrutement spécifique, nous avons donc utilisé notre système *in vitro* et des hélices amphipathiques modèles.
Nous avons montré que le recrutement des HAs sur des CLs artificiels dépend directement de la composition en lipides neutres de leur noyau, et que cet effet n'est pas dû à une différence de densité de phospholipides à la surface des CLs, dépendante de la nature du noyau huileux. Plus encore, nos données suggèrent que la composition en acides aminés des HAs détermine l'affinité de l'HA avec les lipides neutres du noyau des CLs, et que la densité de phospholipides est un levier secondaire régulant l'accessibilité des HAs au noyau de lipides neutres.
D'un point de vue plus général, nos résultats permettent d'avancer que la modulation de l'affinité HAs–lipides neutres permettrait de favoriser un recrutement spécifique à la surface de CLs enrichis avec certaines espèces de lipides neutres. Ainsi des protéines présentant ces HAs particulières pourraient de cette manière cibler des sous-groupes de CLs présentant une accumulation de lipides neutres spécifiques. Notre étude souligne donc la contribution sous-évaluée des lipides neutres dans le recrutement des HAs à la surface des CLs.

L'ensemble de nos résultats montre comment des concepts de la matière molle permettent d'appréhender d'une manière originale la biogenèse des CLs et d'affiner nos connaissances sur les mécanismes qui la contrôlent. Les outils de physique des émulsions que nous avons

mis en place nous ont aussi permis d'apporter notre expertise et de participer à deux publications de collaborateurs (Cf Annexe A et B).

Néanmoins, si nos travaux ont abordé le comportement des CLs dans une bicouche, les paramètres régulant leur émergence du RE et le recrutement d'hélices amphipathiques à leur surface, ils sont loin d'avoir décrit toutes les étapes de la formation des CLs.
Dans l'optique de poursuivre ce travail de recherche et d'investigation, il serait extrêmement intéressant d'aborder les autres étapes de la vie d'un CL en gardant notre approche de physicien.
On peut par exemple penser à la naissance du CL où les molécules d'huile dispersées dans le RE se rassemblent pour former un proto-CL. Cette étape, qui suit probablement un mécanisme de nucléation, pourrait en effet être directement influencée par les caractéristiques physicochimiques de la membrane telles que sa courbure, sa tension, son affinité avec l'huile et donc sûrement sa composition phospholipidique. On pourrait aussi penser à décrire plus précisément la jonction qui relie le CL émergé à la membrane du RE dont il est issu.

La physique des émulsions peut encore beaucoup apporter à la compréhension des phénomènes du vivant, en particulier grâce aux modèles *in vitro* qui permettent de contrôler très précisément les paramètres physicochimiques des systèmes étudiés.

Annexes :

Autres travaux en collaboration

Annexe A :

Collaboration avec Ben M'barek et al. 2017

ER Membrane Phospholipids and Surface Tension Control Cellular Lipid Droplet Formation.

Travaux publiés dans Developmental CELL

Le développement du système de manipulation et de mesure de tension de surface des Droplet Embeded Vesicules (DEV) nous a permis d'être capables de mesurer les tensions de surface d'objets micrométriques. Nous avons donc pu utiliser ce système pour mesurer la tension de surface de CLs directement extraits de cellules et ce, pour la première fois à notre connaissance. Grâce à ces données, nous avons obtenu un ordre de grandeur des tensions de surface des ces organelles, ce qui a permis de mieux caractériser leur physico-chimie et d'éclairer son implication dans la formation des CLs.Ces résultats ont été utilisés pour une publication dans le journal Developmental CELL en 2017 qui est présentée dans cette annexe.

Résumé de cette publication (Ben M'Barek et al. 2017[64]) :

Les cellules transforment leur excès d'énergie en lipides neutres qui sont produits au niveau du réticulum endoplasmique (RE). Les lipides neutres sont alors rassemblés dans des gouttes lipidiques sphériques couvertes par une monocouche de phopholipides que l'on appelle corps lipidiques (CLs). Les CLs jouent un rôle clé dans l'homéostasie et le métabolisme énergétique de la cellule. Une des questions qui reste en suspens à propos des CLs est de savoir comment ils émergent du RE. Cette étude aborde ce sujet en étudiant le bourgeonnement de CLs artificiels à partir de bicouches modèles. Nous avons trouvé que la composition phospholipidique de la bicouche et la tension de surface sont des paramètres clés du bourgeonnement. Suivant leur type, les phopholipides ont des aptitudes différentes à induire le bourgeonnement, et ceux qui le favorisent abaissent la tension de surface. Nous

avons observé qu'une diminution de la tension aidait la sortie des CLs du RE et leur bourgeonnement. En cellule, ces conditions aboutissent à la production de petits CLs. Ces résultats révèlent l'importance de la physico-chimie du RE pour le contrôle de la formation cellulaire des CLs.

Article

Developmental Cell

ER Membrane Phospholipids and Surface Tension Control Cellular Lipid Droplet Formation

Graphical Abstract

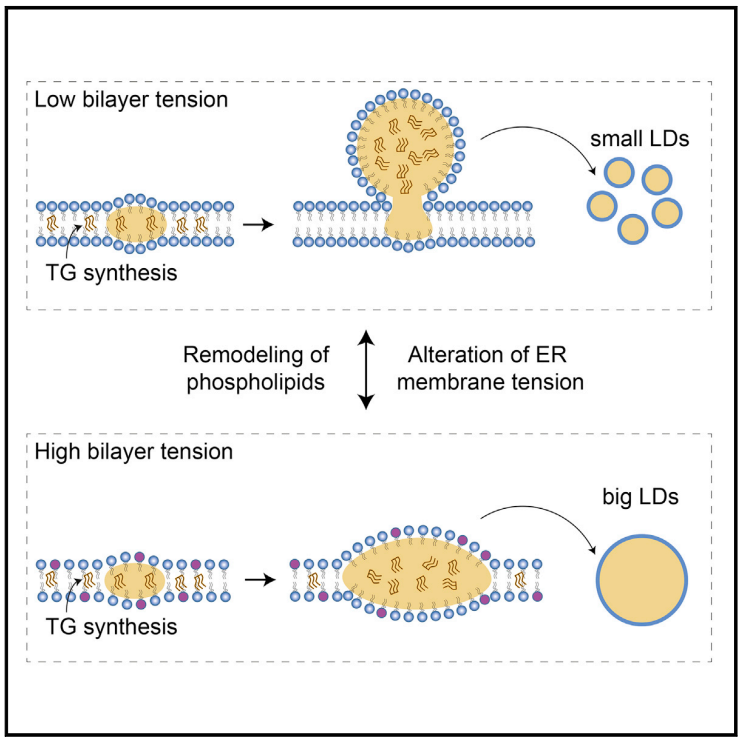

Highlights

- LD formation size is controlled by ER membrane phospholipids and surface tension
- Low tensions favor neutral lipid removal from the ER bilayer and LD budding
- Specific phospholipids decrease tension and favor the formation of small LDs
- Altering ER phospholipid content or tension enables controlled LD formation

Authors

Kalthoum Ben M'barek, Dalila Ajjaji, Aymeric Chorlay, Stefano Vanni, Lionel Forêt, Abdou Rachid Thiam

Correspondence

thiam@lps.ens.fr

In Brief

Lipid droplets (LDs) are intracellular emulsion droplets that regulate cellular energy metabolism. How LDs physically bud from the endoplasmic reticulum (ER) is still unknown. Ben M'barek et al. reconstituted LD formation topology and find that ER bilayer surface tension, modulated by the bilayer phospholipid composition, determines LD formation and size.

Ben M'barek et al., 2017, Developmental Cell *41*, 1–14
June 19, 2017
http://dx.doi.org/10.1016/j.devcel.2017.05.012

CellPress

Please cite this article in press as: Ben M'barek et al., ER Membrane Phospholipids and Surface Tension Control Cellular Lipid Droplet Formation, Developmental Cell (2017), http://dx.doi.org/10.1016/j.devcel.2017.05.012

Developmental Cell
Article

CellPress

ER Membrane Phospholipids and Surface Tension Control Cellular Lipid Droplet Formation

Kalthoum Ben M'barek,[1] Dalila Ajjaji,[1] Aymeric Chorlay,[1] Stefano Vanni,[2] Lionel Forêt,[1] and Abdou Rachid Thiam[1,3,*]
[1]Laboratoire de Physique Statistique, Département de Physique de l'ENS, École Normale Supérieure, PSL Research University, Université Paris Diderot, Sorbonne Paris Cité, Sorbonne Universités, UPMC Université Paris 06, CNRS, 75005 Paris, France
[2]Department of Biology, University of Fribourg, 1700 Fribourg, Switzerland
[3]Lead Contact
*Correspondence: thiam@lps.ens.fr
http://dx.doi.org/10.1016/j.devcel.2017.05.012

SUMMARY

Cells convert excess energy into neutral lipids that are made in the endoplasmic reticulum (ER) bilayer. The lipids are then packaged into spherical or budded lipid droplets (LDs) covered by a phospholipid monolayer containing proteins. LDs play a key role in cellular energy metabolism and homeostasis. A key unanswered question in the life of LDs is how they bud off from the ER. Here, we tackle this question by studying the budding of artificial LDs from model membranes. We find that the bilayer phospholipid composition and surface tension are key parameters of LD budding. Phospholipids have differential LD budding aptitudes, and those inducing budding decrease the bilayer tension. We observe that decreasing tension favors the egress of neutral lipids from the bilayer and LD budding. In cells, budding conditions favor the formation of small LDs. Our discovery reveals the importance of altering ER physical chemistry for controlled cellular LD formation.

INTRODUCTION

Nearly all cells and organisms are able to store excess nutrients so as to buffer energy fluxes. In storage conditions, nutrients are transformed into neutral lipids (oils) such as triglycerides, sterol esters, or squalene, which are packaged into organelles called lipid droplets (LDs) (Martin and Parton, 2006). LDs are dynamic organelles playing a central role in cellular lipid metabolism and homeostasis (Walther and Farese, 2012). LD full function is yet more complex than currently known, as illustrated by the expanding list of unforeseen implications of LD in cell biology (Welte, 2015).

Despite their multiple functions, how LDs form is poorly understood (Pol et al., 2014; Thiam and Beller, 2017; Wilfling et al., 2014a). LD biogenesis starts in the endoplasmic reticulum (ER) wherein a cascade of enzymatic reactions mediates the synthesis of neutral lipids that are encapsulated within the ER intermonolayer space. At a critical concentration, the lipids presumably demix from the ER membrane to nucleate a lipid lens (i.e., gathering of the lipids into a lens-like shape) (Choudhary et al., 2015; Pol et al., 2014; Thiam and Foret, 2016). By acquiring more neutral lipids, the lens grows and buds into a spherical LD that is covered by a phospholipid monolayer containing proteins.

How LDs bud off from the ER is barely understood (Guo et al., 2009; Ohsaki et al., 2014). Whether proteins at the LD surface can physically bud LDs from the ER, similarly to coat-induced vesicle budding, is unknown (Ohsaki et al., 2014). Another hypothesis suggests that LDs undergo spontaneous structural shape changes in the ER to become spherical (Guo et al., 2009; Ohsaki et al., 2014; Pol et al., 2014), but the mechanical basis for this membrane remodeling is also unclear. Related to this model, LD may spontaneously bud from the ER depending on the affinity of the neutral lipids with the ER bilayer (Thiam and Foret, 2016). Which of these two main models best describes LD formation is not known thus far.

Currently a group of proteins, including for example Seipin or the fat storage-inducing transmembrane proteins, has been identified as important for LD formation (Cartwright et al., 2015; Choudhary et al., 2015; Pol et al., 2014; Szymanski et al., 2007; Wang et al., 2016). These proteins probably regulate different steps in LD formation up to LD budding, but their exact functions are still unclear. Interestingly, except for ER enzymes that are implicated in the synthesis of neutral lipids and thereby provide materials for making LDs, there are no other proteins whose absence from all cell lines examined completely abolishes LD formation (Guo et al., 2008). This even encompasses perilipins, which are the most abundant LD proteins. The phenotype associated with the single deletion of a gene encoding a protein associated with LD formation or regulation is often a change in LD size and number (Guo et al., 2008; Yang et al., 2012). Across various cell lines, the deletion of specific genes associated with LD formation or regulation can additionally cause significant accumulation of neutral lipids in the ER bilayer (Adeyo et al., 2011; Gubern et al., 2008; Kadereit et al., 2008; Yang et al., 2012). These observations support the notion that a redundant combination of proteins are necessary to physically bud LD from the ER or proteins simply modulate other factors such as lipids or membrane physical properties that may govern the mechanical formation of LDs (Thiam and Foret, 2016).

As oil droplets, covered by a phospholipid monolayer in the cytosol, LDs can be seen as the disperse phase of an emulsion (i.e., oil-in-water droplets) (Thiam et al., 2013b). Consequently, LDs have particular interfacial properties as compared with the bilayer interface that surrounds most cellular organelles.

Please cite this article in press as: Ben M'barek et al., ER Membrane Phospholipids and Surface Tension Control Cellular Lipid Droplet Formation, Developmental Cell (2017), http://dx.doi.org/10.1016/j.devcel.2017.05.012

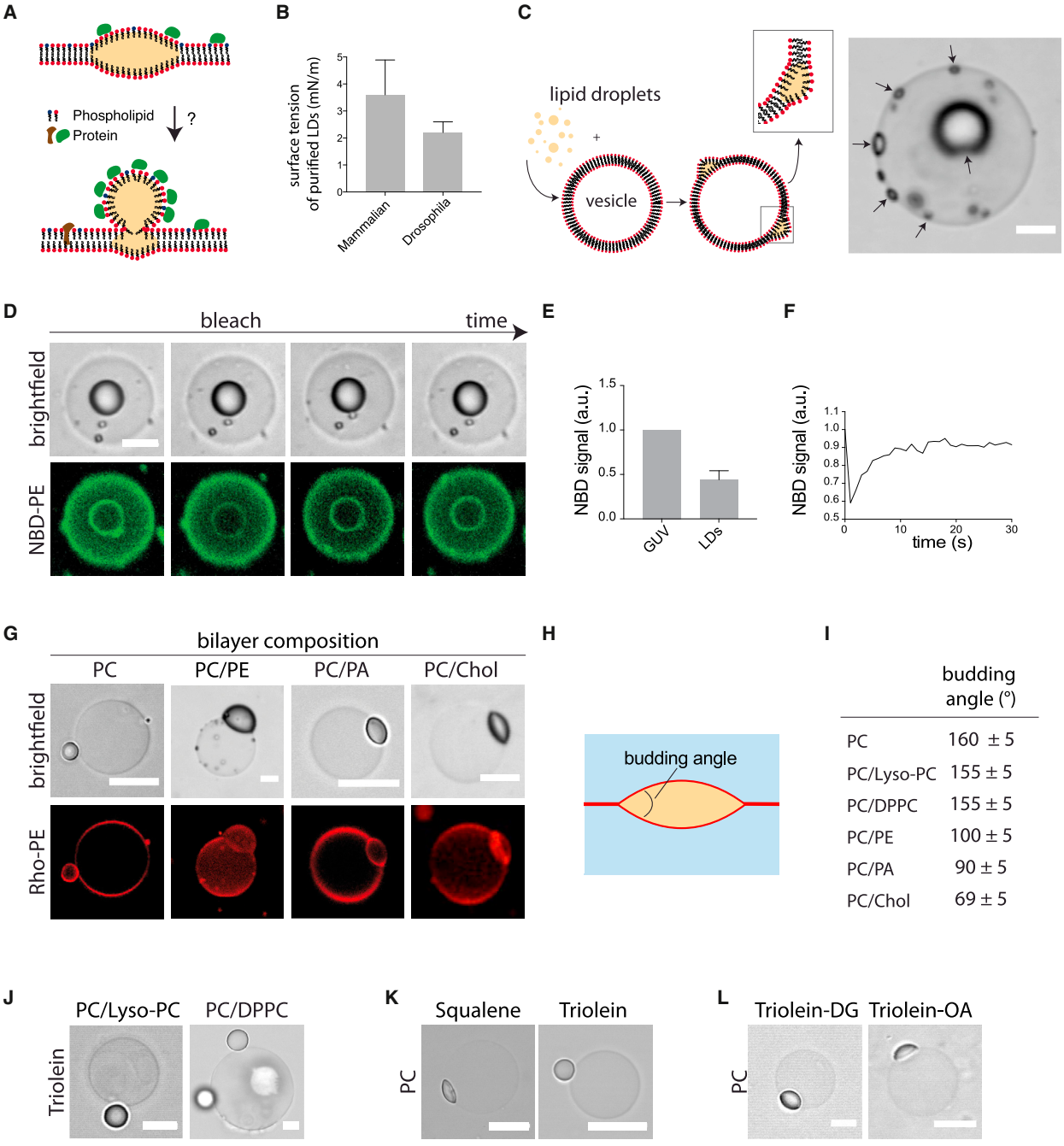

Figure 1. Lipids, Not Coat Proteins, Can Physically Mediate LD Budding

(A) Illustration of lipid droplet (LD) budding step. The contribution of proteins and lipids on LD budding is unknown.

(B) Surface tension values of LDs purified from mammalian (Cos 7) and *Drosophila* (Kc167) cells (Figure S1). Error bars represent the SD.

(C) Reconstitution of the LD formation topology in the ER. Giant unilamellar vesicles (GUVs) are mixed with artificial LDs that are included in the intermonolayer space of the GUV membrane. A bright-field image of the resulting product is shown: many artificial LDs depicted by the arrows are embedded in the bilayer. The bigger LD is on the apex of the GUV because of buoyancy difference with water. Scale bar, 10 μm.

(D) The NBD-DOPE signal of a GUV relocates to the artificial LD. The droplet is on the apex of the GUV. Scale bar, 10 μm.

(E) The signal of the artificial LD is twice as low as the signal of the GUV. Error bars represent the SD.

(F) Completely photobleaching the artificial LD signal leads to recovery, demonstrating the continuity between the GUV and the artificial LD.

(legend continued on next page)

For example, creating an interface between oil and water has a considerable energy cost because of the immiscibility of the two fluids (Thiam et al., 2013b). The parameter describing this energy cost is termed surface tension, which is the energy cost per generated area between the two phases (Penno et al., 2013; Thiam et al., 2013b). To minimize energy, surface tension will minimize the contact area between oil and water, which is attained by making droplets spherical. Thus, in the context of LD budding from the ER, surface tension can be expected to play an important role. However, the implication of surface tension in LD formation has not been explored so far (Thiam and Foret, 2016).

Here, we investigate the mechanism of LD budding from the ER membrane. We developed model systems reconstituting LD formation topology, and provide evidence that ER membrane phospholipids and surface tension are key parameters of LD formation. LD spherical formation is a spontaneous process determined by these parameters. Our results highlight the importance of remodeling ER lipid composition and tension for controlled cellular LD formation.

RESULTS

A Vesicular Budding Model for LD Formation Is Energetically Too Costly

In the coat-induced budding model (Figure 1A), the lateral interaction energy per area between two proteins has to be larger than the membrane surface tension (Chernomordik and Kozlov, 2003), which is the energy per created area between two compartments. Coat proteins such as clathrin or complex protein I polymerize to induce budding. The energy they provide should reflect the amount of energy required for proteins to mediate LD budding.

The interaction energy between clathrin proteins, or complex protein I coat proteins, is in the range of 0.1–0.5 mN/m (Chernomordik and Kozlov, 2003; Foret, 2014; Saleem et al., 2015; Thiam and Pincet, 2015). For the vesicular budding model of LDs to be possible, these values have to be larger than the surface tension of LDs. By using microaspiration techniques, we measured the surface tension of LDs purified from mammalian and *Drosophila* cells. The tension values were above 2 mN/m (Figure 1B), much larger than the interaction energy between coat proteins. Consequently, LD budding from the ER by coat-like proteins is unlikely. For illustration, budding a 100-nm-sized LD would require an energy input of over 10^4 k_BT at least (Figure S1B), while complex protein I, for example, can only provide at maximum $\sim 2 \times 10^3$ k_BT (Thiam and Pincet, 2015).

In Vitro Reconstitution of LD Formation

We next focused on the alternative mechanism by which neutral lipids would naturally assemble and adopt a spherical shape. We tested this hypothesis in vitro. We made giant unilamellar vesicles (GUVs) and mixed them with artificial LDs, which were incorporated into the intermonolayer space of the GUV membrane (Figures 1C, S1C, and S1D). Indeed, by making GUVs containing fluorescent phospholipids, the fluorescence partitioned to the artificial LDs. We observed 2-fold less fluorescence signal on the LD than on the GUV, showing that the LD is covered by a single phospholipid monolayer (Figures 1D and 1E). In addition, LD recovered fluorescence following complete photobleaching of the fluorophore (Figures 1D and 1F; Movie S1), proving that there is continuity between the GUV bilayer and the LD monolayer. Based on these observations, we think that this system reproduces well the topology of LD formation.

We next made GUVs containing various phospholipids and mixtures thereof, and added artificial LDs (Figures 1G and S1C). Alternatively, we made GUVs of fixed phospholipid composition and then added artificial LDs that contained the phospholipid of interest (Figure S1D). With both strategies, we observed that the artificial LDs had different budding shapes that depended on the phospholipid and neutral lipid composition (Figures 1G and 1J–1L). To characterize the droplet shape, e.g., the budding shape, we defined the budding angle as the angle formed between the two monolayers enclosing the oil phase (Figure 1H). A small angle corresponds to a lens-shaped LD, whereas formation of a spherical LD, which we call here LD budding, requires a budding angle close to 180°.

For artificial LDs made of triolein (one of the main triglycerides in cellular LDs), when GUVs were composed of phosphatidylcholine (PC) or a mixture of PC and lyso-phosphatidylcholine (Lyso-PC), the LDs adopted a budded shape (Figure 1J). In contrast, when the GUVs contained a mixture of PC and phosphatidylethanolamine (PE), or PC and phosphatidic acid (PA), the artificial LDs did not bud (Figure 1G). Moreover, in PC GUVs, squalene-containing artificial LDs did not bud, while triolein-containing LDs budded (Figure 1K). We studied other biologically relevant conditions and found various budding states depending on the lipid composition (Figures 1J and 1L). Finally, we found that altering the local concentration of lipids such as free fatty acids dynamically reformed the LD shape (Figures S1E and S1F; Movie S2). Our results therefore suggest that (1) LDs can spontaneously bud from the ER membrane, i.e., without the mechanical action of proteins, (2) ER phospholipids play a critical role in LD budding, and (3) phospholipids have different budding aptitudes.

(G) GUVs made with different phospholipids and mixtures thereof have different artificial droplet shapes. PC, phosphatidylcholine; PE, phosphatidylethanolamine; PA, phosphatidic acid; Chol, cholesterol. Rhodamine-PE is used to visualize the membranes by fluorescence. Representative images are shown for each condition. Scale bar, 10 μm.

(H) The budding shape is characterized by the budding angle: the angle formed between the two monolayers enclosing the lipid oil phase.

(I) The budding angles are determined for different phospholipid conditions and triolein as the neutral lipid phase: PC (n = 15), PC/PE (n = 12), PC-Lyso-PC (n = 12), PC/DPPC (n = 12), PC/PA (n = 20), and PC/Chol (n = 5).

(J) The artificial LDs are almost fully budded when the GUV bilayer is made of PC containing Lyso-PC or saturated PC (dipalmitic phosphatidylcholine). Scale bar, 10 μm.

(K) Squalene-containing artificial LDs are non-budded in PC GUVs while triolein LDs are budded. Scale bar, 10 μm.

(L) Dioleoyl glycerol (DG)- and oleic acid (OA)-containing artificial LDs are non-budded. Scale bar, 10 μm.

See also Figure S1; Movies S1 and S2.

Deciphering the Differential Budding Aptitudes of Phospholipids

The model vesicles difficultly formed with particular lipid compositions, and were often multilamellar. To be able to evaluate the individual budding capacity of each lipid component, we decided to switch to a more controllable system based on micrometric adhesive emulsion droplets (Figure 2A), termed droplet interface bilayer (Bayley et al., 2008; Poulin and Bibette, 1998; Thiam et al., 2011, 2012). The topology of these emulsion droplets recapitulates the configuration of an LD in the ER membrane, as the bilayer splits up into two monolayers covering oil (Figure 2A). The size and curvature of the buffer droplets do not affect the angle between the two monolayers (see STAR Methods). The angle of the droplet interface bilayer system thus describes the budding angle (Figure 2A) and the shape of a forming LD in a bilayer (Figure 2B). Formation of a spherical LD, called LD budding, also corresponds here to an angle close to 180° (Figure 2B).

Experimentally, we made buffer drops in neutral lipids containing lipid surfactants (i.e., amphiphilic molecules, including phospholipids) that absorbed to the surface of the drops and formed a monolayer (Figure 2A). When two drops were close enough to each other, they spontaneously formed a bilayer that is continuous with the two monolayers, resulting in a budding angle (Figure 2B and Movie S3). With this technique we wanted to determine the ability of various lipid surfactants to bud neutral lipids. We worked with PC, PE, PA, phosphaidylinositol (PI), 1-monooleoyl glycerol, 1,2-dioleoyl glycerol, cholesterol, and oleic acid. We varied the acyl chains of PC, testing dimyristelaidoyl PC (14:1, PC), dipalmitic PC, polyunsaturated PC, and Lyso-PC. Lyso-PC constituted a particular case as the buffer drops systematically fused; we chose to mix Lyso-PC with PA at 20:80, which was the maximum Lyso-PC amount that allowed the formation of stable droplet interface bilayers. All of these lipid surfactants are present in the ER membrane but at different levels, depending on the cell type or metabolic state; the differences between the phospholipids are their headgroups, or their acyl chain number, length, and saturation. For the neutral lipid phases we used triolein, a triolein-sterol ester mixture (75:25, w/w), and squalene (Figures 2C, 2D, and S2B). These neutral lipids are the most abundant ones and their concentrations in LDs depend on the cell type or metabolic condition.

For each neutral lipid and phospholipid combination, we measured the budding angle (Figures 2E, 2F, and S2C–S2D). We found three main classes of lipid surfactants and phospholipids (Figure 2E). First, saturated phospholipids, PI, and Lyso-PC met the budding condition for LDs containing any of the neutral lipids (Figure 2E). Second, PC and polyunsaturated phospholipids enabled the budding of specific neutral lipids (Figure 2E). For instance, consistently with Figure 1K, we observed that PC mediated the budding of triolein but not of squalene, or of sterol esters (Figure 2E). Third, lipids such as PE, PA, diacylglycerol, and cholesterol did not meet the budding requirement for any of the neutral lipids (Figure 2E). These results also show that, for a given neutral lipid composition, only specific phospholipids met the budding condition for LDs (Figure 2F).

This droplet interface bilayer approach enabled us to determine the individual contribution of each lipid surfactant and phospholipid on LD budding. Our observations on the differential budding aptitudes of phospholipids are consistent with the shapes of artificial LDs contained in GUVs (Figures 1G and 1I–1L). Altogether, the GUV and droplet interface bilayer experiments suggest that, when a given neutral lipid is synthesized in the ER, increasing the local concentration of specific phospholipids will allow to efficiently package the neutral lipids into spherical LDs.

Neutral Lipids Are Naturally Removed from the Bilayer under Budding Conditions

To make an LD, the neutral lipids in the ER must be removed from the bilayer and transferred into the forming LD. We thus asked whether the differential phospholipid budding aptitudes is related to a differential ability to remove neutral lipids from the bilayer for their packaging into droplets. To address this question we worked with triolein, the most abundant triglyceride, and PC and PE, the most abundant ER phospholipids. We made PE-droplet interface bilayers in a triolein environment containing fluorescent triolein-pyrene, which was used as a reporter for triolein localization (Figure 3A). We observed that PE, which did not promote budding (Figures 2E and 3A), tolerated triolein accumulation in the bilayer (Figure 3A and 3B); the triolein signal located in the bilayer was around 15% of the surrounding triolein signal (Figures 3B and 3E). When we instead used PC, which promoted budding (Figures 2E and 3C), triolein was absent from the bilayer (Figures 3C–3E), despite the massive surrounding triolein environment; similar observations were made with other budding phospholipids such as saturated phospholipids (not shown). Accordingly, we observed that PC/PE (50:50) GUVs containing artificial triolein LDs had more triolein signal in the bilayer than in PC GUVs (Figures S3E and S3F). These observations suggest that phospholipids have different aptitudes for removing neutral lipids from the ER bilayer. Importantly, the budding condition coincided with the egress of free neutral lipids from the bilayer (Figures 3C and 3D).

To follow the neutral lipid egress from the bilayer during budding, we made a droplet interface bilayer with PE and then added PC-in-triolein in the bulk phase (Figure 3F). We recorded the evolution of the triolein-pyrene signal in the bilayer and the budding angle. Over time we observed an increase of the budding angle, which was indicative of PC recruitment to the membranes (Figure S3G). In the meantime, the triolein-pyrene signal in the bilayer decreased (Figures 3F, 3G, and S3H). Consequently, based on the budding angle increase, these results support the conclusion that neutral lipids are naturally removed from the bilayer concomitantly with LD budding (Figure 3H). With lipid surfactants or phospholipids that do not promote budding, neutral lipids will accumulate in the bilayer.

The Decrease of the Bilayer Surface Tension Mediates Triolein Egress from the Bilayer and LD Budding

Our previous results support that the molecular affinities between neutral lipids and phospholipids are important for packaging the lipids and budding of LDs (Figures 1, 2, and 3). These molecular interactions are encompassed by the surface tension parameter, which is here the energy cost per generated area between two liquid phases. During LD formation, three surface tensions come into play (Figure 4A): the surface tension of the bilayer separating the ER lumen and the cytosol, the surface

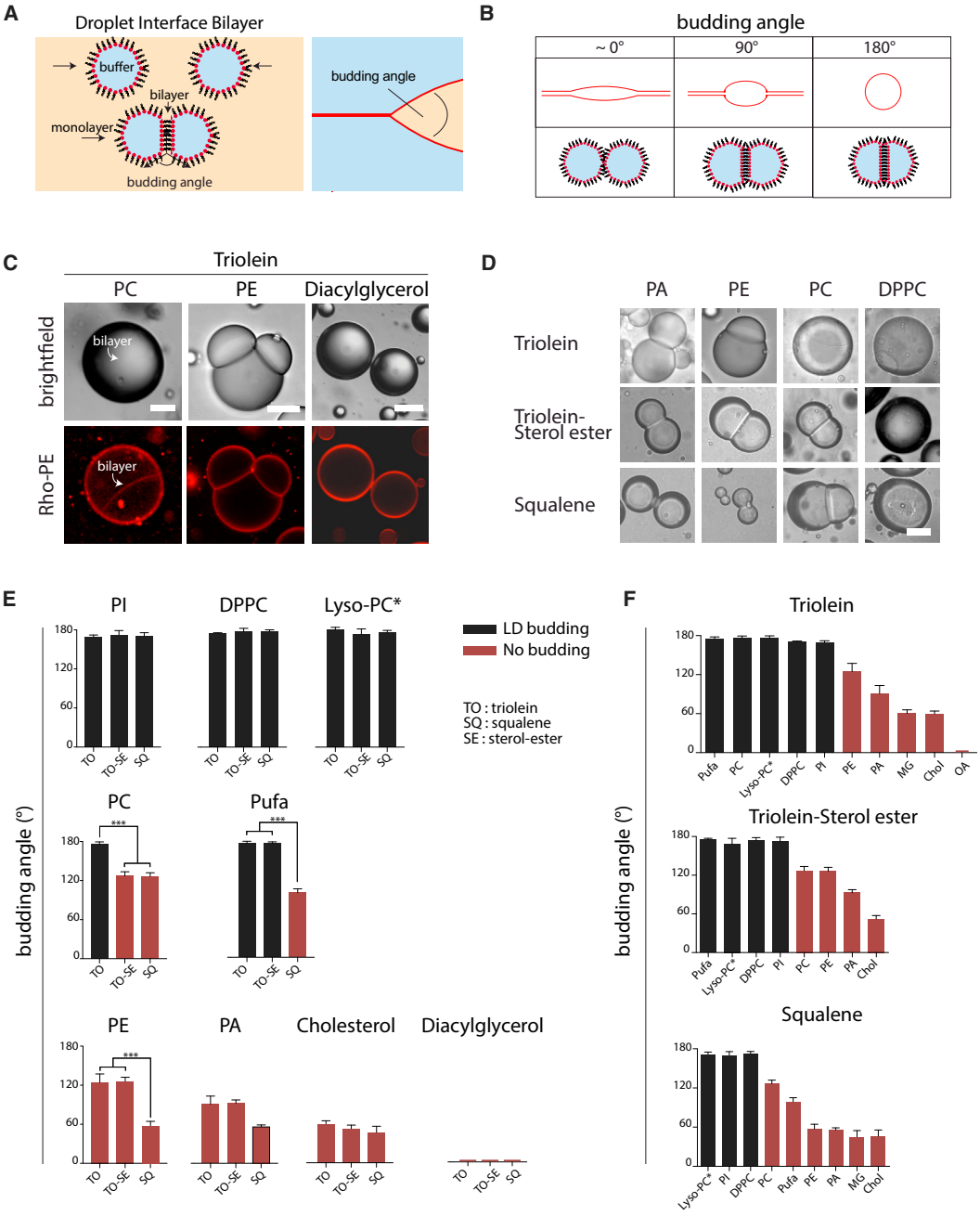

Figure 2. Determination of the Individual Contribution of Phospholipids on LD Budding

(A) Diagram of the principle of the droplet interface bilayer. Right diagram illustrates the analogy with an LD forming in the ER and the budding angle.

(B) Equivalence between the budding shape and the droplet interface bilayer, based on the budding angle.

(C) Example cases of droplet interface bilayers of different angles formed using triolein and phosphatidylcholine (PC), phosphatidylethanolamine (PE), and dioleoyl glycerol. Rhodamine-PE served as a marker for the monolayer and bilayer interfaces. Scale bars represent 10, 20, and 50 μm, respectively.

(D) Images of droplet interface bilayers made with other lipid compositions. Scale bar, 20 μm.

(E) Quantification of the budding angles for the lipid surfactants in the presence of different neutral lipids (red: non-budding compositions, the budding angle is below 180°; black: budding compositions, the budding angle is close to 180°). Lyso-PC* corresponds to a mixture of Lyso-PC and PA at a ratio of 20:80. More than 20 droplet interface bilayer angles were quantified for each composition. Error bars represent the SD. ***$p < 0.0001$.

(F) Representation of the budding angle for given neutral lipids and varied lipid surfactants. Error bars represent the SD.

See also Figure S2 and Movie S3.

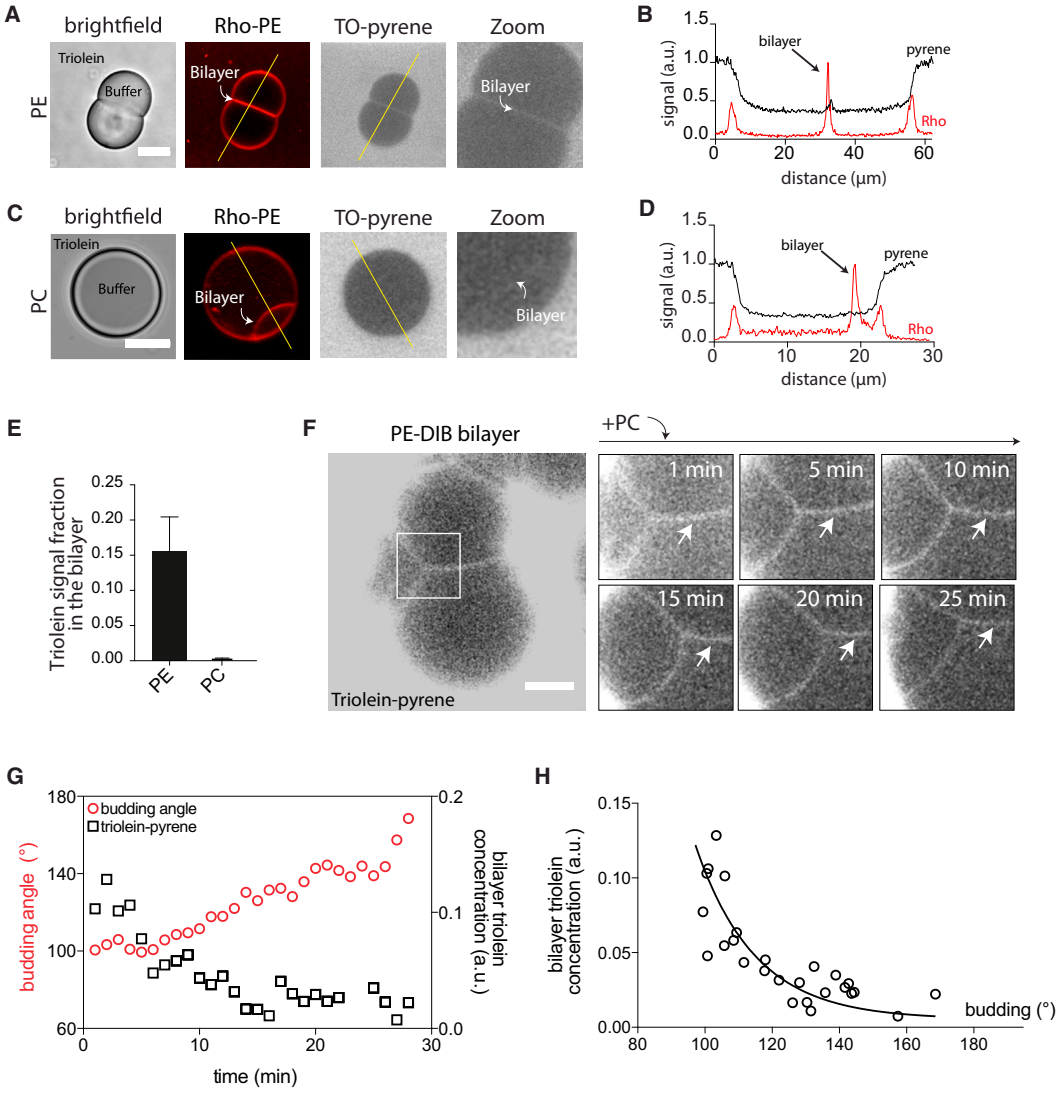

Figure 3. LD Budding Is Concomitant with the Natural Neutral Lipid Egress from the Bilayer

(A) Droplet interface bilayers made with PE in triolein containing 5% triolein-pyrene have the signal in the bilayer (blue signal and zoom). Scale bar, 10 μm.

(B) Rhodamine-PE, marking the bilayer and the monolayer, and triolein-pyrene, marking triolein localization, are plotted over the section made in (A).

(C and D) Almost no triolein signal is detected in PC-droplet interface bilayer. Scale bar, 20 μm.

(E) Concentration of triolein-pyrene in the bilayer compared with the surrounding bulk triolein phase (as in A–D). This concentration is about 15% for PE-droplet interface bilayer and almost 0 for PC-droplet interface bilayer. Error bars represent the SD.

(F) Addition of PC-in-triolein in the phase surrounding a PE-droplet interface bilayer leads over time to the removal of triolein-pyrene from the bilayer and the increase of the angle. The arrows point to the bilayer signal. Scale bar, 30 μm.

(G) Quantification of triolein-pyrene removal from the bilayer. The decrease of the triolein concentration is concomitant with the increase of the budding angle that marks the recruitment of PC to the droplet interface bilayer.

(H) Decrease rate of the triolein bilayer concentration with the budding angle.

See also Figure S3.

tension of the monolayer separating the cytosol and the LD, and the surface tension of the monolayer separating the LD and the ER lumen. The shape of a forming LD (Figure 4A), i.e., the budding angle, would arise from the competition between these tensions (Figure 4A) (Kusumaatmaja and Lipowsky, 2011; Lipowsky, 1993; Thiam and Foret, 2016): the bilayer tension pulls on the edge to flatten the LD (Figure 4A), while the monolayer tensions pull on the opposite direction to make the LD spherical.

In the droplet interface bilayer system, the two monolayers have the same tension γ_m and the bilayer tension is γ_b. The budding angle θ is related to the tensions by the Young equation $\gamma_b = 2\gamma_m \cos(\theta/2)$. For a given lipid composition, we can measure

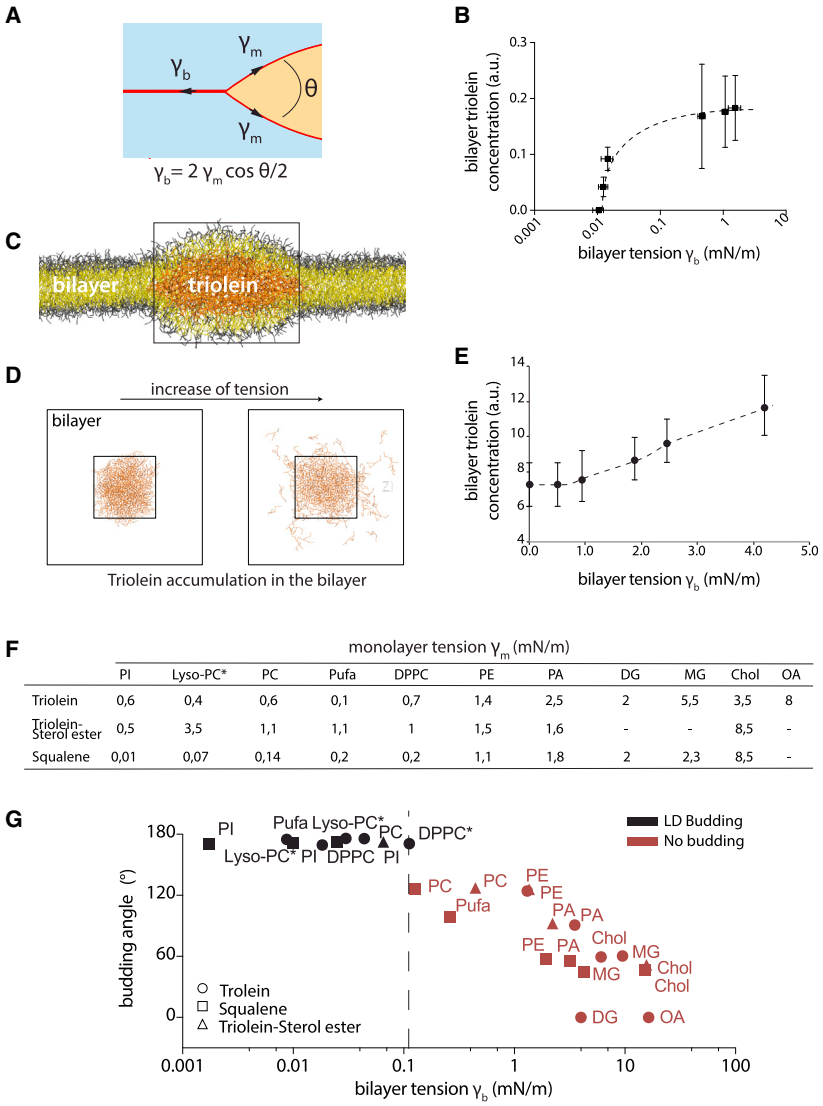

F

monolayer tension γ_m (mN/m)

	PI	Lyso-PC*	PC	Pufa	DPPC	PE	PA	DG	MG	Chol	OA
Triolein	0,6	0,4	0,6	0,1	0,7	1,4	2,5	2	5,5	3,5	8
Triolein-Sterol ester	0,5	3,5	1,1	1,1	1	1,5	1,6	-	-	8,5	-
Squalene	0,01	0,07	0,14	0,2	0,2	1,1	1,8	2	2,3	8,5	-

Figure 4. Surface Tension Controls the Neutral Lipid Egress from the Bilayer and LD Budding

(A) Diagram showing the different surface tensions acting on the neutral lipid phase. The balance between the different surface tensions defines the budding angle through the Young equation. The monolayer tension is γ_m and the bilayer tension is γ_b.

(B) The amount of triolein-pyrene in the droplet interface bilayer increases with the bilayer tension, which is varied by changing PC/PE ratios. Error bars represent the SD.

(C) Side view of the in silico model used to investigate the effect of a PC bilayer surface tension on the free triolein concentration in the bilayer.

(D) Top view of the in silico model in (C); only triolein molecules are shown. During the molecular dynamics simulations, triolein molecules escape the lens and relocate in the bilayer.

(E) Increasing the bilayer surface tension in silico increases the amount of free triolein molecules the bilayer. The fraction of triolein in the bilayer is compared with the amount of PC molecules in the bilayer. Error bars represent the SD.

(F) Monolayer surface tensions for the different lipid conditions probed for budding. Measurements were done by the pendant drop method. Lyso-PC* corresponds to a mixture of Lyso-PC with PA at a ratio of 20:80.

(G) Evolution of the droplet interface bilayer tension with the budding angle. Budding occurs only for lipid conditions leading to a bilayer surface tension below 0.1 mN/m. Lyso-PC* corresponds to a mixture of Lyso-PC with PA at a ratio of 20:80. DPPC* corresponds to a mixture of DPPC with PA at a ratio of 75:25.

See also Figure S4.

the surface tension of the monolayer interface by using the drop tensiometer method (Figure S4A), and determine the bilayer tension by using the previous equation.

We first investigated the relationship between the neutral lipids removal from the bilayer and surface tension. In a triolein-pyrene-rich environment, as in Figures 3A and 3C, we made PC/PE-droplet interface bilayers with controlled ratios between the two phospholipids. For each condition, we measured the surface tensions (Figures S4B and S4C) and determined the triolein intensity in the bilayer. We observed that the amount of triolein in the bilayer decreased with the bilayer tension (Figure 4B), as well as with the monolayer tension (Figure S4D).

With the previous experiment, the bilayer tension cannot be directly controlled. To further test the effect of tension on the accumulation of free triolein molecules in the bilayer, we performed molecular dynamics simulations. This approach enabled us to separately control the bilayer tension and triolein concentration. We generated a system composed of a tensionless PC bilayer bearing a lens of triolein molecules (Figures 4C and 4D). We then ran simulations at different values of the bilayer tension, while keeping the number of triolein and phospholipid molecules constant. We observed that triolein molecules escaped from the lens to relocate into the bilayer (bilayer region in Figures 4D and S4E). As observed experimentally (Figure 4B), the concentration of free triolein molecules in the bilayer decreased with the bilayer tension (Figure 4E).

All of these results support that decreasing membrane tension favors the egress of the neutral lipids from the bilayer and their transfer into forming LDs. Since this egress was concomitant with LD budding (Figure 3H), these results also support that lowering membrane tension should also promote LD budding.

We next probed the effect of tension on LD budding. For all lipid compositions studied in Figure 2, we measured the monolayer tension (Figure 4F) and determined the corresponding bilayer tension (see Figure 4A). We found a clear transition in budding with the bilayer surface tension (Figure 4G). Regardless of the phospholipid or neutral lipid composition, there is critical bilayer tension, ~0.1 mN/m, below which budding occurred

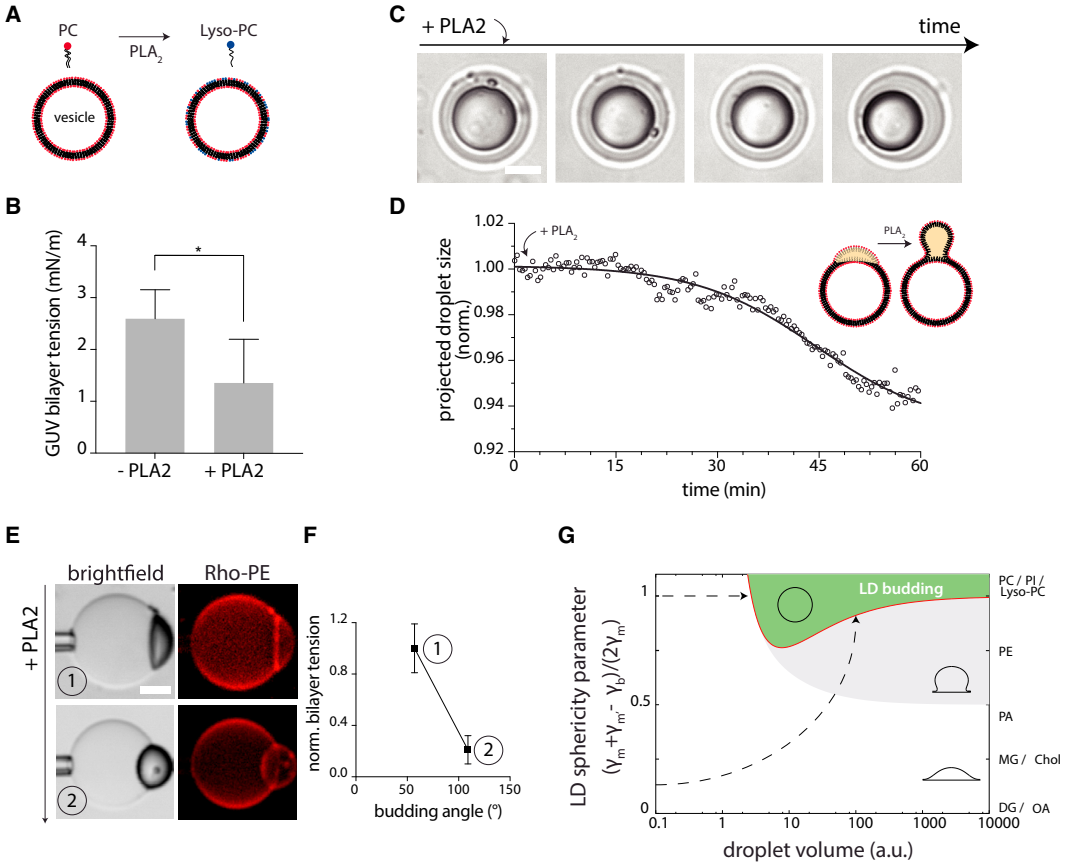

Figure 5. Phospholipase A_2 Activity Decreases the Bilayer Surface Tension and Induces Droplet Budding

(A) Conversion of PC to Lyso-PC by phospholipase A_2 (PLA_2).

(B) GUV bilayers submitted to PLA_2 action have a lower surface tension than control GUVs (n = 13). Error bars represent the SD. *$p < 0.01$.

(C) Top view of an artificial LD embedded in a GUV bilayer (the LD is on the apex of the GUV). The action of PLA_2 on the GUV membrane leads to the budding of the LD (n = 10). Scale bar, 10 μm.

(D) Evolution of the LD diameter over incubation time with PLA_2. The decrease of the diameter reveals the formation of a spherical LD.

(E) Side visualization of an artificial LD budding transition due to PLA_2 action. Scale bar, 10 μm.

(F) The GUV bilayer tension is measured before PLA_2 action (before budding, 1; after budding, 2). The bilayer tension is decreased by 5-fold. Error bars represent the SD.

(G) Illustrative phase diagram showing the LD budding region reached by altering membrane tensions (left axis) and/or phospholipid composition (right axis), considering a triolein neutral lipid phase. The LD sphericity parameter describes the competition between the different tensions for LD formation; it is defined as $(\gamma_m + \gamma_{m'} - \gamma_b)/(2\gamma_m)$.

See also Figure S5 and Movie S4.

(Figure 4G); a less clear transition occurred with the monolayer tension (Figure S4F). This result suggests that (1) decreasing the ER membrane surface tension promotes LD budding, and (2) phospholipids probably control LD budding by differently affecting membrane surface tension (Figure 4G).

Phospholipase A_2 Reduces the Bilayer Surface Tension and Induces LD Budding

Our previous results suggest that remodeling the ER phospholipid composition might control LD formation by regulating membrane surface tension (Figure 4G). We thus reasoned that phospholipid synthesis or remodeling enzymes would be important for LD formation. We decided to particularly focus on lyso-phospholipids that favored LD budding (Figure 2E). The presence of only 20% of Lyso-PC enabled the budding of LDs containing any of the neutral lipid tested (Figure 2E). In cells, lyso-phospholipid levels in the ER membrane depend in part on the activity of the cytosolic phospholipase A_2 (Penno et al., 2013; Pol et al., 2014). We therefore aimed to decipher in vitro the effect of phospholipase A_2 on LD budding.

We made GUVs containing PC/PA (70:30). A fraction of the GUVs was incubated with purified phospholipase A2 for 1 hr (Figure 5A). By using the microaspiration technique (Figure S1A), we determined the surface tension of the two GUV populations and found a lower surface tension for the population subjected to phospholipase A_2 (Figure 5B). Interestingly, the maximum amount of lyso-phospholipids generated by the phospholipase was around 15% of the total phospholipids (Figures S5A and S5B), which is close to lyso-phospholipid levels on LDs (~10%) and on bilayers (~20%) (Figure S5C) (Tauchi-Sato

et al., 2002). This observation suggests that the local production of few Lyso-PC molecules by phospholipase A_2 can decrease the ER bilayer tension.

We next made PC/PA (70:30) GUVs and incorporated artificial triolein LDs, which were in a non-budded state (Figure 5C). We added phospholipase A_2 into the surrounding aqueous phase and systematically observed budding events of the artificial LDs after few minutes (Figures 5C, 5D, and S5H; Movie S4), compared with controls (Figures S5D and S5E). This budding event was indeed associated with a decrease of the GUV bilayer tension (Figures 5E, 5F, S5F, and S5G). This experiment supports that phospholipase A_2 can decrease the ER surface tension to allow LD formation.

All presented data (Figures 4 and 5A–5F) emphasize the major contribution of surface tensions to LD budding. The action of phospholipase A_2 on LD budding illustrates only in part how cells can regulate tension by remodeling ER phospholipid composition. To have a broader and illustrative view of the possible mechanical and biochemical regulatory pathways of LD formation, we built a simplified physical model. This model assumes that an LD deforms only toward the cytosolic side (Figure S5I and STAR Methods). We computed a phase diagram (Figure 5G) showing the relative values of tensions (included in the sphericity parameter of Figure 5G), and volumes, for which an LD buds off. We observed as expected that the LD shape is mainly dictated by the tensions (except at very small sizes, STAR Methods), and budding is obtained by lowering the bilayer surface tension (Figure 5G, left axis). During the LD growth until budding, different regulatory pathways of phospholipids (Figure 5G, right axis) and/or tensions (Figure 5G, left axis) could enable reaching the budding region at different LD formation sizes (Figure 5G, arrows).

Targeted Phospholipid Alteration in Cells Leads to Anticipated LD Size Variation

We wanted to further test in cells our in vitro findings by modulating LD formation. Directly controlling the ER membrane tension is experimentally challenging. We thus decided to modulate phospholipid composition. However, directly imaging the structural shape changes of forming LDs is not easy. Instead, from the differential budding aptitudes of phospholipids (Figures 2 and 3), we can predict LD size variation and phenotype (Figure 6A): budding conditions favor the formation of small LDs; non-budding conditions favor the formation of large LDs that remain connected to the ER membrane, and the accumulation of neutral lipids in the ER membrane.

Before testing our predictions, we first scanned the literature and selected studies where LD size distribution varied (Figure S6A). Most of these studies focused on the function of proteins whose alteration affected LD formation. However, the alteration of the proteins was often associated with important changes on the cellular lipidome (Figure S6A), which might be actually a key reason for the observed LD phenotype (Figure 6A).

To next test our predictions, we first focused on Lyso-PC, which favored budding (Figures 5C–5F) and is normally present in cells at relatively low levels compared with PC. We reasoned that blocking the acylation of Lyso-PC by inhibiting the lysophosphatidylcholine acyltransferase 1 (LPCAT1) (Figure 6B) would increase Lyso-PC levels and favor the formation of small LDs (Figure 6A). We instead observed that LDs were a little larger than in control cells (Figures S6F–S6H) as previously reported (Moessinger et al., 2011). However, Lyso-PC is recycled into Lyso-PA and then to PA, ensuing the action of the plasma secreted lyso-phospholipase D, autotaxin (Figure 6B). We thus conducted concomitant small interfering RNA (siRNA) of LPCAT1 and the pharmacological inhibition of autotaxin. Under this condition, we found that LDs became indeed smaller than in control cells (Figures 6C–6E), and their size was autotaxin inhibitor dose-dependent (Figure S6I).

Second, we found that phospholipases affected LD formation size (Figures 6F–6H and S6J–S6L, and data not shown). The deletion of the cytosolic phospholipase A_2 by siRNA in various cellular types depletes lyso-phospholipids and leads to the accumulation of neutral lipids in the ER (Gubern et al., 2008); LDs do not efficiently bud in this context as we predicted (Figure 6A). Instead of the siRNA approach, we decided to decrease lyso-phospholipid levels by treating HeLa and Huh7 cells with the cytosolic phospholipase A_2 inhibitor methyl arachidonyl fluorophosphonate (Gubern et al., 2008). We observed, as predicted, the occurrence of bigger LDs than in control cells (Figures 6F–6H). We finally probed the opposite case with the overexpression of the cytosolic phospholipase A_2 in HeLa and Huh7 cells. After 24 hr of overexpression, we induced LD formation by oleate loading and determined LD size distribution after 4 hr. We observed, as expected, that LDs were smaller than in control cells (Figures 6F–6H).

Third, we focused on saturated phospholipids that efficiently budded LDs in vitro (Figure 2E). Accumulation of saturated phospholipids should promote the formation of small LDs (Figure 6A). We confirmed this prediction in different cell types. For example, we pharmacologically inhibited stearoyl-coenzyme A desaturase 1 (SCD1) in Huh7 cells for 24 hr to promote the accumulation of saturated phospholipids. We then oleate loaded the cells and observed that LDs were significantly smaller than in control cells (Figures 6I–6K).

Finally, we studied the accumulation of squalene, as it appeared to be the most difficult neutral lipid to package into spherical LDs (Figure 2F). We predicted that increased squalene levels in cells should favor the formation of large LDs (Figure 6A). HeLa cells devoid of LDs were cultured in the presence of mevalonic acid, a precursor of squalene that further is transformed into sterol ester (Figure 6L). We detected by thin-layer chromatography the synthesis of sterol esters (Figure S6M). These cells were considered as control cells and their LD size was measured 4 hr after mevalonic acid loading. We next pretreated the cells with terbinafine, which blocked the squalene epoxidase and favored squalene deposition (Figures 6L and S6M). We observed, as predicted, the formation of numerous and bigger LDs compared with control cells (Figures 6M–6O). Finally, we repeated the same experiment but with inhibition of SCD1 for 24 hr, prior to terbinafine treatment and mevalonic acid loading. This strategy was adopted to favor the accumulation of saturated phospholipids that should facilitate the budding of smaller squalene-containing LDs (Figures 2E and 6A). As anticipated, we detected that the additional SCD1 inhibition shifted LD size toward smaller ones (Figures 6M–6O).

These experiments with cells matched our predictions and support the conclusion that ER phospholipids control LD formation, possibly by modulating ER membrane tension. Differences

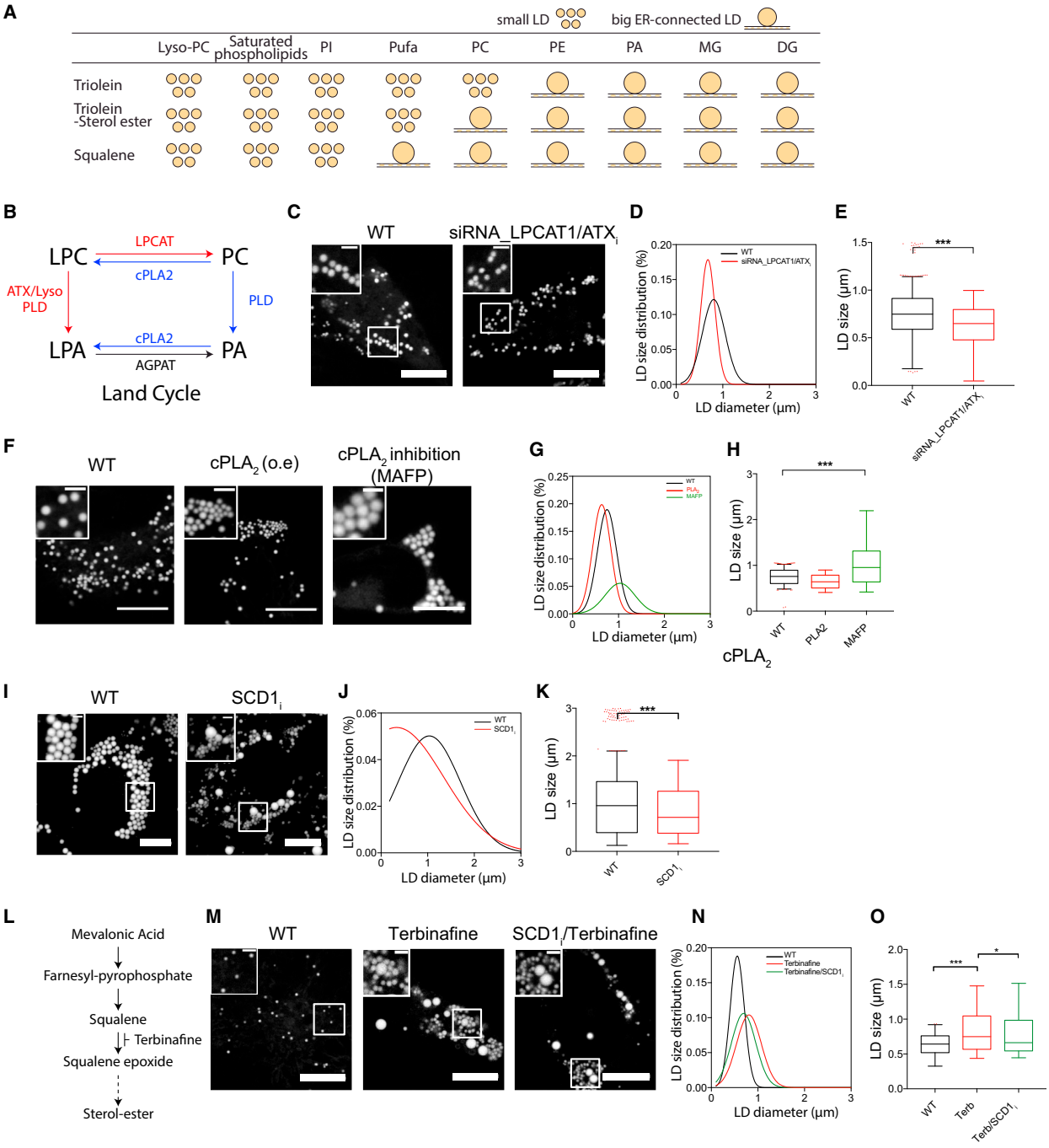

Figure 6. Targeted Alteration of Cellular Lipid Composition Modulates LD Formation Size in a Predictable Manner

(A) Predicted phenotypes for different lipid compositions. Budding conditions are predicted to mediate the formation of small LDs. Non-budding conditions are predicted to mediate the formation of big LDs connected with the ER, and to potentially mediate the accumulation of neutral lipids in the ER bilayer.

(B) Phospholipid biosynthesis pathways in the Land cycle.

(C–E) In HeLa cells, the double inhibition of LPCAT1, by siRNA, and ATX/Lyso-phospholipase D, by an autotaxin inhibitor, ATXi (C), favors the formation of smaller LDs than in wild-type (WT) (D and E). Scale bars, 10 μm. ***$p < 0.0001$.

(F–H) The overexpression of c-PLA$_2$ in HeLa cells decreases LD size distribution, after 4 hr oleate loading, as compared with WT (F). Inhibition of the PLA$_2$ by the methyl arachidonyl fluorophosphonate (MAFP) increases LD size distribution under the same conditions (G and H). ***$p < 0.0001$. Scale bars, 10 μm.

(I–K) The pharmacological inhibition of SCD1 in Huh7 cells (I) leads to a significant shift of LD size to smaller ones (J and K). Scale bars, 10 μm. ***$p < 0.0001$.

(legend continued on next page)

in ER phospholipid compositions, e.g., between cell lines or types, likely underlie differences in LD formation size.

DISCUSSION

We have investigated how LDs form from the ER, one of the most important questions of LD biology. We have uncovered in detail that ER phospholipids and surface tension determine LD formation. The LD formation size is determined by these chemical and physical parameters of the ER. Mechanistically, phospholipids affect the ER membrane surface tension whose decrease favors the egress of neutral lipids from the bilayer and their packaging into spherical LDs. Our discovery constitutes a major step in understanding LD biogenesis and regulation. We have highlighted the importance of possible alterations of ER phospholipids and tension on LD regulation. The action of proteins on LD regulation can now be better probed, and understood, by knowing their impact on these chemical and physical aspects of the ER membrane.

We have found in vitro that PC alone promoted the budding of triglyceride but not of sterol ester LDs. On the contrary, PI or saturated phospholipids promoted the budding of all tested neutral lipids (Figure 2E). Therefore, whenever the ratio between neutral lipids is affected in cells, e.g., due to metabolic shifts, a concomitant alteration of the membrane phospholipid composition in PC and PI, for example, could occur to enable LD formation.

In some biological cases, synthesized neutral lipids fail to integrate LDs and stay in the ER. This is the case, for example, of squalene in yeast cells (Spanova et al., 2010), which is probably due to the poor ability of PC, the major ER phospholipid, to bud pure squalene LDs (Figure 2E). In this condition, increasing triglyceride levels facilitates squalene incorporation into LDs (Spanova et al., 2010). Alternatively, squalene can be packaged into LDs by increasing the saturation degree of phospholipids (Figures 2E and 6M–6O).

Saturated phospholipids are usually in the ER at low concentrations because of their role in ER stress. However, their level is increased under lipotoxic conditions to alleviate cells from lipotoxicity, through facilitating LD formation (Iwai et al., 2016). This effect on LD formation is consistent with our finding that saturated phospholipids efficiently package neutral lipids into LDs (Figures 2E and 6M–6O). Furthermore, the presence of saturated phospholipids in the ER depends on the activity of the desaturase enzyme SCD1. When SCD1 is defective the saturation of ER phospholipids increases, which favors the formation of very small LDs (Figures 6A and 6I–6K). This phenotype has been consistently observed in *Caenorhabditis elegans* with defective SCD1 (Shi et al., 2013), or in adipose tissues wherein Seipin dysfunction impaired SCD1 activity (Boutet et al., 2009; Lounis et al., 2016).

There are other examples illustrating the importance of phospholipids on LD budding. For example, triglycerides accumulate in the ER in the dysfunction of Lipin, which converts PA into diacylglycerols (Adeyo et al., 2011). This phenotype is consistent with the inefficiency of LD budding in PA accumulation (Figure 2E) and, more generally, with the accumulation of free neutral lipids in the bilayer under non-budding conditions (Figures 3A, 3B, and 6A). Another example, which is extreme, is the formation of lipoprotein particles, which are particular forms of LDs made in the ER lumen. The budding of triglyceride-containing lipoproteins requires the local production of polyunsaturated phospholipids by LPCAT3 (Hashidate-Yoshida et al., 2015). We have found that these phospholipids specially allowed the budding of triglyceride droplets (Figure 2E).

Instead of a dynamic alteration of phospholipids or surface tension for LD budding, the ER may simply display regions or microdomains (Kassan et al., 2013) enriched with particular phospholipids or that transiently have specific surface tensions. Such segregation could occur between the smooth and rough ER, nuclear and peripheral ER, and ER tubules and sheets (Lagace and Ridgway, 2013). These differences could allow the formation of distinct pools of LDs containing different lipids and proteins and having different sizes (Thiam and Beller, 2017). This could explain the occurrence in various cell types of separated sterol ester and triglyceride LDs, distinctly marked by different perilipin proteins (Hsieh et al., 2012; Meyers et al., 2016), or the existence of metabolically distinct diacylglycerol transferase 1- and 2-LDs, which have different sizes (Wilfling et al., 2013).

Variation of LD size is often observed between cell lines or types, or is due to the dysfunction of some proteins (Thiam and Beller, 2017). The origin of such variability remains very unclear except for very specific cases where LDs split, fuse, or grow (Gong et al., 2011; Long et al., 2012; Tan et al., 2014; Wilfling et al., 2013; Yang et al., 2012). Our results support that LDs can simply form at different sizes as a result of differences in the ER phospholipid composition and/or tension (Figures 5G and 6A). For example, the deletion of proteins such as Rab, Atlastin, Reticulon, or Torsin, which do not necessarily affect ER phospholipids but morphology or shape, modulate LD size probably through modulating ER surface tension (Grillet et al., 2016; Klemm et al., 2013; Zerial and McBride, 2001). Indeed, mechanical pulling on the ER membrane increases tension, works against budding, and increases LD formation size.

Finally, many proteins important for LD functionality target LDs from the ER, either during LD formation or via ER-LD connection bridges (Jacquier et al., 2011; Wilfling et al., 2013, 2014a, 2014b). These proteins encompass the glycerol-3-phosphate acyltransferase enzyme (GPAT4) (Wilfling et al., 2013) that localizes to LD surface to mediate the local synthesis of neutral lipids. Our results suggest that non-budding conditions favor ER-LD connection (Figure 6A), and should enhance the trafficking of proteins between ER and LD. These conditions correspond, for example, to the accumulation of negatively curved lipids such as diacylglycerols, PA, or cholesterol (Figure 1G), which had higher surface

(L) Terbinafine blocks squalene epoxidation that is necessary for the biosynthesis of sterol esters.
(M–O) HeLa cells cultured in the presence of mevalonic acid form LDs whose size is considered WT size. Treatment of the cells with terbinafine prior to mevalonic acid loading (M) induces squalene deposition and promotes the formation of bigger LDs than in WT cells. Inhibition of SCD1, prior terbinafine treatment, and mevalonic loading lead to the formation of LDs smaller than in the single terbinafine treatment (N and O). Scale bars, 10 μm. ***$p < 0.0001$, *$p < 0.01$.
See also Figure S6.

tensions (Figure 4G). Our prediction is consistent with reported regulations of GPAT4 trafficking from ER to LDs: in increased PA levels in the ER membrane of various cell types lacking Seipin protein, a massive transfer of GPAT4 from the ER to almost all LDs is observed in comparison with normal cells (Fei et al., 2011; Pagac et al., 2016; Szymanski et al., 2007; Wang et al., 2016); likewise, under conditions where GPAT4 should exclusively remain in the ER membrane of fly cells (Wilfling et al., 2014b), the induction of cholesterol accumulation in the membrane restored GPAT4 targeting from ER to LDs (Wilfling et al., 2014b). Consequently, ER tension and phospholipid composition seem to be critical for determining the protein composition of LD during formation.

In summary, we have unveiled ER lipid composition and membrane tension as key parameters of LD formation. Our discovery brings major insights on how proteins could regulate LDs. In particular, by locally altering ER phospholipid composition or surface tension, proteins might determine where LDs form and which, and how, proteins target LD surface.

STAR★METHODS

Detailed methods are provided in the online version of this paper and include the following:

- KEY RESOURCES TABLE
- CONTACT FOR REAGENT AND RESOURCE SHARING
- METHOD DETAILS
  - Droplet Interface Bilayer Formation
  - Preparation of the Oil Phase
  - Droplet Interface Bilayer Angle and Bilayer Triolein Signal Determinations
  - Giant Unilamellar Vesicles and Artificial Lipid Droplets Formation
  - Measurement of the Interfacial Tension of the Interface of Artificial Droplets
  - Surface Tension Measurements by Microaspiration
  - Cellular Fractionation
  - Lipid Extraction
  - Thin Layer Chromatography and Lipid Detection
  - Cellular Lipid Droplet Size Measurements
  - Cell Culture
  - Overexpression of Phospholipase A2
  - Enzymes Inhibitions
  - Induction of Squalene Accumulation
  - Relevance of Curvature for Lipid Droplet Budding (Related to Figures 1 and 2)
  - Theoretical Modeling of the Shape of Lipid Droplet Budding (Related to Figure 5G)
  - Molecular Dynamics (MD) Simulations (Related to Figures 4C–4E)
- QUANTIFICATION AND STATISTICAL ANALYSIS
- DATA AND SOFTWARE AVAILABILITY

SUPPLEMENTAL INFORMATION

Supplemental Information includes six figures and four movies and can be found with this article online at http://dx.doi.org/10.1016/j.devcel.2017.05.012.

AUTHOR CONTRIBUTIONS

A.R.T. conceived the project. K.B.M., D.A., A.C., and A.R.T. conducted experiments. L.F. established the mathematical modeling. S.V performed molecular dynamics simulations. K.B.M., D.A., A.C., S.V., L.F., and A.R.T analyzed data. A.R.T. wrote the manuscript with feedback from co-authors K.B.M., S.V., and L.F.

ACKNOWLEDGMENTS

We thank Drs. Frederic Pincet, Philippe Rostaing, Catherine Cantrel, Alain Cagna from Teclis Company, and Simon Kulifaj for technical assistance and helpful discussions. We thank the members of the group for comments and critical discussions. This work was supported by the ATIP-Avenir program and Programme Emergence de la Ville de Paris to A.R.T., the ANRS Agence Autonome de l'Inserm (ECTZ7095, ECTZ20454) to A.R.T. and D.A, and ANR-16-TERC-0002-01.

Received: December 22, 2016
Revised: April 8, 2017
Accepted: May 10, 2017
Published: June 1, 2017

REFERENCES

Adeyo, O., Horn, P.J., Lee, S., Binns, D.D., Chandrahas, A., Chapman, K.D., and Goodman, J.M. (2011). The yeast lipin orthologue Pah1p is important for biogenesis of lipid droplets. J. Cell Biol. *192*, 1043–1055.

Bacle, A., Gautier, R., Jackson, C.L., Fuchs, P.F.J., and Vanni, S. (2017). Interdigitation between Triglycerides and Lipids Modulates Surface Properties of Lipid Droplets. Biophys. J. *112*, 1417–1430.

Bayley, H., Cronin, B., Heron, A., Holden, M.A., Hwang, W.L., Syeda, R., Thompson, J., and Wallace, M. (2008). Droplet interface bilayers. Mol. Biosyst. *4*, 1191–1208.

Boutet, E., El Mourabit, H., Prot, M., Nemani, M., Khallouf, E., Colard, O., Maurice, M., Durand-Schneider, A.M., Chretien, Y., Gres, S., et al. (2009). Seipin deficiency alters fatty acid Delta 9 desaturation and lipid droplet formation in Berardinelli-Seip congenital lipodystrophy. Biochimie *91*, 796–803.

Cartwright, B.R., Binns, D.D., Hilton, C.L., Han, S., Gao, Q., and Goodman, J.M. (2015). Seipin performs dissectible functions in promoting lipid droplet biogenesis and regulating droplet morphology. Mol. Biol. Cell *26*, 726–739.

Chernomordik, L.V., and Kozlov, M.M. (2003). Protein-lipid interplay in fusion and fission of biological membranes. Annu. Rev. Biochem. *72*, 175–207.

Choudhary, V., Ojha, N., Golden, A., and Prinz, W.A. (2015). A conserved family of proteins facilitates nascent lipid droplet budding from the ER. J. Cell Biol. *211*, 261–271.

Ding, W., Palaiokostas, M., Wang, W., and Orsi, M. (2015). Effects of lipid composition on bilayer membranes quantified by all-atom molecular dynamics. J. Phys. Chem. B *119*, 15263–15274.

Fei, W., Shui, G., Zhang, Y., Krahmer, N., Ferguson, C., Kapterian, T.S., Lin, R.C., Dawes, I.W., Brown, A.J., Li, P., et al. (2011). A role for phosphatidic acid in the formation of "supersized" lipid droplets. PLoS Genet. *7*, e1002201.

Foret, L. (2014). Shape and energy of a membrane bud induced by protein coats or viral protein assembly. Eur. Phys. J. E Soft Matter *37*, 42.

Gong, J., Sun, Z., Wu, L., Xu, W., Schieber, N., Xu, D., Shui, G., Yang, H., Parton, R.G., and Li, P. (2011). Fsp27 promotes lipid droplet growth by lipid exchange and transfer at lipid droplet contact sites. J. Cell Biol. *195*, 953–963.

Grillet, M., Dominguez Gonzalez, B., Sicart, A., Pottler, M., Cascalho, A., Billion, K., Hernandez Diaz, S., Swerts, J., Naismith, T.V., Gounko, N.V., et al. (2016). Torsins are essential regulators of cellular lipid metabolism. Dev. Cell *38*, 235–247.

Gubern, A., Casas, J., Barcelo-Torns, M., Barneda, D., de la Rosa, X., Masgrau, R., Picatoste, F., Balsinde, J., Balboa, M.A., and Claro, E. (2008). Group IVA phospholipase A2 is necessary for the biogenesis of lipid droplets. J. Biol. Chem. *283*, 27369–27382.

Guo, Y., Walther, T.C., Rao, M., Stuurman, N., Goshima, G., Terayama, K., Wong, J.S., Vale, R.D., Walter, P., and Farese, R.V. (2008). Functional genomic screen reveals genes involved in lipid-droplet formation and utilization. Nature *453*, 657–661.

Guo, Y., Cordes, K.R., Farese, R.V., Jr., and Walther, T.C. (2009). Lipid droplets at a glance. J. Cell Sci. *122*, 749–752.

Hashidate-Yoshida, T., Harayama, T., Hishikawa, D., Morimoto, R., Hamano, F., Tokuoka, S.M., Eto, M., Tamura-Nakano, M., Yanobu-Takanashi, R., and Mukumoto, Y. (2015). Fatty acid remodeling by LPCAT3 enriches arachidonate in phospholipid membranes and regulates triglyceride transport. Elife *4*, e06328.

Hsieh, K., Lee, Y.K., Londos, C., Raaka, B.M., Dalen, K.T., and Kimmel, A.R. (2012). Perilipin family members preferentially sequester to either triacylglycerol-specific or cholesteryl-ester-specific intracellular lipid storage droplets. J. Cell Sci. *125*, 4067–4076.

Humphrey, W., Dalke, A., and Schulten, K. (1996). VMD: visual molecular dynamics. J. Mol. Graph. *14*, 33–38.

Iwai, T., Kume, S., Chin-Kanasaki, M., Kuwagata, S., Araki, H., Takeda, N., Sugaya, T., Uzu, T., Maegawa, H., and Araki, S.I. (2016). Stearoyl-CoA desaturase-1 protects cells against lipotoxicity-mediated apoptosis in proximal tubular cells. Int. J. Mol. Sci. *17*, E1868.

Jacquier, N., Choudhary, V., Mari, M., Toulmay, A., Reggiori, F., and Schneiter, R. (2011). Lipid droplets are functionally connected to the endoplasmic reticulum in *Saccharomyces cerevisiae*. J. Cell Sci. *124*, 2424–2437.

Julicher, F., and Seifert, U. (1994). Shape equations for axisymmetrical vesicles—a clarification. Phys. Rev. E Stat. Phys. Plasmas Fluids Relat. Interdiscip. Topics *49*, 4728–4731.

Kabalnov, A., and Wennerström, H. (1996). Macroemulsion stability: the oriented wedge theory revisited. Langmuir *12*, 276–292.

Kadereit, B., Kumar, P., Wang, W.J., Miranda, D., Snapp, E.L., Severina, N., Torregroza, I., Evans, T., and Silver, D.L. (2008). Evolutionarily conserved gene family important for fat storage. Proc. Natl. Acad. Sci. USA *105*, 94–99.

Kassan, A., Herms, A., Fernandez-Vidal, A., Bosch, M., Schieber, N.L., Reddy, B.J., Fajardo, A., Gelabert-Baldrich, M., Tebar, F., Enrich, C., et al. (2013). Acyl-CoA synthetase 3 promotes lipid droplet biogenesis in ER microdomains. J. Cell Biol. *203*, 985–1001.

Klemm, R.W., Norton, J.P., Cole, R.A., Li, C.S., Park, S.H., Crane, M.M., Li, L., Jin, D., Boye-Doe, A., Liu, T.Y., et al. (2013). A conserved role for atlastin GTPases in regulating lipid droplet size. Cell Rep. *3*, 1465–1475.

Kusumaatmaja, H., and Lipowsky, R. (2011). Droplet-induced budding transitions of membranes. R. Soc. Chem. *7*, 6914–6919.

Lagace, T.A., and Ridgway, N.D. (2013). The role of phospholipids in the biological activity and structure of the endoplasmic reticulum. Biochim. Biophys. Acta *1833*, 2499–2510.

Lipowsky, R. (1993). Domain-induced budding of fluid membranes. Biophys. J. *64*, 1133–1138.

Long, A.P., Manneschmidt, A.K., VerBrugge, B., Dortch, M.R., Minkin, S.C., Prater, K.E., Biggerstaff, J.P., Dunlap, J.R., and Dalhaimer, P. (2012). Lipid droplet de novo formation and fission are linked to the cell cycle in fission yeast. Traffic *13*, 705–714.

Lounis, M.A., Lalonde, S., Rial, S.A., Bergeron, K.F., Ralston, J.C., Mutch, D.M., and Mounier, C. (2016). Hepatic BSCL2 (Seipin) deficiency disrupts lipid droplet homeostasis and increases lipid metabolism via SCD1 activity. Lipids *52*, 129–150.

Martin, S., and Parton, R.G. (2006). Lipid droplets: a unified view of a dynamic organelle. Nat. Rev. Mol. Cell Biol. *7*, 373–378.

Meyers, A., Del Rio, Z.P., Beaver, R.A., Morris, R.M., Weiskittel, T.M., Alshibli, A.K., Mannik, J., Morrell-Falvey, J., and Dalhaimer, P. (2016). Lipid droplets form from distinct regions of the cell in the fission yeast *Schizosaccharomyces pombe*. Traffic *17*, 657–669.

Moessinger, C., Kuerschner, L., Spandl, J., Shevchenko, A., and Thiele, C. (2011). Human lysophosphatidylcholine acyltransferases 1 and 2 are located in lipid droplets where they catalyze the formation of phosphatidylcholine. J. Biol. Chem. *286*, 21330–21339.

Ohsaki, Y., Suzuki, M., and Fujimoto, T. (2014). Open questions in lipid droplet biology. Chem. Biol. *21*, 86–96.

Pagac, M., Cooper, D.E., Qi, Y., Lukmantara, I.E., Mak, H.Y., Wu, Z., Tian, Y., Liu, Z., Lei, M., and Du, X. (2016). SEIPIN regulates lipid droplet expansion and adipocyte development by modulating the activity of glycerol-3-phosphate acyltransferase. Cell Rep. *17*, 1546–1559.

Penno, A., Hackenbroich, G., and Thiele, C. (2013). Phospholipids and lipid droplets. Biochim. Biophys. Acta *1831*, 589–594.

Pol, A., Gross, S.P., and Parton, R.G. (2014). Review: biogenesis of the multifunctional lipid droplet: lipids, proteins, and sites. J. Cell Biol. *204*, 635–646.

Poulin, P., and Bibette, J. (1998). Adhesion of water droplets in organic solvent. Langmuir *14*, 6341–6343.

Saleem, M., Morlot, S., Hohendahl, A., Manzi, J., Lenz, M., and Roux, A. (2015). A balance between membrane elasticity and polymerization energy sets the shape of spherical clathrin coats. Nat. Commun. *6*, 6249.

Seifert, U., Berndl, K., and Lipowsky, R. (1991). Shape transformations of vesicles—phase-diagram for spontaneous-curvature and bilayer-coupling models. Phys. Rev. A *44*, 1182–1202.

Shi, X., Li, J., Zou, X.J., Greggain, J., Rodkaer, S.V., Faergeman, N.J., Liang, B., and Watts, J.L. (2013). Regulation of lipid droplet size and phospholipid composition by stearoyl-CoA desaturase. J. Lipid Res. *54*, 2504–2514.

Shinoda, W., DeVane, R., and Klein, M.L. (2007). Multi-property fitting and parameterization of a coarse grained model for aqueous surfactants. Mol. Simulation *33*, 27–36.

Spanova, M., Czabany, T., Zellnig, G., Leitner, E., Hapala, I., and Daum, G. (2010). Effect of lipid particle biogenesis on the subcellular distribution of squalene in the yeast *Saccharomyces cerevisiae*. J. Biol. Chem. *285*, 6127–6133.

Szymanski, K.M., Binns, D., Bartz, R., Grishin, N.V., Li, W.P., Agarwal, A.K., Garg, A., Anderson, R.G.W., and Goodman, J.M. (2007). The lipodystrophy protein seipin is found at endoplasmic reticulum lipid droplet junctions and is important for droplet morphology. Proc. Natl. Acad. Sci. USA *104*, 20890–20895.

Tan, J.S.Y., Seow, C.J.P., Goh, V.J., and Silver, D.L. (2014). Recent advances in understanding proteins involved in lipid droplet formation, growth and fusion. J. Genet. Genomics *41*, 251–259.

Tauchi-Sato, K., Ozeki, S., Houjou, T., Taguchi, R., and Fujimoto, T. (2002). The surface of lipid droplets is a phospholipid monolayer with a unique fatty acid composition. J. Biol. Chem. *277*, 44507–44512.

Thiam, A.R., and Beller, M. (2017). The why, when and how of lipid droplet diversity. J. Cell Sci. *130*, 315–324.

Thiam, A.R., and Foret, L. (2016). The physics of lipid droplet nucleation, growth and budding. Biochim. Biophys. Acta *1861*, 715–722.

Thiam, A.R., and Pincet, F. (2015). The energy of COPI for budding membranes. PLoS One *10*, e0133757.

Thiam, A.R., Bremond, N., and Bibette, J. (2011). Adhesive emulsion bilayers under an electric field: from unzipping to fusion. Phys. Rev. Lett. *107*, 068301.

Thiam, A.R., Bremond, N., and Bibette, J. (2012). From stability to permeability of adhesive emulsion bilayers. Langmuir *28*, 6291–6298.

Thiam, A.R., Antonny, B., Wang, J., Delacotte, J., Wilfling, F., Walther, T.C., Beck, R., Rothman, J.E., and Pincet, F. (2013a). COPI buds 60-nm lipid droplets from reconstituted water-phospholipid-triacylglyceride interfaces, suggesting a tension clamp function. Proc. Natl. Acad. Sci. USA *110*, 13244–13249.

Thiam, A.R., Farese, R.V., Jr., and Walther, T.C. (2013b). The biophysics and cell biology of lipid droplets. Nat. Rev. Mol. Cell Biol. *14*, 775–786.

Walther, T.C., and Farese, R.V., Jr. (2012). Lipid droplets and cellular lipid metabolism. Annu. Rev. Biochem. *81*, 687–714.

Wang, H., Becuwe, M., Housden, B.E., Chitraju, C., Porras, A.J., Graham, M.M., Liu, X.N., Thiam, A.R., Savage, D.B., Agarwal, A.K., et al. (2016). Seipin is required for converting nascent to mature lipid droplets. Elife *5*, e16582.

Welte, M.A. (2015). Expanding roles for lipid droplets. Curr. Biol. *25*, R470–R481.

Wilfling, F., Wang, H., Haas, J.T., Krahmer, N., Gould, T.J., Uchida, A., Cheng, J.X., Graham, M., Christiano, R., Frohlich, F., et al. (2013). Triacylglycerol synthesis enzymes mediate lipid droplet growth by relocalizing from the ER to lipid droplets. Dev. Cell *24*, 384–399.

Wilfling, F., Haas, J.T., Walther, T.C., and Farese, R.V., Jr. (2014a). Lipid droplet biogenesis. Curr. Opin. Cell Biol. *29*, 39–45.

Wilfling, F., Thiam, A.R., Olarte, M.-J., Wang, J., Beck, R., Gould, T.J., Allgeyer, E.S., Pincet, F., Bewersdorf, J., and Farese, R.V. (2014b). Arf1/COPI machinery acts directly on lipid droplets and enables their connection to the ER for protein targeting. Elife *3*, e01607.

Yang, H., Galea, A., Sytnyk, V., and Crossley, M. (2012). Controlling the size of lipid droplets: lipid and protein factors. Curr. Opin. Cell Biol. *24*, 509–516.

Zerial, M., and McBride, H. (2001). Rab proteins as membrane organizers. Nat. Rev. Mol. Cell Biol. *2*, 107–117.

STAR★METHODS

KEY RESOURCES TABLE

REAGENT or RESOURCE	SOURCE	IDENTIFIER
Chemicals, Peptides, and Recombinant Proteins		
Phospholipids	Avanti Polar Lipids	https://avantilipids.com/
Triolein	Sigma Aldrich	T7140
Cholesteryl oleate	Sigma Aldrich	C9253
Squalene	Sigma Aldrich	S3626
Triolein-pyrene	Markergene	M0258
Autotaxin inhibitor PF-8380	Sigma Aldrich	SML0715-5MG
Phospholipase A2 from bovine pancreas	Sigma Aldrich	P8913
Terbinafine hydrochloride	Sigma Aldrich	T8826-100MG
HiPerFect Transfection Reagent	Qiagen	301704
1-butanol	Sigma Aldrich	B7906
SCD1 Inhibitor	Caymanchemical company	CAY10566
DMEM 1X+GlutaMAX-1	ThermoFisher	319666-021
Mavalonic acid 5-phosphate trilithium	Alsachim	SVI-ALS-16-267
Farnesyl pyrophosphate	Sigma Aldrich	F6892-1VL
Triolein-pyrene 1,2-Dioleoyl-3-(pyren-1-yl)decanoyl-rac-Glycerol	Marker Gene (Technologies, Inc)	M0258
Oleic Acid	Sigma Aldrich	O1008
Methyl arachidonyl fluorophosphonate	Sigma Aldrich	SLBM8708V
Glyceryl trioctanoate	Sigma Aldrich	T 9126
Experimental Models: Cell Lines		
Human hepatocytes Huh7.5	Apath Missouri	APC 49
Hela Cells	Laboratoire de chimie de l'Ecole Normale Supérieure de Paris	N/A
Drosophila KC 167 cells	Dusseldorf University	N/A
Oligonucleotides		
LPCAT1 silencer Pre-designed siRNA sense GGCCAGUAAGUACGGGAAAtt anti-sense UUUCCCGUACUUACUGGCCtt	Ambion, ThermoFisher scientific	Cat#AM16708
Recombinant DNA		
ORF of PLA_2G4A	VIGENE Biosciences	Cat#CH809193
Software and Algorithms		
Matlab R2016a	Licence of the École Normale Supérieure	https://fr.mathworks.com
Fiji	Online	https://imagej.net/Fiji
Plot2	Online	http://apps.micw.org/apps/plot2/
Corse Grain IT	Online	https://github.com/CG-it
Adobe illustrator CS4	Licence of the École Normale Supérieure	
GraphPad Prism 7.0a	Licence of the École Normale Supérieure	https://graphpad.com/scientific-software/prism/

CONTACT FOR REAGENT AND RESOURCE SHARING

Further information and requests for reagents may be directed to, and will be fulfilled by, the Lead Contact, Abdou Rachid Thiam (thiam@lps.ens.fr).

METHOD DETAILS

Droplet Interface Bilayer Formation

Unless mentioned, in vitro experiments were performed in the following HKM buffer: 50 mM Hepes, 120 mM Kacetate, and 1 mM $MgCl_2$ (in Milli-Q water) at pH 7.4. For the preparation of the droplet interface bilayers, buffer-in-oil emulsion droplets were made using 10 μL HKM dispersed in 40 μL of the lipid oil phase (preparation of the oil phase is described below). The generated emulsion was placed on a glass coverslips coated with chlorotrimethylsilane to prevent the splashing of the aqueous droplets. For the determination of the triolein concentration in the droplet interface bilayer by fluorescence measurements, 5 % of triolein-pyrene was added to the triolein phase.

Preparation of the Oil Phase

Phospholipids used for droplet interface bilayers and artificial LDs formation were purchased from Avanti Polar Lipids, Inc. Chloroform which was dissolving the lipid was evaporated under a stream of argon; the dried lipids were subsequently re-solubilized to the desired concentration in the oil phase notably triolein (TO), trioctanoate, triolein-sterol ester (SE) mixture (TO-SE, 75/25, w/w), and squalene (SQ). Lipid concentrations ranging from 0.1 to 5% w/w were tested, all of which were above the critical concentration for forming stable droplet interface bilayers, i.e. no fusion between buffer droplets.

Droplet Interface Bilayer Angle and Bilayer Triolein Signal Determinations

The budding angle θ defined in Figure 2A is given by: $2\theta = \sin^{-1}(R_b/R_1) + \sin^{-1}(R_b/R_2)$, where R_b, R_1 and R_2 respectively denote for the radii of the bilayer and drops. The fluorescence intensity within the bilayer was measured as follows: $I = (L_1-L_2)/(L_3-L_2)$, where L_1 represents the fluorescence intensity of the bilayer, L_2 the background intensity which is the one of the drop, and L_3 is the reservoir signal of the surrounding triolein-pyrene phase.

Giant Unilamellar Vesicles and Artificial Lipid Droplets Formation

GUVs were prepared by electroformation. Phospholipids and mixtures thereof in chloroform at 0.5 μM was dried on an indium tin oxide (ITO)-coated glass plate. The lipid film was desiccated for 1 h. The chamber was sealed with another ITO- coated glass plate. The lipids were then rehydrated with a sucrose solution (275 mOsm). Electroformation is done using 100 Hz AC voltage at 1.0 to 1.4 Vpp and maintained for at least 1 h. This low voltage was used to avoid hydrolysis of water and dissolution of titanium ions glass plate. GUVs were either stored in the chamber at 4 °C overnight or directly collected with a Pasteur pipette.

To prepare the artificial lipid droplets artificial LDs 5 μL of the lipid oil solution was added to 45 μL of HKM buffer. The mixture was sonicated. The diameter of the resulting droplets is a few hundred nanometers. Guvs were then incubated with the artificial LDs for 5 min.

For LPC accumulation in GUVs mediated by phospholipase c-phospholipase A2, we first made GUVs containing 70/30 (mol/mol) PC/PA and incorporated artificial LDs. The presence of PA led to non-budded droplets. The GUVs - artificial LDs mixture was then placed on a glass coverslip pretreated with 3 % wt/v BSA and washed three times with buffer. Phospholipase A2 activity buffer (25 mM Hepes, 120 mM KCl, and 2 mM $MgCl_2$ in Milli-Q water at pH 8) was added to a final volume of 1 mL. Finally 50 μL of purified phospholipase A2 at 5 mg/mL followed by 150 μL of BSA 0,3 % wt/v was incorporated to the mixture, and observed during one hour at room temperature.

Measurement of the Interfacial Tension of the Interface of Artificial Droplets

Interfacial tension measurements were performed using a drop tensiometer device (Tracker, Teclis-IT Concept, France). The principle of the drop profile analysis is based on the determination of the shape of a liquid drop suspended in another liquid from a video image and its comparison with theoretical profiles calculated from the Gauss Laplace equation. In our case, the pendant drop is the neutral lipid phase, which contains the phospholipids, formed in the aqueous HKM buffer. Immediately, the tension decreases by the continuous absorption of phospholipids to the oil/water interface. Throughout the absorption kinetics, the drop area is maintained constant. Next, the drop is compressed by decreasing its volume (at a withdrawing speed of - 0,03 mm^3/s), until complete saturation of the interface is reached (marked by plateau of tension during compression). Each surface tension experiment was determined by this means and a minimum of 3 measurements was performed for each lipid condition studied.

Surface Tension Measurements by Microaspiration

The surface tensions of purified droplets and GUVs was measured using micromanipulation technique. The device was made up of a micromanipulator and a pipette holder (Narishige, Japan). Pipettes were incubated in a 5% bovine serum albumine (BSA) before use, in order to prevent droplet from adhering on the glass. As shown in Figure S1A, the micromanipulation of a single droplet (or GUV, Figure S4J) allows determining ST through the measurement of the pipette diameter, droplet diameter, and the minimal pressure at which the droplet formed a tongue length comparable to the pipette diameter (Thiam et al., 2013a):

$ST = P_{suc}/[2(1/R_p - 1/R_d)]$, with P_{suc}, R_p and R_g respectively being the suction pressure, the pipette radius and the droplet (GUV) radii. The different sizes were obtained by image analysis (ImageJ). The suction was carried out using a syringe. The resulting pressure was measured with a pressure transducer (DP103 provided by Validyne eng. corp, USA), the output voltage of which was monitored with a digital voltmeter. The pressure transducer (range 55 kPa) was calibrated prior to experiments.

Cellular Fractionation

Cells were harvested, washed with ice-cold PBS, re-suspended in 2 ml of PBS, sonicated (using a Soniprep 150, MSE, London, UK) for 3 cycles at 0°C and 50% cycle duty (0,5 s pulse rate) for 4 minutes. The lysate was sequentially centrifuged at 500 g for 5 minutes and 8 000 g for 15 minutes (at 4°C) to remove unbroken cells, nucleus and mitochondria. To purify LDs the 8 000 g supernatant was mixed with glycerol/HKM (70:30). The gradient was ultracentrifuged at 100 000 g for 1 h and the LDs were collected from the top fraction.

Lipid Extraction

Lipid extraction was performed as described by Folch. Under ventilated hood a pyrex tube containing 10 mL of methanol was heated in a water bath at 90°C. Then the supernatant was removed, the pellet was placed in the boiling methanol for 1-2 minutes then immediately immersed in an ice water bath. The mixture of extract and methanol was then transferred to a potter homogenizer containing 10 mL of chloroform (5 strokes) and left in the ice for 5 minutes. The mixture was introduced to the tube containing 6 ml of NaCl 9 g/L, vortexed several times and stored at 4°C overnight. The bottom layer (chloroform containing lipid extract) was collected with a Pasteur pipette in a pyrex tube. The extracts were concentrated using an evaporator under nitrogen and stored at −20 °C until required for analysis.

Thin Layer Chromatography and Lipid Detection

Lipids were extracted and separated on silica TLC plates (Merck) either in chloroform/methanol/acetone/acetic acid/water (100:20:40:20:10) for phospholipids or in petroleum ether/diethyl ether/acetic acid (90:10:1) for neutral lipids, and detected by iodine vapor staining. Bands were identified by comparison with standards.

Cellular Lipid Droplet Size Measurements

Cells were treated with a solution of 500 μM oleate complexed with BSA. Formed LDs were stained with BODIPY and subsequently imaged. The diameter of LDs was measured by using a customized ImageJ and Matlab hybrid program. A minimum of 25 cells was analyzed for each condition.

Cell Culture

Huh7 and Hela cells were maintained in Dulbecco's modified Eagle's medium (DMEM) supplemented with 10% heat inactivated fetal bovine serum (Life Tech- nologies), 4.5 gL^{-1} D-glucose, 0.1 gL^{-1} sodium pyruvate (Life Technologies) and 1% penicillin-streptomycin (Life Technologies). The cells were cultured at 37°C under a 5% CO2 atmosphere. Confluent monolayers of cells were re-suspended after trypsinization and plated into a 35 mm cell-culture Mattek dishes (with a glass coverslip at the bottom), (MatTek Corp. Ashland, MA).

Overexpression of Phospholipase A2

When indicated Hela cells (60-70% confluence) were transfected with 3 μg of plasmid/mL (PLA_2G4A) in pEnter, with C terminal Flag and His tag (VIGENE Biosciences) using Polyethylenimine HCl MAX (Polysciences, Inc) following the manufacturer's instructions. After 24 hrs transfection, cells were incubated with 500 μM oleic acid coupled to BSA to induce LD formation.

Enzymes Inhibitions

Inhibition of ATX/Lyso-PLD, by ATXi in LPCAT1_siRNA treated cells, was performed as following. siRNA transfection Silencer predesigned siRNAs directed against human LPCAT1 were used: sense GGCCAGUAAGUACGGGAAAtt and anti-sense UUUCCCGUA CUUACUGGCCtt (Ambion siRNA_LPCAT1, #127470, ThermoFisher scientific). Cells were transfected at 60-70% confluence by adding to each cell-culture Mattek disches 4μL of the stock siRNA solution (20 nM) and 3μL of HiPerFect Transfection Reagent (QIAGEN). After 24 hrs, ATXi that is the inhibitor of autotaxin, the enzyme that synthesizes Lyso-PA from Lyso-PC, was added to the culture medium 4 hrs. Next the cells were oleate loaded (500 μM) and analyzed 4 hrs later.

For phospholipase A2 and PLD double inhibition experiments, cells were pretreated with 15 μM of the c-phospholipase A2 inhibitor methyl arachidonyl fluorophosphonate (MAFP), and 0,5% v/v of the primary alcohol 1-butanol inhibitor of PLD for 30 min. Cells were next incubated with oleate for 8 hrs.

The pharmacological inhibition of SCD1 was achieved using SCD1 inhibitor ($SCD1_i$, #CAY10566). Huh7 cells were treated with 2.5 μM SCD_{1i} for 24 hours then oleate loaded for 24 hrs.

Induction of Squalene Accumulation

For squalene accumulation, terbinafine was used to inhibit the squalene epoxidase. Hela cells were treated with (a) 500 μM mevalonic acid and 20 μM farnesyl for 4 hrs (control), or with (b) 300 μM terbinafine for 1 hr prior to mevalonic acid and farnesyl treatment, or (c) treated with SCD_{1i} for 24 hrs, prior terbinafine treatment and mevalonic acid and farnesyl loading.

Relevance of Curvature for Lipid Droplet Budding (Related to Figures 1 and 2)

The deformation of a monolayer is mainly characterized by two parameters:

- The bending rigidity, which is the energy cost for bending the monolayer membrane. It is characterized by the bending rigidity κ, which works against curving the monolayer.
- The surface tension, γ, is the energy cost per generated area between two compartments; it works to decrease the total amount of surface between the compartments.

Budding is not immediately reached with the volume increase of a forming LD. A nascent lens is first reached as observed in cells (Choudhary et al., 2015).

The initial lens shape of a forming LD is owed in part to the bending rigidity of the monolayer, which tends to flatten the forming LD. This rigidity effect is indeed important at the beginning of LD formation because the nanometric scale of the LD induces important curvatures.

Under budding conditions, the monolayer surface tension has the opposite effect of minimizing the lens surface, to favor the formation of a spherical LD.

The monolayer bending rigidity and surface tension have thus antagonist contributions in the early steps of LD formation. There exist a characteristic length λ above which surface tension dominates (Thiam and Foret, 2016)

$$\lambda = \sqrt{\kappa/\gamma_c}$$

For a fluid phospholipid monolayer, κ is beneath $20k_BT$ (Kabalnov and Wennerström, 1996), and γ is $\sim 1 mN/m$, as for the purified cellular LDs (Figure 1A). Consequently:

$$\lambda \sim 10 - 20\, nm$$

Thus surface tensions dominate in budding when the droplet dimension is above 20 *nm*.

This result means that in the giant vesicles and artificial LD experiments (Figure 1), or in the droplet interface bilayer (DIB) (Figure 2), only surface tensions are into play. Curvature, which is inherent to the bending rigidity, is not relevant because the dimensions are well above 20 nm. The curvature of drops in the DIB system does not have effects on the budding angle, controlled by surface tensions.

Theoretical Modeling of the Shape of Lipid Droplet Budding (Related to Figure 5G)

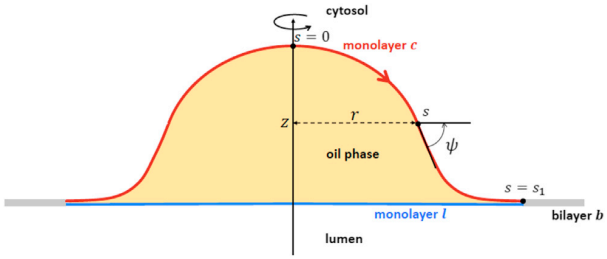

1. Model

A forming LD is considered as an oil phase embedded between two unzipped monolayers of a bilayer, see figure. In a continuous medium description, the monolayers and the bilayer are described as elastic fluid membranes, each characterized by its tension and bending rigidity.

In order to make our model as simple as possible and capture the main physical mechanism of LD budding, we assume that (*i*) the luminal LD monolayer *l* and the bilayer *b* are flat, (*ii*) the LD shape is symmetrical around the z-axis and, (*iii*) the spontaneous curvature of the monolayers is zero. Under these hypothesis, the shape of the LD is determined by the shape of the monolayer of the cytosol side *c* and is controlled by the following parameters: κ, the bending modulus of the monolayer *c*; γ_c, γ_l, and γ_b which are respectively the tensions of the monolayer *c*, the monolayer *l* and the bilayer *b*; the volume *V* of the oil droplet. The equilibrium shape corresponds to the minimum of the free energy:

$$F = \int \frac{\kappa}{2}(C_1 + C_2)^2 dA_c + \gamma_c A_c(\gamma_l - \gamma_b)A_l \qquad \text{(Equation 1)}$$

The first term is the bending elastic energy of the monolayer *l*, with *A* its area, and C_1 and C_2 its two principal curvatures. The next terms are the interfacial energies with A_c the area of the monolayer *c*.

2. Shape Equations

For axisymmetric membranes, the derivation of the equations governing the shape has been standardized; see for example (Foret, 2014; Julicher and Seifert, 1994; Seifert et al., 1991). Computing the shape reduces to compute the 1D contour at a given revolution angle. The position of a point on this contour is given by the arclength *s*. At the boundaries $s = 0$ (on the z-axis) and $s = s_1$ (where the two monolayers meet to form the bilayer). The shape of the contour can be fully characterized by $\psi(s)$, the angle between the tangent and radial vectors, see introductive figure. The functions $r(s)$ and $z(s)$ (see definition in the introductive figure) are then obtained by

integrating $r = \cos(\psi)$ and $z = -\sin(\psi)$, where the dots denote for the derivatives with respect to s. The two principal curvatures are $C_1 = \dot{\psi}$ and $C_2 = \sin(\psi)/r$; the surface element is $dA = 2\pi r ds$. The free energy then reads as follow:

$$F = 2\pi \int_0^{s_1} \left[(\kappa/2)\left(\dot{\psi} + \sin(\psi)/r\right)^2 + \gamma_c \right] r ds + (\gamma_l - \gamma_b)\pi r(s_1)^2 \qquad \text{(Equation 2)}$$

This energy is minimized with respect to $r(s)$ and $\psi(s)$ under the constraints that $\dot{r} = \cos(\psi)$ and,

$$V = \int_0^{s_1} \pi r^2 \sin(\psi) ds \qquad \text{(Equation 3)}$$

These constrains are accounted for by introducing the Lagrange multipliers $t(s)$ and p that is the droplet pressure. The functional to be minimized is then $S = F - pV + 2\pi \int_0^{s_1} t(s)(\dot{r} - \cos(\psi)) ds$, which can be written

$$S[r(s), \psi(s)] = 2\pi \int_0^{s_1} L(\psi, \dot{\psi}, r, \dot{r}) ds + (\gamma_l - \gamma_b)\pi r(s_1)^2$$

$$\text{with} \quad L = (\kappa/2)\left(\dot{\psi} + \sin(\psi)/r\right)^2 r + \gamma_c r + (p/2) r^2 \sin(\psi) + t(\dot{r} - \cos(\psi)) \qquad \text{(Equation 4)}$$

The variation of S reads,

$$\frac{\delta S}{2\pi} = \int_0^{s_1} \left(\left(\frac{\partial L}{\partial \psi} - \frac{d}{ds}\frac{\partial L}{\partial \dot{\psi}} \right) \delta\psi + \left(\frac{\partial L}{\partial r} - \frac{d}{ds}\frac{\partial L}{\partial \dot{r}} \right) \delta r \right) ds - \left.\frac{\partial L}{\partial \dot{\psi}}\right|_0 \delta\psi(0) + \left.\frac{\partial L}{\partial \dot{\psi}}\right|_{s_1} \delta\psi(s_1) - \left.\frac{\partial L}{\partial \dot{r}}\right|_0 \delta r(0) + \left(\left.\frac{\partial L}{\partial \dot{\psi}}\right|_{s_1} + (\gamma_l - \gamma_b) r(s_1) \right) \delta r(s_1) - H \delta s_1 \qquad \text{(Equation 5)}$$

with

$$H = \frac{\partial L}{\partial \dot{\psi}}\dot{\psi} + \frac{\partial L}{\partial \dot{r}}\dot{r} - L = constant$$

At equilibrium, $\delta S = 0$, each term must vanish, which leads to

$$\frac{\partial L}{\partial \psi} - \frac{d}{ds}\frac{\partial L}{\partial \dot{\psi}} = 0 \; and \; \frac{\partial L}{\partial r} - \frac{d}{ds}\frac{\partial L}{\partial \dot{r}} = 0$$

which gives the equations governing the shape,

$$\begin{aligned} \dot{r} &= \cos(\psi) \quad \dot{\psi} = u \quad \dot{t} = \frac{\kappa}{2}u^2 - \frac{\kappa}{2}\frac{\sin^2(\psi)}{r^2} + \gamma_c - pr\sin(\psi) \\ \dot{u} &= -\frac{u\cos(\psi)}{r} + \frac{\cos(\psi)\sin(\psi)}{r^2} + \frac{p}{2\kappa} r\cos(\psi) + \frac{t\sin(\psi)}{\kappa r} \end{aligned} \qquad \text{(Equation 6)}$$

At the boundaries, $\psi(0) = \psi(s_1) = r(0) = 0$ so that $\delta\psi(0) = \delta\psi(s_1) = \delta r(0) = 0$ in (5). The radius of the droplet basis $r(s_1)$ is not fixed a priori but adjusts itself to minimize the energy. According to (5), $r(s_1)$ is such that

$$\left.\frac{\partial L}{\partial \dot{\psi}}\right|_{s_1} + (\gamma_l - \gamma_b) r(s_1) = 0$$

Finally, the length of the contour s_1 is not fixed and thus, according to (5), $H = 0$, which implies $t(0) = 0$. In summary, the boundary conditions are,

$$\psi(0) = 0\,, \quad r(0) = 0\,, \quad t(0) = 0, \quad \psi(s_1) = 0\,, \quad t(s_1) = (\gamma_b - \gamma_l) r(s_1) \qquad \text{(Equation 7)}$$

Solving the shape equations with the boundary conditions gives the equilibrium shape for a given pressure p. This pressure has to be adjusted to obtain the shape with the prescribed volume V.

3. Dimensionless Equations and Numerical Implementation

The natural length scale of this system is

$$\lambda = \sqrt{\frac{\kappa}{\gamma_c}} \qquad \text{(Equation 8)}$$

For droplet with $V \gg \lambda^3$, the bending rigidity of the monolayer should have a negligible effect on the droplet shape, which should be mainly determined by the competition of the surface tensions.

By using λ as the length unit and κ as the energy unit, and doing the variable changes,

$$\frac{s}{\lambda}\rightarrow s\ ,\quad \frac{r}{\lambda}\rightarrow r\ ,\quad \frac{z}{\lambda}\rightarrow z\ ,\quad \frac{t\lambda}{\kappa}\rightarrow t\ ,\quad \frac{F}{\kappa}\rightarrow F\ ,\quad \frac{p\lambda^3}{\kappa}\rightarrow p \qquad \text{(Equation 9)}$$

one obtains the dimensionless shape equations,

$$\dot{r}=\cos(\psi);\ \dot{\psi}=u;\ \dot{t}=\frac{1}{2}u^2-\frac{1}{2}\frac{\sin^2(\psi)}{r^2}+1-pr\sin(\psi);\ \dot{u}=-\frac{u\cos(\psi)}{r}+\frac{\cos(\psi)\sin(\psi)}{r^2}+\frac{p}{2}r\cos(\psi)+\frac{t\sin(\psi)}{r} \qquad \text{(Equation 10)}$$

and the boundary conditions,

$$\psi(0)=0\ ,\quad r(0)=0\ ,\quad t(0)=0,\quad \psi(s_1)=0\ ,\quad \frac{t(s_1)}{r(s_1)}=\frac{\gamma_b-\gamma_l}{\gamma_c} \qquad \text{(Equation 11)}$$

The shape is thus controlled by only two dimensionless parameters: p, which is adjusted to have the correct volume, and $(\gamma_b-\gamma_l)/\gamma_c$, which is nothing but the cosine of the contact angle (the angle that would form the droplet at the monolayer junction in the absence of bending rigidity).

Numerically, the four first order differential equations are integrated with an adaptive step Runge-Kutta algorithm, from the point $s = 0$ until the point s_1 such that $\psi(s_1) = 0$.

The initial condition $u(0)$ is not known and is tuned until the shape is such that the last boundary condition $t(s_1)/r(s_1) = (\gamma_b - \gamma_l)/\gamma_c$ is satisfied (this is a so-called "shooting" method). The pressure p is then tuned to obtain the chosen volume.

For a range of the control parameters V and $(\gamma_b - \gamma_l)/\gamma_c$, several solutions of the shape equations are found, *i.e.* the boundary condition for $t(s_1)/r(s_1)$ is satisfied for different values of $u(0)$ leading to different possible shapes. The correct shape is selected as the one that has the lowest free energy.

For other ranges of the control parameters, no solutions are found. Yet, the spherical shape with an infinitely narrow neck connecting the membrane is still a possible solution (not accessible numerically) and is the only possible shape in this case. This corresponds to the "budding" region of the phase diagram.

In the "wetting" region of the phase diagram, the shapes are "spread" in the sense that they have $\psi < \pi/2$ everywhere. In the yellow region, the shapes correspond to a partially budded droplet with a neck region ($\psi > \pi/2$ for some s).

Molecular Dynamics (MD) Simulations (Related to Figures 4C–4E)

MD simulations were performed using the coarse-grain (CG) lipid model by Klein and coworkers (Shinoda et al., 2007; Bacle et al., 2017). The simulations were performed with the software LAMMPS, and all molecular graphics were generated with visual molecular dynamics (Humphrey et al., 1996). Configurations for the various CG systems were generated by converting atomistic snapshots using the CG-it software (https://github.com/CG-it).

In LAMMPS, pressure and temperature were controlled using a Nosé-Hoover thermostat and barostat, with target temperature and pressure of 300 K and 1 atm, respectively. The lateral *xy* dimensions of the systems were constrained to be equal, while the orthogonal dimension *z* was allowed to fluctuate independently. For simulations at non-zero surface tension, the *xy* lateral dimensions were kept fixed. Van der Waals and electrostatics were truncated at 1.5 nm, with long-range electrostatics beyond this cutoff computed using the particle-particle-particle-mesh (PPPM) solver with an RMS force error of 10^{-5} kcal mol^{-1} Å^{-1} and order 3. In all simulations, a time step of 20 fs was used.

For the "blister formation" simulations, a box consisting of 50 PC molecules and a variable number of TO molecules corresponding to the different TO concentrations was initially prepared. The two PC monolayers were displaced along the *z*-axis in order to allow the insertion of the TO molecules without any steric contact between the molecules. The TO molecules were subsequently randomly placed between the two monolayers. The box was then replicated 8 times along the *x* and *y* axis for a total of 3200 PC molecules in each system. For each concentration 3 independent simulations were performed. The simulations were stopped when blister formation was observed. When no blister formation was observed, the simulations were stopped after 1.5 μs. Error bars are given as standard deviations over the three independent simulations.

For the "triglyceride diffusion" simulations, a system composed of 204 TO molecules in the liquid state was placed between two monolayers of 625 PC molecules each, for a total of 1250 PC molecules. After 1 ns of equilibration to let the two monolayers spontaneously form a bilayer without any leakage of TO molecules from the blister, MD simulations of 1.5 μs were performed at different fixed values for the (x,y) coordinates, resulting in different surface tensions. Analyses were performed on the last 1 μs of the MD run. Error bar are given as standard deviation over the last 1 μs.

In all cases, a TO blister was defined as all TO molecules that are within 2.5 nm of distance of the "core" TO molecules, i.e. those that are not within 2.5 nm of any PC phosphate group. The "free bilayer" for the analysis of the triglyceride diffusion was defined as the bilayer that was not outside the computed initial area of the TO blister after equilibration (the blister radius was determined to be 7 nm).

Lateral pressure and density profiles were computed for a system composed of 3200 PC molecules, with or without 4% TO molecules. The simulations were run for 800 ns and analyses were performed on the last 300 ns.

Lateral pressure profiles (LPPs) $p(z)$ were computed by evaluating, following the protocol described in (Ding et al., 2015):

$$p(z) = P_L(z) - P_N$$

where $P_L(z)$ is the lateral component of the pressure tensor $P_L(z) = \frac{1}{2}(P_{xx}(z) + P_{yy}(z))$ and P_N the normal component ($P_N = P_{zz}$).

A negative $p(z)$ means the system wants to shrink the lateral dimension, a positive $p(z)$ means the system wants to expand the lateral dimension.

Density profiles were computed by averaging the mass density of the various molecules along the z-axis using a grid of 0.1 nm resolution.

For all simulations, surface tension was computed from the diagonal values of the pressure tensor (P_{xx}, P_{yy}, and P_{zz}) using the Kirkwood-Irving method:

$$g = \frac{L}{2}\left<P_{zz} - \frac{1}{2}(P_{xx} + P_{yy})\right>$$

where L is the box length in the z dimension and <> means an ensemble average.

QUANTIFICATION AND STATISTICAL ANALYSIS

For statistical evaluation of LD size variation due to the modulation of enzymes vs. control (in Figures 6E, 6H, 6K, 6O, S6H, and S6L), the data was assessed by d'Agostino & Pearson omnibus normality test. All data followed a non Gaussian distribution. Statistical significance was evaluated by Kolmogorov-Smirnov test using Prism software. Data are presented with the 10-90% box-and-whisker plot, where the central box represents the interquartile ranges (25th to 75th percentiles), the middle line represents the median sample value, and the horizontal lines represent the minimum and the maximum value of observation range.

The statistical comparisons of the contact angles for the lipid surfactants were done by Mann–Whitney non-parametric test (in Figure 2E). All values shown in the text and figures are mean ± S.D., where N=10. Values are from at least 3 independent experiments.

(*** indicates $p < 0.0001$ ** indicates $p < 0{,}001$ * indicates $p < 0.01$).

DATA AND SOFTWARE AVAILABILITY

Computation of the model was done using C++. Simulation was carried on by using the CG-it software (https://github.com/CG-it).

Annexe B :

Collaboration avec Molenaar et al. 2019 :

Lecithin:Retinol Acyl Transferase (LRAT) induces the formation of lipid droplets

Travaux publiés dans BioRxiv en cours de révisions

De nombreuses protéines ciblent spécifiquement les CLs et, comme nous l'avons vu, l'interaction entre les motifs protéiques et le noyau de lipides neutres des CLs impacte directement le recrutement. Le tensiomètre à goutte pendante permet de caractériser les interactions protéines-gouttes de lipides neutres. C'est dans ce contexte que nous avons collaboré avec le groupe de J. Bernd Helms pour caractériser l'affinité spécifique d'une enzyme, la Lecithin:Retinol Acyl Transferase (LRAT) avec les lipides neutres qu'elle produit : les retinyl esters. Le retinyl ester est une huile qui peut être rassemblée par la cellule dans des CLs à l'instar des triglycérides. Le but de l'étude était de savoir si cette enzyme était recrutée spécifiquement sur des CLs contenant du retinyl ester, permettant ainsi d'en accroître la quantité stockée. Grâce au tensiomètre, nous avons montré que l'enzyme LRAT interagissait plus fortement avec le retinyl ester qu'avec les triglycérides qui composent la plupart des CLs. Ces résultats ont donc permis d'étayer l'idée que la structure moléculaire de LRAT est conçue de manière optimale pour aboutir à la formation de grands CLs contenant du retinyl ester.
L'ensemble de cette étude a été déposée sur BioRxiv en attente de publication et constitue le corps de cette annexe :

Résumé de cette publication (Molenaar et al. 2019 [156]) :

Les corps lipidiques (CLs) sont des organelles présentes chez la plupart des êtres vivants qui stockent des lipides neutres dans un noyau hydrophobe recouvert par une monocouche de phopholipides. Les lipides neutres les plus abondants sont les triglycérides et les stérol esters. Mais on ne sait pas si d'autres types de lipides peuvent former des CLs à eux seuls. Cette étude montre que la production de retinyl esters par l'enzyme lecithin:retinol acyl transferase (LRAT) provoque la formation de CLs dans des cellules de levures incapables de produire

des triglycérides et des stérols esters. Une étude par microscopie électronique révèle que ces CLs sont morphologiquement identiques à ceux produits par les cellules Wild Type. Des expériences *In silico* et *In vitro* ont permis de confirmer la propension des retinyl esters à démixer dans une membrane et à former des CLs. La partie N-terminale hydrophobe de LRAT présente des interactions préférentielles avec le retinyl ester présent dans les membranes et favoriserait ainsi la formation de grands CLs contenant du retinyl ester dans des cellules de mammifères. Ces résultats suggèrent que la structure moléculaire de LRAT est conçue de manière optimale pour aboutir à la formation de grands CLs dans les cellules stockeuses de retinyl ester.

Lecithin:Retinol Acyl Transferase (LRAT) induces the formation of lipid droplets

Martijn R. Molenaar§ , Tsjerk A. Wassenaar‡ , Kamlesh K. Yadav# , Alexandre Toulmay# , Muriel C. Mari&, Lucie Caillon£ , Aymeric Chorlay£ , Maya W. Haaker§ , Richard W. Wubbolts§ , Martin Houweling§ , A. Bas Vaandrager§ , Fulvio Reggiori&, Abdou Rachid Thiam£ , William A. Prinz# , J. Bernd Helms§*

§ Department of Biochemistry and Cell Biology, Faculty of Veterinary Medicine, Utrecht University, 3584 CM, Utrecht, The Netherlands

‡ Groningen Biomolecular Sciences and Biotechnology Institute and Zernike Institute for Advanced Materials, University of Groningen, Nijenborgh 7, 9747 AG Groningen, The Netherlands

#National Institute of Diabetes and Digestive and Kidney Diseases, NIH, Bethesda, MD 20892, USA

&Department of Cell Biology, University of Groningen, University Medical Center Groningen, Groningen, Netherlands

£Laboratoire de Physique Statistique, Ecole Normale Supérieure, PSL Research University, Sorbonne Université, UPMC Université Paris 06, Université Paris Diderot, CNRS, Paris, France

Lipid droplets are unique and nearly ubiquitous organelles that store neutral lipids in a hydrophobic core, surrounded by a monolayer of phospholipids. The primary neutral lipids are triacylglycerols and steryl esters. It is not known whether other classes of neutral lipids can form lipid droplets by themselves. Here we show that production of retinyl esters by lecithin:retinol acyl transferase (LRAT) in yeast cells, incapable of producing triacylglycerols and steryl esters, causes the formation of lipid droplets. By electron microscopy, these lipid droplets are morphologically indistinguishable from those in wild-type cells. In silico and in vitro experiments confirmed the propensity of retinyl esters to segregate from membranes and to form lipid droplets. The hydrophobic N-terminus of LRAT displays preferential interactions with retinyl esters in membranes and promotes the formation of large retinyl ester-containing lipid droplets in mammalian cells. Our combined data indicate that the molecular design of LRAT is optimally suited to allow the formation of characteristic large lipid droplets in retinyl ester-storing cells.

Introduction

Lipid droplets (LDs) form a ubiquitous class of organelles, best known for their role as storage of neutral lipids for a multitude of functions such as creating an energy reservoir, a source for building blocks, protection against lipotoxicity, a role in cell cycle, and storage of signaling lipids (Hashemi and Goodman, 2015; Pol et al., 2014; Thiam and Beller, 2017; Walther and Farese, 2012). However, LDs also play important roles in lipid metabolism and homeostasis. Dysfunction of LD synthesis has been linked to a range of diseases. The physiological role of LDs thus appears significantly larger than considered previously (Krahmer et al., 2013; Welte, 2015).

LDs have a unique organellar architecture with a lipid monolayer surrounding a hydrophobic core that consists of neutral lipids. A number of specific proteins associate with LDs regulating organelle and lipid dynamics. Recent advances have started to shed light on the mechanism of LD biogenesis. In the most prevalent view, LD formation is primarily driven by triacylglycerol (TAG) synthesis at the endoplasmic reticulum (ER). TAG accumulates at the interphase of the ER bilayer, until a critical demixing concentration is reached and phase separation occurs, leading to lens formation and membrane deformation (Thiam and Forêt, 2016; Walther et al., 2017). During this process of nucleation, neutral lipids coalesce to form lenses between the two leaflets of the membrane bilayer. Indeed, lenses of about 50nm have been observed in the ER upon induction of LD formation in yeast (Choudhary et al., 2015). As neutral lipid synthesis continues, nascent LDs may bud from the endoplasmic reticulum. Although this process may not require proteins other than TAG synthesizing enzymes such as DGAT 1/2 and ACSL3 (Kassan et al., 2013; Pol et al., 2014; Thiam and Forêt, 2016; Walther et al., 2017), several proteins and lipids have been identified in the regulation of LD number and size as well as LD dynamics.

The abundant presence of large LDs is a hallmark of hepatic stellate cells (HSCs) in normal liver. HSCs are specialized in the storage of retinol (vitamin A) as retinyl esters, giving the LDs their characteristic autofluorescent properties. After liver injury, the fine structure of HSCs changes considerably. They lose their characteristic LDs and transdifferentiate into myofibroblasts, in preparation to secrete collagen (Blaner et al., 2009; Friedman, 2008). Lipidomic analysis revealed complex dynamics of disappearance of different classes of neutral lipids during HSC activation (Testerink et al., 2012). Recent research shows the presence of two different types of LDs, so-called preexisting "original" LDs with relatively slow turnover and rapidly "recycling" LDs that transiently appear during activation of HSCs (Ajat et al., 2017; Molenaar et al., 2017; Tuohetahuntila et al., 2016). Whereas synthesis and breakdown of TAGs in rapidly recycling LDs is mediated by DGAT1 and ATGL (Tuohetahuntila et al., 2016), less is known about the turnover of preexisting LDs. Lysosomes play an important role in the degradation of these LDs (Tuohetahuntila et al., 2017) and this is likely to be related to the observed importance of the autophagic pathway in HSC activation (Hernandez-Gea and Friedman, 2011; Thoen et al., 2011).

Surprisingly, inhibition of DGAT1 does not affect the dynamics of the preexisting LDs nor does it affect the synthesis of retinyl esters in isolated primary HSCs (Ajat et al., 2017; Tuohetahuntila et al., 2016). However, HSCs contain a specialized enzyme called lecithin:retinol acyltransferase (LRAT) that catalyzes a trans-esterification reaction between the *sn-1* position of phosphatidylcholine (PC) and all-*trans*-retinol to form all-*trans*-retinyl ester (Fig. 1A,B) (Golczak et al., 2012; Ruiz and Bok, 2010). As LRAT is the main contributor to retinyl ester storage in the liver (Liu and Gudas, 2005; O'Byrne et al., 2005), we investigated the possibility that LRAT-mediated retinyl ester synthesis drives the generation of the relatively large, retinyl ester-containing LDs in quiescent HSCs.

Results

LRAT expression generates UV-positive lipid droplets

Primary and quiescent HSCs spontaneously transdifferentiate into activated HSCs (myofibroblasts) ex vivo upon isolation and subsequent culture, resulting in LD disappearance. Quiescent and activated HSCs can be identified based on their high expression of desmin, whereas these two HSC populations can be distinguished from each other by an increased alpha smooth muscle actin (α-SMA) expression in activated HSCs (Blaner et al., 2009; Friedman, 2008) (Fig. 1C,D). In addition, LRAT expression decreases (Blaner et al., 2009; Kluwe et al., 2011) (Fig. 1E). We previously presented evidence for neutral lipid dynamics during HSC activation that is consistent with the existence of

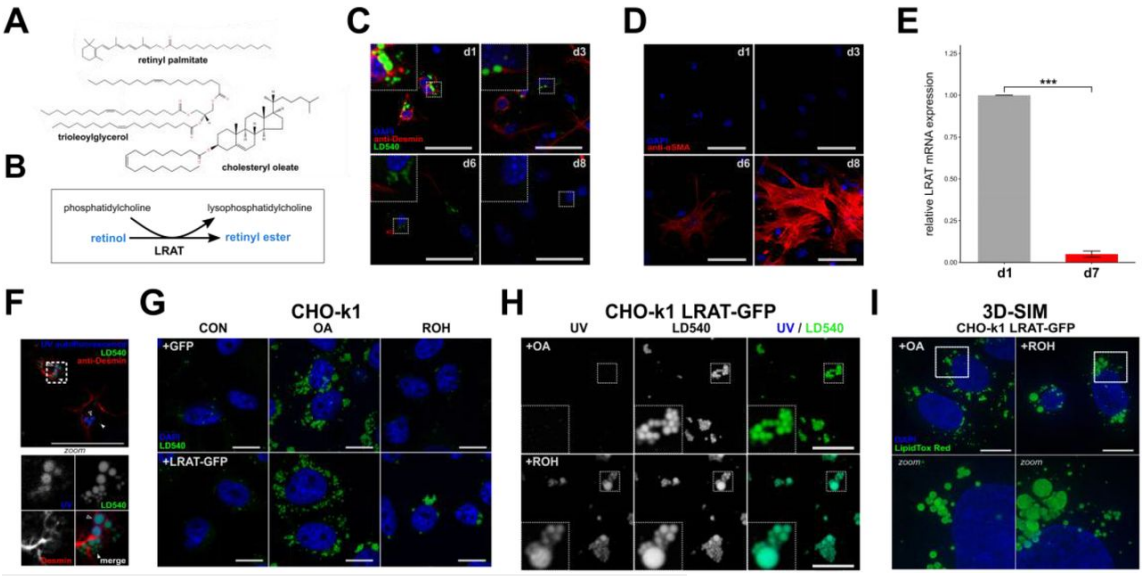

Figure 1.Lipid droplets containing retinyl esters have a distinct morphology. (A) Chemical structures of the neutral lipids retinyl palmitate, cholesteryl oleate, and trioleoylglycerol. (B) Reaction mechanism of LRAT. (C,D) Confocal microscopy of murine hepatic stellate cells (mHSCs) cultured for 1, 3, 6 or 8 days, stained with DAPI (blue), LD540 (green) and anti-desmin (red) (C), or DAPI (blue) and anti-α-SMA (red) (D). Scale bars indicate 50 µm. (E) Relative expression of LRAT mRNAin mHSCs after 1 or 7 days of culture by qPCR. Barplot indicates means ± SEM of 3 animals. Statistical significance was determined by a two-tailed paired Welch's t-test. (F) Confocal microscopy of mHSCs two hours after isolation, showing UV-autofluorescence (blue), LD540 (green) and anti-desmin (red). Bottom panel is a zoomed inset of the area surrounded by dotted lines in the main panel. Closed triangles indicate UV^- LDs, open triangles indicate UV+ LDs. Scale bars indicate 50 µm. (G,H) Confocal microscopy of CHO-k1 cells expressing GFP or LRAT-GFP, incubated overnight in the presence or absence of 20 µM ROH or 200 µM OA. Imaged channels are DAPI (blue) and LD540 (green) (G), or UV-autofluorescence (left) and LD540 (middle) (H). Scale bars indicate 10µm. (I) Full projections of 3D-SIM images of CHO-k1 cells expressing LRAT-GFP, incubated overnight in the presence 20 µM ROH or 200 µM OA. Bottom panels are zoomed insets of areas surrounded by dotted lines in the top panels. Scale bars indicate 10µm. * P < 0.05, ** P < 0.01, *** P < 0.001, NS: not significant.

two different pools of LDs (Molenaar et al., 2017; Tuohetahuntila et al., 2017). To visualize these two different pools, we made use of the autofluorescent properties of retinyl esters in preexisting "original" LDs that are a hallmark of quiescent HSCs (Ajat et al., 2017; Friedman, 2008). After fixation of freshly isolated HSCs, retinyl esters (UV autofluorescence) and LDs (LD540) were imaged by confocal microscopy. We observed two distinct populations of LDs: large UV+LD540+ structures containing high amounts of REs and UV^-LD540^- structures - depleted from REs - with smaller diameters (Fig. 1F). These observations are also in good agreement with our recent findings that LDs in $LRAT^{-/-}$ HSCs were significantly smaller as compared to LDs from wild-type cells (Ajat et al., 2017). Together, these data suggest a role for LRAT in the formation of distinct vitamin A-containing LDs that are a hallmark of hepatic stellate cells (HSCs).

To understand the role of LRAT in LD biology, we stably transfected CHO-k1 cells with a plasmid carrying LRAT-GFP. Lipidomic analysis of CHO cells expressing LRAT showed that retinyl ester synthesis was observed only after addition of retinol (ROH) as substrate to the medium (Fig. 1G (UV^-LDs) and Suppl. Fig. 1A) and revealed the presence of predominantly saturated (16:0 and 18:0) and mono-unsaturated (18:1) fatty acids (Suppl. Fig. 1A). This composition reflects the catalytic activity of LRAT, using fatty acids at the *sn-1* moiety of PC for esterification (Golczak et al., 2012; MacDonald and Ong, 1988). CHO cells do not contain detectable amounts of enzymatic activity of LRAT (Suppl. Fig. 1B) and in the absence of LRAT they can synthesize retinyl esters using a different mechanism involving DGAT1 (Ajat et al., 2017; Orland et al., 2005). This reaction occurs with much lower efficiency and results in a different species profile of retinyl esters (Suppl. Fig. 1C). Inhibition of DGAT1 activity in CHO-k1 cells expressing LRAT-GFP showed no inhibition of retinyl ester synthesis, which confirms that LRAT is the primary retinyl ester synthesizing enzyme (Suppl. Fig. 1D). Both CHO-k1 cells expressing GFP or LRAT-GFP showed increased LD540 fluorescence after incubation with oleic acid (OA). However, only LRAT-GFP expressing cells showed an increase in LDs after incubation with ROH, confirming the ability of LRAT to esterify

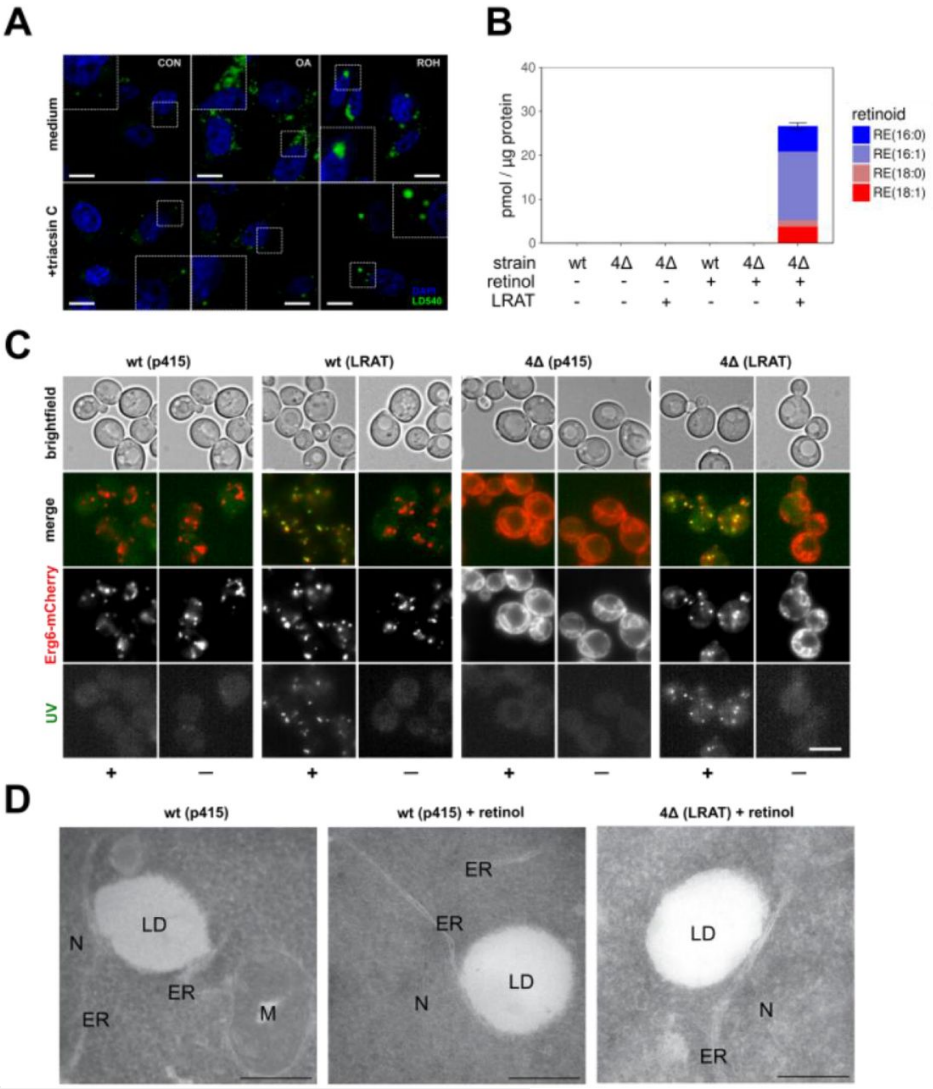

Figure 2.LRAT-mediated LD-formation in the absence of pre-existing LDs (A) Confocal microscopy of CHO-k1 expressing LRAT-GFP. After pre-incubation with medium containing 1% FBS, cells were incubated overnight with or without 200 µM OA or 20 µM ROH, in the presence or absence of 1 µg/mL triacsin C. Cells were stained with DAPI (blue) and LD540 (green). Scale bars indicate 10 µm. (B) Quantification of predominant RE-species by LC-MS/MS of wt and 4Δ yeast cells expressing LRAT, 2 hours after incubation in the presence or absence of 2 mM ROH. Amounts in pmol RE per µg protein. Barplot indicates means ± SD. (C) Wide-field microscopy of Erg6-mCherry expressing wt and 4Δ yeast cells, with or without expressing LRAT, 2 hours after incubation with or without 2 mM ROH ('—' or '+'). Images of UV-autofluorescence (green), Erg6-mCherry (red) and brightfield were taken. Scale bars indicate 5 µm. (D) Electron microscopy of wt and 4Δ yeast cells, with or without expressing LRAT, incubated with or without 2 mM ROH. ER, endoplasmic reticulum; LD, lipid droplet; M, mitochondria; N, nucleus. Scale bars indicate 250 nm. (E) Electron microscopy of yft2Δscs3Δ, and 4Δ yeast cells expressing LRAT, incubated with 2 mM ROH. Scale bars indicate 100 nm. ER, endoplasmic reticulum (yellow lines in right panels); LD, lipid droplet (red lines right panels). (F) Wide-field microscopy of Erg6-mCherry expressing wt yeast cells expressing LRAT. Two time series of UV-autofluorescence (white), Erg6-mCherry (red) and brightfield, taken 2, 4, 6 and 8 minutes after addition of 2 mM ROH. Scale bars indicate 5 µm.

ROH (Fig. 1G). Furthermore, these LDs exhibited UV-autofluorescence and were larger in diameter as compared to OA-stimulated LDs, which in turn were not autofluorescent (Fig. 1H). Similar results were obtained after transfection of human HSC-derived cell line LX-2 with LRAT (Suppl. Fig. 2). To exclude the possibility that the observed large UV-LDs were in fact clusters of small LDs that could not be distinguished due to the limited resolution of conventional confocal microscopy, we also imaged both conditions by super resolution microscopy (3D structured illumination microscopy, 3D-SIM). Using SIM, we observed both small and large sized LDs in LRAT-dependent LD-synthesis and with a clustered appearance (Fig. 1I). In the presence of OA, the LDs displayed a more homogeneous size-distribution of

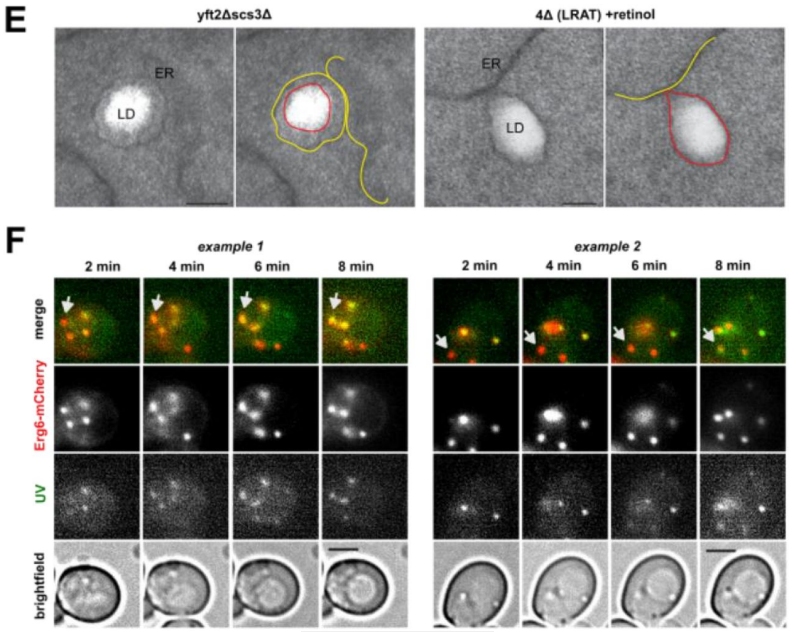

Figure 2.: (Continued)

relative small LDs and a 'dispersed' localization through the cell (Fig. 1I, Suppl. Video 1-2).

LRAT-mediated LD formation is independent of TAG synthesis

TAG synthesis is a driving force in LD biogenesis. The last step in TAG synthesis is performed by DGAT1 or DGAT2, enzymes that transfer activated fatty acids to diacylglycerol. Fatty acid activation is performed by acyl-CoA synthetases and their knockdown or pharmaceutical inhibition after OA-stimulation led to a decreased number of (pre-)LDs (Kassan et al., 2013). Acyl-CoA is, however, not involved in the transesterification reaction of a fatty acid from PC to ROH by LRAT to generate retinyl esters. To determine whether LRAT requires TAG synthesis for retinyl ester synthesis and formation of RE-containing LDs, we pre-incubated LRAT-GFP expressing cells under low serum conditions overnight and subsequently incubated the cells in the presence of triacsin C, a drug that inhibits acyl-CoA synthesizing activities (Igal et al., 1997). In the presence of triacsin C, the number of LDs was strongly reduced, both in the presence and absence of OA (Fig. 2A). In the presence of ROH, however, formation of large LDs was still observed. These results confirm that LRAT does not depend on the presence of acyl-CoA and supports the possibility that LD-formation via LRAT has a distinct mechanism that is independent of TAG (DGAT/ACSL-mediated) LD formation.

Some LDs could still be observed in cells treated with triacsin C and therefore we could not exclude the possibility that, rather than TAG synthesis, TAG-filled LDs are required for RE-containing LD formation. Therefore, we made use of another model system, a *Saccharomyces cerevisiae* mutant strain that lacks the four enzymes responsible for the last steps in triglyceride - Lro1 and Dga1 - and steryl ester (SE) - Are1 and Are2 - synthesis. This mutant strain is viable, but does not contain LDs (Sandager et al., 2002). After introduction of human LRAT into *Irol*Δ *dgal*Δ *arel*Δ *are2*Δ cells (hereafter 4Δ cells), LRAT-GFP co-localizes with Sec63-mCherry, an ER marker in yeast (Suppl. Fig. 3A). The resulting LRAT expressing yeast cells (4ΔLRAT) were able to synthesize REs after the addition of ROH (Fig. 2B). In contrast to mammalian cells, the predominant RE-species was retinyl palmitoleate, RE(16:1). This is in line with the reported fatty acid composition of PC in yeast, which is capable of producing only monounsaturated fatty acids, and contains predominantly PC(32:2) and PC(34:2) (Boumann et al., 2006). In the absence of either LRAT or ROH, both 4Δ and wild-type (wt) yeast cells did not synthesize REs. These results also demonstrate the absence of an endogenous RE synthase activity in yeast by acyl-CoA retinol acyltransferase (ARAT) activity e.g. Dga1 (Fig. 2B). Thus, RE synthesis in yeast depends on LRAT expression. As anticipated, 4Δ LRAT yeast cells were devoid of LD structures in the absence of exogenous ROH, as evidenced by membrane localization of LD-marker Erg6 (Fig. 2C) and BODIPY (Suppl. Fig. 3B). Upon addition of ROH to 4ΔLRAT yeast cells, we observed a clear

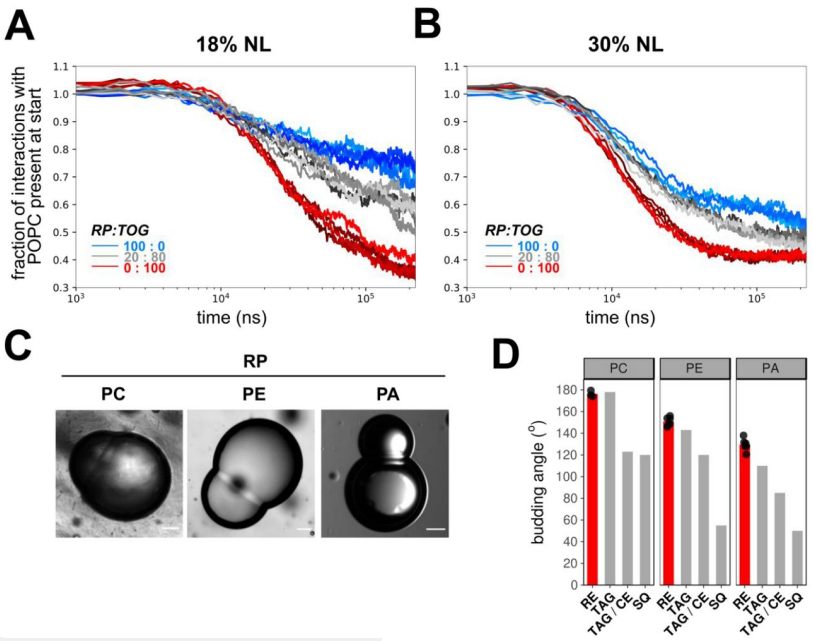

Figure 3.Nucleation and budding properties of RE. **(A,B)** Coarse grain MD simulations of lens formation by 150 (18%) **(A)** and 250 (30%) **(B)** neutral lipids per leaflet in a POPC membrane. Colors indicate the neutral lipid composition, with marine for pure RE and red for pure TOG. The progress of lens formation is shown as fractional loss of interactions between the neutral lipids and POPC as function of time (log-scale). **(C)** Brightfield microscopy images of droplet interface bilayers of droplets containing neutral lipid RP and lipid surfactants PC, PE or PA. Scale bars indicate 20 µm. **(D)** Comparison of quantified budding angles (mean±SD) of RP-containing droplets with lipid surfactants PC (176,2±2,8), PE (150,9±4,0) or PA (129,5±5,7) vs. reported budding angles of TAG and SQ-containing droplets (Ben M'barek et al., 2017). Barplot represent means of at least 8 individual measurements, which are shown as black dots.

presence of autofluorescent LD-like structures and co-localization of these structures with the LD-marker Erg6 (Fig. 2C, Suppl. Fig. 3C) and with BODIPY (Suppl. Fig. 3B). In the absence of LRAT, 4Δ yeast cells could not generate LDs in the presence of ROH.

Electron microscopic examination of the LDs generated in 4Δ LRAT yeast cells revealed the presence of *bona fide* LDs with a cytosolic orientation that were morphologically indistinguishable from TAG/SE-filled LDs generated in wt yeast cells (Fig. 2D,E). These results demonstrate that LRAT induces the formation of LDs in the absence of other LDs or TAGs (Suppl. Fig. 4). To determine whether retinyl esters can partition into existing LDs or exclusively form their own LDs, we determined the co-localization of RE positive LDs (UV^{+}) with all LDs ($Erg6^{+}$) immediately after addition of ROH to *wt* yeast cells expressing LRAT. These cells have TAG-filled LDs present before addition of ROH. As shown in Fig. 2F, 2 min after addition of ROH, co-localization of $Erg6^{+}$ LDs with UV^{+} LDs was observed. In addition, UV^{-} LDs become UV^{+} in the next 6 min, indicating that REs are also transferred into existing LDs.

Spontaneous nucleation and lens formation of retinyl esters in lipid bilayers

The mechanism of LD formation by LRAT-mediated RE synthesis is not known. For TAG-filled LDs it has been shown that TAGs have a limited solubility in biological membranes. Above a critical demixing concentration (~3%), TAG molecules segregate to form TAG lenses that appear as a first step in LD formation (Choudhary et al. 2015; Khandelia et al., 2010; Thiam and Forêt, 2016). After this 'nucleation' process, the lenses grow and can emerge from ER membranes during a 'budding' process. The formation of lenses in TAG containing membranes has been demonstrated and studied in molecular dynamics (MD) simulations (Ben M'barek et al., 2017; Khandelia et al., 2010). Here we built upon that approach and used coarse-grain MD (CG-MD) simulations of 1-palmitoyl-2-oleoyl-sn-glycero-3-phosphocholine (POPC) membranes with different amounts of trioleoylglycerol (TOG) and retinyl palmitate (RP) to assess the propensity of lens formation in those systems. In setups containing only TOG, lens-formation was consistently observed and always completed within 100 ns of simulation. In contrast, setups with only RP took considerable longer to nucleate (Fig. 3A) and more often failed to

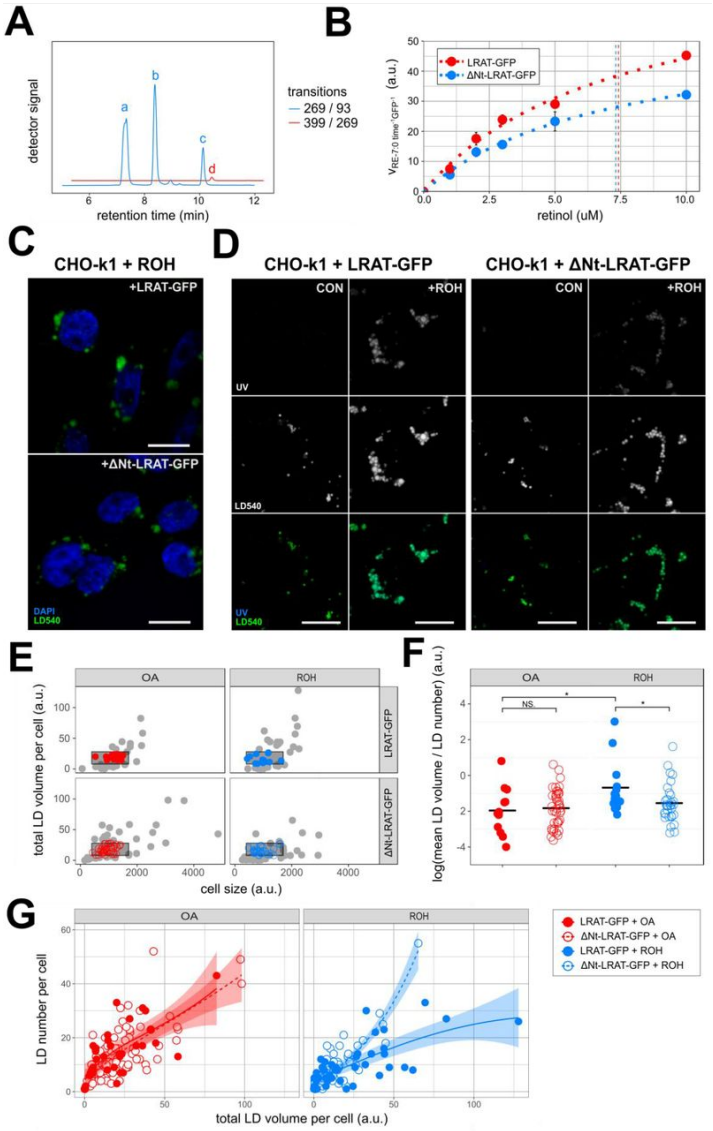

Figure 4.Deletion of N-terminus of LRAT affects LD formation in CHO cells. (A,B) *In vitro* LRAT-activity of CHO-k1 homogenates expressing full-length or ΔNt-LRAT-GFP. After incubation full-length LRAT-GFP with PC(7:0/7:0) and varying concentration of ROH, ROH (peak a), RE(2:0) (internal standard, peak b) and RE(7:0) (peak c) were measured by LC-MS/MS. MRM-transition 269/93 detects all retinoid backbones (blue), whereas 399/269 specifically detects RE(7:0) (red) (A). RE(7:0)-synthesis by full-length or ΔNt-LRAT-GFP was normalized by GFP-levels of the homogenates and plotted against increasing ROH concentrations. Estimated Km values are indicated by vertical dashed lines. A representative plot of three independent experiment is shown (B). (C,D) Confocal microscopy of CHO-k1 cells expressing LRAT-GFP or ΔNt-LRAT-GFP, incubated overnight in the presence or absence of 20 μM ROH. Imaged channels are DAPI (blue) and LD540 (green) (C), or UV-autofluorescence (top) and LD540 (middle) (D). Scale bars indicate 10 μm. (E,F) Quantification of cells imaged by confocal microscopy. Cell sizes were plotted against total LD volume per cell (LRAT-GFP or ΔNt-LRAT-GFP) and cells with similar total LD volumes per cell were gated (black box, LRAT-GFP+OA: 12 cells; ΔNt-LRAT-GFP+OA: 40 cells; LRAT-GFP+ROH: 13 cells; ΔNt-LRAT-GFP+ROH: 31 cells) (E). The gated cells were expressed as log-ratios of mean LD volume vs. LD number. Mean values (±SD) were −1,96±1,34 (LRAT-GFP with OA); −1,83±1,06 (ΔNt-LRAT-GFP with OA); −0,68±1,51 (LRAT-GFP with ROH); and −1,55±1,08 (ΔNt-LRAT-GFP with ROH) Statistical significance was determined by two-tailed unpaired Student's t-tests, P-values were corrected by the Benjamini-Hochberg procedure (F). Cells were incubated overnight with 200 μM OA (red circles) or 20 μM ROH (blue circles) and LD number per cell as a function of total LD volume per cell for LRAT-GFP (closed circles) or ΔNt-LRAT-GFP-expressing (open circles) was analyzed without gating (G). Every data point represents one cell. Lines are moving averages, shades indicate 95% confidence intervals. LRAT-GFP+OA: 35 cells; ΔNt-LRAT-GFP+OA: 79 cells; LRAT-GFP+ROH: 43 cells; ΔNt-LRAT-GFP+ROH: 68 cells. * P < 0.05, ** P < 0.01, *** P < 0.001, NS: not significant.

form lenses on the time scale used for the simulations (250 ns). Lenses formed by RP were also typically less well defined, with more RP remaining dispersed throughout the membrane. Mixtures of TOG and RP showed an intermediate efficiency of lens-formation (Fig. 3A and B). These simulations imply that RP has

a lower propensity to self-aggregate, and hence has a higher nucleation barrier as compared to TOG.

Methods to directly measure the nucleation barrier (or 'critical nucleation volume') do not exist, but in a setting with the same PL-composition, the monolayer surface tension will be a driving force that affects nucleation (Ben M'barek et al., 2017; Deslandes et al. 2017; Thiam and Forêt, 2016). The deformation and budding of a LD monolayer is controlled in part by the monolayer bending rigidity and surface tension – the monolayer bending rigidity will tend to flatten a lens, thereby re-dispersing neutral lipid molecules in the bilayer, while its surface tension will tend to make a lens spherical. However, at a characteristic size, surface tension will essentially control the monolayer deformation. This size will be larger for a lower monolayer surface tension: lower monolayer tensions will likely result in larger 'critical nucleation volumes' or higher nucleation barriers (Ben M'barek et al., 2017; Chorlay and Thiam, 2018; Deslandes et al., 2017; Thiam and Forêt, 2016). We measured the tension of artificial LD containing either RP or TOG and, in line with our MD simulations, tensions were considerably lower in droplets made of RP as compared to their TOG counterparts (Table 1). Moreover, droplets surrounded by DOPC with maximum phospholipid packing showed the same trend. These measurements suggest that RP droplets have higher nucleation barriers, in agreement with the results obtained by CG-MD.

The efficiency of the subsequent budding process of RE-containing LDs can be studied by determination of budding angles in droplet-embedded vesicles or droplet interface bilayers (DIBs) containing neutral lipids (Ben M'barek et al., 2017; Chorlay and Thiam, 2018). By using the DIB system, we compared the budding angles of RP-containing lipid phase with reported values of TAG-LDs (Fig. 3C,D). The budding angles of RP+ droplets with PC and PE monolayers did not differ from reported values of their TOG+ counterparts (Fig. 3D); angles in the case of PA were only slightly higher. These data suggest that RP forms spontaneously LDs as efficiently as TG. In PC tensionless membranes, smaller RP-LD diameters would be thus expected, based on the budding angles, but the delay in nucleation might introduce an increase in the droplet size. This is, however, not observed in yeast cells (Fig. 2C). Thus, other factors must contribute to the characteristic large size of retinyl ester-containing LDs.

N-terminal sequence of LRAT affects lipid droplet morphology

To study a role of LRAT in LD morphology, we considered the possibility that the N-terminus of LRAT aids in the formation of LDs. The N-terminal domain of LRAT (hereafter, LRAT-Nt AH) does not form a trans-membrane domain, despite its high hydrophobicity (Moise et al., 2007). In addition, it was reported that this domain can localize to LDs (Jiang and Napoli, 2012). We stably transfected CHO-k1 cells with a GFP fusion construct of LRAT lacking the N-terminus (ΔNt-LRAT-GFP) and selected clones with similar GFP fluorescence as compared to CHO-k1 cells stably transfected with full-length LRAT-GFP (Fig. 1). LRAT-activity of both homogenates was analyzed in vitro using HPLC-MS/MS by determination of RE(7:0) synthesis upon addition of exogenous PC(7:0/7:0) (Fig. 4A, see Materials and Methods for details). As expected, both enzymes displayed LRAT-activity with similar Km-values for ROH, but reaction rates of ΔNt-LRAT-GFP homogenates were somewhat lower (Fig. 4B). After overnight incubation with ROH, we observed UV+ LDs in both cell lines, but LDs appeared smaller in size in ΔNt-LRAT-GFP expressing cells (Fig. 4C,D). These data show that the N-terminus is not required per se for LD generation, but may have an effect on LD morphology. To rule out the possibility that the reduced LD size in the presence of ΔNt-LRAT-GFP is caused by the reduced activity of this LRAT mutant (Fig. 4B), we developed a single-cell imaging analysis pipeline. To this end, we determined cell size, LD-number per cell and mean LD size per cell by image analysis (see Materials & Methods for details). Total LD volume (representative for total neutral lipid content) was calculated from these parameters. Using this approach, we were able to select ("gate") cells with similar total LD volume and thus neutral lipid content per cell (Fig. 4E). We then compared the log-ratios of LD number vs. LD volume per cell of both cell lines incubated with OA or ROH (Fig. 4F). As expected, no difference was observed when both cell lines were incubated with OA (Fig. 4F, left panel). In contrast, LDs generated in the presence of ROH were smaller in size and larger in number in cells expressing ΔNt-LRAT-GFP as compared to LDs from cells expressing the full-length protein, as reflected by decreased log-ratios (Fig. 4F, right panel). This difference in LD size:number distribution could also be observed in ungated cells; expressing LD-number as function of the total LD volume per cell showed that regression of all

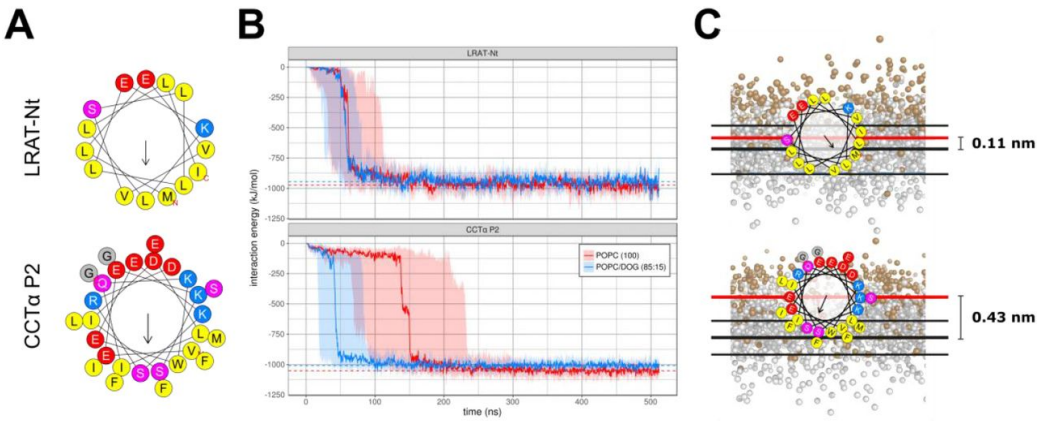

Figure 5.Amphipathic properties of LRAT-Nt and CCT-α P2 helices. (A) Helical wheel projections by HeliQuest of LRAT-Nt (top) and CCT-α P2 (bottom). Colors indicate amino acid categories: hydrophobic (yellow), negatively charged (red), polar (purple), positively charged (blue) and other (gray) residues. The hydrophobic moment is indicated with a black arrow. (B) Peptide-membrane interaction energies for LRAT-Nt (top) and CCT-α P2 with pure POPC (red) and with an 85:15 POPC/DOG mixture (red) over time across DAFT simulation ensembles of 30 simulations each, showing the region from the 1st to 3rd quartile as shaded areas and the median interaction energy for each ensemble of simulations as solid line. (C) Insertion depth of LRAT-Nt and CCT-α P2, showing the helical wheels of LRAT-Nt (top) and CCT-α P2 according to their mean angular orientations, with a red line signifying the position of the helix center, the thick black line denoting the median position of the lipid head groups across simulations and the thinner line denoting the standard deviation of the median across simulations. Colors in the peptides are as described in panel A.

datapoints of LRAT lacking its N-terminus results in a steeper slope as compared to full-length LRAT, indicating more LDs per amount of total neutral lipid (Fig. 4G). Taken together, these results show that the LRAT-Nt has the ability to affect the size:number distribution of retinyl ester-containing LDs in mammalian cells.

N-terminus of LRAT exhibits affinity for retinyl esters *in silico*

The N-terminus of LRAT is predicted to have an alpha-helical structure without hairpin topology, which is flanked by amino acids without a clear secondary structure (Suppl. Fig. 5). HeliQuest analysis (Gautier et al., 2008) showed a clear separation between hydrophobic and polar residues on both sides of the helix, in line with an amphipathic topology (Fig. 5A, upper panel). However, in comparison with canonical amphipathic helices involved in membrane recognition (ALPS motifs) (Bigay et al., 2005), the fraction of hydrophobic over polar residues was considerably higher in the LRAT N-terminal alpha-helix. This is exemplified by comparison of this projection with CCT-α P2, a recently characterized amphipathic domain with LD-affinity (Prévost et al., 2018) that contains an ALPS-like architecture (Fig. 5A, bottom panel). The helical wheel projection of the CCT-α P2 AH revealed a smaller fraction of hydrophobic residues as compared to the LRAT-Nt AH. Membrane-binding of CCT-α P2 is proportional to the amount of lipid packing defects (Prévost et al., 2018). We compared the membrane-binding characteristics of LRAT-Nt with CCT-α P2 by CG-MD using the DAFT-approach (ensemble of 30 simulations per combination of peptide and model membrane) (Wassenaar et al., 2015a). One model membrane consisted of POPC and the other one contained POPC and dioleylglycerol (DOG), a lipid that induces packing defects (Vamparys et al., 2013). We subsequently compared membrane binding of both LRAT-Nt and CCT-α P2. The binding half-time of CCT-α P2 to POPC membranes was 150 ns (Fig. 5B, bottom panel) and in the presence of DOG, this binding was accelerated (50 nsec) (Fig. 5B, bottom panel), confirming the role of packing defects in membrane binding (Prévost et al., 2018). For LRAT-Nt, however, we did not observe a difference in the kinetics of membrane binding between the two model systems (Fig. 5B, top panel; median of about 60 nsec). Interestingly, the results also showed that LRAT-Nt AH docked deeper into the bilayer than the CCT-α P2 AH (Fig. 5C), suggesting that LRAT-Nt has the potential to directly interact with neutral lipids, whereas CCT-α P2 AH binds only to phospholipids.

To investigate a potential interaction of the N-terminal peptide with neutral lipids, we extended the MD setup to a series of POPC membranes containing 10% neutral lipids in different ratios RP:TOG, and in the presence of LRAT-Nt. The simulations showed that LRAT-Nt typically co-localized with neutral lipids (Fig. 6A). Inspection of the localization of LRAT-Nt with respect to the membrane profile (Fig. 6B; Suppl. Fig. 6A) confirmed that the peptide is docked deep into the membrane. Surprisingly, LRAT-

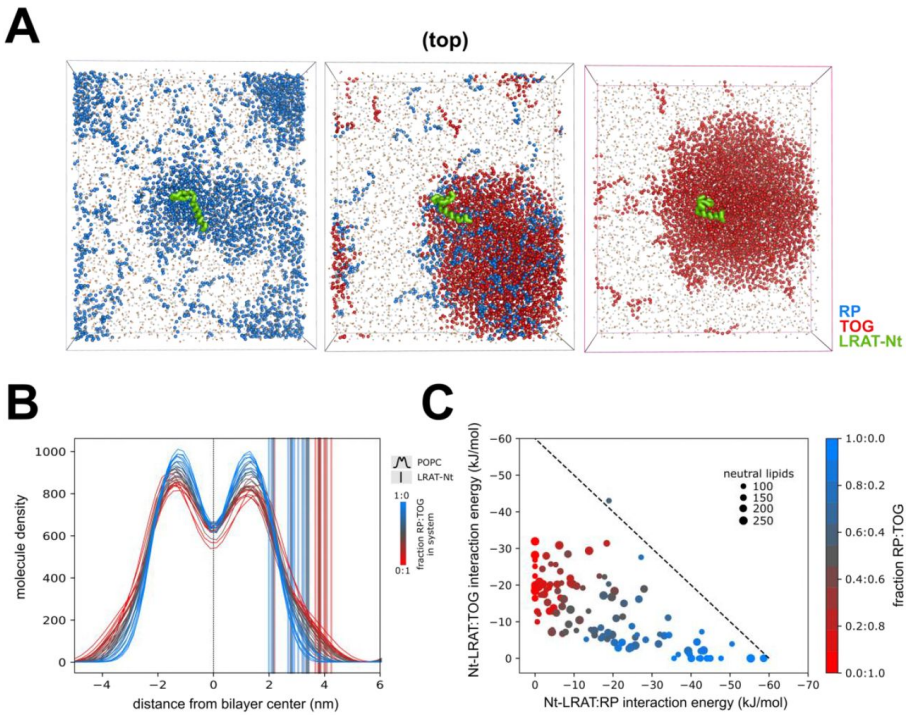

Figure 6.Affinity of LRAT-Nt for retinyl esters in GC-MD. (A) Binding of LRAT-Nt to lenses consisting of 300 molecules RP (left), 120+180 molecules RP+TOG (middle) and 300 molecules TOG (right). The panels show preferential binding of the helix (green) to the region of maximal curvature. The RP and TOG particles are shown in marine and red, respectively. (B) Positions of centers of mass of LRAT-Nt with respect to the membrane as function of the ratio RP:TOG (marine: pure RP to red: pure TOG). The membrane is shown as density profile, while the positions of LRAT-Nt are marked with dashed lines. (C) Specificity of interaction of LRAT-Nt with RP over TOG. Each simulation represents a dot and indicates the interaction energy between LRAT-Nt and RP on the x-axis and between LRAT-Nt and TOG on the y-axis. Dot size reflects the total number of neutral lipids and the color signifies the ratio between RP and TOG as indicated. The dashed line has slope −1 and a parallel profile is indicative of a transition from one pure compound to the other with no preferential interactions. The observations show a lower interaction with TOG as compared to RP, resulting in a profile with a reduced slope.

Nt is docked deeper into the membrane when the neutral lipids consist predominantly of RP as opposed to TOG (Fig. 6B). This is only partly explained by the thicker membrane resulting from the more complete lens formation at higher TOG ratios. Initial inspection of the localization of TOGs and RPs within the lens revealed an asymmetric distribution of the neutral lipid mixture with RPs in closer proximity to the LRAT-Nt peptide (Suppl. Fig. 6B). Assessment of the interaction energies between the LRAT-Nt helix and both RP and TOG confirmed that the helix has stronger interactions with RP than it has with TOG (Fig. 6C). This specific affinity of LRAT-Nt for REs could affect lens and/or LD formation by REs, for example by facilitating the formation of RP containing lenses by decreasing the nucleation energy barrier. This should then be reflected in an enhanced nucleation rate. To study such an influence on lens formation, we performed several series of MD simulations. However, under none of these conditions LRAT-Nt significantly enhanced the rate of lens formation (data not shown).

N-terminus of LRAT exhibits affinity for retinyl esters in vitro

To study the affinity of the LRAT N-terminus to RP in vitro, we synthesized the LRAT-Nt peptide and assessed its recruitment to RP vs. TOG interface. Oil-in-water droplets were formed and the peptide was added (Fig. 7A). Recruitment of the peptide to the droplet interface will decrease the interfacial surface tension (Fig. 7A) (Ajjaji et al., 2019; Small, Wang, & Mitsche, 2009), which happened for both RP and TOG (Fig. 7B). Tension reached an equilibrium value which corresponds to the maximum of adsorbed

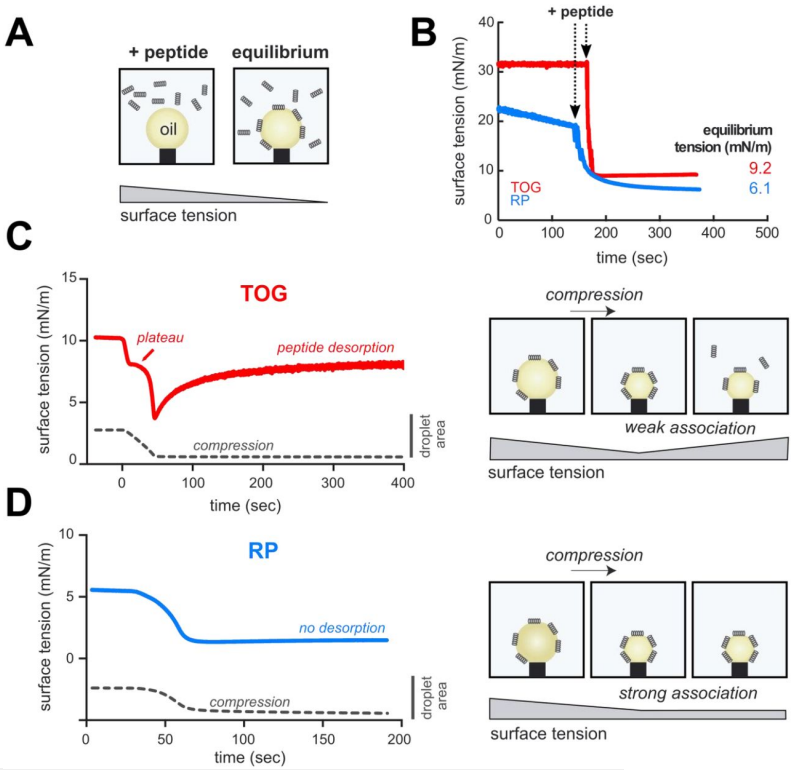

Figure 7.LRAT N-terminal peptide shows strong association with retinyl palmitate droplets. (A) Left, peptide addition to the buffer surrounding a pending oil droplet, trioleoylglycerol (TOG) or retinyl palmitate (RP), results in a decrease of the interface surface tension induced by peptide recruitment. (B) Related surface tension quantification over time for TOG and RP oil droplets. Arrows indicate time of LRAT-Nt peptide injection in the buffer. (C) After, equilibrium is reached, the surface of the TOG-droplet covered by the peptide is compressed, provoking a drop of surface tension. When compression was stopped, surface tension re-increased, indicating desorption of the LRAT-Nt peptide from the TOG-buffer interface. Right panel illustrates the manipulations and consequence on tension and peptide behavior. (D) After the LRAT-Nt peptide was recruited to the RP-droplet surface, the interface was compressed, provoking a surface tension drop. When compression was stopped, surface tension remained constant, indicating a strong association of the peptide with the RP-buffer interface. Right panel illustrates the manipulations and consequence on tension and peptide behavior.

peptides (9.2 mN/m for TOG, and 6.1 mN/m for RP). The peptide recruitment level is determined by the neutral lipid affinity for LRAT-Nt. To further investigate this, we performed a rapid compression experiment whereby, at the equilibrium interfacial tension, the droplet interface was reduced by decreasing its volume (Fig. 7C,D, left, dotted lines). This operation transiently increased the interfacial lateral pressure, i.e. the peptide surface density, and we recorded the relaxation of the system to equilibrium. During compression, surface tension decreased in the case of TOG, reached a transient plateau and subsequently continued decreasing (Fig. 7C). Appearance of the plateau is a signature of a rearrangement of the peptide at the surface, induced by the increase of its surface density (Mitsche & Small, 2013). As soon as compression was stopped, surface tension increased again, which is a signature of the desorption of some of the peptides from the surface. This behavior at the TOG interface is unique to LRAT-Nt, as the 11mer repeat domain of Plin1 does not show such response under similar experimental procedures (Ajjaji et al., 2019). With RP, compression led to a continuous decrease of tension (Fig. 7D) and upon arrest of compression, tension remained constant: the peptide did not desorb from the interface. These results confirm the MD simulations and show that the LRAT-Nt peptide interacts with neutral lipids and with a preference for retinyl esters.

Discussion

Lipid droplet formation starts when neutral lipids accumulate within the bilayer of biological membranes above the a critical demixing concentration (Thiam and Forêt, 2016; Walther et al., 2017). Although the intrinsic capacity of different classes of neutral lipids to form LDs is well accepted based on biophysical considerations (Ben M'barek et al., 2017), *in vivo* this has only been demonstrated for triacylglycerols in yeast (Sandager et al., 2002). As cholesteryl ester synthesizing enzymes also contribute

to TAG synthesis, it remains to be established whether cholesteryl esters are capable of forming lipid droplets in the absence of triacylglycerols (Sandager et al., 2002). Here we show the existence of an alternative route for LD biogenesis, in which synthesis of another class of neutral lipids, retinyl esters, is sufficient to drive LD formation.

Based on biophysical properties of retinyl esters, we show that the spontaneous nucleation of retinyl ester-generated LDs is somewhat less efficient as compared to TAGs. Indeed, molecular dynamic simulations (Fig. 3 A,B) and *in vitro* experiments measuring the tension of artificial droplet interfaces (Table 1) suggest that RP droplets have a higher nucleation barrier, or lower nucleation efficiency than TAGs. Despite these biophysical considerations, retinyl ester-filled LDs are efficiently formed upon exogeneous induction of LRAT in yeast cells that lack the machinery to synthesize TAG/SE-filled LDs (Fig. 2). Surprisingly, the LRAT protein itself is involved in the generation of the large sized LDs that are characteristic for retinyl ester-containing LDs.

LRAT is broadly expressed with highest expression levels in the intestine, liver, testis and eye (Liu and Gudas, 2005; Ruiz et al., 1999). The majority of dietary vitamin A (~75%) is, however, taken up by hepatocytes (Gottesman et al., 2001) and stored as retinyl esters in the liver, primarily in hepatic stellate cells (Blaner et al., 2009; Blomhoff et al., 1991; Friedman, 2008; Gottesman et al., 2001; Ross and Zolfaghari, 2004). LRAT expression is the highest in quiescent HSCs (Fig. 1E), in agreement with previous reports (Mederacke et al., 2013), but this expression is rapidly lost upon activation of HSCs. LRAT expression thus coincides with the presence of large LDs in quiescent HSCs. When LRAT expression is reduced (in activated HSCs, Fig. 1E) or absent in LRAT$^{-/-}$ mice (Ajat et al., 2017; O'Byrne et al., 2005), HSCs lack their characteristic large LDs. These findings show that the presence of LRAT correlates with the existence of the large LDs, consistent with the data now presented here.

LRAT belongs to the papain-like or NlpC/P60 thiol protease superfamily of proteins (Anantharaman and Aravind, 2003). The H-RAS-like suppressor (HRASLS) enzymes, also known as LRAT-like proteins comprise a vertebrate subfamily that includes LRAT and that function in acyl chain remodeling of phospholipids (Golczak et al., 2012; Mardian et al., 2015). The *in vivo* biological substrates and activities of most family members have not yet been elucidated. LRAT is the best characterized family member, which catalyzes the formation of retinyl esters by transferring an acyl group from the *sn-1* position of PC onto ROH. The substrate specificity of LRAT for PC as acyl donor is intriguing. LD size is regulated by several factors including PC synthesis (Krahmer et al., 2011). During LD growth, the expanding LD monolayer activates CTP:Phosphocholine cytidylyltransferase, a key enzyme in PC synthesis. LRAT degrades PC which may result in activation of the same PC synthesizing pathway. Alternatively, reduced PC concentrations may either destabilize LDs and induce coalescence of LDs or increase ER bilayer tension, thereby generating larger (merged) LDs. Concomitant with retinyl ester production, however, PC is converted to lyso-PC. The bilayer surface tension is reduced by lyso-phospholipids, facilitating LD budding and reducing LD size (Ben M'barek et al., 2017). Thus, counteracting forces contributing to LD size are involved in the generation of retinyl ester-loaded LDs. The N-terminus of LRAT tips the balance as it is required for the generation of large LDs in mammalian cells. The effect of the N-terminus of LRAT on LD size is specific for retinyl ester-mediated LD formation: despite its presence in CHO-k1 LRAT-GFP cells, it does not affect the size of TAG filled LDs (Fig. 4). Since the N-terminus of LRAT does not seem to affect the rate of LD formation, it could change the thermodynamic equilibrium and decreases the nucleation concentration. As a result, it would then also dictate where LD formation occurs. However, we did not observe a colocalization of LRAT with nascent LDs (data not shown). Therefore, we consider it more likely that the observed specific affinity of the LRAT N-terminus for retinyl esters is likely to play an important role in affecting LD size, for example by changing the membrane topology of LRAT. LRAT is anchored to the ER membrane by a single transmembrane spanning domain at the C-terminus and with the catalytic domain and the N-terminus oriented towards the cytoplasm (Moise et al., 2007). The production of retinyl esters results in a strongly enhanced membrane binding of the N-terminus as illustrated by the deeper embedding of the N-terminus in the membrane, combined with the specific interaction with retinyl esters. Indeed, in the absence of the N-terminus, LRAT maintains retinyl ester production but fails to generate large LDs. In addition to a direct interaction with retinyl esters, it can however not be excluded that the N-terminus of LRAT also affects lipid droplet size by interfering

with other mechanisms such as lipolysis and/or lipogenesis.

In summary, the molecular design of LRAT is well suited to store retinyl esters in LDs. With its C-terminal transmembrane domain, LRAT is anchored in the endoplasmic reticulum and directs newly synthesized retinyl esters in the lipid bilayer. The retinyl esters have the intrinsic capacity to form lipid droplets and with the N-terminal hydrophobic peptide LRAT specifically affects the size of retinyl ester-loaded lipid droplets.

Materials and Methods

Hepatic stellate cells isolation and cell culturing

Hepatic stellate cells (HSCs) were isolated from 10–12 week-old male mice (C57BL/6J background, wild-type pubs from crossed LRAT$^{-/-}$ heterozygote (Liu and Gudas, 2005 mice) as described before (Riccalton-Banks et al., 2003). Animals were handled according to governmental and international animal experimentation guidelines and laws. Experiments were approved by the Animal Experimentation Committee (Dierexperimen-tencommissie; DEC) of Utrecht University (DEC number 2013.III.02.016). After isolation, cells were protected from light and cultured on coverslips in 24-wells plates (Nunc, Roskilde, Denmark) in Dulbecco Modified Eagle Medium (DMEM) supplemented with 10% fetal bovine serum (FBS), 100 U/mL penicillin and 100 µg/mL streptomycin (all obtained from Gibco, Invitrogen GmbH, Lofer, Germany.

CHO-k1 cells were cultured in Ham's F-12 medium supplemented with 7.5% FBS, 100 units/ml penicillin, and 100 µg/mL streptomycin. The human hepatic stellate cell line LX-2 cells (kindly donated by Dr. Friedman (New York, NY, USA)) were grown in DMEM containing 10% FBS, 100 U/mL penicillin and 100 µg/mL streptomycin. All cells were maintained in a humidified incubator (5% CO2) at 37 °C. Depending on the experiment, cells were incubated with retinol (Sigma, stocks of 30 mM in EtOH), oleic acid (Sigma) coupled to fatty acid free-BSA (Sigma, stocks of 10 mM fatty acid in 12% BSA) and/or triacsin C (Cayman, stocks of 1 mg/mL in DMSO).

Retinol handling

Retinol (Sigma) was dissolved in ethanol (30 mM) and stored in 50 µL aliquots at −80°C. We routinely measured UV absorption spectra of retinol stocks before use and calculated the current stock concentration by making use of the molar extinction coefficient of retinol in EtOH (52,480 mol L^{-1} cm^{-1} at 325 nm) (Ross AC, 1981). In addition, we made use of the observation that after exposure to UV-light, a peak around 240 nm emerged, accompanied with a decrease around 325 nm. We routinely monitored E_{325}/E_{240} ratios and used exclusively stocks with a ratio of 5 or higher, which was estimated to correspond with a retinol integrity of about 70%.

Generation of stable cell lines

Human LRAT cDNA was synthesized and cloned into a pcDNA3.1(+) vector (Clontech, Palo Alto, California, USA) by a third party (GeneArt, Thermo Fisher Scientific, Waltham, MA, USA). In addition, the LRAT sequence was cloned into a pEGFP-N2 vector (Clontech), resulting in LRAT fused to the N-terminus of GFP. The construct coding for the deletion mutant (ΔNt-LRAT-GFP) was generated by site directed mutagenesis (New England Biolabs, Ipswich, MA). CHO-k1 and LX-2 cells were transiently transfected by Lipofectamine 2000 (Thermo Fisher) according to the manufacturer's instructions. Stable CHO-k1 cells expressing the various LRAT variants or control GFP were generated as follows. Cells (2×10^{6}) were electroporated in PBS with 15 µg DNA and a pulse of 260 V. After plating, cells were cultured for 48h in the absence and for 3 weeks in the presence of 1 mg/mL G-418 selection antibiotic (Thermo Fisher). Stable cells expressing GFP-fusion proteins were trypsinized and single GFP+cells with scatter properties (FSC and SSC) similar to their non-transfected counterparts were plated into 96-wells plates by FACS (Influx Cell Sorter, BD Biosciences). A GFP-negative gate was chosen to select monoclonal stable cells expressing non-fluorescent proteins. After plating, the monoclonal cells were allowed to grow until wells reached confluency. Clones with comparable morphology as compared to parental CHO-k1 cells (cell size, nucleus, lipid droplets) were selected. The absence or presence of LRAT enzymatic activity in LRAT, GFP, LRAT-GFP and ΔNt-LRAT-GFP expressing clones was confirmed by determination of retinyl esters (see below) and UV^{+}-autofluorescent lipid droplets in combination with GFP-fluorescence by FACS (FACSCanto II, BD Biosciences) after incubation of cells with retinol.

Confocal microscopy of mammalian cells

Cells were plated on Lab-Tek II 8-chamber slides (Thermo Fisher) and incubated as described in the figure legends. Cells were fixed in 4%

paraformaldehyde (Electron Microscopy Sciences Hatfield, PA, USA). Subsequently, cells were stained with either DAPI, BODIPY 493/503 (Thermo Fisher), and/or LD540 (kindly donated by Dr. C. Thiele, Bonn, Germany) (Spandl et al., 2009). Staining for immunofluorescence was performed with anti-desmin or anti-α smooth muscle actin (both from Thermo Scientific), followed by goat-anti-mouse-alexa647 or donkey-a-rabbit-alexa647 (Life Technologies, Paisley, UK). Cells were mounted with FluorSave (Calbiochem, Billerica, MA, USA) and subsequently imaged with a Leica TCS SPE Laser Scanning Spectral Confocal Microscope (Wetzlar, Germany) or a Nikon A1R confocal microscope (Amsterdam, The Netherlands) using preset settings for the representative dyes. For the detection of retinoid autofluorescence, presets for DAPI were used.

Quantification of cells with lipid droplet parameters

To quantify cells and lipid droplets, z-series of cells were imaged in tile-scan mode. Datasets were generated with either CellProfiler v2.2.0 (Kamentsky et al., 2011) or Imaris v8.2.0 (Bitplane, Belfast, Northern Ireland), both resulting in the identification of lipid droplets associated with individual cells. Data were subsequently expressed for individual cells containing 'cell size' (diameters of cells, in arbitrary units), 'number of lipid droplets per cell', 'mean lipid droplet volume per cell' (mean of all LD diameters of the cell to the 3rd power, in arbitrary units) and 'total lipid droplet volume per cell' (product of 'number of lipid droplets per cell' and 'mean lipid droplet volume per cell', in arbitrary units). Subsequently, the resulting data were processed with R v3.4.4 and RStudio v1.0.153 using R-packages 'openCyto' v1.14.0, 'reshape2' v1.4.2 and 'ggplot2' v2.2.1.

To analyze the lipid droplet size distribution, lipid droplet diameters were not linked to individual cells, but analyzed per condition. Ranges of LD-diameter bins were calculated using the limits of the first, second, third, fourth and fifth diameter quintile of all lipid droplets. LD-presence in each bin was counted per condition and expressed as percentage (all lipid droplets per condition were set to 100%).

Structured illumniation microscopy (3D-SIM)

After treatment, cells were stained with DAPI and HCS LipidTOX Red Neutral Lipid Stain (Thermo Fisher) and mounted with Vectashield Antifade Mounting Medium (Vector Laboratories, Burlingame, CA, USA). Structured illumniation microscopy was performed using a Deltavision OMX-V4 Blaze (GE Healthcare, Chicago, IL, United States) setup equipped with 4 sCMOS (PCO) cameras. Immersion oil with 1.516 refractive index (GE Healthcare) was placed on the 60x objective (Olympus U-PLAN APO, NA 1.42). Fluorophores were excited with a diode 405 nm (Vortran Stradus, 100 mW) and an OPSL 568 nm (Coherent, 100 mW) laser modulated to 1% by Neutral density filters. System supplied filter blocks were used to acquire fluorescence of DAPI (Ex: 382-409, Em: 421-450) and LipidTOX Red (Ex: 561-580, Em: 591-627). Raw images were processed using SoftWoRx software (GE Healthcare) with system OTFs pre-determined with 100 nm fluorescent polystyrene beads (Thermo scientific) and camera alignment parameters for the different channels (see supplemental materials). Acquired images were deconvolved using default settings (omitting Wiener filtering and background subtraction) including negative values (supplied as such in supplemental data) and intensities were linearly adjusted. Images in the figures are supplied as maximum intensity projections (movies are in supplemental data).

Lecithin:retinol acyltransferase activity assay

Lecithin:retinol acyltransferase activity in homogenates expressing various LRAT variants was performed as described previously (Golczak et al., 2015). Briefly, cells were cultured overnight in T-75 culture flasks (CELLSTAR, Greiner Bio-One GmbH, Frick-enhausen, Germany) under normal cell growth conditions. After scraping in ice-cold PBS, cells were homogenized on ice with 26-gauge needles (BD Bioscience, San Jose, CA, USA). Homogenates containing 200 µg total protein were mixed with reaction mix containing 5 mM DTT, 5 mM EDTA, 10 mM Tris-HCl (pH 8.0), 1% BSA, 0.2 µM ascorbic acid, 2 mM PC(7:0/7:0) and increasing amounts of retinol. Subsequently, mixtures were incubated for 60 min at 37oC in amber glass vials. Levels of retinyl heptanoate were determined by LC-MS/MS (see below). Km en vmax values were estimated using Michaelis-Menten kinetics.

Retinoids and neutral lipid determination by LC-MS/MS

Lipids were extracted as previously described (Bligh and Dyer, 1959). To avoid photo isomerization and oxidation of the retinoids, extractions were performed under red light and in amber tubes. In addition, 1 nmol butylated-hydroxytoluene was added to every sample. As internal standard, 250 pmol of retinyl acetate in MeOH/$CHCl_3$ (1:1, v/v) was added. The

combined chloroform phases were dried under nitrogen and stored at – 20 °C until further analysis.
Extract were dissolved in MeOH/CHCl3 (1:1) and stored in amber autosampler vials. To measure retinoids, samples were injected and separated on a 250 × 3.0 mm Synergi™ 4u Max-RP 80A column (4 µm particle size, Phenomenex, CO, USA) with a flow rate of 350 µL min^{-1}. To this end, a gradient (solvent A; acetonitrile:water (95:5), solvent B; acetone:chloroform (85:15), 0 min; 90% A, 5 min; 40% A, 17 min; 0% A, 19 min; 90% A, 25 min; 90% A) was generated by a Flexar UHPLC system (Perkin Elmer, Waltham, MA, USA). The column outlet was connected to a triple quadrupole mass spectrometry (API 4000 QTRAP, MDS Sciex/Applied Biosystems, Foster City, Canada) with an atmospheric pressure chemical ionization (APCI) ionization source (set to 500 °C). Multiple reaction monitoring (MRM) in positive ion mode was used to detect retinyl ester species with settings and m/z transitions as described before (Ajat et al., 2017). Chromatographic peaks were integrated and quantified using Analyst software version 1.4.3 (Applied Biosystems, Foster City, Canada).
To measure other neutral lipids (sterols, triacylglycerols, steryl esters), samples were injected and separated on a Kinetex/HALO C8 column (2.6 µm, 150 × 3.00 mm; Phenomenex, Torrance, CA, USA). A gradient of methanol:H_2O (5:5 v/v, solvent A) and methanol:isopropanol (8:2 v/v, solvent B) was generated by an Infinity II 1290 UPLC (Agilent, Santa Clara, CA, USA) and with a constant flow rate of 600 µL min^{-1} (0 min; 100% A, 2 min; 0% A, 8 min; 0% A, 8.5 min; 100% A, 10 min; 100% A). Lipids were measured using APCI in positive mode coupled to an Orbitrap Fusion mass spectrometer (Thermo Scientific, Waltham, MA, USA). Vendor data files were converted to mzML-format with msConvert (part of ProteoWizard v3.0.913) and processed with XCMS Online v3.7.0 (Tautenhahn et al., 2012).

Growth and fluorescence microscopy of yeast

Yeast strains and plasmids used in this study are described in Supplemental Table 1. Yeast were grown at 30°C in synthetic complete media containing 0.67% yeast nitrogen base without amino acids (United States Biological), 2% glucose, and an amino acid mix (United States Biological). Retinol (Sigma-Aldrich) was added to the medium at 4 mM together with 1% Igepal CA-630 (Sigma-Aldrich). Cells were stained with 0.5 µg/ml BODIPY 493/503 (Invitrogen) for 10 min and being washed once with phosphate buffered saline.
Yeast were imaged at 30 °C in an Environmental Chamber with a DeltaVision Spectris (Applied Precision Ltd.) comprising a wide-field inverted epifluorescence microscope (IX70; Olympus), a 100 Å~ NA 1.4 oil immersion objective (UPlanSAPO; Olympus), and a charge-coupled device Cool-Snap HQ camera (Photometrics).

Western blot analysis

Cells expressing LRAT-GFP and ΔN-LRAT-GFP were growth to logarithmic growth phase and 10 OD600 units of cells were washed once with H_20 and lysed with glass beads in a Precellys 24 homogenizer (Bertin Instruments). The lysate was cleared by centrifugation at 500 *x g* for 10 minutes at 4°C. The protein concentration of the lysate was determined using a Bradford assay (Thermo Scientific) and 10 µg of protein were separated by 4–12% of SDS-PAGE gel (Invitrogen), and transferred to nitrocellulose membranes at 120 V for 2 h. The membrane was analyzed using primary antibodies to GFP (1:1,000; Roche) and anti-porin (1:1,000; Invitrogen). Proteins were visualized using IRDye secondary anti-mouse antibody (Li-COR Biosciences; 1:10,000). The blots were visualized with an Odyssey infrared imaging system (Li-COR Biosciences).

LRAT mRNA expression by quantitative PCR

Expression of LRAT mRNA was determined as described (Tuohetahuntila et al., 2017). Briefly, RNA was isolated with a RNeasy Micro Kit (Qiagen, Venlo, The Netherlands) and cDNA was synthesized with an iScript cDNA Synthesis Kit (Bio-Rad). PCR amplifications were performed using a Bio-Rad detection system with iQ SYBR Green Supermix (Bio-Rad, Veenendaal, The Netherlands). Gene expression was normalized against reference genes, sequences of the primers are listed in Suppl. Table 2.

Molecular dynamics

MD simulations were set up and run using the DAFT protocol (Wassenaar et al., 2015a), according to procedures for building membrane/solvent systems using INSANE (Wassenaar et al., 2015b) and for generating membrane/solvent/protein systems as described in (Wassenaar et al., 2015a). The latter comprises a step for the generation of the LRAT-Nt peptide (sequence MKNPMLEVVSLLL-EKLLLISNFTLFSSGAAGEDKGRNSF; secondary structure LLLLHHHHHHHHHHHHHHLLLLL-LLLLLLLLLLLLLLL) or the CCTα P2 peptide (sequenceVEEKSIDLIQKWEEKSREFIGSFLEMF-G; secondary structure

HHHHHHHHHHHHHHHHHHHHHHHHHHHHHH), which was placed horizontally above the membrane. For docking simulations, the helix was placed at a distance 4 nm from the bilayer center with random rotation around the helix axes, while for assessment of the effect on lens formation speed, the helix was placed at 2.5 nm from the bilayer center, with the hydrophobic side facing towards the membrane. Simulations were performed using the coarse grain Martini 2.2 model (Marrink et al., 2004, 2007; Monticelli et al., 2008).

Simulations for assessing binding of LRAT-Nt AH to membranes with different compositions were set up in a hexagonal prism unit cell with a total number of 250 lipids per leaflet and a height of 9 nm. Simulations for assessing the lens forming propensity and speed, were set up in a hexagonal prism unit cell with base length of 24 nm and height of 10 nm, regardless of the presence or absence of protein. Numbers or ratios or lipids were set as described in the main text. All simulations were performed using Gromacs 2018.x (Pronk et al., 2013), using the automated Martini workflow *martinate* (Wassenaar et al., 2013).

Electron Microscopy

Yeast cells were grown in synthetic drop-out media lacking leucine at 30°C to an OD600 of approximately 0.6. IGEPAL (Sigma-Aldrich) was added to the cell cultures to a final concentration of 1%, prior to addition of retinol (Sigma-Aldrich) to a final concentration of 2 mM. Cells were then incubated for 10 min at 30°C before being processed for electron microscopy as follow. Cells were chemically fixed, embedded with 12% gelatin, cryo-sectioned and stained as previously described (Griffith et al., 2008). Sections were imaged in a FEI CM100bio electron microscope at 80 KV, equipped with a digital camera (Morada; Olympus). Two different grids with sections obtained from the same preparation were statistically evaluated by counting 75 randomly selected cell profiles before determining the average number of lipid droplets per cell section plus standard deviation between the two grids.

Monolayer tension measurements

Tension measurements were performed using a drop tensiometer device (Tracker, Teclis-IT Concept, France) (Ben M'barek et al., 2017). The principle of the drop profile analysis is based on the determination of the shape of a liquid drop suspended in another liquid form from a video image and its comparison with theoretical profiles calculated from the Gauss Laplace equation. The retinyl palmitate (Sigma, R-1512) drop (neutral lipid phase), with or without containing the DOPC phospholipid, was formed in buffer (50mM HEPES, 120mM potassium acetate, 1mM magnesium chloride, pH 7.4) at room temperature. The tension was allowed to stabilize for a few minutes (it decreases by the continuous absorption of phospholipids to the oil/water interface). Then, the drop is compressed by decreasing its volume, until complete saturation of the interface is reached (marked by a plateau of tension during compression).

Droplet interface bilayer (DIB) experiments

The DIB experiments was performed following the previous study of (Ben M'barek et al., 2017). An oil phase containing phospholipids was prepared first. DOPC, DOPE and DOPA were purchased from Avanti Polar Lipids, Inc. Lipids were mixed to the RP (Sigma, R-1512) oil at a final lipid concentration of 0.2% w/w (about 10% chloroform was in the final mixture in the case of DOPC initial stabilization of the DIBs, and we let it evaporate over time; for the other phospholipids, chloroform was evaporated prior to addition of RP). Then, an emulsion was prepared mixing the buffer with RP (1:5 v/v). Finally, the same volumes of emulsion and phospholipids in RP were put together, and the resulting emulsion was placed on a hydrophobic coverslip.

Interfacial tension measurements

A pendent droplet tensiometer designed by Teclis Instruments (Longessaigne, France) was used to measure the interfacial tension of oil/water interfaces. All experiments were conducted at room temperature. To create oil/buffer interfaces, oil drops (10µL) were formed at the tip of a J-needle submerged in 5 mL of HKM buffer.

10 µl of LRAT peptide solution in DMSO was added to the bulk buffer while the tension of trioleoylglycerol/buffer or retinyl palmitate/buffer interface was measured. The resulting concentration of peptide was 4.6 µM for both retinyl palmitate and trioleoylglycerol experiments. Oil-peptide surface tension was determined when the interfacial tension was stabilized.

After tension stabilization, the interface is compressed. The compression was then stopped, and area was kept constant as interfacial tension was recorded. Relaxation of the tension was observed only for trioleoylglycerol/buffer interfaces. Human LRAT peptide (AA 1-39) was synthesized by Bio-Synthesis (Lewisville, Texas, USA).

Statistical analyses

All figures were built in RStudio v1.0.153 (R v3.4.4) and processed in Inkscape v0.92.2. Barplots represent means ± standard deviation (SD) or standard error of the mean (SEM) as indicated in the figure legends. Statistical significance was determined by two-tailed paired or unpaired Welch's t-test or Wilcoxon rank sum test, or by Pearson's Chi-squared test, as indicated. In experiments with multiple testing, P-values were corrected by the Benjamini-Hochberg procedure. P-values below 0.05 were considered statistically significant.

Author Contributions

Conceptualization: J.B.H.; Methodology: M.R.M., T.A.W., A.R.T., W.A.P., J.B.H.; Software: T.A.W.; Formal Analysis: M.R.M., T.A.W.; Investigation: M.R.M., T.A.W., K.K.Y., A.T., M.C.M., L.C., A.C., M.W.H.; Writing – Original Draft: M.R.M., J.B.H.; Writing – Review & Editing: M.R.M., M.H., A.B.V., A.R.T., W.A.P., J.B.H.; Visualization: M.R.M., T.A.W., K.K.Y., M.C.M., L.C., A.C., R.W.W.; Supervision: M.H., A.B.V., F.R., A.R.T., W.A.P., J.B.H.; Project Administration: J.B.H.

References

Ajat, M., Molenaar, M., Brouwers, J.F.H.M., Vaandrager, A.B., Houweling, M., and Helms, J.B. (2017). Hepatic stellate cells retain the capacity to synthesize retinyl esters and to store neutral lipids in small lipid droplets in the absence of LRAT. Biochim. Biophys. Acta 1862, 176–187.
Google Scholar

Ajjaji, D., Ben M'barek, K., Mimmack, M.L., England, C., Herscovitz, H., Do ng, L., Kay, R.G., Patel, S., Saudek, V., Small, D.M., et al. (2019). Dual binding motifs underpin the hierarchical association of perilipins1-3 with lipid droplets. Mol. Biol. Cell 30, 703–716.
CrossRefGoogle Scholar

Anantharaman, V., and Aravind, L. (2003). Evolutionary history, structural features and biochemical diversity of the NlpC/P60 superfamily of enzymes. Genome Biol. 1–12.
Google Scholar

Ben M'barek, K., Ajjaji, D., Chorlay, A., Vanni, S., Forêt, L., and Thiam, A.R. (2017). ER Membrane Phospholipids and Surface Tension Control Cellular Lipid Droplet Formation. Dev. Cell 41, 591–604.e7.
Google Scholar

Bigay, J., Casella, J.-F., Drin, G., Mesmin, B., and Antonny, B. (2005). ArfGAP1 responds to membrane curvature through the folding of a lipid packing sensor motif. EMBO J. 24, 2244–2253.
Abstract/FREE Full TextGoogle Scholar

Blaner, W.S., O'Byrne, S.M., Wongsiriroj, N., Kluwe, J., D'Ambrosio, D.M., Jiang, H., Schwabe, R.F., Hillman, E.M.C. , Piantedosi, R., and Libien, J. (2009). Hepatic stellate cell lipid droplets: a specialized lipid droplet for retinoid storage. Biochim. Biophys. Acta 1791, 467–73.
CrossRefPubMedWeb of ScienceGoogle Scholar

Bligh, E.G., and Dyer, W.J. (1959). A rapid method of total lipid extraction and purification. Can. J. Biochem. Physiol. 37, 911–917.
CrossRefPubMedGoogle Scholar

Blomhoff, R., Green, M.H., Green, J.B., Berg, T., and Norum, K.R. (1991). Vitamin A metabolism: new perspectives on absorption, transport, and storage. Physiol. Rev. 71, 951–990.
PubMedWeb of ScienceGoogle Scholar

Boumann, H.A., Gubbens, J., Koorengevel, M.C., Oh, C.-S., Martin, C.E., Heck, A.J.R., Patton-Vogt, J., Henry, S.A., de Kruijff, B., and de Kroon, A.I.P.M. (2006). Depletion of phosphatidylcholine in yeast induces shortening and increased saturation of the lipid acyl chains: evidence for regulation of intrinsic membrane curvature in a eukaryote. Mol. Biol. Cell 17, 1006–17.
Abstract/FREE Full TextGoogle Scholar

Chelstowska, S., Widjaja-Adhi, M.A.K., Silvaroli, J.A., and Golczak, M. (2017). Impact of LCA-Associated E14L LRAT Mutation on Protein Stability and Retinoid Homeostasis. Biochemistry (Mosc.) 56, 4489–4499.
Google Scholar

Chorlay, A., and Thiam, A.R. (2018). An Asymmetry in Monolayer Tension Regulates Lipid Droplet Budding Direction. Biophys. J. 114, 631–640.
CrossRefPubMedGoogle Scholar

Choudhary, V., Ojha, N., Golden, A., and Prinz, W.A. (2015). A conserved family of proteins facilitates nascent lipid droplet budding from the ER. J. Cell Biol. 211, 261–271.
Abstract/FREE Full TextGoogle Scholar

Deslandes, F., Thiam, A.R., and Forêt, L. (2017). Lipid Droplets Can Spontaneously Bud Off from a Symmetric Bilayer. Biophys. J. 113, 15–18.
Google Scholar

Friedman, S.L. (2008). Hepatic Stellate Cells: Protean, Multifunctional, and Enigmatic Cells of the Liver. Phys. Rev. 125–172.
Google Scholar

Gautier, R., Douguet, D., Antonny, B., and Drin, G. (2008). HELIQUEST: a web server to screen sequences with specific alpha-helical properties. Bioinforma. Oxf. Engl. 24, 2101–2102.
Google Scholar

Golczak, M., Kiser, P.D., Sears, A.E., Lodowski, D.T., Bl aner, W.S., and Palczewski, K. (2012). Structural basis for

the acyltransferase activity of lecithin:retinol acyltransferase-like proteins. J. Biol. Chem. 287, 23790–807.
Abstract/FREE Full TextGoogle Scholar

Golczak, M., Sears, A.E., Kiser, P.D., and Palczewski, K. (2015). LRAT-specific domain facilitates vitamin A metabolism by domain swapping in HRASLS3. Nat. Chem. Biol. 11, 26–32.
CrossRefPubMedGoogle Scholar

Gottesman, M.E., Quadro, L., and Blaner, W.S. (2001). Studies of vitamin A metabolism in mouse model systems. BioEssays 23, 409–419.
CrossRefPubMedWeb of ScienceGoogle Scholar

Griffith, J., Mari, M., Mazière, A.D., and Reggiori, F. (2008). A Cryosectioning Procedure for the Ultrastructural Analysis and the Immunogold Labelling of Yeast Saccharomyces cerevisiae. Traffic 9, 1060–1072.
CrossRefPubMedWeb of ScienceGoogle Scholar

Hashemi, H.F., and Goodman, J.M. (2015). The life cycle of lipid droplets. Curr. Opin. Cell Biol. 33, 119–124.
CrossRefPubMedGoogle Scholar

Hernandez-Gea, V., and Friedman, S.L. (2011). Pathogenesis of liver fibrosis. Annu. Rev. Pathol. 6, 425–56.
CrossRefPubMedGoogle Scholar

Igal, R.A., Wang, P., and Coleman, R.A. (1997). Triacsin C blocks de novo synthesis of glycerolipids and cholesterol esters but not recycling of fatty acid into phospholipid: evidence for functionally separate pools of acyl-CoA. Biochem. J. 324, 529.
Abstract/FREE Full TextGoogle Scholar

Jiang, W., and Napoli, J.L. (2012). Reorganization of cellular retinol-binding protein type 1 and lecithin:retinol acyltransferase during retinyl ester biosynthesis. Biochim. Biophys. Acta 1820, 859–869.
CrossRefPubMedGoogle Scholar

Kamentsky, L., Jones, T.R., Fraser, A., Bray, M.-A., Logan, D.J., Madden, K.L., Ljosa, V., Rueden, C., Eliceiri, K.W., and Carpenter, A.E. (2011). Improved structure, function and compatibility for CellProfiler: modular high-throughput image analysis software. Bioinformatics 27, 1179–1180.
CrossRefPubMedWeb of ScienceGoogle Scholar

Kassan, A., Herms, A., Fernández-Vidal, A., Bosch, M., Schieber, N.L., Reddy, B.J.N., Fajardo, A., Gelabert-Baldrich, M., Tebar, F., Enrich, C., et al. (2013). Acyl-CoA synthetase 3 promotes lipid droplet biogenesis in ER microdomains. J. Cell Biol. 203, 985–1001.
Abstract/FREE Full TextGoogle Scholar

Khandelia, H., Duelund, L., Pakkanen, K.I., and Ipsen, J.H. (2010). Triglyceride blisters in lipid bilayers: implications for lipid droplet biogenesis and the mobile lipid signal in cancer cell membranes. PloS One 5, e12811.
CrossRefPubMedGoogle Scholar

Kluwe, J., Wongsiriroj, N., Troeger, J.S., Gwak, G.-Y., Dapito, D.H., Pradere, J.-P., Jiang, H., Siddiqi, M., Piantedosi, R., O'Byrne, S.M., et al. (2011). Absence of hepatic stellate cell retinoid lipid droplets does not enhance hepatic fibrosis but decreases hepatic carcinogenesis. Gut 1–10.
Google Scholar

Krahmer, N., Guo, Y., Wilfling, F., Hilger, M., Lingrell, S., Heger, K., Newman, H.W., Schmidt-Supprian, M., Vance, D.E., Mann, M., et al. (2011). Phosphatidylcholine synthesis for lipid droplet expansion is mediated by localized activation of CTP:phosphocholine cytidylyltransferase. Cell Metab. 14, 504–15.
CrossRefPubMedWeb of ScienceGoogle Scholar

Krahmer, N., Farese, R.V., and Walther, T.C. (2013). Balancing the fat: lipid droplets and human disease. EMBO Mol. Med. 5, 973–983.
Abstract/FREE Full TextGoogle Scholar

Liu, L., and Gudas, L.J. (2005). Disruption of the lecithin:retinol acyltransferase gene makes mice more susceptible to vitamin A deficiency. J. Biol. Chem. 280, 40226–34.
Abstract/FREE Full TextGoogle Scholar

MacDonald, P.N., and Ong, D.E. (1988). A lecithin:retinol acyltransferase activity in human and rat liver. Biochem. Biophys. Res. Commun. 156, 157–63.
CrossRefPubMedWeb of ScienceGoogle Scholar

Mardian, E.B., Bradley, R.M., and Duncan, R.E. (2015). The HRASLS (PLA/AT) subfamily of enzymes. J. Biomed. Sci. 22, 99.
CrossRefPubMedGoogle Scholar

Marrink, S.J., de Vries, A.H., and Mark, A.E. (2004). Coarse Grained Model for Semiquantitative Lipid Simulations. J. Phys. Chem. B 108, 750–760.
CrossRefGoogle Scholar

Marrink, S.J., Risselada, H.J., Yefimov, S., Tieleman, D. P., and de Vries, A.H. (2007). The MARTINI force field: coarse grained model for biomolecular simulations. J. Phys. Chem. B 111, 7812–7824.
CrossRefPubMedGoogle Scholar

Mederacke, I., Hsu, C.C., Troeger, J.S., Huebener, P., M u, X., Dapito, D.H., Pradere, J.-P., and Schwabe, R.F. (2013). Fate tracing reveals hepatic stellate cells as dominant contributors to liver fibrosis independent of its aetiology. Nat. Commun. 4, 2823.
CrossRefPubMedGoogle Scholar

Moise, A.R., Golczak, M., Imanishi, Y., and Palczewski, K. (2007). Topology and membrane association of lecithin: retinol acyltransferase. J. Biol. Chem. 282, 2081–90.
Abstract/FREE Full TextGoogle Scholar

Molenaar, M.R., Vaandrager, A.B., and Helms, J.B. (2017). Some Lipid Droplets Are More Equal Than Others: Different Metabolic Lipid Droplet Pools in Hepatic Stellate Cells. Lipid Insights 10, 1178635317747281.
Google Scholar

Monticelli, L., Kandasamy, S.K., Periole, X., Larson, R.G. , Tieleman, D.P., and Marrink, S.-J. (2008). The MARTINI Coarse-Grained Force Field: Extension to Proteins. J. Chem. Theory Comput. 4, 819–834.
CrossRefPubMedWeb of ScienceGoogle Scholar

Mitsche, M.A., and Small, D.M. (2013). Surface pressure-dependent conformation change of apolipoprotein-derived amphipathic α-helices. J. Lipid Res. 54, 1578–1588.
Abstract/FREE Full TextGoogle Scholar

O'Byrne, S.M., Wongsiriroj, N., Libien, J., Vogel, S., Goldberg, I.J., Baehr, W., Palczewski, K.,
and Blaner, W.S. (2005). Retinoid absorption and storage is impaired in mice lacking lecithin:retinol acyltransferase (LRAT). J. Biol. Chem. 280, 35647–57.
Abstract/FREE Full TextGoogle Scholar

Orland, M.D., Anwar, K., Cromley, D., Chu, C.-H., Chen, L., Billheimer, J.T., Hussain, M.M.,
and Cheng, D. (2005). Acyl coenzyme A dependent retinol esterification by acyl coenzyme A: diacylglycerol acyltransferase 1. Biochim. Biophys. Acta 1737, 76–82.
CrossRefPubMedGoogle Scholar

Pol, A., Gross, S.P., and Parton, R.G. (2014). Review: biogenesis of the multifunctional lipid droplet: lipids, proteins, and sites. J. Cell Biol. 204, 635–46.
Abstract/FREE Full TextGoogle Scholar

Prévost, C., Sharp, M.E., Kory, N., Lin, Q., Voth, G.A., Farese, R.V., and Walther, T.C. (2018). Mechanism and Determinants of Amphipathic Helix-Containing Protein Targeting to Lipid Droplets. Dev. Cell 44, 73–86.e4.
CrossRefGoogle Scholar

Pronk, S., Páll, S., Schulz, R., Larsson, P., Bjelkmar, P., Apostolov, R., Shirts, M.R., Smith, J.C., Kasson, P.M., van der Spoel, D., et al. (2013). GROMACS 4.5: a high-throughput and highly parallel open source molecular simulation toolkit. Bioinforma. Oxf. Engl. 29, 845–854.
Google Scholar

Riccalton-Banks, L., Liew, C., Bhandari, R., Fry, J.,
and Shakesheff, K. (2003). Long-term culture of functional liver tissue: three-dimensional coculture of primary hepatocytes and stellate cells. Tissue Eng. 9, 401–410.
PubMedGoogle Scholar

Ross, A.C. (1981). Separation of long-chain fatty acid esters of retinol by high-performance liquid chromatography. Anal. Biochem. 115, 324–330.
CrossRefPubMedGoogle Scholar

Ross, A.C., and Zolfaghari, R. (2004). Regulation of Hepatic Retinol Metabolism: Perspectives from Studies on Vitamin A Status. J. Nutr. 134, 269S–275S.
Abstract/FREE Full TextGoogle Scholar

Ruiz, A., and Bok, D. (2010). Focus on molecules: lecithin retinol acyltransferase. Exp. Eye Res. 90, 186–7.
CrossRefPubMedGoogle Scholar

Ruiz, a, Winston, A., Lim, Y.H., Gilbert, B.A., Rando, R.R ., and Bok, D. (1999). Molecular and biochemical characterization of lecithin retinol acyltransferase. J. Biol. Chem. 274, 3834–41.
Abstract/FREE Full TextGoogle Scholar

Sandager, L., Gustavsson, M.H., Stahl, U., Dahlqvist, A., Wiberg, E., Banas, A., Lenman, M., Ronne, H.,
and Stymne, S. (2002). Storage Lipid Synthesis Is Non-essential in Yeast. J. Biol. Chem. 277, 6478–6482.
Abstract/FREE Full TextGoogle Scholar

Small, D.M., Wang, L., and Mitsche, M.A. (2009). The adsorption of biological peptides and proteins at the oil/water interface. A potentially important but largely unexplored field. J. Lipid Res. 50 Suppl, S329–334.
Abstract/FREE Full TextGoogle Scholar

Spandl, J., White, D.J., Peychl, J.,
and Thiele, C. (2009). Live cell multicolor imaging of lipid droplets with a new dye, LD540. Traffic Cph. Den. 10, 1579–84.
Google Scholar

Tautenhahn, R., Patti, G.J., Rinehart, D.,
and Siuzdak, G. (2012). XCMS Online: a web-based platform to process untargeted metabolomic data. Anal. Chem. 84, 5035–5039.
CrossRefPubMedGoogle Scholar

Testerink, N., Ajat, M., Houweling, M., Brouwers, J.F., Pully, V.V., van Manen, H.J., Otto, C., Helms, J.B., and Vaandrager, A.B. (2012). Replacement of retinyl esters by polyunsaturated triacylglycerol species in lipid droplets of hepatic stellate cells during activation. PLoS ONE 7.
Google Scholar

Thiam, A.R., and Beller, M. (2017). The why, when and how of lipid droplet diversity. J. Cell Sci. 130, 315–324.
Abstract/FREE Full TextGoogle Scholar

Thiam, A.R., and Forêt, L. (2016). The physics of lipid droplet nucleation, growth and budding. Biochim. Biophys. Acta 1861, 715–22.
CrossRefGoogle Scholar

Thoen, L.F.R., Guimarães, E.L.M., Dollé, L., Mannaerts, I ., Najimi, M., Sokal, E., and van Grunsven, L. a (2011). A role for autophagy during hepatic stellate cell activation. J. Hepatol. 55, 1353–1360.
CrossRefPubMedWeb of ScienceGoogle Scholar

Tuohetahuntila, M., Molenaar, M.R., Spee, B., Brouwers, J.F.J.F., Houweling, M., Vaandrager, A.B.,
and Helms, J.B.B. (2016). ATGL and DGAT1 are involved in the turnover of newly synthesized triacylglycerols in hepatic stellate cells. J. Lipid Res. 57, 1162–1174.
Abstract/FREE Full TextGoogle Scholar

Tuohetahuntila, M., Molenaar, M.R., Spee, B., Brouwers, J.F.J.F., Wubbolts, R., Houweling, M., Yan, C., Du, H., Vander Ven, B.C.B.C., Vaandrager, A.B., et al. (2017). Lysosome-mediated degradation of a distinct pool of lipid droplets during hepatic stellate cell activation. J. Biol. Chem. 292, 12436–12448.
Abstract/FREE Full TextGoogle Scholar

Vamparys, L., Gautier, R., Vanni, S., Bennett, W.F.D., Tieleman, D.P., Antonny, B., Etchebest, C., and Fuchs, P.F.J. (2013). Conical lipids in flat bilayers induce packing defects similar to that induced by positive curvature. Biophys. J. 104, 585–593.
CrossRefPubMedWeb of ScienceGoogle Scholar

Walther, T.C., and Farese, R.V. (2012). Lipid droplets and cellular lipid metabolism. Annu. Rev. Biochem. 81, 687–714.
CrossRefPubMedWeb of ScienceGoogle Scholar

Walther, T.C., Chung, J., and Farese, R.V. (2017). Lipid Droplet Biogenesis. Annu. Rev. Cell Dev. Biol. 33, 491–510.
CrossRefPubMedGoogle Scholar

Wassenaar, T.A., Ingólfsson, H.I., Priess, M., Marrink, S.J., and Schäfer, L.V. (2013). Mixing MARTINI: electrostatic coupling in hybrid atomistic-coarse-grained biomolecular simulations. J. Phys. Chem. B 117, 3516–3530.
CrossRefPubMedGoogle Scholar

Wassenaar, T.A., Pluhackova, K., Moussatova, A., Sengupta, D., Marrink, S.J., Tieleman, D.P., and Böckmann, R.A. (2015a). High-Throughput Simulations of Dimer and Trimer Assembly of Membrane Proteins. The DAFT Approach. J. Chem. Theory Comput. 11, 2278–91.
Google Scholar

Wassenaar, T.A., Ingólfsson, H.I., Böckmann, R.A., Tieleman, D.P., and Marrink, S.J. (2015b). Computational lipidomics with insane: A versatile tool for generating custom membranes for molecular simulations. J. Chem. Theory Comput. 11, 2144–2155.
CrossRefPubMedGoogle Scholar

Welte, M.A. (2015). Expanding roles for lipid droplets. Curr. Biol. 25, R470–R481.
CrossRefPubMedGoogle Scholar

Bibliographie

1. Tracie DeVries-Seimon, I. T., Yankun Li, Pin Mei Yao, Elizabeth Stone, Yibin Wang, Roger J. Davis, Richard Flavell. Cholesterol-induced macrophage apoptosis requires ER stress pathways and engagement of the type A scavenger receptor. *J. Cell Biol.* **171**, 61–73 (2005).
2. Suneil K. Koliwad, R. V. F., Ryan S. Streeper, Mara Monetti, Ivo Cornelissen, Liana Chan, Koji Terayama, Stephen Naylor, Meghana Rao, Brian Hubbard. DGAT1-dependent triacylglycerol storage by macrophages protects mice from diet-induced insulin resistance and inflammation. *J. Clin. Invest.* **120**, 756–767 (2010).
3. Laura L. Listenberger, J. E. S., Xianlin Han, Sarah E. Lewis, Sylvaine Cases, Robert V. Farese, Daniel S. Ory. Triglyceride accumulation protects against fatty acid-induced lipotoxicity. *Proc. Natl. Acad. Sci.* **100**, 3077–3082 (2003).
4. Zhihuan Li, M. A. W., Katharina Thiel, Peter J. Thul, Mathias Beller, Ronald P. Kühnlein. Lipid Droplets Control the Maternal Histone Supply of Drosophila Embryos. *Curr. Biol.* **22**, 2104–2113 (2012).
5. Richard Altmann. *Die Elementarorganismen und ihre Beziehungen zu den Zellen.* (Veit, 1894).
6. Tauchi-Sato, K., Ozeki, S., Houjou, T. & Taguchi, R. The Surface of Lipid Droplets Is a Phospholipid Monolayer with a Unique Fatty Acid Composition. *J. Biol. Chem.* **277**, 44507–44512 (2002).
7. Martin, S. & Parton, R. G. Lipid droplets: A unified view of a dynamic organelle. *Nat. Rev. Mol. Cell Biol.* **7**, 373–378 (2006).
8. Murphy, D. J. & Vance, J. Mechanisms of lipid-body formation. *Trends Biochem. Sci.* **24**, 109–115 (1999).
9. Yuki Ohsaki, T. F., Takeshi Kawai, Yukichika Yoshikawa, Jinglei Cheng, Eija Jokitalo. PML isoform II plays a critical role in nuclear lipid droplet formation. *J. Cell Biol.* **212**, 29–38 (2016).
10. James A. Olzmann, P. C. Dynamics and functions of lipid droplets. *Nat. Rev. Mol. Cell Biol.* **20**, 1 (2018).
11. Jacquier, N. *et al.* Lipid droplets are functionally connected to the endoplasmic reticulum in Saccharomyces cerevisiae. *J. Cell Sci.* **124**, 2424–2437 (2011).
12. Nicolas Jacquier, R. S., Shirish Mishra, Vineet Choudhary. Expression of oleosin and perilipins in yeast promotes formation of lipid droplets from the endoplasmic reticulum. *J Cell Sci* **126**, 5198–5209 (2013).
13. Buhman, K. K., Chen, H. C. & Farese Jr., R. V. The Enzymes of Neutral Lipid Synthesis. *J. Biol. Chem.* **276**, 40369–40372 (2001).
14. Toyoshi Fujimoto, R. G. P. Not Just Fat: The Structure and Function of the Lipid Droplet. *Cold Spring Harb. Perspect. Biol.* **3**, a004838 (2011).
15. Chao-Wen Wang, Y.-S. C., Yu-Hsuan Miao. Control of lipid droplet size in budding yeast requires the collaboration between Fld1 and Ldb16. *J. Cell Sci.* **127**, 1214–1228 (2014).
16. Antonio Daniel Barbosa, S. S., Hiroshi Sembongi, Wen-Min Su, Susana Abreu, Fulvio Reggiori, George M. Carman. Lipid partitioning at the nuclear envelope controls membrane biogenesis. *Mol. Biol. Cell* **26**, 3641–3657 (2015).

17. Rudolf Zechner, F. M., Robert Zimmermann, Thomas O. Eichmann, Sepp D. Kohlwein, Guenter Haemmerle, Achim Lass. FAT SIGNALS - Lipases and Lipolysis in Lipid Metabolism and Signaling. *Cell Metab.* **15**, 279–291 (2012).
18. Rajat Singh, M. J. C., Susmita Kaushik, Yongjun Wang, Youqing Xiang, Inna Novak, Masaaki Komatsu, Keiji Tanaka, Ana Maria Cuervo. Autophagy regulates lipid metabolism. *Nature* **458**, 1131 (2009).
19. Hong Wang, C. S., Ming Lei, Ru-ching Hsia. Chapter 8 Analysis of Lipid Droplets in Cardiac Muscle. *Methods Cell Biol.* **116**, 129–149 (2013).
20. Huina Zhang, P. L., Yang Wang, Jing Li, Jinhai Yu, Jing Pu, Linghai Li, Hongchao Zhang, Shuyan Zhang, Gong Peng, Fuquan Yang. Proteome of Skeletal Muscle Lipid Droplet Reveals Association with Mitochondria and Apolipoprotein A-I. *J. Proteome Res.* **10**, 4757–4768 (2011).
21. Angelika S. Rambold, J. L.-S., Sarah Cohen. Fatty Acid Trafficking in Starved Cells: Regulation by Lipid Droplet Lipolysis, Autophagy, and Mitochondrial Fusion Dynamics. *Dev. Cell* **32**, 678–692 (2015).
22. Hong Wang, C. S., Urmilla Sreenivasan, Urmilla Sreenevasan, Hong Hu, Andrew Saladino, Brian M. Polster, Linda M. Lund, Da-wei Gong, William C. Stanley. Perilipin 5, a lipid droplet-associated protein, provides physical and metabolic linkage to mitochondria. *J. Lipid Res.* **52**, 2159–2168 (2011).
23. Kannan, M., Lahiri, S., Liu, L.-K., Choudhary, V. & Prinz, W. A. Phosphatidylserine synthesis at membrane contact sites promotes its transport out of the ER. *J. Lipid Res.* jlr.M072959 (2017). doi:10.1194/jlr.M072959
24. Fei, W. *et al.* A role for phosphatidic acid in the formation of 'supersized' Lipid droplets. *PLoS Genet.* **7**, (2011).
25. Guo, Y. *et al.* Functional genomic screen reveals genes involved in lipid-droplet formation and utilization. *Nature* **453**, 657–661 (2008).
26. Julia Petschnigg, S. D. K., Heimo Wolinski, Dagmar Kolb, Günther Zellnig, Christoph F. Kurat, Klaus Natter. Good Fat, Essential Cellular Requirements for Triacylglycerol Synthesis to Maintain Membrane Homeostasis in Yeast. *J. Biol. Chem.* **284**, 30981–30993 (2009).
27. Nicolas Jacquier, R. S., Vineet Choudhary, Muriel Mari, Alexandre Toulmay, Fulvio Reggiori. Lipid droplets are functionally connected to the endoplasmic reticulum in Saccharomyces cerevisiae. *J. Cell Sci.* **124**, 2424–2437 (2011).
28. Horst Robenek, N. J. S., Oliver Hofnagel, Insa Buers, Mirko J. Robenek, David Troyer. Adipophilin-enriched domains in the ER membrane are sites of lipid droplet biogenesis. *J. Cell Sci.* **119**, 4215–4224 (2006).
29. Mishra, S. *et al.* Mature lipid droplets are accessible to ER luminal proteins. *J. Cell Sci.* **129**, 3803–3815 (2016).
30. W Mike Henne, J. M. G., Michael L. Reese. The assembly of lipid droplets and their roles in challenged cells. *EMBO J.* **37**, (2018).
31. Truc B. Nguyen, J. A. O., Sharon M. Louie, Joseph R. Daniele, Quan Tran, Andrew Dillin, Roberto Zoncu, Daniel K. Nomura. DGAT1-Dependent Lipid Droplet Biogenesis Protects Mitochondrial Function during Starvation-Induced Autophagy. *Dev. Cell* **42**, 9-21.e5 (2017).
32. Ofer Moldavski, M. S., Triana Amen, Smadar Levin-Zaidman, Miriam Eisenstein, Ilana Rogachev, Alexander Brandis, Daniel Kaganovich. Lipid Droplets Are Essential for Efficient Clearance of Cytosolic Inclusion Bodies. *Dev. Cell* **33**, 603–610 (2015).

33. Yuki Ohsaki, T. F., Jinglei Cheng, Akikazu Fujita, Toshinobu Tokumoto. Cytoplasmic Lipid Droplets Are Sites of Convergence of Proteasomal and Autophagic Degradation of Apolipoprotein B. *Mol. Biol. Cell* **17**, 2674–2683 (2006).
34. Jordan L. Cocchiaro, R. H. V., Yadunanda Kumar, Elizabeth R. Fischer, Ted Hackstadt. Cytoplasmic lipid droplets are translocated into the lumen of the Chlamydia trachomatis parasitophorous vacuole. *Proc. Natl. Acad. Sci.* **105**, 9379–9384 (2008).
35. Xiaoyu Hu, M. L. R., Derk Binns. The coccidian parasites Toxoplasma and Neospora dysregulate mammalian lipid droplet biogenesis. *J. Biol. Chem.* **292**, 11009–11020 (2017).
36. Sabrina J. Nolan, I. C., Julia D. Romano. Host lipid droplets: An important source of lipids salvaged by the intracellular parasite Toxoplasma gondii. *PLOS Pathog.* **13**, e1006362 (2017).
37. Charles Harris, M. O., Eva Herker, Robert V. Farese. Hepatitis C Virus Core Protein Decreases Lipid Droplet Turnover A MECHANISM FOR CORE-INDUCED STEATOSIS. *J. Biol. Chem.* **286**, 42615–42625 (2011).
38. KopiCoVá, Z. & VaVreiNoVá, S. Occurrence of squalene and cholesterol in various species of Czech freshwater fish. *Czech J. Food Sci.* **25**, 195 (2007).
39. Kayama, M., Tsuchiya, Y. & Nevenzel, J. C. The Hydrocarbons of Shark Liver Oils. *NIPPON SUISAN GAKKAISHI* **35**, 653–664 (1969).
40. Baker. Baker, E.A. (1982) Chemistry and Morphology of Plant Epicuticular Waxes. In Cutler, D.F., Alvin, K.L. and Price, C.E., Eds., The Plant Cuticle, Academic Press, London, 139-166. - References - Scientific Research Publishing. (1982). Available at: https://www.scirp.org/(S(i43dyn45teexjx455qlt3d2q))/reference/ReferencesPapers.aspx?ReferenceID=2107960. (Accessed: 26th September 2019)
41. Thiam, A. R. & Beller, M. The why, when and how of lipid droplet diversity. *J. Cell Sci.* **130**, 315–324 (2017).
42. Kumi Tauchi-Sato, T. F., Shintaro Ozeki, Toshiaki Houjou, Ryo Taguchi. The Surface of Lipid Droplets Is a Phospholipid Monolayer with a Unique Fatty Acid Composition. *J. Biol. Chem.* **277**, 44507–44512 (2002).
43. Wilfling, F. *et al.* Arf1/COPI machinery acts directly on lipid droplets and enables their connection to the ER for protein targeting. *eLife* **2014**, (2014).
44. Thiam, A. R., Farese Jr., R. V. & Walther, T. C. The biophysics and cell biology of lipid droplets. *Nat. Rev. Mol. Cell Biol.* **14**, 775–786 (2013).
45. Penno, A., Hackenbroich, G. & Thiele, C. Phospholipids and lipid droplets. *Biochim. Biophys. Acta - Mol. Cell Biol. Lipids* **1831**, 589–594 (2013).
46. Hongyuan Yang, M. C., Anne Galea, Vladimir Sytnyk. Controlling the size of lipid droplets: lipid and protein factors. *Curr. Opin. Cell Biol.* **24**, 509–516 (2012).
47. Li Yang, P. L., Yunfeng Ding, Yong Chen, Shuyan Zhang, Chaoxing Huo, Yang Wang, Jinhai Yu, Peng Zhang, Huimin Na, Huina Zhang, Yanbin Ma. The proteomics of lipid droplets: structure, dynamics, and functions of the organelle conserved from bacteria to humans. *J. Lipid Res.* **53**, 1245–1253 (2012).
48. Monica A. Schmidt, E. M. H. Suppression of Soybean Oleosin Produces Micro-Oil Bodies that Aggregate into Oil Body/ER Complexes. *Mol. Plant* **1**, 910–924 (2008).
49. Qiang Gao, J. M. G., Derk D. Binns, Lisa N. Kinch, Nick V. Grishin, Natalie Ortiz, Xiao Chen. Pet10p is a yeast perilipin that stabilizes lipid droplets and promotes their assembly. *J Cell Biol* **216**, jcb.201610013 (2017).
50. Carole Sztalryd, D. L. B. The perilipin family of lipid droplet proteins: Gatekeepers of intracellular lipolysis. *Biochim. Biophys. Acta BBA - Mol. Cell Biol. Lipids* **1862**, 1221–1232 (2017).

51. Dawn L. Brasaemle, C. L., Therese Barber, Alan R. Kimmel. Post-translational Regulation of Perilipin Expression STABILIZATION BY STORED INTRACELLULAR NEUTRAL LIPIDS. *J. Biol. Chem.* **272**, 9378–9387 (1997).
52. Si Young Cho, T. R. L., Eui Seok Shin, Pil Joon Park, Dong Wook Shin, Hui Kyoung Chang, Daegun Kim, Hyoung Ho Lee, Jeong Ho Lee, Shin Hyoung Kim, Min Jung Song, Ih-Seop Chang, Ok Sub Lee. Identification of Mouse Prp19p as a Lipid Droplet-associated Protein and Its Possible Involvement in the Biogenesis of Lipid Droplets. *J. Biol. Chem.* **282**, 2456–2465 (2007).
53. Natalie Krahmer, T. C. W., Maximiliane Hilger, Nora Kory, Florian Wilfling, Gabriele Stoehr, Matthias Mann, Robert V. Farese. Protein Correlation Profiles Identify Lipid Droplet Proteins with High Confidence. *Mol. Cell. Proteomics* **12**, 1115–1126 (2013).
54. Nathan E. Wolins, P. E. B., Dawn L. Brasaemle. A proposed model of fat packaging by exchangeable lipid droplet proteins. *FEBS Lett.* **580**, 5484–5491 (2006).
55. Natalie Krahmer, T. C. W., Yi Guo, Florian Wilfling, Maximiliane Hilger, Susanne Lingrell, Klaus Heger, Heather W. Newman, Marc Schmidt-Supprian, Dennis E. Vance, Matthias Mann, Robert V. Farese. Phosphatidylcholine Synthesis for Lipid Droplet Expansion Is Mediated by Localized Activation of CTP:Phosphocholine Cytidylyltransferase. *Cell Metab.* **14**, 504–515 (2011).
56. Florian Wilfling, T. C. W., Huajin Wang, Joel T. Haas, Natalie Krahmer, Travis J. Gould, Aki Uchida, Ji-Xin Cheng, Morven Graham, Romain Christiano, Florian Fröhlich, Xinran Liu, Kimberly K. Buhman, Rosalind A. Coleman, Joerg Bewersdorf, Robert V. Farese. Triacylglycerol Synthesis Enzymes Mediate Lipid Droplet Growth by Relocalizing from the ER to Lipid Droplets. *Dev. Cell* **24**, 384–399 (2013).
57. Hsieh, K. *et al.* Perilipin family members preferentially sequester to either triacylglycerol-specific or cholesteryl-esterspecific intracellular lipid storage droplets. *J. Cell Sci.* **125**, 4067–4076 (2012).
58. Christoph Thiele, J. S. Cell biology of lipid droplets. *Curr. Opin. Cell Biol.* **20**, 378–385 (2008).
59. Daniela Georgieva, D. L., Véronique Schmitt, Fernando Leal-Calderon. On the Possible Role of Surface Elasticity in Emulsion Stability. *Langmuir* **25**, 5565–5573 (2009).
60. Ella R. Hinson, P. C. The antiviral protein, viperin, localizes to lipid droplets via its N-terminal amphipathic α-helix. *Proc. Natl. Acad. Sci.* **106**, 20452–20457 (2009).
61. Alenka Čopič, C. L. J., Sandra Antoine-Bally, Manuel Giménez-Andrés, César La Torre Garay, Bruno Antonny, Marco M. Manni, Sophie Pagnotta, Jeanne Guihot. A giant amphipathic helix from a perilipin that is adapted for coating lipid droplets. *Nat. Commun.* **9**, 1332 (2018).
62. Abdou Rachid Thiam, T. C. W., Robert V. Farese Jr. The biophysics and cell biology of lipid droplets. *Nat. Rev. Mol. Cell Biol.* **14**, nrm3699 (2013).
63. Arpita Upadhyaya, M. P. S. Tension in Tubulovesicular Networks of Golgi and Endoplasmic Reticulum Membranes. *Biophys. J.* **86**, 2923–2928 (2004).
64. Kalthoum Ben M'barek, A. R. T., Dalila Ajjaji, Aymeric Chorlay, Stefano Vanni, Lionel Forêt. ER Membrane Phospholipids and Surface Tension Control Cellular Lipid Droplet Formation. *Dev. Cell* **41**, 591-604.e7 (2017).
65. Weiss, S. B., Kennedy, E. P. & Kiyasu, J. Y. The enzymatic synthesis of triglycerides. *J. Biol. Chem.* **235**, 40–44 (1960).
66. Sylvaine Cases, R. V. F., Sabine Novak, Yao-Wu Zheng, Heather M. Myers, Steven R. Lear, Eric Sande, Carrie B. Welch, Aldons J. Lusis, Thomas A. Spencer, Brian R. Krause, Sandra K. Erickson. ACAT-2, A Second Mammalian Acyl-CoA:Cholesterol

Acyltransferase ITS CLONING, EXPRESSION, AND CHARACTERIZATION. *J. Biol. Chem.* **273**, 26755–26764 (1998).

67. Sylvaine Cases, R. V. F., Scot Stone, Ping Zhou, Eric Yen, Bryan Tow, Kathryn D. Lardizabal, Toni Voelker. Cloning of DGAT2, a second mammalian diacylglycerol acyltransferase, and related family members. *J. Biol. Chem.* **276**, 38870–38876 (2001).
68. Kathryn D. Lardizabal, D. J. H., Jennifer T. Mai, Nicholas W. Wagner, Annette Wyrick, Toni Voelker. DGAT2 Is a New Diacylglycerol Acyltransferase Gene Family PURIFICATION, CLONING, AND EXPRESSION IN INSECT CELLS OF TWO POLYPEPTIDES FROM MORTIERELLA RAMANNIANA WITH DIACYLGLYCEROL ACYLTRANSFERASE ACTIVITY. *J. Biol. Chem.* **276**, 38862–38869 (2001).
69. Charles A. Harris, R. V. F., Joel T. Haas, Ryan S. Streeper, Scot J. Stone, Manju Kumari, Kui Yang, Xianlin Han, Nicholas Brownell, Richard W. Gross, Rudolf Zechner. DGAT enzymes are required for triacylglycerol synthesis and lipid droplets in adipocytes. *J. Lipid Res.* **52**, 657–667 (2011).
70. Chi-Liang Eric Yen, R. V. F., Mara Monetti, Betty J. Burri. The triacylglycerol synthesis enzyme DGAT1 also catalyzes the synthesis of diacylglycerols, waxes, and retinyl esters. *J. Lipid Res.* **46**, 1502–1511 (2005).
71. Claudio J. Villanueva, R. V. F., Mara Monetti, Michelle Shih, Ping Zhou, Steve M. Watkins, Sanjay Bhanot. Specific role for acyl CoA:Diacylglycerol acyltransferase 1 (Dgat1) in hepatic steatosis due to exogenous fatty acids. *Hepatology* **50**, 434–442 (2009).
72. Lars Kuerschner, C. T., Christine Moessinger. Imaging of Lipid Biosynthesis: How a Neutral Lipid Enters Lipid Droplets. *Traffic* **9**, 338–352 (2008).
73. Scot J. Stone, R. V. F., Malin C. Levin, Ping Zhou, Jiayi Han, Tobias C. Walther. The Endoplasmic Reticulum Enzyme DGAT2 Is Found in Mitochondria-associated Membranes and Has a Mitochondrial Targeting Signal That Promotes Its Association with Mitochondria. *J. Biol. Chem.* **284**, 5352–5361 (2009).
74. Zehra Irshad, V. A. Z., Federica Dimitri, Mark Christian. Diacylglycerol acyltransferase 2 links glucose utilization to fatty acid oxidation in the brown adipocytes. *J. Lipid Res.* **58**, 15–30 (2017).
75. Jenson Qi, M. A. C., Wensheng Lang, John G. Geisler, Ping Wang, Ioanna Petrounia, Selyna Mai, Charles Smith, Hossein Askari, Geoffrey T. Struble, Robyn Williams, Sanjay Bhanot, Brett P. Monia, Shariff Bayoumy, Eugene Grant, Gary W. Caldwell, Matthew J. Todd, Yin Liang, Micheal D. Gaul, Keith T. Demarest. The use of stable isotope-labeled glycerol and oleic acid to differentiate the hepatic functions of DGAT1 and -2. *J. Lipid Res.* **53**, 1106–1116 (2012).
76. Haja R. Wurie, V. A. Z., Linda Buckett. Diacylglycerol acyltransferase 2 acts upstream of diacylglycerol acyltransferase 1 and utilizes nascent diglycerides and de novo synthesized fatty acids in HepG2 cells. *FEBS J.* **279**, 3033–3047 (2012).
77. Hongyuan Yang, S. L. S., Martin Bard, Debora A. Bruner, Anne Gleeson, Richard J. Deckelbaum, Gordana Aljinovic, Thomas M. Pohl, Rodney Rothstein. Sterol Esterification in Yeast: A Two-Gene Process. *Science* **272**, 1353–1356 (1996).
78. Richard A. Anderson, L. L. R., Charles Joyce, Matthew Davis, Jerry W. Reagan, Michelle Clark, Gregory S. Shelness. Identification of a Form of Acyl-CoA:Cholesterol Acyltransferase Specific to Liver and Intestine in Nonhuman Primates. *J. Biol. Chem.* **273**, 26747–26754 (1998).

79. Peter Oelkers, S. L. S., Ajay Behari, Debra Cromley, Jeffrey T. Billheimer. Characterization of Two Human Genes Encoding Acyl Coenzyme A:Cholesterol Acyltransferase-related Enzymes. *J. Biol. Chem.* **273**, 26765–26771 (1998).
80. Amélie Bacle, S. V., Romain Gautier, Catherine L. Jackson, Patrick F. J. Fuchs. Interdigitation between Triglycerides and Lipids Modulates Surface Properties of Lipid Droplets. *Biophys. J.* **112**, 1417–1430 (2017).
81. Choudhary, V., Ojha, N., Golden, A. & Prinz, W. A. A conserved family of proteins facilitates nascent lipid droplet budding from the ER. *J. Cell Biol.* **211**, 261–271 (2015).
82. Abdou Rachid Thiam, L. F. The physics of lipid droplet nucleation, growth and budding. *Biochim. Biophys. Acta BBA - Mol. Cell Biol. Lipids* **1861**, 715–722 (2016).
83. J A Hamilton, D. M. S. Solubilization and localization of triolein in phosphatidylcholine bilayers: a 13C NMR study. *Proc. Natl. Acad. Sci.* **78**, 6878–6882 (1981).
84. Choudhary, V. *et al.* Architecture of Lipid Droplets in Endoplasmic Reticulum Is Determined by Phospholipid Intrinsic Curvature. *Curr. Biol.* **28**, 915-926.e9 (2018).
85. Anna V. Bulankina, S. H., Anke Deggerich, Dirk Wenzel, Kudzai Mutenda, Julia G. Wittmann, Markus G. Rudolph, Koert N. J. Burger. TIP47 functions in the biogenesis of lipid droplets. *J. Cell Biol.* **185**, 641–655 (2009).
86. Boutet, E. *et al.* Seipin deficiency alters fatty acid Δ9 desaturation and lipid droplet formation in Berardinelli-Seip congenital lipodystrophy. *Biochimie* **91**, 796–803 (2009).
87. Cartwright, B. R. *et al.* Seipin performs dissectible functions in promoting lipid droplet biogenesis and regulating droplet morphology. *Mol. Biol. Cell* **26**, 726–739 (2015).
88. Wang, S. *et al.* Seipin and the membrane-shaping protein Pex30 cooperate in organelle budding from the endoplasmic reticulum. *Nat. Commun.* **9**, (2018).
89. Adam Kassan, A. P., Albert Herms, Andrea Fernández-Vidal, Marta Bosch, Nicole L. Schieber, Babu J. N. Reddy, Alba Fajardo, Mariona Gelabert-Baldrich, Francesc Tebar, Carlos Enrich, Steven P. Gross, Robert G. Parton. Acyl-CoA synthetase 3 promotes lipid droplet biogenesis in ER microdomains. *J. Cell Biol.* **203**, 985–1001 (2013).
90. Florian Wilfling, R. V. F. J., Joel T. Haas, Tobias C. Walther. Lipid droplet biogenesis. *Curr. Opin. Cell Biol.* **29**, 39–45 (2014).
91. Wilfling, F. *et al.* Triacylglycerol synthesis enzymes mediate lipid droplet growth by relocalizing from the ER to lipid droplets. *Dev. Cell* **24**, 384–399 (2013).
92. Ohsaki, Y. *et al.* Biogenesis of cytoplasmic lipid droplets: From the lipid ester globule in the membrane to the visible structure. *Biochim. Biophys. Acta - Mol. Cell Biol. Lipids* **1791**, 399–407 (2009).
93. Abdou Rachid Thiam, M. B. The why, when and how of lipid droplet diversity. *J Cell Sci* **130**, jcs.192021 (2017).
94. David Paul, R. B., Vanesa Madan. Hepatitis C Virus RNA Replication and Assembly: Living on the Fat of the Land. *Cell Host Microbe* **16**, 569–579 (2014).
95. Stephen L. Sturley, M. M. H. Lipid droplet formation on opposing sides of the endoplasmic reticulum. *J. Lipid Res.* **53**, 1800–1810 (2012).
96. James H. Hurley, B. R., Evzen Boura, Lars-Anders Carlson. Membrane Budding. *Cell* **143**, 875–887 (2010).
97. Abdou Rachid Thiam, F. P., Bruno Antonny, Jing Wang, Jérôme Delacotte, Florian Wilfling, Tobias C. Walther, Rainer Beck, James E. Rothman. COPI buds 60-nm lipid droplets from reconstituted water–phospholipid–triacylglyceride interfaces, suggesting a tension clamp function. *Proc. Natl. Acad. Sci.* **110**, 13244–13249 (2013).
98. Chernomordik, L. V. & Kozlov, M. M. *Protein-lipid interplay in fusion and fission of biological membranes.* **72**, (2003).

99. Foret, L. Shape and energy of a membrane bud induced by protein coats or viral protein assembly. *Eur. Phys. J. E* **37**, (2014).
100. Saleem, M. *et al.* A balance between membrane elasticity and polymerization energy sets the shape of spherical clathrin coats. *Nat. Commun.* **6**, (2015).
101. Abdou Rachid Thiam, F. P. The Energy of COPI for Budding Membranes. *PLOS ONE* **10**, e0133757 (2015).
102. Thiam, A. R. & Pincet, F. The energy of COPI for budding membranes. *PLoS ONE* **10**, (2015).
103. Thiam, A. R. & Forêt, L. The physics of lipid droplet nucleation, growth and budding. *Biochim. Biophys. Acta - Mol. Cell Biol. Lipids* **1861**, 715–722 (2016).
104. Adeyo, O. *et al.* The yeast lipin orthologue Pah1p is important for biogenesis of lipid droplets. *J. Cell Biol.* **192**, 1043–1055 (2011).
105. Carolina Lundin, I. N., Rickard Nordström, Klaus Wagner, Christian Windpassinger, Helena Andersson, Gunnar von Heijne. Membrane topology of the human seipin protein. *FEBS Lett.* **580**, 2281–2284 (2006).
106. Veijo T Salo, E. I., Ilya Belevich, Shiqian Li, Leena Karhinen, Helena Vihinen, Corinne Vigouroux, Jocelyne Magré, Christoph Thiele, Maarit Hölttä-Vuori, Eija Jokitalo. Seipin regulates ER–lipid droplet contacts and cargo delivery. *EMBO J.* **35**, 2699–2716 (2016).
107. Huajin Wang, R. V. F., Michel Becuwe, Benjamin E. Housden, Chandramohan Chitraju, Ashley J. Porras, Morven M. Graham, Xinran N. Liu, Abdou Rachid Thiam, David B. Savage, Anil K. Agarwal, Abhimanyu Garg, Maria-Jesus Olarte, Qingqing Lin, Florian Fröhlich, Hans Kristian Hannibal-Bach, Srigokul Upadhyayula, Norbert Perrimon, Tomas Kirchhausen, Christer S. Ejsing, Tobias C. Walther. Seipin is required for converting nascent to mature lipid droplets. *eLife* **5**, e16582 (2016).
108. Derk Binns, J. M. G., SungKyung Lee, Christopher L. Hilton, Qiu-Xing Jiang. Seipin Is a Discrete Homooligomer. *Biochemistry* **49**, 10747–10755 (2010).
109. C. Londos, A. R. K., D. L. Brasaemle, J. Gruia-Gray, D. A. Servetnick, C. J. Schultz, D. M. Levin. Perilipin: unique proteins associated with intracellular neutral lipid droplets in adipocytes and steroidogenic cells. *Biochem. Soc. Trans.* **23**, 611–615 (1995).
110. McManaman, J. L. Lipid Transport in the Lactating Mammary Gland. *J. Mammary Gland Biol. Neoplasia* **19**, 35–42 (2014).
111. Welte, M. A. Expanding roles for lipid droplets. *Curr. Biol.* **25**, R470–R481 (2015).
112. Blanchette-Mackie, E. J. *et al.* Perilipin is located on the surface layer of intracellular lipid droplets in adipocytes. *J. Lipid Res.* **36**, 1211–1226 (1995).
113. René Bartz, K. D. C., Wen-Hong Li, Barney Venables, John K. Zehmer, Mary R. Roth, Ruth Welti, Richard G. W. Anderson, Pingsheng Liu. Lipidomics reveals that adiposomes store ether lipids and mediate phospholipid traffic,. *J. Lipid Res.* **48**, 837–847 (2007).
114. Diana N. D'Ambrosio, W. S. B., José L. Walewski, Robin D. Clugston, Paul D. Berk, Richard A. Rippe. Distinct Populations of Hepatic Stellate Cells in the Mouse Liver Have Different Capacities for Retinoid and Lipid Storage. *PLoS ONE* **6**, e24993 (2011).
115. Andrew P. Bailey, A. P. G., Grielof Koster, Christelle Guillermier, Elizabeth M. A. Hirst, James I. MacRae, Claude P. Lechene, Anthony D. Postle. Antioxidant Role for Lipid Droplets in a Stem Cell Niche of Drosophila. *Cell* **163**, 340–353 (2015).
116. Lucy Liu, H. J. B., Ke Zhang, Hector Sandoval, Shinya Yamamoto, Manish Jaiswal, Elisenda Sanz, Zhihong Li, Jessica Hui, Brett H. Graham, Albert Quintana. Glial Lipid Droplets and ROS Induced by Mitochondrial Defects Promote Neurodegeneration. *Cell* **160**, 177–190 (2015).

117. Thiam, A. R., Farese Jr, R. V. & Walther, T. C. The biophysics and cell biology of lipid droplets. *Nat. Rev. Mol. Cell Biol.* **14**, 775–786 (2013).
118. Salo, V. T. *et al.* Seipin Facilitates Triglyceride Flow to Lipid Droplet and Counteracts Droplet Ripening via Endoplasmic Reticulum Contact. *Dev. Cell* **50**, 478-493.e9 (2019).
119. Leal-Calderon, F., Schmitt, V. & Bibette, J. *Emulsion Science: Basic Principles.* (Springer-Verlag, 2007).
120. Eigenberg, K. E. & Chan, S. I. The effect of surface curvature on the head-group structure and phase transition properties of phospholipid bilayer vesicles. *Biochim. Biophys. Acta BBA - Biomembr.* **599**, 330–335 (1980).
121. Holmberg, K. *Novel Surfactants: Preparation Applications And Biodegradability, Second Edition, Revised And Expanded.* (CRC Press, 2003).
122. Cevc, G. *Phospholipids Handbook.* (CRC Press, 1993).
123. Findenegg, G. H. J. N. Israelachvili: Intermolecular and Surface Forces (With Applications to Colloidal and Biological Systems). Academic Press, London, Orlando, San Diego, New York, Toronto, Montreal, Sydney, Tokyo 1985. 296 Seiten, Preis: $ 65.00. *Berichte Bunsenges. Für Phys. Chem.* **90**, 1241–1242 (1986).
124. Moessinger, C., Kuerschner, L., Spandl, J., Shevchenko, A. & Thiele, C. Human lysophosphatidylcholine acyltransferases 1 and 2 are located in lipid droplets where they catalyze the formation of phosphatidylcholine. *J. Biol. Chem.* **286**, 21330–21339 (2011).
125. Prévost, C. *et al.* Mechanism and Determinants of Amphipathic Helix-Containing Protein Targeting to Lipid Droplets. *Dev. Cell* **44**, 73-86.e4 (2018).
126. Upadhyaya, A. & Sheetz, M. P. Tension in Tubulovesicular Networks of Golgi and Endoplasmic Reticulum Membranes. *Biophys. J.* **86**, 2923–2928 (2004).
127. Gubern, A. *et al.* Group IVA phospholipase A2 is necessary for the biogenesis of lipid droplets. *J. Biol. Chem.* **283**, 27369–27382 (2008).
128. Robin W. Klemm, H. Y. M., Justin P. Norton, Ronald A. Cole, Chen S. Li, Seong H. Park, Matthew M. Crane, Liying Li, Diana Jin, Alexandra Boye-Doe, Tina Y. Liu, Yoko Shibata, Hang Lu, Tom A. Rapoport, Robert V. Farese, Craig Blackstone, Yi Guo. A Conserved Role for Atlastin GTPases in Regulating Lipid Droplet Size. *Cell Rep.* **3**, 1465–1475 (2013).
129. Evans, null & Rawicz, null. Entropy-driven tension and bending elasticity in condensed-fluid membranes. *Phys. Rev. Lett.* **64**, 2094–2097 (1990).
130. Oglęcka, K., Rangamani, P., Liedberg, B., Kraut, R. S. & Parikh, A. N. Oscillatory phase separation in giant lipid vesicles induced by transmembrane osmotic differentials. *eLife* **3**, e03695 (2014).
131. Aymeric Chorlay, A. R. T. An Asymmetry in Monolayer Tension Regulates Lipid Droplet Budding Direction. *Biophys. J.* **114**, 631–640 (2018).
132. François Deslandes, L. F., Abdou Rachid Thiam. Lipid Droplets Can Spontaneously Bud Off from a Symmetric Bilayer. *Biophys. J.* **113**, 15–18 (2017).
133. Vineet Choudhary, W. A. P., Namrata Ojha, Andy Golden. A conserved family of proteins facilitates nascent lipid droplet budding from the ER. *J. Cell Biol.* **211**, 261–271 (2015).
134. Pouton, C. W. Lipid formulations for oral administration of drugs: non-emulsifying, self-emulsifying and 'self-microemulsifying' drug delivery systems. *Eur. J. Pharm. Sci.* **11**, S93–S98 (2000).
135. Thiam, A. R., Bremond, N. & Bibette, J. From stability to permeability of adhesive emulsion bilayers. *Langmuir* **28**, 6291–6298 (2012).

136. Ryan C Hayward, D. A. W., Andrew S. Utada, Nily Dan. Dewetting Instability during the Formation of Polymersomes from Block-Copolymer-Stabilized Double Emulsions. *Langmuir* **22**, 4457–4461 (2006).
137. Yanhong Li, R. D., Halim Kusumaatmaja, Reinhard Lipowsky. Wetting-Induced Budding of Vesicles in Contact with Several Aqueous Phases. *J. Phys. Chem. B* **116**, 1819–1823 (2012).
138. Kusumaatmaja, H. & Lipowsky, R. Droplet-induced budding transitions of membranes. *Soft Matter* **7**, 6914–6919 (2011).
139. Pierre-Gilles de Gennes, D. Q., Françoise Brochard-Wyart. Capillarity and Wetting Phenomena, Drops, Bubbles, Pearls, Waves. (2004). doi:10.1007/978-0-387-21656-0
140. N.E. Hotrum, G. A. van A., T. van Vliet, M. A. Cohen Stuart. Monitoring Entering and Spreading of Emulsion Droplets at an Expanding Air/Water Interface: A Novel Technique. *J. Colloid Interface Sci.* **247**, 125–131 (2002).
141. Daniel Bonn, E. R., Jens Eggers, Joseph Indekeu, Jacques Meunier. Wetting and spreading. *Rev. Mod. Phys.* **81**, 739–805 (2009).
142. Frumkin A. Die Kapillarkurve der höheren Fettsäuren und die Zustandsgleichung der Oberflächenschicht. *Z. Für Phys. Chem.* **116U**, 466 (1925).
143. V L Kolev, A. M., K. D. Danov, P. A. Kralchevsky, G. Broze. Comparison of the van der Waals and Frumkin Adsorption Isotherms for Sodium Dodecyl Sulfate at Various Salt Concentrations. *Langmuir* **18**, 9106–9109 (2002).
144. Anton, N., Pierrat, P., Lebeau, L., Vandamme, T. F. & Bouriat, P. A study of insoluble monolayers by deposition at a bubble interface. *Soft Matter* **9**, 10081–10091 (2013).
145. Yuki Ohsaki, T. F., Jinglei Cheng, Michitaka Suzuki, Yuki Shinohara, Akikazu Fujita. Biogenesis of cytoplasmic lipid droplets: From the lipid ester globule in the membrane to the visible structure. *Biochim. Biophys. Acta BBA - Mol. Cell Biol. Lipids* **1791**, 399–407 (2009).
146. Ohsaki, Y., Suzuki, M. & Fujimoto, T. Open questions in lipid droplet biology. *Chem. Biol.* **21**, 86–96 (2014).
147. Lagace, T. A. & Ridgway, N. D. The role of phospholipids in the biological activity and structure of the endoplasmic reticulum. *Biochim. Biophys. Acta - Mol. Cell Res.* **1833**, 2499–2510 (2013).
148. Adam J. Aitchison, N. D. R., Daniel J. Arsenault. Nuclear-localized CTP:phosphocholine cytidylyltransferase α regulates phosphatidylcholine synthesis required for lipid droplet biogenesis. *Mol. Biol. Cell* **26**, 2927–2938 (2015).
149. Jason D. Vevea, L. A. P., Enrique J. Garcia, Robin B. Chan, Bowen Zhou, Mei Schultz, Gilbert Di Paolo, J. Michael McCaffery. Role for Lipid Droplet Biogenesis and Microlipophagy in Adaptation to Lipid Imbalance in Yeast. *Dev. Cell* **35**, 584–599 (2015).
150. W. Robert Bishop, R. M. B. Assembly of the endoplasmic reticulum phospholipid bilayer: the phosphatidylcholine transporter. *Cell* **42**, 51–60 (1985).
151. Tobias C. Walther, R. V. F. Jr. Lipid Droplets and Cellular Lipid Metabolism. *Annu. Rev. Biochem.* **81**, 687–714 (2012).
152. Kai Hsieh, A. R. K., Yun Kyung Lee, Constantine Londos, Bruce M. Raaka, Knut Tomas Dalen. Perilipin family members preferentially sequester to either triacylglycerol-specific or cholesteryl-ester-specific intracellular lipid storage droplets. *J Cell Sci* **125**, 4067–4076 (2012).
153. Beate Katharina Straub, P. S., Pamela Stoeffel, Hans Heid, Ralf Zimbelmann. Differential pattern of lipid droplet-associated proteins and de novo perilipin expression in hepatocyte steatogenesis. *Hepatology* **47**, 1936–1946 (2008).

154. Thiam, A. R. *et al.* COPI buds 60-nm lipid droplets from reconstituted water-phospholipid- triacylglyceride interfaces, suggesting a tension clamp function. *Proc. Natl. Acad. Sci. U. S. A.* **110**, 13244–13249 (2013).
155. Giménez-Andrés, M., Čopič, A. & Antonny, B. The Many Faces of Amphipathic Helices. *Biomolecules* **8**, 45 (2018).
156. Molenaar, M. *et al.* Lecithin:Retinol Acyl Transferase (LRAT) induces the formation of lipid droplets. (2019). doi:10.1101/733931

RÉSUMÉ

En présence de surplus d'énergie, les cellules synthétisent des lipides neutres dans la bicouche du réticulum endoplasmique (RE). Ils démixent ensuite pour former de nouvelles organelles, les corps lipidiques (CLs), qui émergent principalement dans le cytoplasme et régulent le métabolisme énergétique et de nombreux processus cellulaires. Cette thèse étudie les mécanismes de cette biogenèse directionnelle des CLs à l'aide de la physique des émulsions. Pour cela, nous avons développé un système in vitro reproduisant la topologie des CLs en formation et avons montré que le comportement du CL dans une membrane était régit par un équilibre de tension de surface comme dans un système de mouillage à trois phases. La directionnalité de l'émergence des CLs est régulée par une asymétrie de tension entre les feuillets de la membrane. Nous avons ensuite essayé de comprendre comment la cellule pouvait imposer une telle différence de tension et avons découvert que les CLs artificiels émergeaient du feuillet présentant la meilleure couverture résultant de l'insertion de protéines ou de phospholipides. In vivo, l'émergence de CLs dépeuple le feuillet cytosolique du RE de ses phospholipides qui doivent être constamment remplacés pour assurer la bonne émergence des futurs CLs dans le cytoplasme. En accord avec cette hypothèse, des cellules manquant de phospholipides présentent de plus nombreux CLs en contact avec le lumen et un RE remodelé. Nos résultats révèlent une coopération active entre phospholipides et protéines pour extraire les CLs du RE. Les fonctions cellulaires des CLs sont essentiellement déterminées par leur protéome de surface. Les protéines y sont souvent recrutées spécifiquement à l'aide d'hélices amphipathiques (HAs) selon des mécanismes peu connus. Nos résultats montrent que les lipides neutres jouent un rôle prépondérant dans le recrutement spécifique des HAs et que la densité des phopholipides module simplement l'accès des HAs aux lipides neutres. Cette découverte permet de comprendre le recrutement de certaines HAs sur des sous-populations spécifiques de CLs. Cette thèse illustre comment la physique des émulsions peut apporter une compréhension originale des mécanismes régulant la biogenèse des CLs.

MOTS CLÉS

Métabolisme Lipidique, Corps Lipidiques, Physico-chimie des Emulsions, Biophysique des Membranes, Bourgeonnement et Démouillage, Recrutement de Protéines

ABSTRACT

Cells store excess energy in the form of neutral lipids that are synthesized and encapsulated within the inter-monolayer space of the endoplasmic reticulum (ER). Then these neutral lipids demix to form a new organelle named lipid droplets (LDs), which, surprisingly, bud off mostly toward the cytosol where they regulate metabolism and multiple biological processes. The purpose of this thesis is to investigate LD directional biogenesis through soft matter physics. We reconstituted LD formation topology by embedding artificial LDs into the inter-monolayer space of bilayer vesicles. We provide evidence that the droplet behavior in the membrane is recapitulated by the physics of three-phase wetting systems, controlled by the equilibrium of surface tensions. More precisely, slight tension asymmetries between the membrane monolayers regulate the droplet budding side. We then investigated how cells are able to impose the required tension asymmetry and found that model LDs emerge on the membrane leaflet of higher coverage resulting from the insertion of both proteins and phospholipids. In cells, continuous LD emergence on the cytosol would require a constant refill of phospholipids to the ER's cytosolic leaflet. Consistent with this model, cells deficient in phospholipids present an increased number of LDs exposed to the ER lumen and compensate the deficiency by remodeling the ER's shape. Our results reveal an active cooperation between phospholipids and proteins to extract LDs from the ER. LDs have several biological implications determined by proteins specifically targeted to their surface, mostly through amphipathic helix (AH) motifs. How such specificity is achieved remains elusive. Our results support that neutral lipids play a key role in determining AH binding specificity, and phospholipid packing simply modulates the amount of accessible surface. These findings help to understand how AHs bind to specific LD populations. In summary, our work offers new insights on the mechanisms regulating LDs biogenesis by using well-known soft matter physics tools.

KEYWORDS

Lipid Metabolism, Lipid Droplet, Emulsion Physical chemistery, Membrane Biophysic Science, Budding and Dewetting, Protein Binding